Universidade do Minho
Escola de Ciências

Natália Sofia Brandão Vilaça

Zeolite structures as cancer-targeted drug delivery carriers

fevereiro de 2018

Natália Sofia Brandão Vilaça **Zeolite structures as cancer-targeted drug delivery carriers**

UMinho | 2018

FCT Fundação para a Ciência e a Tecnologia
POPH QUALIFICAR E CRESCER
QREN QUADRO DE REFERÊNCIA ESTRATÉGICO NACIONAL
GOVERNO DA REPÚBLICA PORTUGUESA
UNIÃO EUROPEIA Fundo Social Europeu
NORTE2020 PROGRAMA OPERACIONAL REGIONAL DO NORTE
COMPETE 2020
PORTUGAL 2020

Universidade do Minho
Escola de Ciências

Natália Sofia Brandão Vilaça

Zeolite structures as cancer-targeted drug delivery carriers

Tese de Doutoramento em Ciências
Especialidade em Química

Trabalho efetuado sob a orientação da
Professora Doutora Isabel Correia Neves
da
Professora Doutora Fátima Baltazar
e da
Professora Doutora Luísa de Cola

fevereiro de 2018

STATEMENT OF INTEGRITY

I hereby declare having conducted my thesis with integrity. I confirm that I have not used plagiarism or any form of falsification of results in the process of the thesis elaboration.

I further declare that I have fully acknowledged the Code of Ethical Conduct of the University of Minho.

University of Minho, February, 2018

Full name: Natália Sofia Brandão Vilaça

Signature: Natália Sofia Brandão Vilaça

ACKNOWLEDGEMENTS

This thesis represents the end of one more step in my academic way. It was a difficult journey with many moments of discouragement, but during these four years of hard work I grew up and challenged myself to learn new things and to overcome the difficulties. No conquest is successful in an easy way without effort, so, in the end and despite all the problems, these were fruitful years!

The completion of this thesis was only possible by the contact, shared experiences and support from many people. Therefore, this is the place to write some words to express my gratitude to all these people.

First, I would like to address my acknowledgements to my supervisor, **Professor Isabel Correia Neves** for the opportunity to work with her and giving me her confidence to do this PhD thesis. Thank you for everything that I have learnt from you, for all your commitment, availability and support. Thank you also for the huge optimism and for every kind word when I was more discouraged and for never letting me give up.

To my supervisor, **Professor Fátima Baltazar**, I would like to say thanks for the opportunity to work with her and her group. Thank you for all your support, every kind word, availability and knowledge that you have shared with me.

To my co-supervisor, **Professor Luisa De Cola**, I would like to say thanks for accepting me in her group and giving me all that I need to develop a good work during my stay in Strasbourg.

To **Eko Adi Prasetyanto**, I would like to say thanks for his huge support during my stay in Strasbourg and during all my PhD work. Eko, you were always available to help me, even though you have other million things to do. Thank you for everything that you taught me and for all your support.

To **Professor António Maurício Fonseca**, I would like to say thanks for all his help and availability during my work.

To **Ricardo Totovao,** I would like to say thanks for all his help. Ric, you know how important were your support and friendship during my stay in Strasbourg. Thank you for all your help, for every lunch and “cake time” and for all the moments of laugh. You know, without you, my stay in Strasbourg would have been a bit harder.

To **all the colleagues** that I knew in Strasbourg, I would like to say thank you for all your support and for being nice to me during my stay in Strasbourg. Thank you all for welcoming me so warmly. It was a great pleasure to work with all of you!

To **Manuel Banõbre**, I would like to say thanks for the opportunity to work in his group at International Iberian Nanotechnology Laboratory (INL) and giving me his confidence to develop my work there.

For the whole **INL group**, thanks all for all the help, for every shared knowledge, and all the great moments that I had at INL. Thank you all for welcoming me so warmly. It was a great pleasure to work with you!

To **Liliana, Juliana and Soraia** that I had a pleasure to know in staying at INL, I would like to say thank you for every great moment that we had together, for every “coffee time”, for every “break time”, for every laugh, for every vent. Thanks so much for everything.

To **Filipa Santos** and **Sara Granja,** I would like to say thanks for all the help during the cellular experiments and during CAM assay experiments respectively.

For the whole **ICVS group** and every people that I met there, I would like to say thank you for all the support.

To **every people** that I met in the **Chemistry Department**, I would like to say thanks for all the support, for every “break time”, for every laugh and for every kind word.

To **Fundação para a Ciência e Tecnologia** (FCT), I would like to acknowlegde for the Ph.D. fellowship (SFRH/BD/97797/2013).

To **my friends**, for always being present to help, for always encouraging me and for every good moments that we had together.

To **my family**, thanks for always being present both in good and in bad times, for the teachings handed down, all the support, the affection, the dedication, being patient with me and for the encouragement in every moment.

Finally, to **Hugo**. Thanks for always being patient with me even during my ill-tempered days, for always being present, for never letting me give up, for your affection… Together we have been growing up and become stronger. I could write much more things on how important you are for me, but you already know that!

The research work here presented was financially supported by an individual fellowship (SFRH/BD/97797/2013) and by the strategic fundings of Centre of Chemistry (UID/QUI/00686/2013 and UID/QUI/0686/2016) and ICVS/3B's (POCI-01-0145-FEDER-007038) from the Fundação para Ciência e Tecnologia (FCT) and European Regional Development Fund (FEDER) funds, through the Competitiveness Factors Operational Programme (COMPETE). The projects: NORTE-01-0145-FEDER-000013 and BioTecNorte (operation NORTE-01-0145-FEDER-000004), from Northern Portugal Regional Operational Programme (NORTE 2020), under the Portugal 2020 Partnership Agreement, were also sponsoring this work. Part of this work was also partially supported by the NORTE 2020 and the FEDER under the Grant NORTE-45-2015-02, and by European Union's Horizon 2020 research and innovation programme under grant agreement Nº686009.

ABSTRACT

Cancer is one of the major health problems worldwide, counting thousands of new cases and deaths annually. The current modalities for cancer treatment include surgery, chemotherapy, radiotherapy and immunotherapy. However, occasionally some of these modalities cannot be used due to the stage of the tumor or have insufficient effect in tumor regression, whereby new therapy strategies are needed. The application of nanotechnology in cancer treatment opened the opportunity to develop new strategies, and drug delivery systems (DDS) can be found among them. The use of DDS has been reported in several studies as a promising approach for delivering drugs to the place of action and reduce the drawbacks of conventional drug administration. To develop these systems, biocompatible and non-toxic materials are needed, where the selected drug can be loaded. Among the several materials that could be used for DDS preparation, are zeolites.

The main objective of this work was the development of effective DDS based on zeolites to be used in breast and colorectal cancer treatment. Thus, several structures and their potential as carriers were investigated, as well as the mechanisms underlying zeolite internalization, exploring surface functionalization on zeolite toxicity and uptake by human cells and exploring the use of zeolites as magnetic resonance imaging agents.

The potential of the use of the anti-inflammatory drug salicylic acid, for breast cancer treatment, loaded into silica microporous and mesoporous structures, was assessed. It was observed that mesoporous structures had higher drug loading capacity than microporous structures. In terms of cytotoxicity, only DDS prepared with mesoporous structures were able to decrease cell growth. Overall, the results indicated the potential of salicylic acid for cancer treatment when loaded into mesoporous structures, but not when loaded into microporous structures. So, in order to study the potential of the microporous structures as host for DDS, an anticancer drug was used.

Then, three different zeolites (NaY, NaA and ZSM5) and one titanosilicate (ETS-10) were investigated as carriers for the anticancer drug 5-fluorouracil (5-FU) in order to select the most promising zeolite structures for further studies. The results showed the biocompatibility of these microporous structures since they were not toxic to colon or breast cancer cells. In addition, loading 5-FU in these structures led to potentiation of 5-FU and allowed the selection of two zeolites, NaY and LTL for the next studies.

To finalize the exploration of the potential of zeolite for DDS preparation, DDS were prepared, and their *in vitro* and *in vivo* efficacy were assessed. Results of the *in vitro* studies confirmed the potential of the DDS prepared with NaY and LTL (Zeo L) for breast, colorectal and melanoma cancers treatment since there was a significant inhibition of cell growth when cells are treated with the DDS, with potentiation of 5-FU effect compared to the free drug.

However, *in vivo* studies using the chick embryo chorioallantoic membrane as model (CAM) revealed that DDS induced a reduction in tumor perimeter for breast cancer cells, while no reduction was detected for colon tumors, under the used concentration of DDS.

Zeolite NaY magnetization revealed its potential as magnetic resonance imaging agent, opening new opportunities to prepare hybrid systems combining the encapsulating and delivery properties of the zeolites and the magnetic properties of biocompatible magnetite nanoparticles.

Considering the scarce studies on the internalization mechanisms of zeolite nanoparticles, the endocytic mechanisms involved in their internalization by human cells were explored. The results showed that zeolite internalization is likely mediated by caveolin-dependent endocytosis and it is also dependent on microtubule polymerization pathways. In these studies, the uptake of zeolite nanoparticles was assessed in the same cell lines. It was found that cancer cells internalize higher amounts of zeolite nanoparticles and at a faster rate than normal cells. The effect of zeolite surface functionalization plays also an important role in the cellular uptake. Based on the observations from these studies, it was possible to observe that positively-charged zeolite nanoparticles present higher uptake rates than negatively-charged zeolite nanoparticles.

This work provides a valuable contribution to the use of zeolites as carriers for DDS preparation and presents novel evidences about the biological mechanisms enrolled in the uptake of zeolite nanoparticles by human cells. Thus, the work performed in this thesis is not an end of a research project, but an important contribution to a better design of DDS based on zeolitic structures, opening new horizons for the application of these DDS in cancer treatment.

RESUMO

O cancro constitui um dos maiores problemas de saúde no mundo, contando anualmente com milhares de novos casos e mortes. As atuais abordagens de tratamento do cancro incluem cirurgia, quimioterapia, radioterapia e imunoterapia. Contudo, por vezes algumas não podem ser utilizadas devido à fase avançada do tumor ou por apresentarem pouco efeito na regressão do mesmo, pelo que são necessárias novas abordagens terapêuticas. A aplicação da nanotecnologia no tratamento do cancro, abriu a oportunidade de desenvolver novas estratégias, contando-se entre estas os sistemas de libertação de fármacos. Vários estudos têm reportado o uso destes sistemas como uma abordagem promissora para a entrega de fármacos no local de ação e na redução dos efeitos secundários associados aos sistemas de administração convencionais. Para o desenvolvimento de sistemas de libertação de fármacos, são necessários materiais biocompatíveis e não tóxicos onde o fármaco possa ser inserido. Entre o grande número de materiais que podem ser usados para a preparação destes sistemas, encontram-se os zeólitos.

O principal objetivo deste trabalho foi desenvolver sistemas de libertação de fármacos baseados em zeólitos para o tratamento do cancro colorretal e da mama. Assim, foram exploradas várias estruturas e avaliado o seu potencial como transportadores de fármacos, bem como os mecanismos subjacentes à internalização das partículas de zeólitos por células humanas tumorais. Foi também avaliado o efeito da funcionalização da superfície na toxicidade e internalização das nanopartículas nas células e explorado o uso de zeólitos como agentes para imagem de ressonância magnética (MRI).

Foi avaliado o potencial do uso do anti-inflamatório ácido salicílico para o tratamento do cancro da mama quando encapsulado em estruturas de sílica micro- e mesoporosas. Observou-se que as estruturas mesoporosas apresentavam maior capacidade de encapsulamento do fármaco do que as estruturas microporosas. Em termos de citotoxicidade, apenas os sistemas de libertação de fármacos preparados com estruturas mesoporosas foram capazes de reduzir o crescimento celular. No geral, os resultados indicaram o potencial do ácido salicílico para o tratamento do cancro quando encapsulado em estruturas mesoporosas, mas não quando encapsulado em estruturas microporosas. Assim, para estudar o potencial do uso das estruturas microporosas como material para a preparação de sistemas de libertação, foi utilizado um fármaco antineoplásico. Neste contexto, três zeólitos diferentes (NaY, NaA e ZSM5) e um titanosilicato (ETS-10) foram explorados como suportes para o fármaco antineoplásico 5-fluorouracilo (5-FU), de forma a selecionar as estruturas mais promissoras para os estudos seguintes. Os resultados demonstraram que estes materiais são biocompatíveis, uma vez que não se revelaram tóxicos para células do cancro colorretal e mama. Além disso, o encapsulamento do 5-FU nestas estruturas, levou a uma potenciação

do seu efeito. Este estudo permitiu a seleção de duas estruturas zeolíticas, NaY e LTL, para os estudos subsequentes.

Para finalizar a exploração do potencial dos zeólitos para a preparação de sistemas de libertação de fármacos, foram preparados sistemas usando os zeólitos NaY e L, e a sua eficácia *in vitro* e *in vivo* foi avaliada. Os resultados dos estudos *in vitro* confirmaram o potencial dos sistemas de libertação preparados com os zeólitos NaY e LTL (Zeo L) no tratamento do cancro da mama, colorretal e melanoma, uma vez que se verificou uma inibição significativa do crescimento celular quando as células foram tratadas com os sistemas. Verificou-se ainda uma potenciação do 5-FU quando comparado com o fármaco livre. Contudo, os estudos *in vivo* usando o modelo membrana corioalantóide de embrião de galinha (CAM), mostraram que, na concentração usada, os DDS induziram a redução dos tumores da linha Hs 578T, mas não dos tumores da linha RKO.

A magnetização do zeólito NaY revelou o seu potencial como agente para MRI, abrindo novas oportunidades para a preparação de sistemas híbridos que combinem as propriedades de encapsulação e libertação dos zeólitos e, as propriedades das nanopartículas magnéticas.

Uma vez que há poucos estudos sobre os mecanismos de internalização das nanopartículas de zeólitos, foram também estudados os mecanismos envolvidos na sua internalização em células humanas. Os resultados mostraram que a internalização dos zeólitos é principalmente mediada pela endocitose dependente da caveolina, sendo também dependente das vias envolvidas na polimerização dos microtúbulos. Nestes estudos, verificou-se ainda a internalização dos zeólitos em células humanas e observou-se que as células cancerígenas internalizam maior quantidade de zeólito a uma taxa mais rápida do que as células normais. Concluiu-se também que o efeito da funcionalização da superfície dos zeólitos desempenha um papel importante na internalização celular. Os resultados obtidos mostraram que nanopartículas de zeólitos positivamente carregadas têm maior capacidade de internalização do que partículas negativamente carregadas.

Em suma, este trabalho fornece uma contribuição importante sobre o uso de zeólitos para a preparação de sistemas de libertação controlada de fármacos e apresenta novas evidências sobre os mecanismos biológicos envolvidos na internalização dos zeólitos em células humanas. Assim, o trabalho desenvolvido nesta tese poderá contribuir para o desenvolvimento de melhores sistemas de libertação de fármacos baseados em estruturas zeolíticas, abrindo novos horizontes para a sua aplicação no tratamento do cancro.

CONTENTS

LIST OF FIGURES

CHAPTER 1

CHAPTER 2

SUBCHAPTER 2.1

SUBCHAPTER 2.2

SUBCHAPTER 2.3

CHAPTER 3

CHAPTER 4

SUBCHAPTER 4.1

SUBCHAPTER 4.2

LIST OF TABLES

CHAPTER 1

CHAPTER 2

SUBCHAPTER 2.1

SUBCHAPTER 2.2

SUBCHAPTER 2.3

ABBREVIATIONS

^{13}C CPMAS NMR	Solid-state cross-polarization magic angle spinning carbon-13 nuclear magnetic resonance
^{1}H NMR	Proton nuclear magnetic resonance
4sPCLDEAS	Four arm star-shaped Poly(ε-caprolactone)-b-poly((N,N-diethylaminoethyl methacrylate)-r-(N-(3-sulfopropyl)-N-methacryloxyethy-N,N-diethylammoniumbetaine)) micelles
5- FdUrd	5-fluoro-2'-deoxyuridine
5-FdUDP	5-fluoro-2'-deoxyuridine-5'-diphosphate;
5-FdUMP	5-fluoro-2'-deoxyuridine-5'-monophosphate;
5-FdUrd	5-fluoro-2'-deoxyuridine;
5-FdUTP	5-fluoro-2'-deoxyuridine-5'-triphosphate;
5-FU	5-fluorouracil
5-FUDP	5-fluorouridine-5'-diphosphate;
5-FUDP-sugars	5-FU-nucleotide sugars;
5-FUH2	5-fluoro-5,6-dihydro-uracil
5-FUrd	5-fluorouridine
5-FUTP	5-fluorouridine-5'-triphosphate;
AFM	Atomic force microscopy
AGS	Gastric adenocarcinoma cells
Apt1	RNA aptamer
ATCC	American Type Culture Collection
BF	Body fluid conditions
BSA	Bovine serum albumin
C3, C4 and C5	Complement fragments
CCPs	Clathrin-coated pits
CCVs	Clathrin-coated vesicles
CHO K1	Chinese Hamster Ovary cells
CLICs	Clathrin-independent carriers
CLZ	Clofazimine
COX-1	Cyclooxygenase-1
COX-2	Cyclooxygenase-2
COXs	Cyclooxygenases
CPT	Camptothecin
CR	Complement receptor
CRC	Curcumin

CRC-TCS-NPs/5-FU-TCS-NPs Curcumin/5-fluorouracil loaded thiolated chitosan nanoparticles

Cyt D	Cytochalasin D
DCX	Docetaxel
DDS	Drug delivery systems
DMEM	Dulbecco's modified Eagle's medium
DMEM/F12	Dulbecco's modified Eagle's medium F12
DNA	Deoxyribonucleic acid
DN-dyn2,	Dominant-negative protein dynamin 2
DN-Eps15,	Dominant-negative protein Eps 15
Dn-Rab5	Dominant-negative protein Rab5
DOX	Doxorubicin
DSF	Disulfiram
dTMP	Thymidine-5'-monophosphate
dUMP	2'-deoxyuridine-5'-monophosphate;
DXP	N,N'-bis(2,6-dimethylphenyl)perylene-3,4,9,10-tetracarboxylic diimide
EGF	Epidermal growth factor
EPR	Enhanced permeability and retention effect
ER	Estrogen receptor
ETS-10	Engelhard Titano Silicate
FACS	Flow citometry analysis
FAU	Faujasite
FBS	Fetal bovine serum
FDA	Food and Drug Administration
FdUMP	Fluoro-deoxyuridine monophosphate
FdUTP	5′-fluoro-2′deoxyuridine-5′-trifosfato
FE-SEM	Field emission scanning electron microscopy
FT	Ftorafur
FTIR	Fourier-transform infrared spectroscopy
FUMP	5-fluorouridine-5'-monophosphate
FUTP	5-fluorouridine-5′-triphosphate
GEEC	GPI-anchored protein-enriched early endosomal compartment
HER2	Epidermal growth factor receptor 2
hMSCs	Human mesenchymal stem cells
HNPCC	Hereditary nonpolyposis colorectal cancer
HPMC	Hydroxypropyl methyl cellulose
HPV	Human papilloma virus

Ig	Immunoglobulins
IZA	International Zeolite Association
Ki67LI	Ki67 labelling index
LDHs	Layered double hydroxides
LTL	Linde type L
MAS NMR	Magic-angles spinning nuclear magnetic resonance
MNNG/HOS	Human osteosarcoma cells
MNPs	Magnetic nanoparticles
MOF	Metal-organic framework
MSNs	Mesoporous silica nanoparticles
NPs	Nanoparticles
NPs-CLZ	Clofazimine in PLGA nanoparticles
NSAIDs	Non-steroidal anti-inflammatory drugs
P/S	Penicillin – Streptomycin
PAO	Phenylarsine oxide
PBS	Phosphate-buffered saline
PLGA	Poly(lactic-co-glycolic acid)
PLL	Poly-L-lysine
PNPs	Polymeric nanoparticles
pORF-hTRAIL	Therapeutic gene encoding human tumor necrosis factor-related apoptosis- inducing ligand
PR	Progesterone receptor
PRPP	5′-phosphoribosyl-1-pyrophosphate;
PTX	Paclitaxel
PVA	Polyvinyl alcohol
R8	Octaarginine peptide
RES	Reticuloendothelial system
RF	Radio-frequency
RNA	Ribonucleic acid
RT	Room temperature
SA	Salicylic acid
SEM	Scanning electron microscopy
SiRNA	Small interfering RNA
SLNs:	Solid lipid nanoparticles
SRB	Sulforhodamine B
TAT	Transactivator of transcription
TCA	Trichloroacetic acid

TEM	Transmission electron microscopy
TGA	Thermogravimetric analysis
THZ	Thioridazine
TiO_2/ZnS	Semiconductors zinc sulfide quantum dots
TNBC	Triple negative breast cancer
TS	Thymidylate syntase
UV/vis	Ultraviolet-visible spectroscopy
VER	Verapamil
XRD	Powder X-ray diffraction analysis

RESEARCH MOTIVATION AND THESIS OUTLINE

Developing drug delivery systems (DDS) for cancer treatment using nanomaterials as carriers is an important and developing area of research. A great effort has been put into this area, though there is still a need to further optimize the current DDS in order to develop more efficient systems.

Motivated by that, the ultimate goal of the work developed in this thesis is the development of efficient DDS based on zeolites structures to be used in the cancer context using breast and colorectal cancer cells as models. However, to achieve this goal, many steps had to be performed, namely: 1) evaluation, selection and synthesis of different porous structures to be used as nanocarriers for the encapsulation of drugs used in the treatment of breast and colorectal cancer; 2) assessment of the efficacy of DDS based on zeolite using *in vitro* and *in vivo* models; 3) exploration of the use of zeolites as hybrid materials to be used in magnetic resonance imaging (MRI) or hyperthermia treatments; 4) elucidating the internalization mechanisms associated with zeolite particles uptake by cells; 5) functionalization of the surface of zeolites to enhance their internalization and 5) assess the cytotoxicity of the materials *in vitro*.

This thesis is organized in five chapters, as follows:

Chapter 1: This introductory chapter aims to present a general overview about the necessary concepts to understand the work of this thesis.

Chapter 2: Exploration of zeolite structures as nanocarriers for encapsulated drugs for cancer treatment.

This chapter is composed by three subchapters:

Subchapter 2.1 consists in the use of salicylic acid (SA) encapsulated in porous materials as DDS for cancer treatment. In this chapter micro and mesoporous structures were selected as hosts for DDS using SA as drug model in breast and colon cancer cell lines, in order to investigate if the use of this anti-inflammatory drug loaded into zeolites is a promising strategy for cancer therapy.

Subchapter 2.2 is dedicated to the assessment of the most promising porous structures as DDS using 5-fluorouracil (5-FU) as anticancer drug. 5-FU, chemotherapeutic drug used for the treatment of several types of cancer, was loaded in the different microporous structures to

identify which structure is more promising. From this study, the zeolite structures NaY and LTL were selected for the following studies.

Subchapter 2.3 reports the preparation of DDS and assessment of their effect using *in vitro* and *in vivo* models. For this study, the chick embryo chorioallantoic membrane (CAM) was used as *in vivo* model, which allows to study tumor growth and angiogenesis.

Chapter 3 covers the exploration of the potential of the zeolite NaY as a hybrid material for MRI use and host for DDS. In the previous chapter, the potential of zeolites to be use as carriers to delivery drugs was already reported. This chapter goes deeper into the use of zeolite NaY and demonstrates the potential of this zeolite to be used as MRI agent.

Chapter 4: Characterization of the mechanisms involved in the uptake of zeolite nanocarriers by human cells.

This chapter is composed by two subchapters:

Subchapter 4.1 characterizes the biological mechanisms involved in the uptake of zeolite nanoparticles by cancer and normal human cells. In this chapter pharmacological inhibitors were used to investigate the endocytic pathways involved in zeolite internalization and the uptake of zeolite by human cells was also verified. The results suggested that the internalization of zeolite L is mediated by caveolin-dependent process.

Subchapter 4.2 goes deeper into the internalization mechanisms of zeolite L and describes the effect of the surface functionalization in the cellular uptake. This subchapter validates the studies performed in subchapter 4.1, using for this purpose six pharmacological inhibitors. The effect of zeolite L surface functionalization on cellular uptake was also studied using microscopy techniques to achieve this purpose.

Finally, **chapter 5** summarizes and integrates the main conclusions withdrawn from this work. Also, some suggestions for future work are presented.

The work developed in this thesis was carried out at the School of Sciences, Chemistry Department and School of Medicine, Life and Health Sciences Research Institute (ICVS), University of Minho, Braga, Portugal, and at the Institut de Science et d'Ingénierie Supramoléculaire (ISIS), University of Strasbourg, Strasbourg, France and at the International Iberian Nanotechnology Laboratory (INL), Braga, Portugal.

Scientific output

From this work six scientific papers were prepared. From that, three are already published, and three are submitted for publication in international peer review journals.

List of publications:

Chapter 2

Subchapter 2.1

N. Vilaça, F. Morais-Santos, A. F. Machado, A. Sirkecioğlu, M. F. R. Pereira, M. Sardo, J. Rocha, P. Parpot, A. M. Fonseca, F. Baltazar and I. C. Neves, Micro- and Mesoporous Structures as Drug Delivery Carriers for Salicylic Acid, *J. Phys. Chem. C*, 2015, **119**, 3589–3595.

Subchapter 2.2

N. Vilaça, A. F. Machado, F. Morais-Santos, R. Amorim, A. P. Neto, E. Logodin, M. F. R. Pereira, M. Sardo, J. Rocha, P. Parpot, A. M. Fonseca, F. Baltazar, I. C. Neves, Comparison of different silica microporous structures as drug delivery systems for *in vitro* models of solid tumors, *RSC Adv.*, 2017, **7**, 13104–13111.

Subchapter 2.3

N. Vilaça, S. Granja, E. A. Prasetyanto, A. M. Fonseca, L. De Cola, F. Baltazar, I. C. Neves, 5-FU drug delivery systems based on zeolites for cancer therapy: *in vitro* and *in vivo* studies, *submitted*.

Chapter 3

N. Vilaça, J. Gallo, R. Fernandes, F. Figueiredo, A. M. Fonseca, F. Baltazar, I. C. Neves, M. Bañobre-López, Synthesis, characterization and *in vitro* validation of magnetic NaY zeolite with T_2-MRI properties, *submitted*.

Chapter 4

Subchapter 4.1

N. Vilaça, R. Totovao, E. A. Prasetyanto, V. Miranda-Gonçalves, F. Morais-Santos, R. Fernandes, F. Figueiredo, M. Bañobre-López, A. M. Fonseca, L. De Cola, F. Baltazar, I. C. Neves, Internalization Studies of Zeolite Nanoparticles by Human Cells, *J. Mater. Chem. B*, 2018, **6**, 469-476.

Subchapter 4.2

N. Vilaça, E. A. Prasetyanto, R. Fernandes, F. Figueiredo, A. M. Fonseca, L. De Cola, F. Baltazar, I. C. Neves, Endorsement of endocytic pathway involved in the internalization of zeolite nanoparticles by human cells, *submitted*.

List of poster abstracts:

N. Vilaça, A. M. Fonseca, F. Baltazar, I. C. Neves, 5-fluorouracil encapsulated into zeolites as nanocarriers for cancer therapy, 21st International Symposium on Microencapsulation, 2017, Faro, Portugal.

N. Vilaça, A. M. Fonseca, F. Baltazar, I. C. Neves, Investigation of the internalization mechanisms of zeolite L nanoparticles in breast cells, 1st ICVS open day, 2017, Braga, Portugal.

N. Vilaça, F. Santos, R. Amorim, R. Totovao, E. A. Prasetyanto, A. M. Fonseca, L. De Cola, F. Baltazar, I. C. Neves, Internalization of zeolites as carriers for cellular delivery, 10º Encontro Nacional de Catálise e Materiais Porosos, 2016, Lisboa, Portugal.

N. Vilaça, F. Morais-Santos, R. Amorim, A. M. Fonseca, I. C. Neves, F. Baltazar, Effect of surface functionalization of zeolite L on cellular uptake in breast cancer and epithelial mammary cells, 2nd ASPIC International Congress, 2016, Porto, Portugal.

N. Vilaça, F. Santos, R. Amorim, R. Totovao, E. A. Prasetyanto, A. M. Fonseca, L. De Cola, F. Baltazar, I. C. Neves, Internalization and cytotoxicity of zeolites in breast cancer cells, AFM Biomed Conference, 2016, Porto, Portugal.

R. Totovao, **N. Vilaça,** E. A. Prasetyanto, L. De Cola, Stimuli-responsive hybrid organic / inorganic mesoporous silica nanoparticles for biomedical applications, Biointerfaces International, 2016, Zürich, Switzerland.

N. Vilaça, R. Amorim, P. Parpot, A. M. Fonseca, I. C. Neves, F. Baltazar, Zeolites as drug delivery systems for encapsulation of 5-fluorouracil *in vivo* an *in vitro* model of colorectal cancer, 1st ASPIC International Congress, 2014, Lisboa, Portugal.

N. Vilaça, F. Baltazar, A. M. Fonseca, I. C. Neves, Zeolites as helpful tools in carcinoma therapy, E3 Forum, 2014, Lisboa, Portugal.

CHAPTER 1

INTRODUCTION

The objective of this chapter is to focus on the general considerations about the preparation and applications of drug delivery systems (DDS) based on porous materials for the treatment of cancer, as this thesis has been outlined.

There are many porous materials used in the preparation of DDS, which present several advantages comparing with the conventional administration of drugs and allow to enhance the efficiency of disease treatment and to improve the quality of life of the patient. In the different porous materials described, zeolite aluminosilicates are good candidates to pursue these challenges since their inner and outer surfaces allow modifications. They are very attractive as nanocarriers because they are commercially available or can be synthesized easily, their surface allows modification and their size is tunable. Moreover, zeolites are essentially nontoxic, biocompatible, lack immunogenicity and their multifunctional potential, among others, make them highly attractive in many aspects of medicine. A description of the mechanisms of internalization of the particles and living cells is also presented, with a description of the different pathways involved, with a special focus on endocytosis. The factors influencing endocytosis are also reviewed, as well as the tools to identify the endocytic pathways involved in the endocytosis of nanoparticles. All these features, in combination with the ability of the zeolites to enter cells by endocytic pathways, naturally make them good carriers for delivering drugs inside cells.

1.1. CANCER

1.1.1. FACTS ABOUT CANCER

Cancer results from a breakdown of the regulatory mechanisms that govern normal cell behavior, resulting in uncontrolled cell growth and division, invading adjacent normal tissues and organs and eventually spreading throughout the body.[1,2] Abnormal proliferation can occur in any of the different cells in the body, and this is the reason why there are more than a hundred different types of cancer, which can have different behaviors and response to treatment. This abnormal growth results in a mass of cells, called tumor that may be either benign or malignant.[1] A benign tumor is confined to its original site and does not invade the normal tissue nor spreads to distant body sites. In turn, a malignant tumor is capable of spreading throughout the body via the circulatory or lymphatic systems, originating metastasis and invading surrounding normal tissues.[3]

Cancer is one of the leading causes of morbidity and death worldwide, counting approximately 14 million new cases in 2012 and 8.8 million deaths in 2015.[4] Bearing in mind the remarkable progress in medicine, with better ways of prevention, detection and treatment of cancer over the last decades, why is there still such a high number of new cases? In our day-to-day life, we are exposed to hazardous substances that are able to cause cancer, such as, radiation, chemicals and viruses. These agents are called **carcinogens** and can damage the DNA and induce mutations. Some examples are: the ultraviolet radiation, responsible for skin cancer; tobacco smoke, which is a major cause of lung cancer, as well as being involved in cancers of the oral cavity, pharynx, larynx, esophagus and others; aflatoxin, a food contaminant which can cause liver cancer; and human papilloma virus (HPV), responsible agent for cervical cancer.[5–7] Other carcinogens, called tumor promoters, can contribute to cancer development by stimulating cell proliferation rather than by inducing mutations. **Tumor promoter** forms principally benign tumors that could progress into cancer by multiple genetic changes. Important tumor promoters are hormones, especially estrogens. When the cells of the endometrium are exposed to excess of estrogen, it significantly increases the probability of a woman to develop endometrial cancer.[5] Beyond these factors, others can contribute to the development of cancer, for instance ageing since the incidence of cancer rises dramatically with age, the use of alcohol and unhealthy diet. Recently scientists concluded that the consumption of red and processed meat likely can have a carcinogenic effect.[8–10]

Cancer cells can be characterized by the following “hallmarks” of cancer proposed by Hanahan and Weinberg[11] (Figure 1.1): **Sustaining proliferative signaling**. Cancer cells are capable of sustaining chronic proliferation by producing growth signals that stimulate their own proliferation, leading to continuous autostimulation of cell division (autocrine growth

stimulation) and by having overactive signal receptors;[12] **Evading growth suppressors**. Growth suppressors are important to stop cell growth and proliferation; however, cancer cells can interrupt or ignore these factors as a result of mutations or alterations in tumor suppressor genes; **Activating invasion and metastasis**. Cancer cells lose the function of cell adhesion molecules, which contribute to their capacity to metastasize, spreading throughout the body and interfering with the function of normal tissues and organs; **Enabling replicative immortality**. After DNA damage, normal cells normally undergo apoptosis. In turn, cancer cells fail this mechanism, which contributes substantially to tumor development. In addition to evading apoptosis, cancer cells generally acquire the capacity for unlimited replication as a result of expression of telomerase, which is required to maintain the ends of eukaryotic chromosomes (telomeres);[5] **Inducing angiogenesis.** Cancer cells are able to stimulate the formation of new blood vessels (angiogenesis), to supply the tumor with oxygen and adequate nutrients for its growth. These new vessels are formed as response to growth factors secreted by cancer cells and are important not only in supporting the tumor growth, but also in metastasis; **Resisting cell death.** Contrary to what happens with normal cells that die by apoptosis when becoming old or damaged, cancer cells avoid this mechanism of cell death and continue to accumulate in the body.[11]

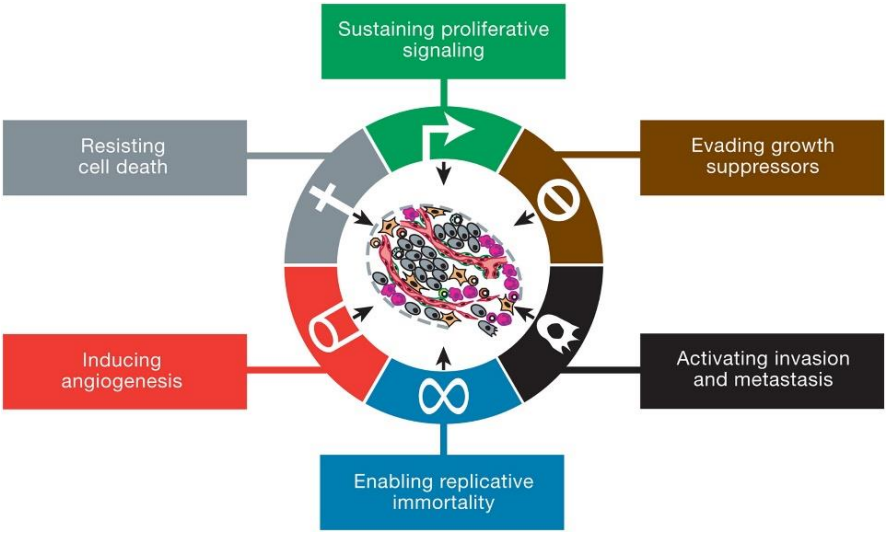

Figure 1.1: The six Hallmarks of Cancer.[11]

Despite the six hallmarks of cancer, nowadays there are two additional hallmarks suggested, involved in the pathogenesis of some and perhaps all cancers. The first one is related to the capability of cancer cells to modify and reprogram their cellular metabolism, allowing a better neoplastic proliferation. The second one refers to the capability of cancer cells to evade the immunological system, especially T and B lymphocytes, macrophages and natural killer cells.[11]

1.1.2. BREAST AND COLORECTAL CANCER

There are more than 100 types of cancer, however lung, breast, prostate and colorectal constitute over half of the overall incidence in Europe.[13,14] Despite a significant increase in lung cancer incidence in women in recent years (12% of all female cancers) as a result of tobacco epidemics, breast cancer is still the most common invasive tumor in women worldwide and the most frequent cause of death in women, which covers 25% of all cancer types.[15–18] Almost 362.000 new cases of breast cancer are diagnosed annually in Europe and was responsible for 92.000 deaths in 2012.[19] Whereas breast cancer incidence rates are still increasing in most of the European countries, mortality rates have been decreasing, as a result of earlier diagnosis and improved therapies.[17,20]

Breast cancer is a heterogeneous disease and can be divided into different subtypes related with human epidermal growth factor receptor 2 (HER2/ERBB2), expression of estrogen and progesterone receptor (ER and PR) and Ki67 protein. This cancer could be classified as luminal A, luminal B, HER2-positive, basal-like, normal-like and triple negative breast cancer (TNBC) (Table 1.1).[21,22] Breast cancer controlled by ERs and PR hormonal receptors has the best prognosis and its treatment is based on hormonal therapy. HER2 is a membrane receptor involved in cell proliferation signal transduction and breast cancer related with this receptor is very often sensitive to treatment with anti-HER2 therapies, such as humanized monoclonal antibodies or specific inhibitors. Ki67 is a proliferation protein marker that can be detected in proliferating cells by immunohistochemistry, Ki67 labelling index (Ki67LI). Ki67LI corresponds to the percentage of invasive cancer cell nuclei positive for Ki67 immunostaining, over the total invasive cancer cell nuclei present in a histological sample.[23] According to Ki67 index, tumors can be classified as low, intermediate, and highly proliferating for Ki67LI of ≤15%, 16%–30%, and >30%, respectively.[24] Ki67 can be used to classify a tumor as luminal A or B, allowing to find the best treatments. Tumors with high Ki67 expression (>15%) have a poor prognosis.[25,26] In turn, TNBC constitutes about 15-20% of all breast cancers. ERs and PRs receptors are absent in this type of cancer and HER2 has low expression or is absent. TNBC has a poor prognosis and has high propensity to exacerbate, being more common in young women.[27,28] In Table 1.1, it is possible to observe the breast cancer molecular subtypes and their main treatments. Luminal B tumors are positive for ER/PR receptors and can be positive or negative for HER2, and the patients with these tumors have worse prognosis than those with luminal A tumors.[29]

Table 1.1: The different subtypes of breast cancer, their main treatments and cell lines representative of each subtype.[25]

Subtype	EP/PR	HER2	Ki67	Treatment	Cell lines
Luminal A	+/+	-	< 15%	Antihormonal	MCF-7, T47D
Luminal B	+/+	-/+	> 15%	Antihormonal	BT474
HER2-type	-/-	+		Anti-HER2	SkBr3, AU565
TNBC	-/-	-/-	> 15%	Chemotherapy	Hs 578T, MDA-MB231

Colorectal cancer is the third most common cancer in men with 746.000 cases, representing 10.0% of the total cancers and the second in women with 614.000 cases, representing 9.2% of the total worldwide.[30,31] Every year, 345.000 new cases are diagnosed and 152.000 deaths are registered in both genders in Europe,[19,30,32] being the most frequently diagnosed cancer and second common cause of cancer related death.[33] The high incidence of this type of cancer could be related to various risk factors such as lack of physical activity, obesity, a diet low in fruits and vegetables, higher consumption of red and processed meat and smoking.[32,34–36] A large proportion of this cancer is associated with environmental factors, since only 20% of the colorectal cancer cases have a hereditary cause; and some are associated with very defined syndromes, namely familial adenomatous polyposis or Lynch syndrome (hereditary nonpolyposis colorectal cancer (HNPCC)).[37,38] Most colorectal cancers originate from the sigmoid colon or rectum and normally start to appear as benign polyps higher than one centimeter. Polyps with more than two centimeters can suffer from malignant alterations and polyps smaller than five millimeters rarely suffer from those alterations.[39]

The options for colorectal cancer treatment include surgery, chemotherapy and radiation. Recently, new therapies have been developed to target specific signaling pathways involved in colorectal carcinogenesis, such as epidermal growth factor receptor (EGFR) signaling and angiogenesis, called targeted therapy.[40] Targeted therapy then acts by different ways, the **anti-angiogenesis therapy** which blocks the process of making new blood vessels by blocking the VEGF signaling pathway and consequently the tumors do not get the nutrients and oxygen that they need to grow;[41] and **EGFR inhibition** where EGFR is blocked, preventing colorectal cancer cell proliferation.[42]

1.1.3. CANCER TREATMENTS

There are several types of cancer treatment such as surgery, radiotherapy, chemotherapy, immunotherapy, hyperthermia and others.[43,44] The kind of treatment depends on the type of

cancer and the stage of development at the time of diagnosis. In radiotherapy, tissues are exposed to ionizing radiation to induce DNA damage in malignant cells, cause apoptosis and thus shrink tumors and its impact depends on the sensitivity of the tumor to radiation.[45–47] This treatment is used as an adjuvant in chemotherapy in about 60% of all cancers, however this could have impact on healthy tissues.[47,48] In immunotherapy, some parts of a person's immune system are used to fight the cancer.[49,50] For this purpose, the immune system could be stimulated to attack cancer cells or could be given immune system components, such as proteins prepared from the immune system of the patient.[51] Dendritic cells are also used in immunotherapy as they can initiate strong and long-lived tumor-specific T- cell responses.[52,53] Hyperthermia treatment could be used as thermal sensitizer or thermal ablator.[54] It consists in increasing the temperature of a region of the tumor to 40-43 °C and is used as adjuvant of other cancer treatments such as chemotherapy and radiotherapy.[43,55,56]

When cancer is in early stage, surgery is normally the first option, since it is associated with high levels of success in terms of remission and cure, as it aims to remove 100% of the malignant cells.[47] However, many times when cancer is detected, it is already in advanced stage and, in these cases, beyond surgery other treatments, such as chemotherapy, are required.[57] Chemotherapy is needed in 70-80% of cancer patients, becoming one of the most commonly used treatments. This treatment prevents the proliferation of cancer cells, tumor recurrence and metastasis and consequently prolongs patient life time.[58,59] Despite its wide use, traditional chemotherapy is limited and has numerous short-term side effects, such as nausea and vomiting, hair loss, fatigue and bone marrow suppression, because chemotherapy affects not only cancer cells but also healthy cells of rapidly proliferation[60–62] and long-term side effects, such as cardiovascular diseases and infections.[63,64]

1.1.4. DRUGS USED IN CHEMOTHERAPY TREATMENTS

There are many drugs used in chemotherapy and they can be divided into classic chemotherapeutic drugs and targeted therapeutic drugs.

The most commonly used drugs in **breast cancer** treatments are paclitaxel (PTX), docetaxel (DCX), doxorubicin (DOX), 5-fluorouracil (5-FU), disulfiram (DSF) and camptothecin (CPT) which are classified as **classic chemotherapeutic drugs** and tamoxifen and torimefene which are classified as **targeted chemotherapeutic drugs.**[65–67] Tamoxifen and toremifene are selective estrogen receptor modulators (SERM) recommended for treatment of premenopausal women with hormone-sensitive (ER) disease and for the treatment of hormone receptor positive breast cancer, respectively.[67,68]

Some drugs approved for **colorectal cancer** treatment are irinotecan hydrochloride, oxaliplatin, capecitabine, 5-fluorouracil (5-FU) which are classified as **classic**

chemotherapeutic drugs and bevacizumab (Avastin®) which was the first anti-angiogenic monoclonal antibody approved by the American Food and Drug Administration (FDA),[69,70] cetuximab, panitumumab and ramucirumab which are classified as **targeted chemotherapeutic drugs**.[40,71–73] Cetuximab and panitumumab exert their effect on EGFR and ramucirumab inhibits VEGF and VEGF receptor.[74]

5-FU (Figure 1.2), a low molecular weight drug, was the first chemotherapeutic drug and it was discovered in 1957 by Charles Heidelberger.[59,75] This drug is used for the treatment of various types of solid cancers, including breast and colorectal cancers.[76,77]

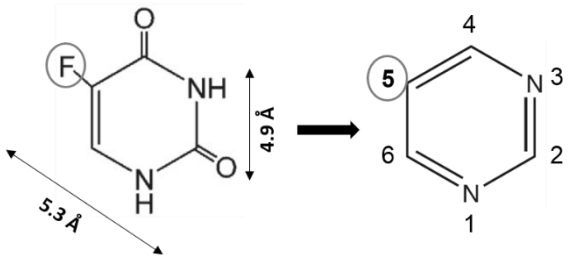

Figure 1.2: Chemical structure and molecular dimensions of 5-fluorouracil (left) and pyrimidine ring (right). The fluorine atom of 5-FU replaces the hydrogen at the 5-position of the pyrimidine ring. Adapted from.[78–80]

5-FU is an uracil analogue because it has a fluorine atom in carbon-5 position of the pyrimidine ring, instead of a hydrogen and thus to exert its cytotoxic effects, it needs cell uptake and conversion to its active forms.[81] The drug is quickly metabolized after its administration and originates different fluoronucleotides which have antineoplastic properties since it interferes with nucleic acid synthesis, retarding cancer cells growth.[82,83] 5-FU mechanism of action is associated with thymidylate syntase (TS) inhibition by fluoro-deoxyuridine monophosphate (FdUMP) and its incorporation into DNA and RNA.[81,84] After entering cells, 5-FU is incorporated into DNA when it is converted to 5′-fluoro-2′deoxyuridine-5′-trifosfato (FdUTP) and into RNA when it is converted to 5-fluorouridine-5′-triphosphate (FUTP). 5-FU can be metabolized by two metabolic pathways: i) the catabolic way, which inactivates the 80% of the drug in the liver, originating 5-fluoro-5,6-dihydro-uracil (5-FUH2) as metabolite; ii) the anabolic way, which originates active metabolites responsible for the cytotoxic effect of 5-FU on tumor cells, 5-fluorouridine-5'-monophosphate (FUMP), 5-fluorouridine (5-FUrd), 5-fluoro-2'-deoxyuridine (5- FdUrd) and their derivatives (Figures 1.3 and 1.4).[82]

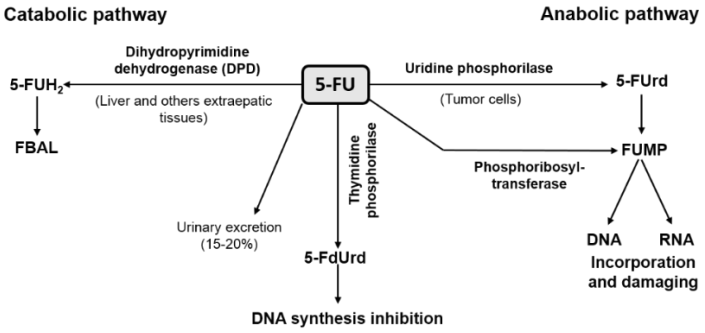

Figure 1.3: The catabolic and anabolic pathways of 5-flurouracil in human cells. Abbreviations: 5-FU, 5-fluorouracil; 5-FUH2, 5-fluoro-5,6-dihydro-uracil; 5-FUrd, 5-fluorouridine; 5-FdUrd, 5-fluoro-2'-deoxyuridine; FUMP, 5-fluorouridine-5'-monophosphate. Adapted from.[82]

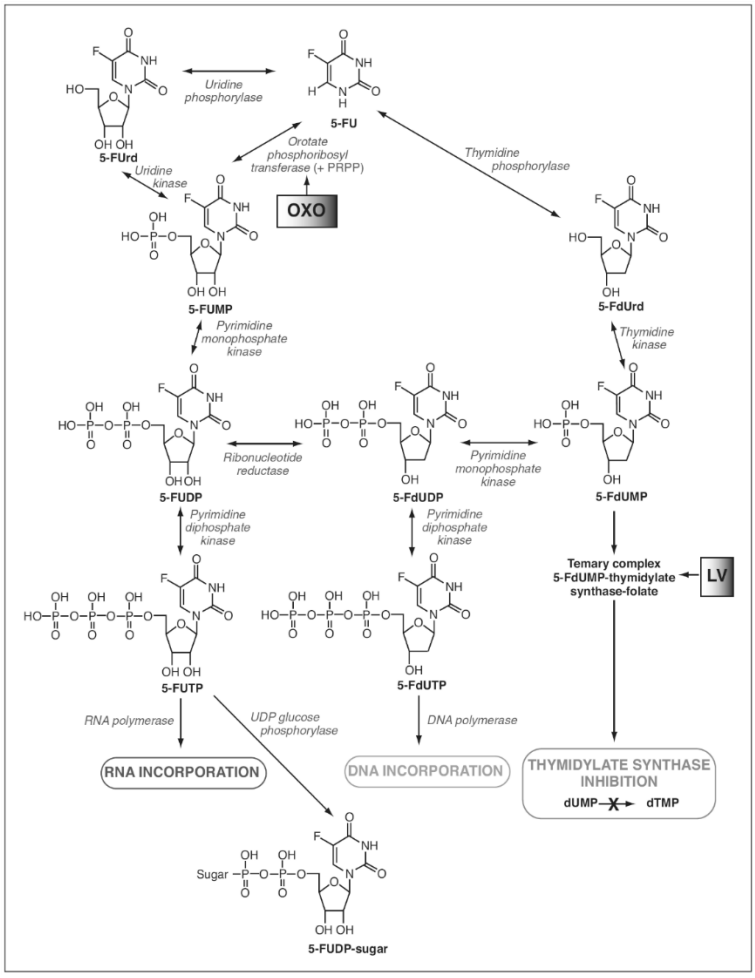

Figure 1.4: Intracellular anabolism of 5-fluorouracil (5-FU). All of the compounds are represented in neutral form. LV (leucovorin) and OXO (potassium oxonate) are biochemical modulators of 5-FU. Abbreviations: 5-FUrd: 5-fluorouridine; PRPP: 5′-phosphoribosyl-1-pyrophosphate; 5-FUMP: 5-fluorouridine-5 -monophosphate; 5-FUDP: 5-fluorouridine-5'-diphosphate; 5-FUTP: 5-fluorouridine-5'-triphosphate; 5-FUDP-sugars: 5-FU-nucleotide sugars; 5-FdUrd: 5-fluoro-2'-deoxyuridine; 5-FdUMP: 5-fluoro-2'-deoxyuridine-5'-monophosphate; 5-FdUDP: 5-fluoro-2'-deoxyuridine-5'-diphosphate; 5-FdUTP: 5-fluoro-2'-deoxyuridine-5'-triphosphate; dUMP: 2'-deoxyuridine-5'-monophosphate; dTMP: thymidine-5'-monophosphate.[83]

5-FU has an erratic oral bioavailability, whereby this drug is administered intravenously. This drug has a short half-life ($t_{1/2}$) (5 to 20 min), whereby cells are exposed to its active metabolites for a short time.[83] Thus, it was necessary to develop different approaches to administer the drug and keep its concentration in the blood stream for longer periods of time and enhance 5-FU effect,[83] such as the combination ftorafur (tetrahydrofuranyl-5-fluorouracil, tegafur, FT) and uracil.[59,85] 5-Fluorouracil can also be associated to leucovorin and methotrexate to enhance its anticancer effect.[76]

The use of 5-FU is limited by its side-effects which includes diarrhea, myelosuppression and thrombophlebitis of peripheral veins, as well as cardiotoxicity.[59,86] For these reasons, researchers have been looking for strategies that allow an oral administration of 5-FU and at the same time reduce its systemic side-effects.[87] One approach reports the use of capecitabine, one 5-fluorouracil oral pro-drug that is capable to cross the gastrointestinal barrier by remaining intact and then after three steps it is converted into 5-FU by the action of carboxylesterase and cytidine deaminase, which converts capecitabine into 5′-deoxy-5-fluorouridine (5′DFUR) in the liver, and finally 5'DFUR by the action of thymidine phosphorylase, an enzyme with higher activity in tumor than in normal tissues, is converted to 5-FU.[76,83] Unfortunately, this drug also presents important side effects such as cardiotoxicity.[86,88] One promising approach is the encapsulation of 5-FU into nanocarriers.

Anirudhan *et al*. developed a novel drug delivery system with 3-methacryloxypropyl trimethoxy silane coated magnetic nanoparticles polymerized with glycidylmethacrylate-grafted- maleated cyclodextrin for controlled release of 5-FU.[89] Faria *et al.*[90] developed a hybrid material using TiO_2 nanotubes coated with semiconductors zinc sulfide quantum dots (TiO_2/ZnS) and loaded it with 5-FU. The cytotoxic effect of TiO_2/ZnS was tested in Chinese Hamster Ovary cells (CHO K1), revealing no signs of toxicity against mammalian cells and the release studies showed that these nanotubes could provide desirable release kinetics and controllable release time for 5-FU, proving its usefulness as drug-releasing materials in cancer therapy.[90] In 2014, Patel *et al*.[91] loaded 5-FU into solid lipid nanoparticles (SLNs) and the anticancer effect of 5-FU loaded SLNs was assessed in Caco-2 cell line, revealing that the effect in cell viability is concentration-dependent. The authors verified a potentiation of 5-FU anticancer activity when loaded in SLNs compared to pure 5-FU.[91]

Another approach that has been studied is the combination of more than one cancer therapeutic agent and, in this way, it is an attempt to prevent mutation and resistance. Using two or more chemotherapeutic drugs the probability of killing more cancer cells rises since cancer cells are attacked by multiple drugs that disrupt different stages of the cell reproduction cycle. Combined chemotherapy has taken the following principles into account: using drugs with activity as single agents, avoiding the overlapping of drug toxicities, no cross-drug

resistance, different mechanisms of action, targeting different cell cycle phases and generating anticancer synergy.[92,93] The development of nanomedicine has also created the opportunity to load different drugs into nanocarriers and overcome some problems encountered by free drug combination therapies. There are several ways to deliver multiple drugs using nanocarriers: one drug in its free form and another one loaded into a nanocarrier (free drug+nano), or both drugs loaded into different nanocarriers (nano+nano), or both drugs loaded into the same nanocarrier (co-encapsulation) (Figure 1.5).[92]

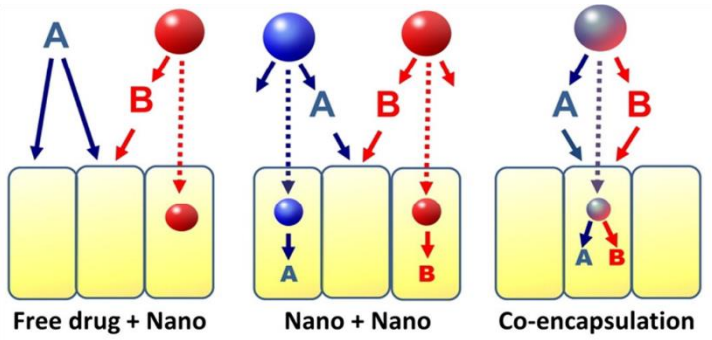

Figure 1.5: Different approaches of combined chemotherapy using nanocarriers.[92]

Co-encapsulation of synergistic drug combinations presents many benefits as it has been demonstrated by different studies.[94–99] For instance, Anitha *et al.*[98] evaluated the combinatorial effects of curcumin/5-fluorouracil loaded into thiolated chitosan nanoparticles (CRC-TCS-NPs/5-FU-TCS-NPs) *in vitro* using colon cancer cells (HT29) and *in vivo* by the analysis of pharmacokinetics and biodistribution of CRC-TCS-NPs/5-FU-TCS-NPs in a mouse model. Using *in vitro* studies, they proved that the combinatorial anticancer effects enhance 2.5 to 3-fold the anticancer effects and pharmacokinetic studies confirmed the improved plasma concentrations of 5-FU and curcumin loaded into thiolated chitosan nanoparticles up to 72 h, unlike bare curcumin and 5-FU.[98] Tardi *et al.* combined irinotecan and cisplatin, loaded them into liposomes and evaluated the effect *in vitro* and *in vivo*, revealing that irinotecan/cisplatin 7:1 molar ratio had superior antitumor activity when encapsulated in liposomes compared with the free-drug cocktail.[99]

In the recent years, there has been an increasing number of studies showing a correlation between the use anti-inflammatory drugs and reduced incidence of cancer. Non-steroidal anti-inflammatory drugs (NSAIDs) are used by their anti-inflammatory, antipyretic and analgesic effects, and aspirin is also effective in both the primary and secondary prevention of cardiovascular diseases.[100] There is reliable data which correlate the use of NSAIDs in prevention of colorectal and breast cancers. NSAIDs exert their effect by inhibition of

cyclooxygenases (COXs), thus inhibiting the conversion of arachidonic acid into thromboxanes and prostaglandins.[100] COX-1 is expressed in platelets and the gastric mucosa and COX-2 is expressed mainly in the human brain and kidneys and in many sites during inflammation, wound-healing and cancer.[100,101] COX-2 overexpression stimulates angiogenesis in tumors, being the most frequent anti-inflammatory/anticancer target.[102] Anti-inflammatory drugs inhibit COX-2 expression, which make them effective as chemo-preventive agents if the clinical benefits compensate the toxic effects.[103] Despite the numerous studies showing the promising activity of NSAIDs in the prevention and treatment of cancer, only treatment with aspirin combines the benefit of protection against cardiovascular disease with the potential to reduce the risk of some types of cancer.[104–110]

1.2. NANOMATERIALS AS CARRIERS FOR DRUG DELIVERY SYSTEMS

In the last years, the use of nanocarriers to improve drug delivery has been a flourishing strategy for cancer treatment. An ideal nanocarrier should have high drug loading capacity, be biocompatible and/or biodegradable and should deliver the drug on a specific site to avoid normal cells and tissues.[111,112] Nanocarriers are used as hosts to develop drug delivery systems (DDS). DDS enable to overcome many of the limitations common to chemotherapeutic agents.[57] When a drug is administered in the conventional way, it can have more limited effectiveness, lack of selectivity and poor biodistribution. When a drug is loaded into a nanocarrier (originating a DDS), it can be delivered on the target place, minimizing the undesirable side effects on healthy tissues, the drug is protected from rapid degradation or clearance and the drug concentration increases in the target tissues.[113] These features clearly demonstrate the utmost importance of DDS in order to increase drug efficacy while decreasing their side effects and, in this way, overcome the present limitations of cancer therapy.[114] The release of the drug from nanocarriers occurs by one or more mechanisms, such as diffusion, desorption of the drug bound to the surface, matrix erosion, diffusion through the capsule shell and a combined erosion-diffusion process.[115]

There are several carriers that could be used to load drugs (Figure 1.6), including polymeric nanoparticles,[116–118] liposomes,[52,119] dendrimers,[120–122] nanoemulsions,[123–125] mesoporous silica nanoparticles,[126–128] magnetic nanoparticles (MNPs),[129–131] and zeolites.[132–134] The current research results will focus on some of them.

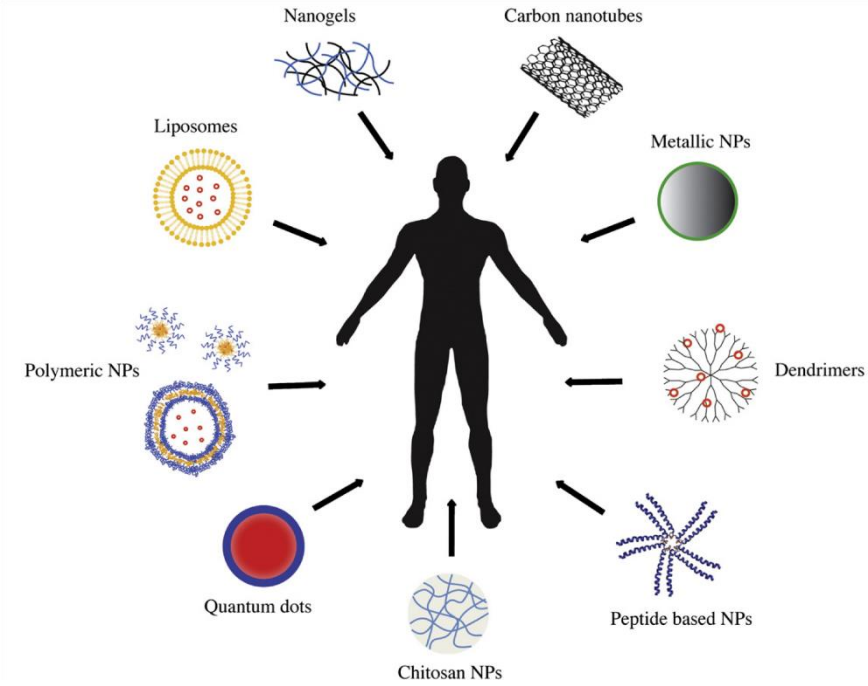

Figure 1.6: Established therapeutic nanocarriers in preclinical development.[135]

1.2.1. POLYMERIC NANOPARTICLES

Polymeric nanoparticles (PNPs) are based on polymers and have a good potential as DDS.[136] After the creation of the first DDS based in polyglycolic acid, polymers have been gaining application as DDS since this material allows the preparation of efficient systems for drug delivery.[137–139] These nanoparticles can be obtained by two methods: dispersion of the preformed polymers and polymerization of monomers.[137] In the dispersion of the preformed polymers, nanoparticles can be prepared by several methods, such as solvent evaporation, salting-out, dialysis and supercritical fluid technology.[137,140] In polymerization of monomers, various techniques are used, for instance, surfactant-free emulsion, micro-emulsion, mini-emulsion and interfacial polymerization.[140] Normally, PNPs are nanospheres or nanocapsules. When hydrophobic compounds are encapsulated into a polymeric matrix, the structures are called nanospheres, while compounds, independently of their physicochemical properties, are encapsulated into an aqueous or oily liquid core, the structures are named as nanocapsules (Figure 1.7).[141] PNPs are prepared with biodegradable polymers, which allow their use for biomedical applications since these polymers do not accumulate in the body and are non-toxic.[141]

It is possible to find many examples of the use of PNPs in the literature for the preparation of DDS. The works of Chaves *et al.*[142] show that clofazimine (CLZ) loaded in PLGA nanoparticles (NPs-CLZ) reduce its toxicity. The effect of NPs-CLZ was assessed on intestinal cells, Caco-2 and HT29-MTX, revealing that NPs-CLZ show no toxicity to cells compared to

free CLZ solutions.[142] Han *et al.*[143] prepared poly(lactic-co-glycolic acid) nanoparticles with phospholipid shell and covered with polydopamine that allowed the conjugation of TAT peptide on the surface. They found that the nanoparticles modified with amidated TAT peptide (NLpT-CA and NPpT-CA) avoided interactions with LS174T colon cancer cells and J774A.1 macrophages at pH 7.4 but restored the ability to interact with LS174T cells at pH 6.5, delivering paclitaxel efficiently to the cells following a brief contact time.[143]

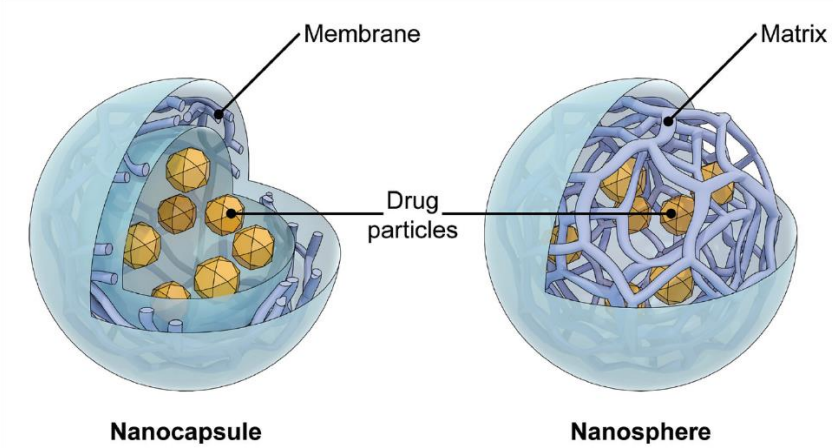

Figure 1.7: Schematic representation of a nanocapsule and a nanosphere.[144]

1.2.2. DENDRIMERS

Dendrimers are polymeric molecules composed of a high number of branches that derive outward from a central core and surface groups, providing versatile building blocks (Figure 1.8).[145,146] Dendrimers are relatively easy to prepare, water soluble and have a high number of peripheral groups to functionalize, which make them appropriate to be used in different biomedical applications and to be administered by many routes, such as oral, transdermal diffusion and intravenous.[147,148]

There are many studies about the use of dendrimers for biomedical applications. For example, Han *et al.*[149] developed a DDS based on a polysaccharide-modified dendrimer responsive to the tumor microenvironment. The results showed that this strategy enhanced drug penetration and improved therapeutic efficacy.[149] Lee *et al*.[150] used a biodegradable dendrimer loaded with doxorubicin and evaluated its effect in mice bearing C-26 colon carcinomas. The results revealed that after 72 h of exposure, doxorubicin loaded into the dendrimer was more than ten times less toxic than free doxorubicin.[150] Liu *et al.*[151] synthetized a multifunctional delivery system combining DOX and pORF-hTRAIL to accumulate in brain glioma and to kill cancer cells, inducing apoptosis with lower side effects. The results showed a synergistic growth inhibition in U87MG cells.[151]

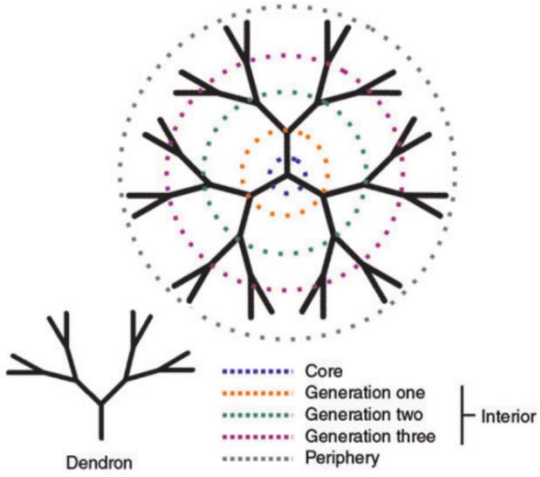

Figure 1.8: Structure of a dendrimer.[145]

1.2.3. LIPOSOMES

Liposomes are spherical vesicles most often constituted of phospholipids, comprising at least one lipid bilayer like a cellular membrane which surrounds an aqueous solution core (Figure 1.9).[152] Due to their features, liposomes can load hydrophilic or hydrophobic drugs in the core or in the bilayer, respectively, and their vesicles can vary from 25 nm to 2.5 μm in diameter.[152,153] Due to their properties, liposomes are good candidates for the delivery of drugs to cells and they can also be functionalized with different ligands.[154] Liposomes were the first nanocarriers approved by the American FDA for anticancer treatment (Doxils), where liposomes were loaded with doxorubicin.[155]

Jiang *et al.*[156] reported a dual-functional liposome system which comprised extracellular pH response and mitochondrial targeting properties in order to increase drug accumulation in mitochondria and consequently contribute to kill drug-resistant cancer cells by apoptosis. The results demonstrated that these dual-functional liposomes had great efficacy in A549 cells and A549/Taxol cells and in drug-resistant lung cancer A549/Taxol cells xenografted onto nude mice, resulting in 86.7% of tumor growth inhibition.[156] Alshaer *et al.*[157] conjugated onto PEGylated liposomes surface a 2′-F-pyrimidine-containing RNA aptamer (Apt1), previously selected for CD44. The results demonstrated higher sensitivity and selectivity for Apt1 conjugated with liposomes compared to maleimide-functionalized liposomes, which show that Apt1 conjugated with liposomes is a promising specific DDS.[157] Liu *et al.* created a pH-responsive molecule (i.e., malachite green carbinol base (MG)) and liposome conjugated with HER-2 antibody for the co-delivery of doxorubicin (DOX) and verapamil (VER) to suppress drug resistance in HER-2 positive breast cancer.[158]

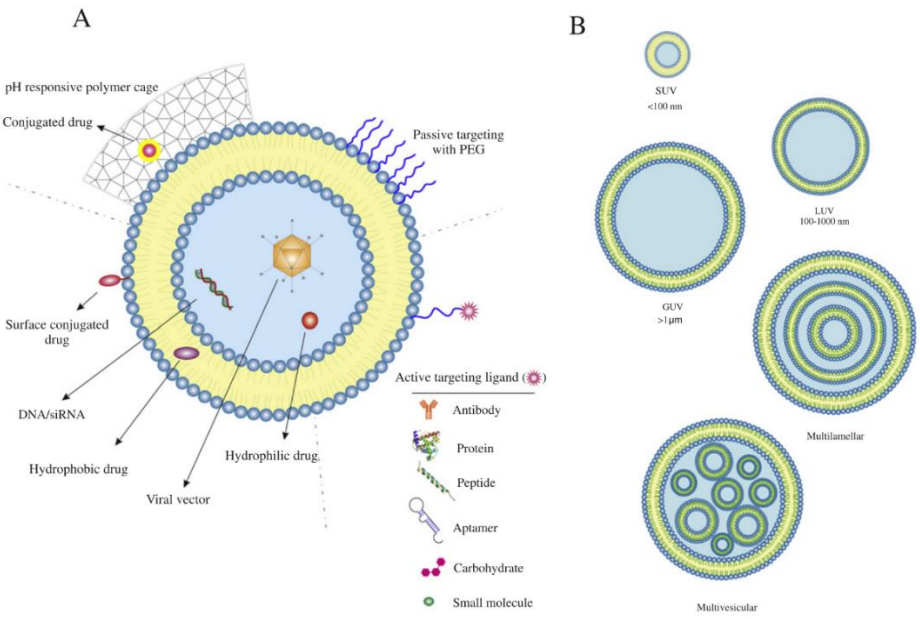

Figure 1.9: Structure of a liposome. A) Representation of structural and design considerations for drug delivery using liposomes. Liposomes can be designed with polyethylene glycol (PEG) being a passive target and with different cargos ligands such as antibodies, peptides, proteins, carbohydrates, and also drug loaded being active targets. B) The usual classification system of vesicle size and lamellarity: vesicles with diameters less than 100 nm are classified as small unilamellar vesicles (SUV); vesicles with diameters between 100 and 1000 nm are classified as large unilamellar vesicles (LUV); vesicles larger than 1 µm are classified as giant unilamellar vesicles (GUV); vesicles with many layers are classified as multilamellar and vesicles encapsulating smaller vesicles cells are classified as multivesicular.[153]

1.2.4. MESOPOROUS SILICA NANOPARTICLES

Mesoporous silica nanoparticles (MSNs) are amorphous inorganic nanoparticles comprising silicon dioxide units and pores not greater than 2 nm.[159] This material has large specific surface area and pore volume, a controllable particle size and a good biocompatibility, which makes it widely studied for several applications, including the use as carrier for drug delivery (Figure 1.10).[160,161] MSNs are more stable to degradation and mechanical stress than liposomes or dendrimers due to the strong Si-O bond.[162]

Freitas *et al.* prepared a system based on MCM-41 to be used in controlled drug delivery and imaging for cancer treatments.[163] Maggini *et al.* prepared redox responsive mesoporous organo-silica nanoparticles for targeted drug delivery and proved that these particles have a higher cytotoxic effect on glioma C6 cells than non-breakable particles.[164] Also, Kotcherlakota *et al.* loaded the anticancer drug curcumin in mesoporous silica materials to be used in cancer treatment, showing that curcumin loaded into MSNs revealed higher cytotoxicity to cancer cells and cellular uptake compared to pristine curcumin.[165]

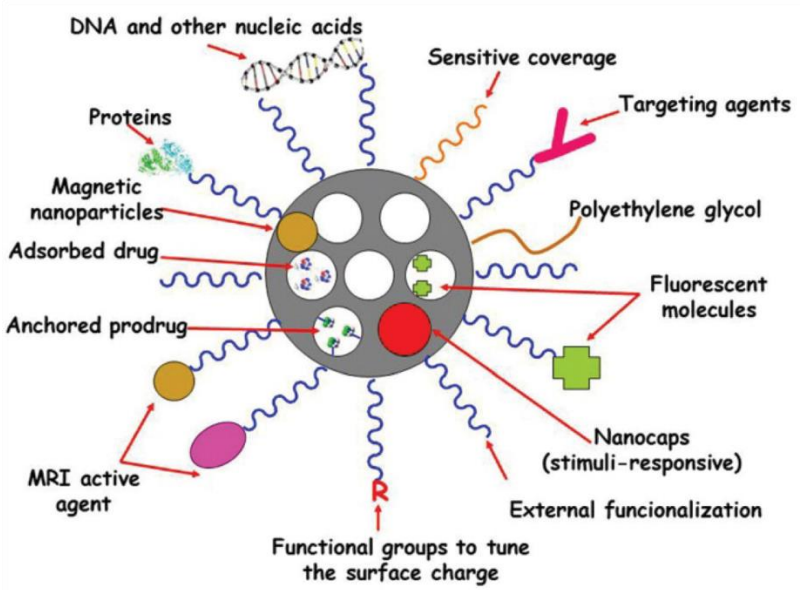

Figure 1.10: Representation of mesoporous silica nanoparticles and their cargo loading possibilities.[166]

1.2.5. MAGNETIC NANOPARTICLES

In the last decade, magnetic nanoparticles (MNPs) have gained attention as very promising candidates for biomedical applications (Figure 1.11). MNPs are biocompatible and can be used in different applications such as magnetic resonance imaging (MRI), drug delivery and hyperthermia.[167–169] In hyperthermia, MNPs can be injected into the tumor region and a magnetic field is applied. The generated heat increases the tumor tissue temperature to around 42-45 °C which will kill cancer cells, whereas the healthy cells will survive because they are stronger tolerant to thermal heating.[170,171]

MNPs nanoparticles could be conjugated with other materials, creating hybrid materials that can conjugate the features of both. In the literature, it is possible to find some examples of the conjugation of MNPs with other materials. Wan *et al.* created a hybrid material conjugating nanohydroxyapatite and magnetic nanoparticles to be used as nanocarrier for controlled delivery of 5-fluorouracil.[172] Wang *et al.* developed a material composed by hydroxypropyl methyl cellulose (HPMC), polyvinyl alcohol (PVA) and magnetic nanoparticles for magnetic hyperthermia ablation of tumors.[173]

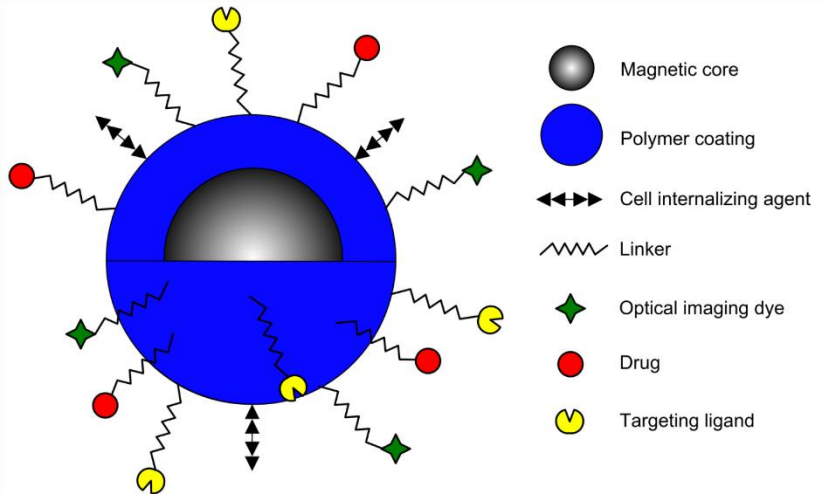

Figure 1.11: Structure of a magnetic nanoparticle and the possibilities for modification.[174]

1.2.6. ZEOLITES

Zeolites are crystalline aluminosilicates comprising silicon (Si), aluminum (Al), oxygen (O) and water molecules, characterized by three dimensional channels and cavities whose dimensions are comparable with small organic molecules.[175–177] Their framework is assembled by TO_4 tetrahedra where T is silicon or aluminum atoms bridged by oxygen, originating SiO_4 and AlO_4^-.[178] The negative charge of the zeolite generated by the substitution of Si^{4+} by Al^{3+} in the tetrahedra, could be neutralized by cationic exchange with H^+, Na^+ or K^+. However, theses cations could be replaced by other transition metal ions since they are very mobile.[179]

The way the tetrahedra are linked to each other originates a wide variety of different structures, more than 200, which are listed by the International Zeolite Association (IZA).[180] For example, zeolite NaY belongs to the faujasite family (FAU) and has a tridimensional structure with pores of 0.73 nm (Figure 1.12A).[180] The basic structural units of zeolite NaY are sodalite cages (or β cages) with an internal diameter of 0.62 nm that are linked by hexagonal prisms to form a spherical supercage with 1.18 nm of diameter.[181,182] Zeolite L belongs to Linde Type L family (LTL), presents unidimensional channels which are linked by cancrinite cages and hexagonal prisms, forming a cylindrical crystal shape and it has 0.71 nm pores (Figure 1.12B).[183] Zeolite L nanocrystals are easy to synthesize, to functionalize and presents a defined and controlled morphology and porosity.[184]

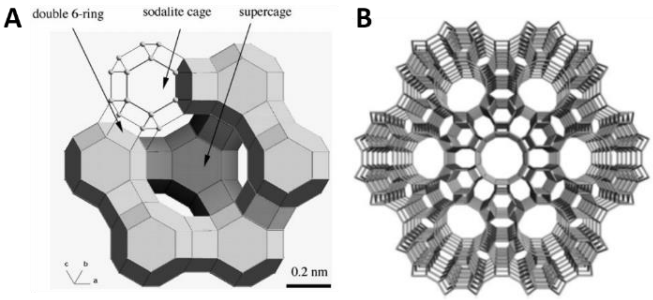

Figure 1.12: Zeolite structures of A) NaY[185] and B) L.[186]

Comparing with other nanocarriers, zeolites have the advantage of being used for biomedical applications since they are relatively cost-effective, biocompatible, present low toxicity, are stable at pH variations, can load small drug molecules and it is possible to tune zeolite properties by changing the SiO_2/Al_2O_3 ratio, the commutable cation and the surface functional groups.[187,188] It is possible to find numerous examples of the use of zeolites in biomedical applications in the literature, including drug delivery,[80,189–192] radiotherapy,[193] wound-healing,[194] imaging,[195] which demonstrate the versatility of these structures.

1.3. TOOLS TO DETERMINE ENDOCYTIC PATHWAYS

Understanding the interaction between particles and living cells is crucial for assessments if a material is available to reach a desired intracellular compartment and if it is deemed suitable for theranostic use.[196] There are some established approaches to determine the endocytic pathways involved in the endocytosis of nanoparticles: using pharmacological inhibitors, molecular inhibition and co-localization studies.[197,198]

1.3.1. PHARMACOLOGICAL INHIBITORS

Pharmacological inhibitors can block specific endocytic pathways and can be used to study the pathway responsible for cellular uptake of nanoparticles. There are many inhibitors to be used in these studies like chlorpromazine, filipin, dynasore, nystatin, genistein, nocodazole, LY94002 and others.[198] These inhibitors block specific pathways: chlorpromazine is used to block clathrin-dependent endocytosis,[199,200] filipin and nystatin block caveolae-mediated endocytosis by interacting with cholesterol,[201–204] dynasore is a GTPase inhibitor that rapidly and reversibly inhibits dynamin activity, preventing endocytosis,[205,206] genistein impedes caveolae-dependent endocytosis by inhibiting several tyrosine kinases,[207,208] nocodazole is a microtubule-depolymerizing agent inhibiting microtubule dependent pathways,[209,210] and LY294002 inhibits micropinocytosis[209] (Table 1.2). When assays with pharmacological

inhibitors are performed, the concentration and incubation times of the inhibitors need to be optimized to avoid cytotoxic side effects to cells used in the assays.[197,198] These studies have some disadvantages since one inhibitor could interfere with different pathways at the same time.[211]

Table 1.2: Effect of pharmacological inhibitors used to study endocytosis.

Affected mechanism	Inhibitor(s)	Action
Clathrin-dependent endocytosis	Chlorpromazine	Inhibits Rho GTPase
Caveolae-dependent endocytosis	Filipin Nystatin	Interacts with cholesterol
Caveolae-dependent endocytosis	Genistein	Inhibitor of several tyrosine kinases
Clathrin and caveolin-dependent endocytosis	Dynasore	Inhibits dynamin function
Microtubule dependent pathways	Nocodazole	Promotes the depolymerization of microtubule
Macropinocytosis	LY294002	Inhibits phosphatidylinositol 3-kinase

1.3.2. MOLECULAR INHIBITION

The use of mutated proteins can be used to block endocytic mechanisms at the protein level.[197,198] For this purpose, mutated proteins like DN-Eps15, DN-dyn2, Dn-Rab5, are introduced in cells and they will interfere with the function of their endogenous analogues and consequently blocks the endocytic mechanism for which the protein is required.[198] With this approach, it is possible to bind a fluorescent protein to a mutated protein, allowing microscopic observation and selection of the transfected cells, which represent an advantage of this approach.[198] Though, this method presents some disadvantages like higher concentration of mutated protein compared to the normal endogenous protein, which can originate lower-affinity interactions not detected in cells missing such mutated proteins.[197] It is also possible to use siRNA to downregulate crucial endocytic proteins.[198] However, this approach also has some considerations that should be taken in account: knockdown of proteins could take 2-5 days, which could lead to cellular changes, resulting in observations not relevant for the target protein;[197] since protein downregulation does not occur in the same way in all cells, it is complicated to perform a quantitative analysis;[198] to introduce the siRNA in cells, transfection

agents need to be used, which can cause cellular stress and consequently affect the endocytic profile.[198]

1.3.3. FLUORESCENCE LOCALIZATION OF NANOPARTICLES

The cellular uptake and transport of nanoparticles could also be studied using fluorescent nanoparticles and confocal microscopy. By confocal microscopy it is possible to evaluate the intracellular localization of nanoparticles and if the endosomes are labelled after the internalization, enabling to obtain information about the endocytic mechanism under study.[198] However, for the confocal experiments, it is necessary to fix and permeabilize the cells, which can originate some artefacts. Moreover, sometimes it is difficult to conclude if the nanoparticles are inside or just bound to the cell surface.[197] However, this limitation could be solved using electron microscopies: scanning electron microscopy (SEM), atomic force microscopy (AFM) and transmission electron microscopy (TEM). SEM and AFM could be used to investigate the initial phase of the endocytic events since these techniques allow the surface visualization of cells and have a maximum resolution of 1 nm and 30 nm for the lateral resolution and up to 0.1 nm for the vertical resolution, respectively.[198] TEM could be used to examine the localization of nanoparticles inside the cells since this technique allows the observation of ultrathin sections of cells.[198] In the work of Cacchioli *et al.,* on *in vitro* cytocompatibility of SiC/SiO_2 core-shell nanowires, SEM and TEM were used to investigate the cellular internalization of SiC/SiO_2 nanowires.[212] Havrdova *et al.* used field emission scanning electron microscopy (FE-SEM) to detect nanoparticles inside human mesenchymal stem cells (hMSCs).[167]

1.4. MECHANISMS OF INTERNALIZATION

When the materials interact with cells, their internalization can occur by different pathways: energy-independent or non-endocytic and endocytic pathways (Figure 1.13). These pathways can be determined by several factors, namely the cell type and the physicochemical properties of particles like size, shape and surface charge.[213,214] Some studies demonstrated that the size of particles can influence the internalization pathways and showed that smaller particles are taken up more rapidly than larger ones.[215,216] The shape of the nanoparticles also has influence on the internalization process since particles presenting a good aspect ratio, the ratio of length to width of a particle, are the fastest internalized.[217,218] Gratton *et al.* found that HeLa cells internalized 4 times faster high-aspect-ratio particles (diameter (d) = 150 nm and height (h) = 450 nm) than low-aspect-ratio particles (d = 200 nm and h = 200 nm).[215] The surface charge influences the internalization of nanoparticles since their charge will interact with the surface

charge of the cell membrane. It seems to be a pattern that shows that positively charged particles are endocytosed more efficiently than negatively charged particles.[197,219] Another factor that influences nanoparticles internalization is the cell type. Cells could have different proteins involved in the internalization which will determine the endocytic pathway responsible for nanoparticles internalization. Furthermore, normal and cancer cells could use different endocytic pathways.[219]

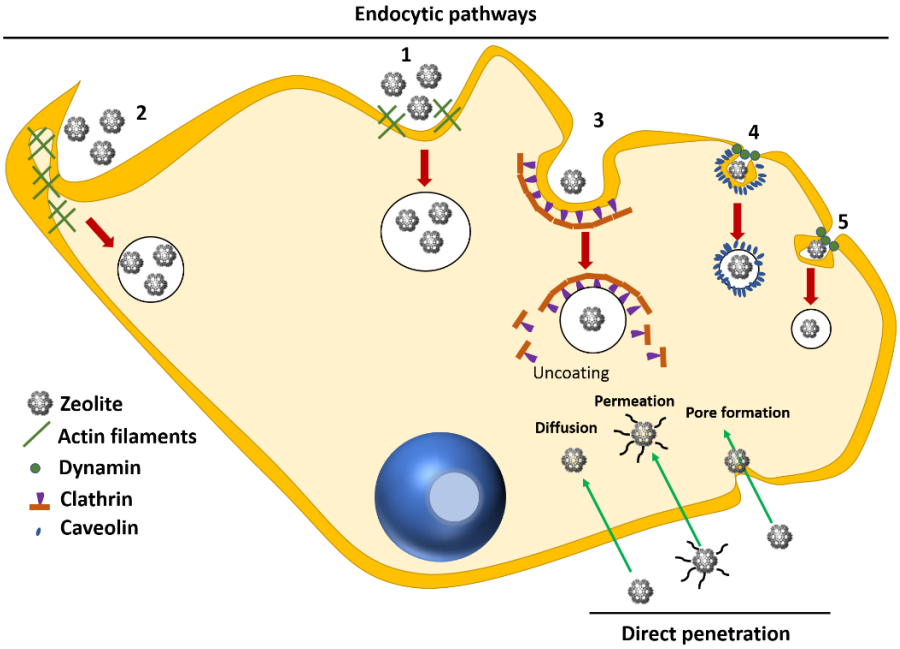

Figure 1.13: Schematic representation of the different cellular uptake pathways in mammal cells. The processes represented on the top are related to endocytic pathways. The processes represented at the bottom right side are related to direct penetration. 1) Phagocytosis; 2) Macropinocytosis; 3) Clathrin-dependent endocytosis; 4) Caveolin-dependent endocytosis; and 5) Clathrin and caveolin-independent endocytosis. Adapted from.[220,221]

1.4.1. DIRECT PENETRATION

Direct penetration is a non-endocytic pathway and nanoparticles enter the cells via energy-independent pathways. There are different mechanisms involved in the internalization of nanoparticles by this pathway, such as pore formation, micelle formation, the carpet-like model and the membrane thinning model.[222,223] The inverted micelle model occurs as a result of electrostatic interactions between cationic particles and negatively charged phospholipids of the cell membrane, which results in the destabilization of the membrane and the formation of an invagination. A reorganization of adjacent lipids occurs and leads to the formation of an inverted micelle that encloses nanoparticles in a hydrophilic core. In the pore formation model, transient pores are created in the cell membrane, leading to the cellular internalization of particles. In the carpet model, there is a transient disruption of the cellular membrane, which

contributes to the cellular uptake.[211,222–224] Normally, direct penetration is associated with the internalization of cell penetrating peptides.[204,225–227]

1.4.2. ENDOCYTIC PATHWAYS

1.4.2.1. ENDOCYTOSIS

A nanoparticle can interact with the cell membrane and enter the cell by endocytosis. In the endocytosis process the nanoparticles are engulfed by the cellular membrane forming the endosomes. The endosomes transport the nanoparticles for different specialized vesicular structures and consequently the nanoparticles are distributed in different destinations. When the nanoparticles deliver their compounds to the cells, they are recycled to the extracellular milieu or carried across the cells.[228] This is the most common way for internalization of nanoparticles and it is divided into phagocytosis and pinocytosis (Figure 1.14). Phagocytosis refers to the uptake of large particles and it is specific of phagocytic cells such as macrophages.[228,229] Pinocytosis refers to the uptake of fluids and solutes and is present in all types of cells. Pinocytosis is divided in clathrin-mediated endocytosis, caveolae-mediated endocytosis, macropinocytosis and clathrin- and caveolae-independent endocytosis.[218,219,228,230]

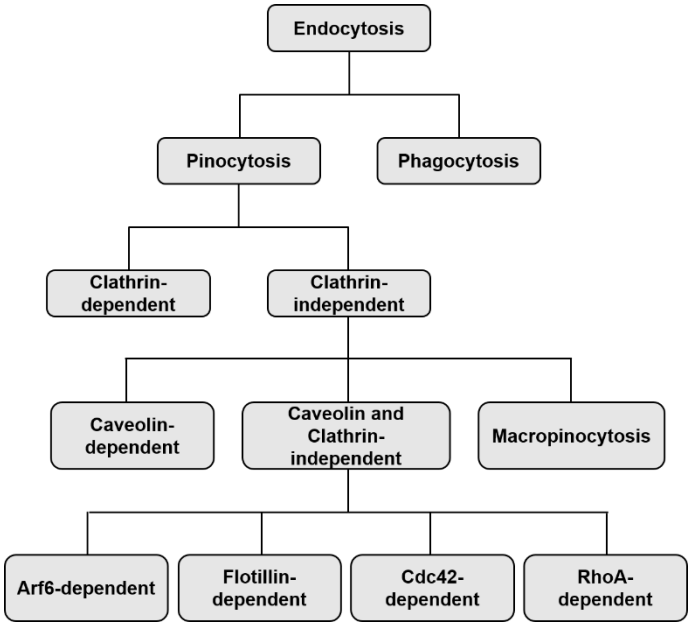

Figure 1.14: Classification of endocytosis based on endocytosis proteins that are involved in the initial entry of particles and solutes. Adapted from.[228]

Clathrin-dependent endocytosis

In the clathrin-dependent endocytosis that occurs in mammalian cells, the nanoparticles interact with receptors of the cellular membrane which is polymerized on the cytosolic side by different adaptor and accessory proteins.[218,231] The nanoparticles are internalized and form clathrin-coated pits (CCPs) and subsequently clathrin-coated vesicles (CCVs).[219,232] The formation of CCPs occurs in the initial phase of clathrin-mediated endocytosis, consisting in transmembrane receptors and clathrin, a triskelion-shaped scaffold protein and the heterotetrameric protein AP-2.[233,234] The formation of CCVs is dependent of several accessory proteins and it proceeds through five stages: initiation, cargo selection, coat assembly, scission and uncoating.[233,235] GTPase activity of dynamin pinches off the vesicles with nanoparticles and CCVs are formed. Then, these CCVs move inside the cells through actin activity and then are released in the cytosol.[219,235] The uptake of low-density lipoproteins and transferrin is mediated by this pathway.[234] Ng *et al*.[236] investigated the mechanism of uptake for gold nanoparticles in MRC5 lung fibroblasts and Chang liver cells. Cells treated with concanavalin A and chlorpromazine demonstrated a significant decrease of nanoparticle uptake by cells, implying that the uptake of these nanoparticles was facilitated by clathrin-mediated endocytosis.[236] Oh *et al.*[237] prepared different sized LDH nanoparticles with narrow size distribution by modulating the crystal growth rate and labelled each layered double hydroxides (LDHs) particles with a fluorophore. The cellular uptake rate of LDHs by human osteosarcoma (MNNG/HOS) cells was found to be highly dependent on the particle size (50 > 200 > 100 > 350 nm), in which those ranging of 50 to 200 nm were selectively internalized into cells through clathrin-mediated endocytosis with enhanced permeability and retention.[237] Forte *et al.*[238] evaluated the endocytic mechanism involved in the internalization of 44 nm (NP44) and 100 nm (NP100) unmodified polystyrene nanoparticles (PS-NPs) into gastric adenocarcinoma (AGS) cells. They proved that NP44 accumulate rapidly and more efficiently compared to NP100 in the cytoplasm of AGS; both PS-NPs showed an energy-dependent mechanism of internalization and a clathrin-mediated endocytosis pathway.[238]

Caveolin-dependent endocytosis

Caveolin-dependent endocytosis is dependent on the protein caveolin. Three isoforms of caveolin are known in mammalian cells: caveolin-1 and -2 are present in endothelial cells, fibroblasts and adipocytes and caveolin-3 is specific to muscle.[219,228] In this way, membrane invaginations are formed with size of around 50-100 nm, caveolae, mediated by caveolin-1.[231,232,239,240] The nanoparticles bind to the cell surface and move along the membrane to caveolae vesicles where they are kept through receptor-ligand interactions.[232] The caveolae vesicles are pinched off from cellular membrane by the GTPase dynamin, originating the

cytosolic caveolar vesicle.[232] Nanomaterials with carrier compounds sensitive to enzymatic action should be designed to use this pathway since this enables to escape from lysosomal enzymes.[232,241] Cao *et al.*[242] loaded the anticancer drug doxorubicin in four arm star-shaped poly(ε-caprolactone)-b-poly((N,N-diethylaminoethyl methacrylate)-r-(N-(3-sulfopropyl)-N-methacryloxyethy-N,N-diethylammoniumbetain)) (4sPCLDEAS) micelles and tracked their endocytosis in HeLa cancer cells. The results demonstrated that caveolae-dependent endocytosis was the main pathway for the internalization of 4sPCLDEAS micelles.[242] Wang *et al.*[243] explored the uptake of bovine serum albumin (BSA)-coated nanoparticles of different sizes (40 and 100 nm) in endothelial cell monolayers. They observed that BSA-coated nanoparticles were internalized via caveolae-dependent endocytosis and only nanoparticles smaller than caveolae were internalized. The results also demonstrated that the transport of 40 nm particles was 2-fold greater than that of 100 nm ones.[243]

Macropinocytosis

Macropinocytosis occurs in almost all the cells with few exceptions, such as brain microvessel endothelial cells which is one of the clathrin-independent endocytosis.[219,232] This route is a fluid-phase endocytosis since it internalizes large amounts of plasma membrane and extracellular medium, leading to the formation of macropinosomes which are fused membrane protrusions generally bigger than 1 µm and sometimes bigger than 5 µm.[240,244,245] Macropinosomes are larger than the clathrin-coated vesicles, which provides the cells a way to internalize large amounts of solute and membrane.[246] Macropinocytic vesicles undergo a maturation process, shrink and move toward the lysosomes, acquiring and losing various endocytic protein markers during this process.[246] Wadia *et al.* showed that TAT-fusion proteins are rapidly internalized in cells by lipid raft-dependent macropinocytosis.[247] In another study, Khalil *et al.*[248] investigated the internalization mechanism associated with liposomes modified with different densities of the octaarginine (R8) peptide. They observed that liposomes modified with high R8 density were taken up mainly by macropinocytosis, whereas those modified with low R8 density were internalized via clathrin-mediated endocytosis.[248]

Phagocytosis

Phagocytosis occurs predominantly in specialized cells of the immune system: macrophages, monocytes, neutrophils and dendritic cells.[245] It is a receptor-mediated process and removes particles larger than 500 nm. Phagocytosis comprises three different steps: (1) recognition of the particle by opsonization in the bloodstream; (2) adhesion of the opsonized particles onto the cell membrane and (3) ingestion of the particles by cells (Figure 1.15).

Particles are recognized by opsonins (opsonization process), including G or M immunoglobolins (Ig), as well as complement fragments (C3, C4 and C5), in addition to other blood serum proteins like fibronectin, laminin or C-reactive protein.[232,245,249] In the opsonization process, opsonins tag the stranger nanoparticles and send a signal to macrophages. Then, the opsonized particles bind to the macrophage surface via specific receptor-ligand interactions like Fc receptor or complement receptor (CR) that can attach respectively to the constant fragment of Ig or complement molecules adsorbed at the particle.[232,250] Receptor ligation initiates a signaling cascade, which leads to actin rearrangement, formation of pseudopodia that zipper up around the particles and engulf them, forming the phagosome. The phagosome is matured through numerous fission and fusion events, the cargo fused with late endosomes and ultimately with lysosomes originating phagolysosomes.[228,232,245] The number of these consecutive events is dependent on the physicochemical properties of the ingested particles, typically persists from 30 minutes to several hours.[245,251]

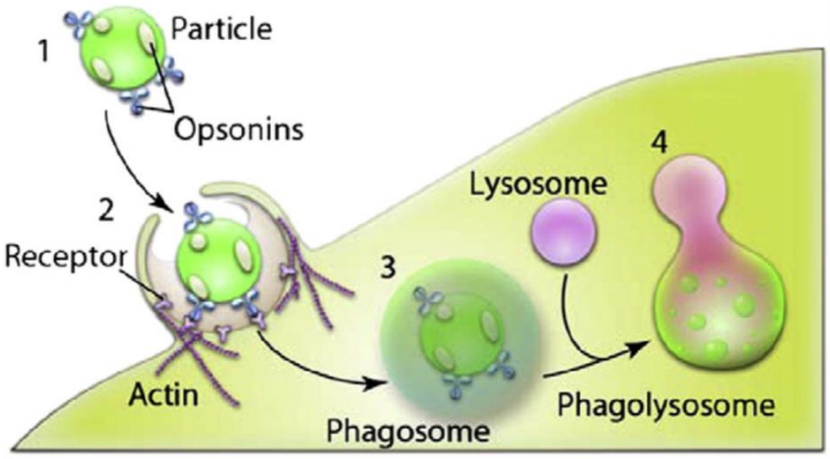

Figure 1.15: The steps of phagocytosis: 1) Particles undergo recognition in the bloodstream through opsonization i.e. adsorption of proteins (immunoglubulins (Ig) G and M, complement components (C3, C4, C5); blood serum proteins (including laminin, fibronectin, etc.); 2) Opsonized particles attach onto the cell membrane through receptors present on the cell surface of a phagocyte; 3) The particles are ingested into phagosomes and 4) The phagosomes mature, fuse with lysosomes and become acidified, leading to the enzyme-rich phagolysosomes where the particles are prone to degradation.[228]

Clathrin- and caveolin-independent endocytosis

Recent investigations demonstrated that some endocytic pathways cannot be included into the previously described categories since many of them are clathrin- and caveolin-independent endocytosis. These pathways are classified as Arf-6-dependent, Cdc42-dependent and Rhoa-dependent, depending on the type of protein that regulates the internalization.[221,252,253]. The involved endocytic apparatus might comprise clathrin-independent carriers (CLICs) or GPI-

anchored protein-enriched early endosomal compartment (GEEC).[254] However, studies about these pathways are still scarce and need further research.

1.4.3. PASSIVE TRANSPORT: ENHANCED PERMEABILITY AND RETENTION EFFECT

The enhanced permeability and retention (EPR) effect consists in the accumulation of nanocarriers in the tumor as a result of their transport through the hyperpermeable tumor vasculature.[70,255] The characteristic of leak vasculature allows the enhanced permeability of particles like proteins, liposomes, micelles and other soluble particles.[70] The size of nanocarriers allows their extravasation and accumulation in the interstitial space of the tumors due to the incomplete lymphatic drainage system and the nanocarrier may stay retained in the tumor bed.[256,257] To take advantage of the EPR effect, nanocarriers should be viable to stay in circulation for enough time to accumulate in the tumor, resist to blood stream aggregation and premature drug leakage and should avoid the reticuloendothelial system (RES) and renal filtration. To avoid being eliminated before their action, nanocarriers should be larger than 10 nm, since particles smaller than 10 nm are subject to clearance by the kidney.[258] This via is not sufficient to control the side effects of cytotoxic drugs and fully exploit the benefits of targeted delivery.[114]

1.5. FACTORS INFLUENCING ENDOCYTIC PATHWAYS

The size, shape and surface charge of the nanoparticles are the main factors that could influence endocytic pathways, as well as the cell type used.

The **size** of the nanoparticles could influence the uptake by cells via either direct penetration through cellular membrane or by endocytosis. There are many studies that show the effect of nanoparticle size on the endocytic pathways used by cells. For example, Rejman *et al.* showed in their work that particles > 500 nm were internalized by a caveolin-mediated process while particles of 200 nm are internalized by a clathrin-mediated process.[259] Suen and Chau demonstrated in their work that 50 and 120 nm folate-decorated nanoparticles were internalized via both clathrin- and caveolin-mediated endocytosis while the particles of 250 nm were internalized by caveolin-mediated endocytosis.[260] Saw *et al.*[261] investigated the effect of four sizes (30, 60, 80 and 100 nm) of cystine/citric acid-coated confeito-like gold nanoparticles (confeito-AuNPs) on cellular uptake. The results demonstrated that the smallest size of confeito-AuNPs (30 nm) have the highest cellular internalization rate via clathrin- and caveolae-mediated endocytosis. However, the other three sizes (60, 80 and 100 nm) use clathrin-mediated endocytosis for cellular uptake.[261]

The **shape** of nanoparticles could affect the uptake rate and the biodistribution, the cytotoxicity and the internalization process. However, there is no consensus about which shape is more internalized. Some works demonstrated that rod-shaped NPs are faster and more internalized than that of the spherical nanoparticles.[215,232] Conversely, other studies showed that the internalization of spherical nanoparticles is higher and faster than of those rod-shaped.[262] Qiu *et al.* demonstrated the influence of the shape on the cellular uptake of Gold nanorods (Au NRs).[263] Xie *et al*.[264] synthesized three different shapes (stars, rods, and triangles) of methylpolyethylene glycol coated-anisotropic gold nanoparticles and investigated their internalization in RAW264.7 cells. They verified that star-shaped nanoparticles had the lowest internalization rate, followed by rod- and triangle-shaped nanoparticles which had the highest one and they also found that nanoparticles with different shapes tend to use different endocytic routes.[264]

The efficiency and the pathways of cellular uptake of nanoparticles are highly dependent on their **surface charge** since there are many biomolecules with distinct charges in biological systems.[265]

The cell membrane is negatively charged, which could affect the rate of internalization of the nanoparticles. The internalization of positively charged nanoparticles seems to be in favor compared with those negatively charged due to the electrostatic interactions between the negatively charged cellular membrane and the positively charged nanoparticles.[266] In fact, in the literature it is possible to find several studies reporting that positively charged nanoparticles have higher rates of internalization than those negatively charged. Steinbach *et al.* modified the surface of nanoparticles with several different cell penetrating peptides with cationic regions and showed that the modified nanoparticles have greatest cell internalization than those unmodified.[267] Bannunah *et al.*[268] investigated the effect of surface charge on the interaction with Caco-2 monolayers as a model of the intestinal epithelium. They showed that the internalization and transport of positively charged nanoparticles are significantly affected in the presence of a clathrin pathway inhibitor (via chlorpromazine), by macropinocytosis inhibition (via 5-(N-ethyl-N-isopropyi)-amiloride) and under cholesterol depletion (via methyl-β-cyclodextrin), but remained unaffected by the inhibition of lipid raft associated uptake (caveolae) by genistein.[268] On the other hand, they observed that the internalization and transport of negatively charged nanoparticles is mostly reduced by inhibition of the lipid raft-associated pathway (caveolae inhibition by genistein) and it was not significantly affected by the inhibition of clathrin pathway.[268]

The information about how the **cell type** affects the cellular trafficking is still scarce. Further studies on the different endocytic pathways are needed since the distinct features between

cancer cells and normal cells could dictate the strategy to adopt for nanomaterials to reach the tumor and avoid effects on normal tissues.[228] It is possible to find some studies in the literature that show that the cell type defined the internalization pathway, such as the study of Chung *et al.*, which evaluated the effect of surface charge of mesoporous silica nanoparticles (MSNs) on cellular uptake and *in vitro* cytotoxicity using human mesenchymal stem cells (hMSCs) and 3T3-L1 cells.[269] Clathrin- and an actin-dependent endocytosis were involved in the internalization of unmodified MSNs in both cells since they were inhibited by phenylarsine oxide (PAO) and cytochalasin D (Cyt D).[269] However, for strongly positive-charged MSNs, inhibitory effects were only observed for 3T3-L1 cells, which show that the MSNs uptake is cell type-dependent.[269] Santos *et al.*[270] used various pharmacological inhibitors in a range of representative human cell lines, including HeLa (cervical cancer), A549 (lung carcinoma) and 1321N1 (brain astrocytoma) to study the uptake mechanisms of carboxylated polysterene nanoparticles of 40 and 200 nm. The results indicated that NP uptake in HeLa and 1321N1 cells was strongly affected by actin depolymerisation, while A549 cells showed a stronger inhibition of NP uptake (in comparison to the other cell types), after microtubule disruption and treatment with genistein.[270] A strong reduction of NP uptake was observed after chlorpromazine treatment only in the case of 1321N1 cells, suggesting that the same nanoparticles could use different endocytic pathways depending on the cell type.[270]

1.6. REFERENCES

1 M. Estanqueiro, M. H. Amaral, J. Conceição and J. M. Sousa Lobo, Nanotechnological carriers for cancer chemotherapy: The state of the art, *Colloids Surfaces B Biointerfaces*, 2015, **126**, 631–648.

2 M. F. Ullah and M. Aatif, The footprints of cancer development: Cancer biomarkers, *Cancer Treat. Rev.*, 2009, **35**, 193–200.

3 What Is Cancer? - National Cancer Institute at the National Institutes of Health, https://www.cancer.gov/about-cancer/understanding/what-is-cancer, (accessed 8 September 2017).

4 C. Fitzmaurice, D. Dicker, A. Pain, H. Hamavid, M. Moradi-Lakeh, M. F. MacIntyre, C. Allen, G. Hansen, R. Woodbrook, C. Wolfe, R. R. Hamadeh, A. Moore, A. Werdecker, B. D. Gessner, B. Te Ao, B. McMahon, C. Karimkhani, C. Yu, G. S. Cooke, D. C. Schwebel, D. O. Carpenter, D. M. Pereira, D. Nash, D. S. Kazi, D. De Leo, D. Plass, K. N. Ukwaja, G. D. Thurston, K. Yun Jin, E. P. Simard, E. Mills, E.-K. Park, F. Catalá-López, G. DeVeber, C. Gotay, G. Khan, H. D. Hosgood, I. S. Santos, J. L. Leasher, J. Singh, J. Leigh, J. B. Jonas, J. Sanabria, J. Beardsley, K. H. Jacobsen, K. Takahashi,

R. C. Franklin, L. Ronfani, M. Montico, L. Naldi, M. Tonelli, J. Geleijnse, M. Petzold, M. G. Shrime, M. Younis, N. Yonemoto, N. Breitborde, P. Yip, F. Pourmalek, P. A. Lotufo, A. Esteghamati, G. J. Hankey, R. Ali, R. Lunevicius, R. Malekzadeh, R. Dellavalle, R. Weintraub, R. Lucas, R. Hay, D. Rojas-Rueda, R. Westerman, S. G. Sepanlou, S. Nolte, S. Patten, S. Weichenthal, S. F. Abera, S.-M. Fereshtehnejad, I. Shiue, T. Driscoll, T. Vasankari, U. Alsharif, V. Rahimi-Movaghar, V. V. Vlassov, W. S. Marcenes, W. Mekonnen, Y. A. Melaku, Y. Yano, A. Artaman, I. Campos, J. MacLachlan, U. Mueller, D. Kim, M. Trillini, B. Eshrati, H. C. Williams, K. Shibuya, R. Dandona, K. Murthy, B. Cowie, A. T. Amare, C. A. Antonio, C. Castañeda-Orjuela, C. H. van Gool, F. Violante, I.-H. Oh, K. Deribe, K. Soreide, L. Knibbs, M. Kereselidze, M. Green, R. Cardenas, N. Roy, T. Tillmann, Y. Li, H. Krueger, L. Monasta, S. Dey, S. Sheikhbahaei, N. Hafezi-Nejad, G. A. Kumar, C. T. Sreeramareddy, L. Dandona, H. Wang, S. E. Vollset, A. Mokdad, J. A. Salomon, R. Lozano, T. Vos, M. Forouzanfar, A. Lopez, C. Murray and M. Naghavi, The Global Burden of Cancer 2013., *JAMA Oncol.*, 2015, **1**, 505–527.

5 M. G. Cooper and E. R. Hausman, *The Cell: A molecular approach*, ASM Press, Washington, 3th edn., 2004.

6 J. A. Nicolazzo and B. C. Finnin, in *Drug Absorption Studies: In Situ, In Vitro and In Silico Models*, eds. C. Ehrhardt and K.-J. Kim, Springer US, Boston, MA, 2008, pp. 89–111.

7 F. ud Din, W. Aman, I. Ullah, O. S. Qureshi, O. Mustapha, S. Shafique and A. Zeb, Effective use of nanocarriers as drug delivery systems for the treatment of selected tumors., *Int. J. Nanomedicine*, 2017, **12**, 7291–7309.

8 V. Bouvard, D. Loomis, K. Z. Guyton, Y. Grosse, F. El Ghissassi, L. Benbrahim-Tallaa, N. Guha, H. Mattock and K. Straif, Carcinogenicity of consumption of red and processed meat, *Lancet Oncol.*, 2015, **16**, 1599–1600.

9 H. Fujiki, E. Sueoka and M. Suganuma, Tumor promoters: from chemicals to inflammatory proteins, *J. Cancer Res. Clin. Oncol.*, 2013, **139**, 1603–1614.

10 K. P. Glover, L. K. Markell, E. M. Donner and X. Han, Protein kinase C-activating tumor promoters modulate the DNA damage response in UVC-irradiated TK6 cells, *Toxicol. Lett.*, 2014, **229**, 210–219.

11 D. Hanahan and R. A. Weinberg, Hallmarks of cancer: The next generation, *Cell*, 2011, **144**, 646–674.

12 S. Rakoff-Nahoum, Why Cancer and Inflammation?, *Yale J. Biol. Med.*, 2006, **79**, 123–130.

13 R. L. Siegel, K. D. Miller and A. Jemal, Cancer statistics, 2016, *CA. Cancer J. Clin.*, 2016, **66**, 7–30.

14 J. Ferlay, E. Steliarova-Foucher, J. Lortet-Tieulent, S. Rosso, J. W. W. Coebergh, H. Comber, D. Forman and F. Bray, Cancer incidence and mortality patterns in Europe: Estimates for 40 countries in 2012, *Eur. J. Cancer*, 2013, **49**, 1374–1403.

15 M. Shahdordizadeh, R. Yazdian-Robati, M. Ramezani, K. Abnous and S. M. Taghdisi, Aptamer application in targeted delivery systems for diagnosis and treatment of breast cancer, *J. Mater. Chem. B*, 2016, **4**, 7766–7778.

16 K. A. Ban and C. V. Godellas, Epidemiology of Breast Cancer, *Surg. Oncol. Clin. N. Am.*, 2014, **23**, 409–422.

17 J. R. Benson and I. Jatoi, The global breast cancer burden., *Future Oncol.*, 2012, **8**, 697–702.

18 S. Pudkasam, K. Tangalakis, N. Chinlumprasert, V. Apostolopoulos and L. Stojanovska, Breast cancer and exercise: The role of adiposity and immune markers, *Maturitas*, 2017, **105**, 16–22.

19 J. Ferlay, I. Soerjomataram, R. Dikshit, S. Eser, C. Mathers, M. Rebelo, D. M. Parkin, D. Forman and F. Bray, Cancer incidence and mortality worldwide: Sources, methods and major patterns in GLOBOCAN 2012, *Int. J. Cancer*, 2015, **136**, E359–E386.

20 S. A. Narod, J. Iqbal and A. B. Miller, Why have breast cancer mortality rates declined?, *J. Cancer Policy*, 2015, **5**, 8–17.

21 S. K. Yeo and J.-L. Guan, Breast Cancer: Multiple Subtypes within a Tumor?, *Trends in Cancer*, 2017, **3**, 753–760.

22 Y. Mao, E. T. Keller, D. H. Garfield, K. Shen and J. Wang, Stromal cells in tumor microenvironment and breast cancer, *Cancer Metastasis Rev.*, 2013, **32**, 303–315.

23 N. Melling, C. M. Kowitz, R. Simon, C. Bokemeyer, L. Terracciano, G. Sauter, J. R. Izbicki and A. H. Marx, High Ki67 expression is an independent good prognostic marker in colorectal cancer, *J. Clin. Pathol.*, 2016, **69**, 209 LP-214.

24 L. T. Li, G. Jiang, Q. Chen and J. N. Zheng, Ki67 is a promising molecular target in the diagnosis of cancer (Review), *Mol. Med. Rep.*, 2015, **11**, 1566–1572.

25 M. Losada-Echeberría, M. Herranz-López, V. Micol and E. Barrajón-Catalán, Polyphenols as Promising Drugs against Main Breast Cancer Signatures, *Antioxidants*, 2017, **6**, 88.

26 C. M. Schlotter, L. Tietze, U. Vogt, C. V. Heinsen and A. Hahn, Ki67 and lymphocytes in the pretherapeutic core biopsy of primary invasive breast cancer: positive markers of therapy response prediction and superior survival, *Horm. Mol. Biol. Clin. Investig.*, DOI:10.1515/hmbci-2017-0022.

27 M.-T. Hsieh, L.-C. Chang, H.-Y. Hung, H.-Y. Lin, M.-H. Shih, C.-H. Tsai, S.-C. Kuo and K.-H. Lee, New bis(hydroxymethyl) alkanoate curcuminoid derivatives exhibit activity against triple-negative breast cancer *in vitro* and *in vivo*, *Eur. J. Med. Chem.*, 2017, **131**, 141–151.

28 M. R. Nathan and P. Schmid, The emerging world of breast cancer immunotherapy, *The Breast*, 2017, **37**, 200–206.

29 Z. Li, P. Hu, J. Tu and N. Yu, Luminal B breast cancer: patterns of recurrence and clinical outcome, *Oncotarget*, 2016, **7**, 65024–65033.

30 GLOBOCAN, Estimated Cancer Incidence, Mortality and Prevalence Worldwide in 2012, http://globocan.iarc.fr/Pages/fact_sheets_cancer.aspx, (accessed 27 July 2017).

31 E. Altobelli, A. Lattanzi, R. Paduano, G. Varassi and F. di Orio, Colorectal cancer prevention in Europe: Burden of disease and status of screening programs, *Prev. Med. (Baltim).*, 2014, **62**, 132–141.

32 K. Esposito, P. Chiodini, A. Capuano, G. Bellastella, M. I. Maiorino, C. Rafaniello, D. B. Panagiotakos and D. Giugliano, Colorectal cancer association with metabolic syndrome and its components: a systematic review with meta-analysis, *Endocrine*, 2013, **44**, 634–647.

33 A. Ahmadi, M. Noroozi, M. A. Pourhoseingholi and S.-S. Hashemi-Nazari, Effect of metabolic syndrome and its components on survival in colorectal cancer: a prospective study, *J. Ren. Inj. Prev.*, 2015, **4**, 15–19.

34 R. L. Ahmed, K. H. Schmitz, K. E. Anderson, W. D. Rosamond and A. R. Folsom, The metabolic syndrome and risk of incident colorectal cancer, *Cancer*, 2006, **107**, 28–36.

35 M. M. Center, A. Jemal, R. A. Smith and E. Ward, Worldwide Variations in Colorectal Cancer, *CA. Cancer J. Clin.*, 2009, **59**, 366–378.

36 A. Farinetti, V. Zurlo, A. Manenti, F. Coppi and A. V. Mattioli, Mediterranean Diet and Colorectal Cancer: a systematic review, *Nutrition*, 2017, **43–44**, 83–88.

37 J. Terzić, S. Grivennikov, E. Karin and M. Karin, Inflammation and Colon Cancer, *Gastroenterology*, 2017, **138**, 2101–2114.e5.

38 H. Sonoda, S. Kohnoe, T. Yamazato, Y. Satoh, G. Morizono, K. Shikata, M. Morita, A. Watanabe, M. Morita, Y. Kakeji, F. Inoue and Y. Maehara, Colorectal cancer screening with odour material by canine scent detection., *Gut*, 2011, **60**, 814–819.

39 G. Wilkes and K. Hartshorn, Colon, Rectal, and Anal Cancers, *Semin. Oncol. Nurs.*, 2009, **25**, 32–47.

40 H. Verdaguer, J. Tabernero and T. Macarulla, Ramucirumab in metastatic colorectal cancer: evidence to date and place in therapy, *Ther. Adv. Med. Oncol.*, 2016, **8**, 230–242.

41 N. S. Vasudev and A. R. Reynolds, Anti-angiogenic therapy for cancer: current progress, unresolved questions and future directions, *Angiogenesis*, 2014, **17**, 471–494.

42 D. L. H. Chan, E. Segelov, R. S. Wong, A. Smith, R. A. Herbertson, B. T. Li, N. Tebbutt, T. Price and N. Pavlakis, Epidermal growth factor receptor (EGFR) inhibitors for metastatic colorectal cancer., *Cochrane database Syst. Rev.*, 2017, **6**, CD007047.

43 A. Chicheł, J. Skowronek, M. Kubaszewska and M. Kanikowski, Hyperthermia - Description of a method and a review of clinical applications, *Reports Pract. Oncol. Radiother.*, 2007, **12**, 267–275.

44 P. Martinkova, M. Brtnicky, J. Kynicky and M. Pohanka, Iron Oxide Nanoparticles: Innovative Tool in Cancer Diagnosis and Therapy., *Adv. Healthc. Mater.*, 2017, 1700932.

45 S. Smith and S. Prewett, Principles of chemotherapy and radiotherapy, *Obstet. Gynaecol. Reprod. Med.*, 2017, **27**, 206–212.

46 L. J. Murray and M. H. Robinson, Radiotherapy: technical aspects, *Medicine (Baltimore).*, 2016, **44**, 10–14.

47 B. B. S. Cerqueira, A. Lasham, A. N. Shelling and R. Al-Kassas, Nanoparticle therapeutics: Technologies and methods for overcoming cancer, *Eur. J. Pharm. Biopharm.*, 2015, **97**, 140–151.

48 M. Mazonakis and J. Damilakis, Cancer risk after radiotherapy for benign diseases, *Phys. Medica*, 2017, **42**, 285–291.

49 L. M. Weiner, M. V Dhodapkar and S. Ferrone, Monoclonal antibodies for cancer immunotherapy, *Lancet*, 2017, **373**, 1033–1040.

50 B. Rini, Future Approaches in Immunotherapy, *Semin. Oncol.*, 2017, **41**, S30–S40.

51 W. Asghar, R. El Assal, H. Shafiee, S. Pitteri, R. Paulmurugan and U. Demirci, Engineering cancer microenvironments for *in vitro* 3-D tumor models, *Mater. Today*, 2015, **18**, 539–553.

52 N. Akhtar and R. A. Khan, Liposomal systems as viable drug delivery technology for skin cancer sites with an outlook on lipid-based delivery vehicles and diagnostic imaging inputs for skin conditions', *Prog. Lipid Res.*, 2016, **64**, 192–230.

53 L. H. Stockwin, D. McGonagle, I. G. Martin and G. E. Blair, Dendritic cells: Immunological sentinels with a central role in health and disease, *Immunol. Cell Biol.*, 2000, **78**, 91–102.

54 N. R. Datta, S. G. Ordóñez, U. S. Gaipl, M. M. Paulides, H. Crezee, J. Gellermann, D. Marder, E. Puric and S. Bodis, Local hyperthermia combined with radiotherapy and-/or chemotherapy: Recent advances and promises for the future, *Cancer Treat. Rev.*, 2015, **41**, 742–753.

55 P. Wust, B. Hildebrandt, G. Sreenivasa, B. Rau, J. Gellermann, H. Riess, R. Felix and P. Schlag, Hyperthermia in combined treatment of cancer, *Lancet Oncol.*, 2002, **3**, 487–497.

56 N. R. Datta, S. Krishnan, D. E. Speiser, E. Neufeld, N. Kuster, S. Bodis and H. Hofmann, Magnetic nanoparticle-induced hyperthermia with appropriate payloads: Paul Ehrlich's 'magic (nano)bullet' for cancer theranostics?, *Cancer Treat. Rev.*, 2016, **50**, 217–227.

57 A. G. Arranja, V. Pathak, T. Lammers and Y. Shi, Tumor-targeted nanomedicines for cancer theranostics, *Pharmacol. Res.*, 2017, **115**, 87–95.

58 Y.-X. Li, Y.-L. Jiang, Y.-P. Yi, W.-L. Liu, Y.-X. Tang, Y.-X. Liu and Y.-F. Liu, Application of auricular acupoints therapy in relieving the gastrointestinal side effects induced by chemotherapy: an integrative review, *Chinese Nurs. Res.*, 2016, **3**, 58–61.

59 K. Krukiewicz and J. K. Zak, Biomaterial-based regional chemotherapy: Local anticancer drug delivery to enhance chemotherapy and minimize its side-effects, *Mater. Sci. Eng. C*, 2016, **62**, 927–942.

60 B. Colagiuri, H. Dhillon, P. N. Butow, J. Jansen, K. Cox and J. Jacquet, Does assessing patients' expectancies about chemotherapy side effects influence their occurrence?, *J. Pain Symptom Manage.*, 2013, **46**, 275–281.

61 K. Bergkvist and Y. Wengström, Symptom experiences during chemotherapy treatment - With focus on nausea and vomiting, *Eur. J. Oncol. Nurs.*, 2006, **10**, 21–29.

62 S. Tummala, M. N. Satish Kumar and A. Prakash, Formulation and characterization of 5-Fluorouracil enteric coated nanoparticles for sustained and localized release in treating colorectal cancer, *Saudi Pharm. J.*, 2015, **23**, 308–314.

63 S. P. Lee, M. Y. Leu, J. B. Smathers, W. H. McBride, R. G. Parker, H. R. Withers, A. A. M. Hart, W. J. Klokman, M. A. Kuenen, G. M. Ouwens, H. Bartelink and F. E. van Leeuwen, Biologically effective dose distribution based on the linear quadratic model and its clinical relevance., *Int. J. Radiat. Oncol. Biol. Phys.*, 1995, **33**, 375–89.

64 K. Rugbjerg, L. Mellemkjaer, J. D. Boice, L. Kober, M. Ewertz and J. H. Olsen, Cardiovascular Disease in Survivors of Adolescent and Young Adult Cancer: A Danish Cohort Study, 1943-2009, *JNCI J. Natl. Cancer Inst.*, 2014, **106**, dju110-dju110.

65 C. Núñez, J. L. Capelo, G. Igrejas, A. Alfonso, L. M. Botana and C. Lodeiro, An overview of the effective combination therapies for the treatment of breast cancer, *Biomaterials*, 2016, **97**, 34–50.

66 Shagufta and I. Ahmad, Tamoxifen a pioneering drug: An update on the therapeutic potential of tamoxifen derivatives., *Eur. J. Med. Chem.*, 2017, **143**, 515–531.

67 M. V. J. Mustonen, S. Pyrhönen and P.-L. Kellokumpu-Lehtinen, Toremifene in the treatment of breast cancer, *World J. Clin. Oncol.*, 2014, **5**, 393–405.

68 A. Di Leo, G. Curigliano, V. Diéras, L. Malorni, C. Sotiriou, C. Swanton, A. Thompson, A. Tutt and M. Piccart, New approaches for improving outcomes in breast cancer in Europe, *The Breast*, 2015, **24**, 321–330.

69 E. Pérez-Herrero and A. Fernández-Medarde, Advanced targeted therapies in cancer: Drug nanocarriers, the future of chemotherapy, *Eur. J. Pharm. Biopharm.*, 2015, **93**, 52–79.

70 F. Danhier, To exploit the tumor microenvironment: Since the EPR effect fails in the clinic, what is the future of nanomedicine?, *J. Control. Release*, 2016, **244**, 108–121.

71 H. Hurwitz, L. Fehrenbacher, W. Novotny, T. Cartwright, J. Hainsworth, W. Heim, J. Berlin, A. Baron, S. Griffing, E. Holmgren, N. Ferrara, G. Fyfe, B. Rogers, R. Ross and F. Kabbinavar, Bevacizumab plus Irinotecan, Fluorouracil, and Leucovorin for Metastatic Colorectal Cancer, *N. Engl. J. Med.*, 2004, **350**, 2335–2342.

72 S. P. Chandran, S. B. Natarajan, S. Chandraseharan and M. S. B. Mohd Shahimi, Nano drug delivery strategy of 5-fluorouracil for the treatment of colorectal cancer, *J. Cancer Res. Pract.*, 2017, **4**, 45–48.

73 D. J. Jonker, C. J. O'Callaghan, C. S. Karapetis, J. R. Zalcberg, D. Tu, H.-J. Au, S. R. Berry, M. Krahn, T. Price, R. J. Simes, N. C. Tebbutt, G. van Hazel, R. Wierzbicki, C. Langer and M. J. Moore, Cetuximab for the Treatment of Colorectal Cancer, *N. Engl. J. Med.*, 2007, **357**, 2040–2048.

74 A. Françoso and P. U. Simioni, Immunotherapy for the treatment of colorectal tumors: focus on approved and in-clinical-trial monoclonal antibodies, *Drug Des. Devel. Ther.*, 2017, **11**, 177–184.

75 Q. Luo, P. Wang, Y. Miao, H. He and X. Tang, A novel 5-fluorouracil prodrug using hydroxyethyl starch as a macromolecular carrier for sustained release, *Carbohydr. Polym.*, 2012, **87**, 2642–2647.

76 D. B. Longley, D. P. Harkin and P. G. Johnston, 5-Fluorouracil: Mechanisms of Action and Clinical Strategies., *Nat Rev Cancer*, 2003, **3**, 330–8.

77 I. A. Alsarra and M. N. Alarifi, Validated liquid chromatographic determination of 5-fluorouracil in human plasma, 2004, **804**, 435–439.

78 P. Li, Y. Wang, Z. Peng, F. She and L. Kong, Development of chitosan nanoparticles as drug delivery systems for 5-fluorouracil and leucovorin blends, *Carbohydr. Polym.*, 2011, **85**, 698–704.

79 T. Bano, N. Kumar and R. Dudhe, Free radical scavenging properties of pyrimidine derivatives, *Org. Med. Chem. Lett.*, 2012, **2**, 34.

80 R. A. Al-Thawabeia and H. A. Hodali, Use of Zeolite ZSM-5 for Loading and Release of 5-Fluorouracil, *J. Chem.*, 2015, **2015**, 1–9.

81 R. Matuo, F. G. Sousa, A. E. Escargueil, I. Grivicich, D. Garcia-Santos, J. A. B. Chies, J. Saffi, A. K. Larsen and J. A. P. Henriques, 5-Fluorouracil and its active metabolite FdUMP cause DNA damage in human SW620 colon adenocarcinoma cell line, *J. Appl. Toxicol.*, 2009, **29**, 308–316.

82 F. Casale, R. Canaparo, L. Serpe, E. Muntoni, C. Della Pepa, M. Costa, L. Mairone, G. P. Zara, G. Fornari and M. Eandi, Plasma concentrations of 5-fluorouracil and its metabolites in colon cancer patients, *Pharmacol. Res.*, 2004, **50**, 173–179.

83 M. Malet-Martino and R. Martino, Clinical Studies of Three Oral Prodrugs of 5-Fluorouracil (Capecitabine, UFT, S-1): A Review, *Oncologist*, 2002, **7**, 288–323.

84 H. Akhdar, P. Loyer, C. Rauch, A. Corlu, A. Guillouzo and F. Morel, Involvement of Nrf2 activation in resistance to 5-fluorouracil in human colon cancer HT-29 cells, *Eur. J. Cancer*, 2009, **45**, 2219—2227.

85 F. Tanaka, T. Fukuse and H. W. and M. Fukushima, The History, Mechanism and Clinical Use of Oral 5-Fluorouracil Derivative Chemotherapeutic Agents, *Curr. Pharm. Biotechnol.*, 2000, **1**, 137–164.

86 M. F. Sorrentino, J. Kim, A. E. Foderaro and A. G. Truesdell, 5-fluorouracil induced cardiotoxicity: Review of the literature, *Cardiol. J.*, 2012, **19**, 453–458.

87 F. K. Alanazi, A. E. Yassin, M. El-badry, H. A. Mowafy and I. A. Alsarra, Validated High-Performance Liquid Chromatographic Technique for Determination of 5-Fluorouracil : Applications to Stability Studies and Simulated Colonic Media, *J. Chromatogr. Sci.*, 2009, **47**, 558–563.

88 C. Focaccetti, A. Bruno, E. Magnani, D. Bartolini, E. Principi, K. Dallaglio, E. O. Bucci, G. Finzi, F. Sessa, D. M. Noonan and A. Albini, Effects of 5-Fluorouracil on Morphology, Cell Cycle, Proliferation, Apoptosis, Autophagy and ROS Production in Endothelial Cells and Cardiomyocytes, *PLoS One*, 2015, **10**, e0115686.

89 T. S. Anirudhan, P. L. Divya and J. Nima, Synthesis and characterization of silane coated magnetic nanoparticles/glycidylmethacrylate-grafted-maleated cyclodextrin composite hydrogel as a drug carrier for the controlled delivery of 5-fluorouracil, *Mater. Sci. Eng. C*, 2015, **55**, 471–481.

90 H. A. M. Faria and A. A. A. de Queiroz, A novel drug delivery of 5-fluorouracil device based on TiO2/ZnS nanotubes, *Mater. Sci. Eng. C*, 2015, **56**, 260–268.

91 M. N. Patel, S. Lakkadwala, M. S. Majrad, E. R. Injeti, S. M. Gollmer, Z. A. Shah, S. H. S. Boddu and J. Nesamony, Characterization and Evaluation of 5-Fluorouracil-Loaded Solid Lipid Nanoparticles Prepared via a Temperature-Modulated Solidification Technique, *AAPS PharmSciTech*, 2014, **15**, 1498–1508.

92 R. X. Zhang, H. L. Wong, H. Y. Xue, J. Y. Eoh and X. Y. Wu, Nanomedicine of synergistic drug combinations for cancer therapy – Strategies and perspectives, *J. Control. Release*, 2016, **240**, 489–503.

93 W. Dai, X. Wang, G. Song, T. Liu, B. He, H. Zhang, X. Wang and Q. Zhang, Combination antitumor therapy with targeted dual-nanomedicines, *Adv. Drug Deliv. Rev.*, 2017, **115**, 23–45.

94 R. X. Zhang, P. Cai, T. Zhang, K. Chen, J. Li, J. Cheng, K. S. Pang, H. A. Adissu, A. M. Rauth and X. Y. Wu, Polymer–lipid hybrid nanoparticles synchronize pharmacokinetics of co-encapsulated doxorubicin–mitomycin C and enable their spatiotemporal co-delivery and local bioavailability in breast tumor, *Nanomedicine Nanotechnology, Biol. Med.*, 2016, **12**, 1279–1290.

95 J. R. Hasenstein, H.-C. Shin, K. Kasmerchak, D. Buehler, G. S. Kwon and K. R. Kozak, Antitumor Activity of Triolimus: A Novel Multidrug-Loaded Micelle Containing Paclitaxel, Rapamycin, and 17-AAG, *Mol. Cancer Ther.*, 2012, **11**, 2233–2242.

96 A. J. Shuhendler, P. Prasad, R. X. Zhang, M. A. Amini, M. Sun, P. P. Liu, R. G. Bristow, A. M. Rauth and X. Y. Wu, Synergistic Nanoparticulate Drug Combination Overcomes Multidrug Resistance, Increases Efficacy, and Reduces Cardiotoxicity in a Nonimmunocompromised Breast Tumor Model, *Mol. Pharm.*, 2014, **11**, 2659–2674.

97 P. Prasad, A. Shuhendler, P. Cai, A. M. Rauth and X. Y. Wu, Doxorubicin and mitomycin C co-loaded polymer-lipid hybrid nanoparticles inhibit growth of sensitive and multidrug resistant human mammary tumor xenografts, *Cancer Lett.*, 2017, **334**, 263–273.

98 A. Anitha, N. Deepa, K. P. Chennazhi, V. K. Lakshmanan and R. Jayakumar, Combinatorial anticancer effects of curcumin and 5-fluorouracil loaded thiolated chitosan nanoparticles towards colon cancer treatment, *Biochim. Biophys. Acta - Gen. Subj.*, 2014, **1840**, 2730–2743.

99 P. G. Tardi, N. Dos Santos, T. O. Harasym, S. A. Johnstone, N. Zisman, A. W. Tsang, D. G. Bermudes and L. D. Mayer, Drug ratio–dependent antitumor activity of irinotecan and cisplatin combinations *in vitro* and in vivo, *Mol. Cancer Ther.*, 2009, **8**, 2266–2275.

100 D. Pereg and M. Lishner, Non-steroidal anti-inflammatory drugs for the prevention and treatment of cancer, *J. Intern. Med.*, 2005, **258**, 115–123.

101 F. Guadagni, P. Ferroni, R. Palmirotta, G. Del Monte, V. Formica and M. Roselli, Non-steroidal anti-inflammatory drugs in cancer prevention and therapy., *Anticancer Res.*, 2007, **27**, 3147–3162.

102 E. R. Rayburn, S. J. Ezell and R. Zhang, Anti-Inflammatory Agents for Cancer Therapy, *Mol. Cell. Pharmacol.*, 2009, **1**, 29–43.

103 J. Cuzick, F. Otto, J. A. Baron, P. H. Brown, J. Burn, P. Greenwald, J. Jankowski, C. La Vecchia, F. Meyskens, H. J. Senn and M. Thun, Aspirin and non-steroidal anti-inflammatory drugs for cancer prevention: an international consensus statement, *Lancet Oncol.*, 2009, **10**, 501–507.

104 X. Garcia-Albeniz and A. T. Chan, Aspirin for the prevention of colorectal cancer, *Best Pract. Res. Clin. Gastroenterol.*, 2011, **25**, 461–472.

105 E. Giovannucci, K. M. Egan, D. J. Hunter, M. J. Stampfer, G. A. Colditz, W. C. Willett and F. E. Speizer, Aspirin and the Risk of Colorectal Cancer in Women, *N. Engl. J. Med.*, 1995, **333**, 609–614.

106 S. A. Khuder and A. B. Mutgi, Breast cancer and NSAID use: a meta-analysis, *Br. J. Cancer*, 2001, **84**, 1188–1192.

107 E. Rahme, J. Ghosn, K. Dasgupta, R. Rajan and M. Hudson, Association between frequent use of nonsteroidal anti-inflammatory drugs and breast cancer, *BMC Cancer*, 2005, **5**, 159.

108 L. A. García Rodríguez and A. González-Pérez, Risk of breast cancer among users of aspirin and other anti-inflammatory drugs, *Br. J. Cancer*, 2004, **91**, 525–529.

109 R. E. Harris, J. Beebe-Donk and H. M. Schuller, Chemoprevention of lung cancer by non-steroidal anti-inflammatory drugs among cigarette smokers., *Oncol. Rep.*, 2002, **9**, 693–695.

110 M. F. Leitzmann, M. J. Stampfer, J. Ma, J. M. Chan, G. A. Colditz, W. C. Willett and E. Giovannucci, Aspirin use in relation to risk of prostate cancer., *Cancer Epidemiol. Biomarkers Prev.*, 2002, **11**, 1108–1111.

111 X. Xu, W. Ho, X. Zhang, N. Bertrand and O. Farokhzad, Cancer nanomedicine: From targeted delivery to combination therapy, *Trends Mol. Med.*, 2015, **21**, 223–232.

112 G. L. Hornyak and A. K. Rao, in *Nanoscience in Dermatology*, eds. M. R. Hamblin, P. Avci and T. W. Prow, Academic Press, Boston, 2016, pp. 15–29.

113 A. Z. Wilczewska, K. Niemirowicz, K. H. Markiewicz and H. Car, Nanoparticles as drug delivery systems, *Pharmacol. Reports*, 2012, **64**, 1020–1037.

114 A. Wicki, D. Witzigmann, V. Balasubramanian and J. Huwyler, Nanomedicine in cancer therapy: Challenges, opportunities, and clinical applications, *J. Control. Release*, 2015, **200**, 138–157.

115 B. Felice, M. P. Prabhakaran, A. P. Rodríguez and S. Ramakrishna, Drug delivery vehicles on a nano-engineering perspective, *Mater. Sci. Eng. C*, 2014, **41**, 178–195.

116 R. Gupta, J. Shea, C. Scafe, A. Shurlygina and N. Rapoport, Polymeric micelles and nanoemulsions as drug carriers: Therapeutic efficacy, toxicity, and drug resistance, *J. Control. Release*, 2015, **212**, 70–77.

117 K. Avgoustakis, PLGA–mPEG nanoparticles of cisplatin: *in vitro* nanoparticle degradation, *in vitro* drug release and in vivo drug residence in blood properties, *J. Control. Release*, 2002, **79**, 123–135.

118 K. Liu, W. Chen, T. Yang, B. Wen, D. Ding, M. Keidar, J. Tang and W. Zhang, Paclitaxel and quercetin nanoparticles co-loaded in microspheres to prolong retention time for pulmonary drug delivery, *Int. J. Nanomedicine*, 2017, **12**, 8239–8255.

119 I. Singh, R. Swami, M. K. Jeengar, W. Khan and R. Sistla, p-Aminophenyl-α-d-mannopyranoside engineered lipidic nanoparticles for effective delivery of docetaxel to brain, *Chem. Phys. Lipids*, 2015, **188**, 1–9.

120 A. S. Chauhan, N. K. Jain, P. V. Diwan and A. J. Khopade, Solubility Enhancement of Indomethacin with Poly(amidoamine) Dendrimers and Targeting to Inflammatory Regions of Arthritic Rats, *J. Drug Target.*, 2004, **12**, 575–583.

121 P. K. Tripathi, A. J. Khopade, S. Nagaich, S. Shrivastava, S. Jain and N. K. Jain, Dendrimer grafts for delivery of 5-fluorouracil., *Pharmazie*, 2002, **57**, 261–264.

122 T. U. Ly, N. Q. Tran, T. K. D. Hoang, K. N. Phan, H. N. Truong and C. K. Nguyen, Pegylated dendrimer and its effect in fluorouracil loading and release for enhancing antitumor activity., *J. Biomed. Nanotechnol.*, 2013, **9**, 213–220.

123 J. Seki, S. Sonoke, A. Saheki, H. Fukui, H. Sasaki and T. Mayumi, A nanometer lipid emulsion, lipid nano-sphere (LNS®), as a parenteral drug carrier for passive drug targeting, *Int. J. Pharm.*, 2004, **273**, 75–83.

124 G. Hadrich, G. R. Vaz, M. Maidana, J. M. Kratz, G. Loch-Neckel, D. C. Favarin, A. de P. Rogerio, F. M. R. J. da Silva, A. L. Muccillo-Baisch and C. L. Dora, Anti-inflammatory Effect and Toxicology Analysis of Oral Delivery Quercetin Nanosized Emulsion in Rats., *Pharm. Res.*, 2016, **33**, 983–993.

125 N.-T. Tung, V.-T. Huyen and S.-C. Chi, Topical delivery of dexamethasone acetate from hydrogel containing nanostructured liquid carriers and the drug., *Arch. Pharm. Res.*, 2015, **38**, 1999–2007.

126 B. Tian, S. Liu, S. Wu, W. Lu, D. Wang, L. Jin, B. Hu, K. Li, Z. Wang and Z. Quan, pH-responsive poly (acrylic acid)-gated mesoporous silica and its application in oral colon targeted drug delivery for doxorubicin, *Colloids Surfaces B Biointerfaces*, 2017, **154**, 287–296.

127 Y. Wang, J. Wang, Y. Yang, Y. Sun, Y. Yuan, Y. Li and C. Liu, In situ biodegradable crosslinking of cationic oligomer coating on mesoporous silica nanoparticles for drug delivery, *Colloids Surfaces B Biointerfaces*, 2017, **153**, 272–279.

128 Z. Tian, Y. Xu and Y. Zhu, Aldehyde-functionalized dendritic mesoporous silica nanoparticles as potential nanocarriers for pH-responsive protein drug delivery, *Mater. Sci. Eng. C*, 2017, **71**, 452–459.

129 T. K. Jain, J. Richey, M. Strand, D. L. Leslie-Pelecky, C. A. Flask and V. Labhasetwar, Magnetic nanoparticles with dual functional properties: Drug delivery and magnetic resonance imaging, *Biomaterials*, 2008, **29**, 4012–4021.

130 G. Tokajuk, K. Niemirowicz, P. Deptuła, E. Piktel, M. Cieśluk, A. Z. Wilczewska, J. R. Dąbrowski and R. Bucki, Use of magnetic nanoparticles as a drug delivery system to improve chlorhexidine antimicrobial activity, *Int. J. Nanomedicine*, 2017, **12**, 7833–7846.

131 V. Zamora-Mora, M. Fernández-Gutiérrez, Á. González-Gómez, B. Sanz, J. S. Román, G. F. Goya, R. Hernández and C. Mijangos, Chitosan nanoparticles for combined drug delivery and magnetic hyperthermia: From preparation to *in vitro* studies, *Carbohydr. Polym.*, 2017, **157**, 361–370.

132 R. Amorim, N. Vilaça, O. Martinho, R. M. Reis, M. Sardo, J. Rocha, A. M. Fonseca, F. Baltazar and I. C. Neves, Zeolite structures loading with an anticancer compound as drug delivery systems, *J. Phys. Chem. C*, 2012, **116**, 25642–25650.

133 N. Vilaça, R. Amorim, A. F. Machado, P. Parpot, M. F. R. Pereira, M. Sardo, J. Rocha, A. M. Fonseca, I. C. Neves and F. Baltazar, Potentiation of 5-fluorouracil encapsulated in zeolites as drug delivery systems for *in vitro* models of colorectal carcinoma, *Colloids Surfaces B Biointerfaces*, 2013, **112**, 237–244.

134 O. Martinho, N. Vilaça, P. J. G. Castro, R. Amorim, A. M. Fonseca, F. Baltazar, R. M. Reis and I. C. Neves, *In vitro* and in vivo studies of temozolomide loading in zeolite structures as drug delivery systems for glioblastoma, *RSC Adv.*, 2015, **5**, 28219–28227.

135 R. Lehner, X. Wang, S. Marsch and P. Hunziker, Intelligent nanomaterials for medicine: Carrier platforms and targeting strategies in the context of clinical application, *Nanomedicine Nanotechnology, Biol. Med.*, 2017, **9**, 742–757.

136 S. Lazzari, D. Moscatelli, F. Codari, M. Salmona, M. Morbidelli and L. Diomede, Colloidal stability of polymeric nanoparticles in biological fluids, *J. Nanoparticle Res.*, 2012, **14**, 920.

137 K. S. Soppimath, T. M. Aminabhavi, A. R. Kulkarni and W. E. Rudzinski, Biodegradable polymeric nanoparticles as drug delivery devices, *J. Control. Release*, 2001, **70**, 1–20.

138 O. Pillai and R. Panchagnula, Polymers in drug delivery, *Curr. Opin. Chem. Biol.*, 2001, **5**, 447–451.

139 N. Kamaly, B. Yameen, J. Wu and O. C. Farokhzad, Degradable Controlled-Release Polymers and Polymeric Nanoparticles: Mechanisms of Controlling Drug Release, *Chem. Rev.*, 2016, **116**, 2602–2663.

140 J. P. Rao and K. E. Geckeler, Polymer nanoparticles: Preparation techniques and size-control parameters, *Prog. Polym. Sci.*, 2011, **36**, 887–913.

141 F. Sauvage, S. Messaoudi, E. Fattal, G. Barratt and J. Vergnaud-Gauduchon, Heat shock proteins and cancer: How can nanomedicine be harnessed?, *J. Control. Release*, 2017, **248**, 133–143.

142 L. L. Chaves, S. A. Costa Lima, A. C. C. Vieira, L. Barreiros, M. A. Segundo, D. Ferreira, B. Sarmento and S. Reis, Development of PLGA nanoparticles loaded with clofazimine for oral delivery: Assessment of formulation variables and intestinal permeability, *Eur. J. Pharm. Sci.*, 2018, **112**, 28–37.

143 N. Han, L. Pang, J. Xu, H. Hyun, J. Park and Y. Yeo, Development of Surface-Variable Polymeric Nanoparticles for Drug Delivery to Tumors, *Mol. Pharm.*, 2017, **14**, 1538–1547.

144 G. Suffredini, J. E. East and L. M. Levy, New Applications of Nanotechnology for Neuroimaging, *Am. J. Neuroradiol.*, 2014, **35**, 1246–1253.

145 C. C. Lee, J. A. MacKay, J. M. J. Fréchet and F. C. Szoka, Designing dendrimers for biological applications, *Nat. Biotechnol.*, 2005, **23**, 1517–1526.

146 E. M. Pridgen, R. Langer and O. C. Farokhzad, Biodegradable, polymeric nanoparticle delivery systems for cancer therapy, *Nanomedicine*, 2007, **2**, 669–680.

147 X. You, Y. Kang, G. Hollett, X. Chen, W. Zhao, Z. Gu and J. Wu, Polymeric nanoparticles for colon cancer therapy: overview and perspectives, *J. Mater. Chem. B*, 2016, **4**, 7779–7792.

148 S. Mignani, J. Rodrigues, H. Tomas, M. Zablocka, X. Shi, A.-M. Caminade and J.-P. Majoral, Dendrimers in combination with natural products and analogues as anti-cancer agents, *Chem. Soc. Rev.*, 2018, **47**, 514–532.

149 M. Han, M.-Y. Huang-Fu, W.-W. Guo, N. Guo, J. Chen, H. Liu, Z. Xie, M. Lin, Q. Wei and J. Gao, MMP-2 Sensitive HA end-conjugated poly(amidoamine) dendrimers via click reaction to enhance drug penetration into solid tumor, *ACS Appl. Mater. Interfaces*, 2017, **9**, 42459–42470.

150 C. C. Lee, E. R. Gillies, M. E. Fox, S. J. Guillaudeu, J. M. J. Fréchet, E. E. Dy and F. C. Szoka, A single dose of doxorubicin-functionalized bow-tie dendrimer cures mice bearing C-26 colon carcinomas, *Proc. Natl. Acad. Sci. U. S. A.*, 2006, **103**, 16649–16654.

151 S. Liu, Y. Guo, R. Huang, J. Li, S. Huang, Y. Kuang, L. Han and C. Jiang, Gene and doxorubicin co-delivery system for targeting therapy of glioma, *Biomaterials*, 2012, **33**, 4907–4916.

152 M. van Elk, B. P. Murphy, T. Eufrásio-da-Silva, D. P. O'Reilly, T. Vermonden, W. E. Hennink, G. P. Duffy and E. Ruiz-Hernández, Nanomedicines for advanced cancer treatments: Transitioning towards responsive systems, *Int. J. Pharm.*, 2016, **515**, 132–164.

153 S. Zununi Vahed, R. Salehi, S. Davaran and S. Sharifi, Liposome-based drug co-delivery systems in cancer cells, *Mater. Sci. Eng. C*, 2016, **71**, 1327–1341.

154 B. S. Pattni, V. V Chupin and V. P. Torchilin, New Developments in Liposomal Drug Delivery, *Chem. Rev.*, 2015, **115**, 10938–10966.

155 S. Behzadi, V. Serpooshan, W. Tao, M. A. Hamaly, M. Y. Alkawareek, E. C. Dreaden, D. Brown, A. M. Alkilany, O. C. Farokhzad and M. Mahmoudi, Cellular uptake of nanoparticles: journey inside the cell, *Chem. Soc. Rev.*, 2017, **46**, 4218–4244.

156 L. Jiang, L. Li, X. He, Q. Yi, B. He, J. Cao, W. Pan and Z. Gu, Overcoming drug-resistant lung cancer by paclitaxel loaded dual-functional liposomes with mitochondria targeting and pH-response, *Biomaterials*, 2015, **52**, 126–139.

157 W. Alshaer, H. Hillaireau, J. Vergnaud, S. Ismail and E. Fattal, Functionalizing Liposomes with anti-CD44 Aptamer for Selective Targeting of Cancer Cells, *Bioconjug. Chem.*, 2015, **26**, 1307–1313.

158 Y. Liu, L.-L. Li, G.-B. Qi, X.-G. Chen and H. Wang, Dynamic disordering of liposomal cocktails and the spatio-temporal favorable release of cargoes to circumvent drug resistance, *Biomaterials*, 2014, **35**, 3406–3415.

159 A. Petushkov, N. Ndiege, A. K. Salem and S. C. Larsen, in *Advances in Molecular Toxicology*, ed. J. C. Fishbein, Elsevier, 2010, vol. 4, pp. 223–266.

160 Y. Wang, Q. Zhao, N. Han, L. Bai, J. Li, J. Liu, E. Che, L. Hu, Q. Zhang, T. Jiang and S. Wang, Mesoporous silica nanoparticles in drug delivery and biomedical applications, *Nanomedicine Nanotechnology, Biol. Med.*, 2015, **11**, 313–327.

161 K. Möller and T. Bein, Talented Mesoporous Silica Nanoparticles, *Chem. Mater.*, 2017, **29**, 371–388.

162 C. Bharti, U. Nagaich, A. K. Pal and N. Gulati, Mesoporous silica nanoparticles in target drug delivery system: A review., *Int. J. Pharm. Investig.*, 2015, **5**, 124–33.

163 L. B. de O. Freitas, L. de M. Corgosinho, J. A. Q. A. Faria, V. M. dos Santos, J. M. Resende, A. S. Leal, D. A. Gomes and E. M. B. de Sousa, Multifunctional mesoporous silica nanoparticles for cancer-targeted, controlled drug delivery and imaging, *Microporous Mesoporous Mater.*, 2017, **242**, 271–283.

164 L. Maggini, I. Cabrera, A. Ruiz-Carretero, E. A. Prasetyanto, E. Robinet and L. De Cola, Breakable mesoporous silica nanoparticles for targeted drug delivery, *Nanoscale*, 2016, **8**, 7240–7247.

165 R. Kotcherlakota, A. K. Barui, S. Prashar, M. Fajardo, D. Briones, A. Rodriguez-Dieguez, C. R. Patra and S. Gomez-Ruiz, Curcumin loaded mesoporous silica: an effective drug delivery system for cancer treatment, *Biomater. Sci.*, 2016, **4**, 448–459.

166 M. Colilla, B. Gonzalez and M. Vallet-Regi, Mesoporous silica nanoparticles for the design of smart delivery nanodevices, *Biomater. Sci.*, 2013, **1**, 114–134.

167 M. Havrdova, K. Polakova, J. Skopalik, M. Vujtek, A. Mokdad, M. Homolkova, J. Tucek, J. Nebesarova and R. Zboril, Field emission scanning electron microscopy (FE-SEM) as an approach for nanoparticle detection inside cells, *Micron*, 2014, **67**, 149–154.

168 P. Yang, S. Gai and J. Lin, Functionalized mesoporous silica materials for controlled drug delivery, *Chem. Soc. Rev.*, 2012, **41**, 3679.

169 Z. Hedayatnasab, F. Abnisa and W. M. A. W. Daud, Review on magnetic nanoparticles for magnetic nanofluid hyperthermia application, *Mater. Des.*, 2017, **123**, 174–196.

170 A. Y. Zubarev, L. Y. Iskakova and A. F. Abu-Bakr, Magnetic hyperthermia in solid magnetic colloids, *Phys. A Stat. Mech. its Appl.*, 2017, **467**, 59–66.

171 M. Bañobre-López, Y. Piñeiro, M. A. López-Quintela and J. Rivas, in *Handbook of Nanomaterials Properties*, Springer Berlin Heidelberg, Berlin, Heidelberg, 2014, pp. 457–493.

172 H. Luo, D. Ji, C. Li, Y. Zhu, G. Xiong and Y. Wan, Layered nanohydroxyapatite as a novel nanocarrier for controlled delivery of 5-fluorouracil, *Int. J. Pharm.*, 2016, **513**, 17–25.

173 F. Wang, Y. Yang, Y. Ling, J. Liu, X. Cai, X. Zhou, X. Tang, B. Liang, Y. Chen, H. Chen, D. Chen, C. Li, Z. Wang, B. Hu and Y. Zheng, Injectable and thermally contractible hydroxypropyl methyl cellulose/Fe3O4 for magnetic hyperthermia ablation of tumors, *Biomaterials*, 2017, **128**, 84–93.

174 L. Hajba and A. Guttman, The use of magnetic nanoparticles in cancer theranostics: Toward handheld diagnostic devices, *Biotechnol. Adv.*, 2016, **34**, 354–361.

175 I. Braschi, S. Blasioli, L. Gigli, C. E. Gessa, A. Alberti and A. Martucci, Removal of sulfonamide antibiotics from water: Evidence of adsorption into an organophilic zeolite Y by its structural modifications, *J. Hazard. Mater.*, 2010, **178**, 218–225.

176 L. Wang, L. L. Li, Y. S. Fan and H. Wang, Host-guest supramolecular nanosystems for cancer diagnostics and therapeutics, *Adv. Mater.*, 2013, **25**, 3888–3898.

177 W. Song, R. E. Justice, C. A. Jones, V. H. Grassian and S. C. Larsen, Size-dependent properties of nanocrystalline silicalite synthesized with systematically varied crystal sizes, *Langmuir*, 2004, **20**, 4696–4702.

178 Y. Pan, Y. Liu, G. Zeng, L. Zhao and Z. Lai, Rapid synthesis of zeolitic imidazolate framework-8 (ZIF-8) nanocrystals in an aqueous system., *Chem. Commun.*, 2011, **47**, 2071–2073.

179 H. Faghihian, M. Moayed, A. Firooz and M. Iravani, Evaluation of a new magnetic zeolite composite for removal of Cs+ and Sr2+ from aqueous solutions: Kinetic, equilibrium and thermodynamic studies, *Comptes Rendus Chim.*, 2014, **17**, 108–117.

180 K. Kim, T. Lee, Y. Kwon, Y. Seo, J. Song, J. K. Park, H. Lee, J. Y. Park, H. Ihee, S. J. Cho and R. Ryoo, Lanthanum-catalysed synthesis of microporous 3D graphene-like carbons in a zeolite template, *Nature*, 2016, **535**, 131–135.

181 L. Ferreira, A. M. Fonseca, G. Botelho, C. A. Aguiar and I. C. Neves, Antimicrobial activity of faujasite zeolites doped with silver, *Microporous Mesoporous Mater.*, 2012, **160**, 126–132.

182 H. Awala, J.-P. Gilson, R. Retoux, P. Boullay, J.-M. Goupil, V. Valtchev and S. Mintova, Template-free nanosized faujasite-type zeolites., *Nat. Mater.*, 2015, **14**, 447–51.

183 J. T. Wong, E. P. Ng and F. Adam, Microscopic investigation of nanocrystalline zeolite L synthesized from rice husk ash, *J. Am. Ceram. Soc.*, 2012, **95**, 805–808.

184 N. S. Kehr, B. Ergün, H. Lülf and L. De Cola, Spatially controlled channel entrances functionalization of zeolites l, *Adv. Mater.*, 2014, **26**, 3248–3252.

185 B. Gu, L. Wang, S. Wang, D. Zhao, V. H. Rotberg and R. C. Ewing, The effect of H irradiation on the Cs-ion exchange capacity of zeolite-NaY, *J. Mater. Chem.*, 2000, **10**, 2610–2616.

186 A. Z. Ruiz, D. Brühwiler, T. Ban and G. Calzaferri, Synthesis of Zeolite L. Tuning Size and Morphology, *Monatshefte für Chemie*, 2005, **136**, 77–89.

187 A. Datt, D. Fields and S. C. Larsen, An Experimental and Computational Study of the Loading and Release of Aspirin from Zeolite HY, *J. Phys. Chem. C*, 2012, **116**, 21382–21390.

188 M. GutiéRrez, M. Escudey, J. Escrig, J. C. Denardin, D. Altbir, J. D. Fabris, L. C. D. Cavalcante and M. T. García-GonzáLez, Preparation and characterization of magnetic composites based on a natural zeolite, *Clays Clay Miner.*, 2010, **58**, 589–595.

189 N. Vilaça, R. Amorim, O. Martinho, R. M. Reis, F. Baltazar, A. M. Fonseca and I. C. Neves, Encapsulation of a-cyano-4-hydroxycinnamic acid into a NaY zeolite., *J. Mater. Sci.*, 2011, **46**, 7511–7516.

190 M. Spanakis, N. Bouropoulos, D. Theodoropoulos, L. Sygellou, S. Ewart, A. M. Moschovi, A. Siokou, I. Niopas, K. Kachrimanis, V. Nikolakis, P. A. Cox, I. S. Vizirianakis and D. G. Fatouros, Controlled release of 5-fluorouracil from microporous zeolites, *Nanomedicine Nanotechnology, Biol. Med.*, 2014, **10**, 197–205.

191 C. Algieri, E. Drioli and L. Donato, Development of mixed matrix membranes for controlled release of ibuprofen, *J. Appl. Polym. Sci.*, 2013, **128**, 754–760.

192 B. de Gennaro, L. Catalanotti, P. Cappelletti, A. Langella, M. Mercurio, C. Serri, M. Biondi and L. Mayol, Surface modified natural zeolite as a carrier for sustained diclofenac release: A preliminary feasibility study, *Colloids Surfaces B Biointerfaces*, 2015, **130**, 101–109.

193 A. Piotrowska, E. Leszczuk, F. Bruchertseifer, A. Morgenstern and A. Bilewicz, Functionalized NaA nanozeolites labeled with224,225Ra for targeted alpha therapy, *J. Nanoparticle Res.*, 2013, **15**, 2082–2087.

194 M. Neidrauer, U. K. Ercan, A. Bhattacharyya, J. Samuels, J. Sedlak, R. Trikha, K. A. Barbee, M. S. Weingarten and S. G. Joshi, Antimicrobial efficacy and wound-healing property of a topical ointment containing nitric-oxide-loaded zeolites., *J. Med. Microbiol.*, 2014, **63**, 203–209.

195 F. Mayer, W. Zhang, T. Brichart, O. Tillement, C. S. Bonnet, É. Tóth, J. A. Peters and K. Djanashvili, Nanozeolite-LTL with Gd(III) deposited in the large and Eu(III) in the small cavities as a magnetic resonance optical imaging probe, *Chemistry*, 2014, **20**, 3358–3364.

196 M. Ekkapongpisit, A. Giovia, C. Follo, G. Caputo and C. Isidoro, Biocompatibility, endocytosis, and intracellular trafficking of mesoporous silica and polystyrene nanoparticles in ovarian cancer cells: effects of size and surface charge groups, *Int. J. Nanomedicine*, 2012, **7**, 4147–4158.

197 T.-G. Iversen, T. Skotland and K. Sandvig, Endocytosis and intracellular transport of nanoparticles: Present knowledge and need for future studies, *Nano Today*, 2011, **6**, 176–185.

198 D. Vercauteren, J. Rejman, T. F. Martens, J. Demeester, S. C. De Smedt and K. Braeckmans, On the cellular processing of non-viral nanomedicines for nucleic acid delivery: Mechanisms and methods, *J. Control. Release*, 2012, **161**, 566–581.

199 J. A. Daniel, N. Chau, M. K. Abdel-Hamid, L. Hu, L. von Kleist, A. Whiting, S. Krishnan, P. Maamary, S. R. Joseph, F. Simpson, V. Haucke, A. McCluskey and P. J. Robinson, Phenothiazine-Derived Antipsychotic Drugs Inhibit Dynamin and Clathrin-Mediated Endocytosis, *Traffic*, 2015, **16**, 635–654.

200 D. Vercauteren, R. E. Vandenbroucke, A. T. Jones, J. Rejman, J. Demeester, S. C. De Smedt, N. N. Sanders and K. Braeckmans, The use of inhibitors to study endocytic pathways of gene carriers: optimization and pitfalls., *Mol. Ther.*, 2010, **18**, 561–569.

201 J. Rejman, A. Bragonzi and M. Conese, Role of clathrin- and caveolae-mediated endocytosis in gene transfer mediated by lipo- and polyplexes, *Mol. Ther.*, 2005, **12**, 468–474.

202 H. Gao, Z. Yang, S. Zhang, S. Cao, S. Shen, Z. Pang and X. Jiang, Ligand modified nanoparticles increases cell uptake, alters endocytosis and elevates glioma distribution and internalization, *Sci. Rep.*, 2013, **3**, 2534–2541.

203 W. Rima, L. Sancey, M. T. Aloy, E. Armandy, G. B. Alcantara, T. Epicier, A. Malchère, L. Joly-Pottuz, P. Mowat, F. Lux, O. Tillement, B. Burdin, A. Rivoire, C. Boulé, I. Anselme-Bertrand, J. Pourchez, M. Cottier, S. Roux, C. Rodriguez-Lafrasse and P. Perriat, Internalization pathways into cancer cells of gadolinium-based radiosensitizing nanoparticles, *Biomaterials*, 2013, **34**, 181–195.

204 R. Pan, W. Xu, Y. Ding, S. Lu and P. Chen, Uptake Mechanism and Direct Translocation of a New CPP for siRNA Delivery, *Mol. Pharm.*, 2016, **13**, 1366–1374.

205 G. Preta, J. G. Cronin and I. M. Sheldon, Dynasore - not just a dynamin inhibitor, *Cell Commun. Signal.*, 2015, **13**, 24–30.

206 K. Mishev, W. Dejonghe and E. Russinova, Small molecules for dissecting endomembrane trafficking: A cross-systems view, *Chem. Biol.*, 2013, **20**, 475–486.

207 M. Derieppe, K. Rojek, J.-M. Escoffre, B. D. de Senneville, C. Moonen and C. Bos, Recruitment of endocytosis in sonopermeabilization-mediated drug delivery: a real-time study, *Phys. Biol.*, 2015, **12**, 46010.

208 R. Marega, E. A. Prasetyanto, C. Michiels, L. De Cola and D. Bonifazi, Fast Targeting and Cancer Cell Uptake of Luminescent Antibody-Nanozeolite Bioconjugates, *Small*, 2016, **12**, 5431–5441.

209 M. A. E. M. van der Aa, U. S. Huth, S. Y. Häfele, R. Schubert, R. S. Oosting, E. Mastrobattista, W. E. Hennink, R. Peschka-Süss, G. A. Koning and D. J. A. Crommelin, Cellular Uptake of Cationic Polymer-DNA Complexes Via Caveolae Plays a Pivotal Role in Gene Transfection in COS-7 Cells, *Pharm. Res.*, 2007, **24**, 1590–1598.

210 C. S. O. Paulo, M. M. Lino, A. A. Matos and L. S. Ferreira, Differential internalization of amphotericin B – Conjugated nanoparticles in human cells and the expression of heat shock protein 70, *Biomaterials*, 2013, **34**, 5281–5293.

211 Z. Li, Y. Zhang, D. Zhu, S. Li, X. Yu, Y. Zhao, X. Ouyang, Z. Xie and L. Li, Transporting carriers for intracellular targeting delivery via non-endocytic uptake pathways, *Drug Deliv.*, 2017, **24**, 45–55.

212 A. Cacchioli, F. Ravanetti, R. Alinovi, S. Pinelli, F. Rossi, M. Negri, E. Bedogni, M. Campanini, M. Galetti, M. Goldoni, P. Lagonegro, R. Alfieri, F. Bigi and G. Salviati, Cytocompatibility and Cellular Internalization Mechanisms of SiC/SiO2 Nanowires, *Nano Lett.*, 2014, **14**, 4368–4375.

213 P. Bozavikov, D. Rajshankar, W. Lee and C. A. McCulloch, Particle size influences fibronectin internalization and degradation by fibroblasts, *Exp. Cell Res.*, 2014, **328**, 172–185.

214 S. Zhang, H. Gao and G. Bao, Physical Principles of Nanoparticle Cellular Endocytosis, *ACS Nano*, 2015, **9**, 8655–8671.

215 S. E. A. Gratton, P. A. Ropp, P. D. Pohlhaus, J. C. Luft, V. J. Madden, M. E. Napier and J. M. DeSimone, The effect of particle design on cellular internalization pathways, *Proc. Natl. Acad. Sci. U. S. A.*, 2008, **105**, 11613–11618.

216 S. K. Lai, K. Hida, C. Chen and J. Hanes, Characterization of the Intracellular Dynamics of a Non-Degradative Pathway Accessed by Polymer Nanoparticles, *J. Control. Release*, 2008, **125**, 107–111.

217 L. Chen, S. Xiao, H. Zhu, L. Wang and H. Liang, Shape-dependent internalization kinetics of nanoparticles by membranes, *Soft Matter*, 2016, **12**, 2632–2641.

218 K. Murugan, Y. E. Choonara, P. Kumar, D. Bijukumar, L. C. du Toit and V. Pillay, Parameters and characteristics governing cellular internalization and trans-barrier trafficking of nanostructures., *Int. J. Nanomedicine*, 2015, **10**, 2191–206.

219 L. Kou, J. Sun, Y. Zhai and Z. He, The endocytosis and intracellular fate of nanomedicines: Implication for rational design, *Asian J. Pharm. Sci.*, 2013, **8**, 1–8.

220 M. S. H. Akash, K. Rehman and S. Chen, Polymeric-based particulate systems for delivery of therapeutic proteins, *Pharm. Dev. Technol.*, 2016, **21**, 367–378.

221 S. Mayor and R. E. Pagano, Pathways of clathrin-independent endocytosis, *Nat. Rev. Mol. Cell Biol.*, 2007, **8**, 603–612.

222 A. Gräslund, F. Madani, S. Lindberg, Ü. Langel and S. Futaki, Mechanisms of cellular uptake of cell-penetrating peptides, *J. Biophys.*, 2011, **2011**, 414729.

223 B. Layek, L. Lipp and J. Singh, Cell Penetrating Peptide Conjugated Chitosan for Enhanced Delivery of Nucleic Acid, *Int. J. Mol. Sci.*, 2015, **16**, 28912–28930.

224 A. Falanga, M. Galdiero and S. Galdiero, Membranotropic cell penetrating peptides: The outstanding journey, *Int. J. Mol. Sci.*, 2015, **16**, 25323–25337.

225 I. D. Alves, N. Goasdoué, I. Correia, S. Aubry, C. Galanth, S. Sagan, S. Lavielle and G. Chassaing, Membrane interaction and perturbation mechanisms induced by two cationic cell penetrating peptides with distinct charge distribution, *Biochim. Biophys. Acta - Gen. Subj.*, 2008, **1780**, 948–959.

226 I. Mäger, E. Eiríksdóttir, K. Langel, S. El Andaloussi and Ü. Langel, Assessing the uptake kinetics and internalization mechanisms of cell-penetrating peptides using a quenched fluorescence assay, *Biochim. Biophys. Acta*, 2010, **1798**, 338–343.

227 A. Rydström, S. Deshayes, K. Konate, L. Crombez, K. Padari, H. Boukhaddaoui, G. Aldrian, M. Pooga and G. Divita, Direct Translocation as Major Cellular Uptake for CADY Self-Assembling Peptide-Based Nanoparticles, *PLoS One*, 2011, **6**, e25924.

228 G. Sahay, D. Y. Alakhova and A. V. Kabanov, Endocytosis of nanomedicines, *J. Control. Release*, 2010, **145**, 182–195.

229 P. Pereira, S. S. Pedrosa, J. M. Wymant, E. Sayers, A. Correia, M. Vilanova, A. T. Jones and F. M. Gama, siRNA Inhibition of Endocytic Pathways to Characterize the Cellular Uptake Mechanisms of Folate-Functionalized Glycol Chitosan Nanogels, *Mol. Pharm.*, 2015, **12**, 1970–1979.

230 M. Breunig, S. Bauer and A. Goepferich, Polymers and nanoparticles: Intelligent tools for intracellular targeting?, *Eur. J. Pharm. Biopharm.*, 2008, **68**, 112–128.

231 G. J. Doherty and H. T. McMahon, Mechanisms of Endocytosis, *Annu. Rev. Biochem.*, 2009, **78**, 857–902.

232 H. Hillaireau and P. Couvreur, Nanocarriers' entry into the cell: Relevance to drug delivery, *Cell. Mol. Life Sci.*, 2009, **66**, 2873–2896.

233 S. A. Mousavi, L. Malerød, T. Berg and R. Kjeken, Clathrin-dependent endocytosis., *Biochem. J.*, 2004, **377**, 1–16.

234 D. A. Kuhn, D. Vanhecke, B. Michen, F. Blank, P. Gehr, A. Petri-Fink and B. Rothen-Rutishauser, Different endocytotic uptake mechanisms for nanoparticles in epithelial cells and macrophages, *Beilstein J. Nanotechnol.*, 2014, **5**, 1625–1636.

235 H. T. McMahon and E. Boucrot, Molecular mechanism and physiological functions of clathrin-mediated endocytosis, *Nat Rev Mol Cell Biol*, 2011, **12**, 517–533.

236 C. T. Ng, F. M. A. Tang, J. J. Li, C. Ong, L. L. Y. Yung and B. H. Bay, Clathrin-Mediated Endocytosis of Gold Nanoparticles *In Vitro*, *Anat. Rec.*, 2015, **298**, 418–427.

237 J.-M. Oh, S.-J. Choi, G.-E. Lee, J.-E. Kim and J.-H. Choy, Inorganic metal hydroxide nanoparticles for targeted cellular uptake through clathrin-mediated endocytosis., *Chem. Asian J.*, 2009, **4**, 67–73.

238 M. Forte, G. Iachetta, M. Tussellino, R. Carotenuto, M. Prisco, M. De Falco, V. Laforgia and S. Valiante, Polystyrene nanoparticles internalization in human gastric adenocarcinoma cells, *Toxicol. Vitr.*, 2016, **31**, 126–136.

239 S. Guo, X. Zhang, M. Zheng, X. Zhang, C. Min, Z. Wang, S. H. Cheon, M. H. Oak, S. Y. Nah and K. M. Kim, Selectivity of commonly used inhibitors of clathrin-mediated and caveolae-dependent endocytosis of G protein-coupled receptors, *Biochim. Biophys. Acta - Biomembr.*, 2015, **1848**, 2101–2110.

240 J. M. Gamboa and K. W. Leong, *In vitro* and *in vivo* models for the study of oral delivery of nanoparticles, *Adv. Drug Deliv. Rev.*, 2013, **65**, 800–810.

241 A. L. Kiss and E. Botos, Endocytosis via caveolae: alternative pathway with distinct cellular compartments to avoid lysosomal degradation?, *J. Cell. Mol. Med.*, 2009, **13**, 1228–1237.

242 J. Cao, X. Xie, A. Lu, B. He, Y. Chen, Z. Gu and X. Luo, Cellular internalization of doxorubicin loaded star-shaped micelles with hydrophilic zwitterionic sulfobetaine segments, *Biomaterials*, 2014, **35**, 4517–4524.

243 Z. Wang, C. Tiruppathi, R. D. Minshall and A. B. Malik, Nanoparticle Internalization and Transport by Caveolae, *FASEB J.*, 2010, **24**, 820.1-820.1.

244 T. M. U. de Carvalho, E. S. Barrias and W. de Souza, Macropinocytosis: a pathway to protozoan infection, *Front. Physiol.*, 2015, **6**, 106.

245 H. Kettiger, A. Schipanski, P. Wick and J. Huwyler, Engineered nanomaterial uptake and tissue distribution: From cell to organism, *Int. J. Nanomedicine*, 2013, **8**, 3255–3269.

246 J. P. Lim and P. A. Gleeson, Macropinocytosis: an endocytic pathway for internalising large gulps, *Immunol. Cell Biol.*, 2011, **89**, 836–843.

247 J. S. Wadia, R. V Stan and S. F. Dowdy, Transducible TAT-HA fusogenic peptide enhances escape of TAT-fusion proteins after lipid raft macropinocytosis., *Nat. Med.*, 2004, **10**, 310–315.

248 I. A. Khalil, K. Kogure, S. Futaki and H. Harashima, High density of octaarginine stimulates macropinocytosis leading to efficient intracellular trafficking for gene expression., *J. Biol. Chem.*, 2006, **281**, 3544–3551.

249 D. E. Owens and N. A. Peppas, Opsonization, biodistribution, and pharmacokinetics of polymeric nanoparticles, *Int. J. Pharm.*, 2006, **307**, 93–102.

250 D. M. Richards and R. G. Endres, The Mechanism of Phagocytosis: Two Stages of Engulfment, *Biophys. J.*, 2014, **107**, 1542–1553.

251 M. A. Dobrovolskaia and S. E. McNeil, Immunological properties of engineered nanomaterials, *Nat. Nanotechnol.*, 2007, **2**, 469–478.

252 S. Kumari, S. Mg and S. Mayor, Endocytosis unplugged: multiple ways to enter the cell, *Cell Res.*, 2010, **20**, 256–275.

253 M. T. Howes, M. Kirkham, J. Riches, K. Cortese, P. J. Walser, F. Simpson, M. M. Hill, A. Jones, R. Lundmark, M. R. Lindsay, D. J. Hernandez-Deviez, G. Hadzic, A. McCluskey, R. Bashir, L. Liu, P. Pilch, H. McMahon, P. J. Robinson, J. F. Hancock, S. Mayor and R. G. Parton, Clathrin-independent carriers form a high capacity endocytic sorting system at the leading edge of migrating cells, *J. Cell Biol.*, 2010, **190**, 675–691.

254 S. Mayor, R. G. Parton and J. G. Donaldson, Clathrin-Independent Pathways of Endocytosis, *Cold Spring Harb. Perspect. Biol.*, 2014, **6**, a016758.

255 V. J. Venditto and F. C. Szoka, Cancer nanomedicines: So many papers and so few drugs!, *Adv. Drug Deliv. Rev.*, 2013, **65**, 80–88.

256 J. Kreuter, Drug delivery to the central nervous system by polymeric nanoparticles: What do we know?, *Adv. Drug Deliv. Rev.*, 2014, **71**, 2–14.

257 Y. Nakamura, A. Mochida, P. L. Choyke and H. Kobayashi, Nanodrug Delivery: Is the Enhanced Permeability and Retention Effect Sufficient for Curing Cancer?, *Bioconjug. Chem.*, 2016, **27**, 2225–2238.

258 J. H. Lee and Y. Yeo, Controlled drug release from pharmaceutical nanocarriers, *Chem. Eng. Sci.*, 2015, **125**, 75–84.

259 J. Rejman, V. Oberle, I. S. Zuhorn and D. Hoekstra, Size-dependent internalization of particles via the pathways of clathrin- and caveolae-mediated endocytosis, *Biochem. J*, 2004, **377**, 159–169.

260 W.-L. L. Suen and Y. Chau, Size-dependent internalisation of folate-decorated nanoparticles via the pathways of clathrin and caveolae-mediated endocytosis in ARPE-19 cells, *J. Pharm. Pharmacol.*, 2014, **66**, 564–573.

261 W. S. Saw, M. Ujihara, W. Y. Chong, S. H. Voon, T. Imae, L. V. Kiew, H. B. Lee, K. S. Sim and L. Y. Chung, Size-dependent effect of cystine/citric acid-capped confeito-like gold nanoparticles on cellular uptake and photothermal cancer therapy, *Colloids Surfaces B Biointerfaces*, 2018, **161**, 365–374.

262 B. D. Chithrani, A. A. Ghazani and W. C. W. Chan, Determining the Size and Shape Dependence of Gold Nanoparticle Uptake into Mammalian Cells, *Nano Lett.*, 2006, **6**, 662–668.

263 Y. Qiu, Y. Liu, L. Wang, L. Xu, R. Bai, Y. Ji, X. Wu, Y. Zhao, Y. Li and C. Chen, Surface chemistry and aspect ratio mediated cellular uptake of Au nanorods, *Biomaterials*, 2010, **31**, 7606–7619.

264 X. Xie, J. Liao, X. Shao, Q. Li and Y. Lin, The Effect of shape on Cellular Uptake of Gold Nanoparticles in the forms of Stars, Rods, and Triangles, *Sci. Rep.*, 2017, **7**, 3827.

265 N. Oh and J.-H. Park, Endocytosis and exocytosis of nanoparticles in mammalian cells, *Int. J. Nanomedicine*, 2014, **9**, 51–63.

266 G. Wang, H. Yin, J. C. Yin Ng, L. Cai, J. Li, B. Z. Tang and B. Liu, Polyethyleneimine-grafted hyperbranched conjugated polyelectrolytes: synthesis and imaging of gene delivery, *Polym. Chem.*, 2013, **4**, 5297–5304.

267 J. M. Steinbach, Y.-E. Seo and W. M. Saltzman, Cell penetrating peptide-modified poly(lactic-co-glycolic acid) nanoparticles with enhanced cell internalization., *Acta Biomater.*, 2016, **30**, 49–61.

268 A. M. Bannunah, D. Vllasaliu, J. Lord and S. Stolnik, Mechanisms of nanoparticle internalization and transport across an intestinal epithelial cell model: effect of size and surface charge, *Mol Pharm*, 2014, **11**, 4363–4373.

269 T. H. Chung, S. H. Wu, M. Yao, C. W. Lu, Y. S. Lin, Y. Hung, C. Y. Mou, Y. C. Chen and D. M. Huang, The effect of surface charge on the uptake and biological function of mesoporous silica nanoparticles in 3T3-L1 cells and human mesenchymal stem cells, *Biomaterials*, 2007, **28**, 2959–2966.

270 T. dos Santos, J. Varela, I. Lynch, A. Salvati and K. A. Dawson, Effects of Transport Inhibitors on the Cellular Uptake of Carboxylated Polystyrene Nanoparticles in Different Cell Lines, *PLoS One*, 2011, **6**, e24438.

CHAPTER 2

EXPLORATION OF ZEOLITE STRUCTURES AS NANOCARRIERS FOR ENCAPSULATED DRUGS FOR CANCER TREATMENT

In this chapter all work about the use of microporous structures as nanocarriers for encapsulated drugs will be presented. This chapter represents an important part of this thesis, since it allowed the selection of the host porous structures and the drugs for further studies. The drug delivery systems (DDS) based on zeolites were defined and fully characterized.

The first part, subchapter 2.1, includes the results of the study on the use of salicylic acid loaded into zeolite and mesoporous structures for breast cancer treatment. These studies allowed to define the zeolites as the best microporous structures for drug loading for cancer treatment. The selection of these frameworks was essential for obtain the best drug delivery systems.

In the second part, subchapter 2.2 the results of the preparation of DDS with different microporous structures and their effect on colon and breast cancer cells will be presented.

Finally, in the third part, the effect of three DDS *in vitro* using three different cell lines will be demonstrated and the *in vivo* using chick embryo chorioallantoic membrane as model.

SUBCHAPTER 2.1

MICRO- AND MESOPOROUS STRUCTURES AS DRUG DELIVERY CARRIERS FOR SALICYLIC ACID[1]

The potential of salicylic acid (SA) encapsulated in porous materials as drug delivery carriers for cancer treatment was studied. Different porous structures, the microporous zeolite NaY, and the mesoporous SBA-15 and MCM-41 were used as hosts for the anti-inflammatory drug. Characterization with different techniques (FTIR, UV/vis, TGA, ^{1}H NMR, and ^{13}C CPMAS NMR) demonstrated the successful loading of SA into the porous hosts. The mesoporous structures showed to be very efficient to encapsulate the SA molecule. The obtained drug delivery systems (DDS) accommodated 0.74 mmol (341 mg/g_{ZEO}) in NaY and 1.07 mmol (493 mg/g_{ZEO}) to 1.23 mmol (566 mg/g_{ZEO}) for SBA-15 and MCM-41, respectively. Interactions between SA molecules and pore structures were identified. A fast and unrestricted liberation of SA at 10 min of the dissolution assay was achieved with 29.3, 46.6, and 50.1 μg mL^{-1} of SA from NaY, SBA-15, and MCM-41, respectively, in the *in vitro* drug release studies (PBS buffer pH 7.4, 37 °C). Kinetic modeling was used to determine the release patterns of the DDS. The porous structures and DDS were evaluated on Hs 578T and MDA-MB-468 breast cancer cell lines viability. The porous structures are nontoxic to cancer cells. Cell viability reduction was only observed after the release of SA from MCM- 41 followed by SBA-15 in both breast cancer cell lines (see graphical abstract below).

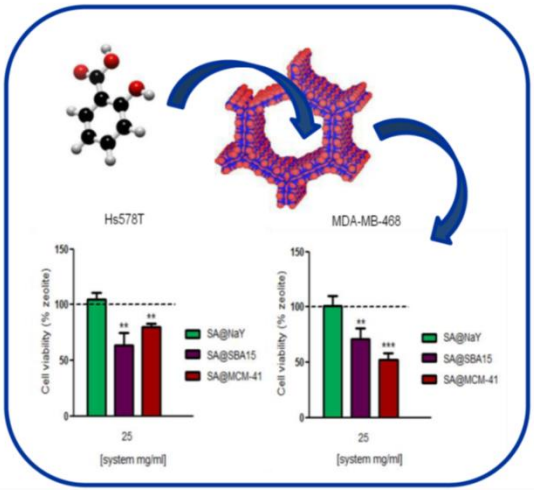

[1] **N. Vilaça**, F. Morais-Santos, A. F. Machado, A. Sirkecioğlu, M. F. R. Pereira, M. Sardo, J. Rocha, P. Parpot, A. M. Fonseca, F. Baltazar and I. C. Neves, Micro- and mesoporous structures as drug delivery carriers for salicylic acid, *J. Phys. Chem. C*, 2015, **119**, 3589–3595.

2.1.1. INTRODUCTION

Salicylic acid (SA) is a β-hydroxy acid, chemically classified as monohydroxy benzoic acid, commonly used to treat comedonal or noninflamed acne. SA is also the major metabolite and active component of aspirin (acetylsalicylic acid).[1] Aspirin is recognized by its analgesic, anti-inflammatory, and antipyretic effects.[2] Several studies have proposed the use of anti-inflammatory drugs as prevention and also as potential treatment of several types of cancer, including breast cancer.[3–5] Recently, it has been suggested that the use of aspirin could reduce the development of different types of cancer such as pancreatic, breast, head, and neck cancer[2,6–9] and can diminish the risk of developing colorectal cancer.[1]

In spite of the emerging research toward the use of anti-inflammatory drugs in cancer therapy, few studies address their application in drug delivery systems.[10,11] Arribo *et al.*[10] developed a new nanohydrogel system able to carry and deliver anti-inflammatory and anticancer drugs simultaneously, prednisolone and paclitaxel, respectively, and show their efficacy in different cancer cell lines. These systems are promising for applications in cancer treatment as combination therapy.

Release of a drug in a preselected target cell requires a delivery carrier in which the drug is not distributed throughout the body in a nonspecific way, targeting the pharmacological site at concentrations with low cytotoxicity.[12] The administration of most anti-inflammatory drugs in therapeutic doses can lead to development of gastrointestinal inflammation or ulcers.[12] To circumvent these problems and have benefits for cancer therapy, encapsulation of anti-inflammatory drugs into various drug carriers should help to achieve the desired goals.

The structural properties and stability in biological environments of the porous structure make them very interesting as hosts for drug delivery.[13–15] In our group we have already lead a detailed investigation on drug delivery systems (DDS) based on different zeolite structures with α-cyano-4-hydroxycinnamic acid or 5-fluorouracil and demonstrated their *in vitro* efficacy against colorectal carcinoma cells.[16–18] In the present study, SA was loaded by diffusion in liquid phase in the void space of three different porous structures: one micro (NaY) and two mesoporous (MCM-41 and SBA-15) structures. Zeolite Y has a Faujasite (FAU)-type structure and is a crystalline microporous aluminosilicate based on sodalite cages joined by O bridges between the hexagonal faces which are arranged in a three-dimensional network. Supercages are 12-membered rings which are formed by the connection of sodalite cages in the framework with a diameter of 1.3 nm and an open diameter of 0.73 nm.[19] In contrast with zeolite Y, MCM-41 and SBA-15 are amorphous inorganic mesoporous silicas. Mesoporous silica materials possess high surface areas, tunable pore diameters, high pore volumes, and well-organized porosity, making them potential candidates for many applications.[20,21] These materials differ in the pore diameters, thickness of the walls, and synthesis conditions.[20] The mesoporous silica

material MCM-41 has a unidimensional hexagonally ordered structure with straight channels. Large pore size materials, namely SBA-15, with pore sizes ranging between 0.2 and 30 nm are potential candidates for such biological applications due to their large range of pore dimensions in comparison to other mesoporous silica.[22,23] In addition to their large pore sizes, SBA-15 materials possess higher hydrothermal stability because their pore walls are thicker than those of MCM-41 materials. Because of its attractive properties, SBA-15 has potential as DDS.[24,25]

In the present study, NaY, MCM-41, and SBA-15 were chosen as hosts for loading an anti-inflammatory drug in order to verify their potential viability for DDS in cancer therapy. For this purpose, SA was chosen as a drug model due to its small molecular size and short biological half-life. The DDS were characterized by a range of methods: FTIR, UV/vis, TGA, ^{1}H NMR, and ^{13}C solid-state CPMAS NMR. The effect of porous structures and of the DDS was evaluated on the viability of breast cancer cells (Hs 578T and MDA-MB-468).

2.1.2. EXPERIMENTAL

2.1.2.1. DRUG LOADING

The microporous zeolite NaY (CBV100, Zeolyst International) and the mesoporous SBA-15 and MCM-41 were used as hosts for the anti-inflammatory drug. The procedures used to synthesize the mesoporous structures, SBA-15 and MCM-41, were previously published.[26] The preparation of DDS was based on a previously established method.[17,18] 300 mg of each structure, previously dehydrated at 120 °C overnight in order to remove water from the pores, was added to a solution of 300 mg (2.17 mmol) of SA (Sigma-Aldrich, S5922) in 30 mL of acetone (Sigma-Aldrich, P.A.). The resulting suspensions at room temperature were stirred (300 rpm) for 48 h. Then, they were filtered off, and the DDS were dried in an oven at 60 °C for 12 h and stored in a desiccator. The pH of the suspensions was monitored during the DDS preparation. Throughout the work, the obtained DDS will be referred to as SA@porous, where porous represents the structure of the parent material used in DDS.

2.1.2.2. DRUG RELEASE STUDIES OF DDS

Drug release from DDS was studied by UV/vis analysis at λ = 295 nm. The simulated body fluid was made using known amounts of sodium monobasic phosphate and sodium dibasic phosphate. Known amounts of the DDS were mixed (10 mg) in 50 mL of simulated body fluid at pH 7.4 and 37 °C, without stirring. 2 mL aliquots of DDS/ simulated body fluid were removed at regular intervals, and an equal amount of fresh simulated body fluid was added to keep constant the volume of the mixture (50 mL). The aliquots were filtered through a 0.20 μm filter

(Whatman) and analyzed by UV/vis. The amount of released SA was calculated using the equation previously described.[19] Experiments were conducted in duplicate, and the values were averaged. The release studies were carried out for 6 h.

2.1.2.3. CHARACTERIZATION METHODS

Textural characterization of the materials was based on the analysis of N_2 adsorption isotherms, measured at -196 °C with a Nova 4200e (Quantachrome Instruments) equipment.

Room temperature Fourier transform infrared (FTIR) spectra of the samples in KBr pellets were measured using a Bomem MB104 spectrometer in the range 4000-500 cm^{-1} by averaging 32 scans at a maximum resolution of 8 cm^{-1}.

The magic-angle spinning nuclear magnetic resonance (MAS NMR) spectra were acquired on a Bruker Avance III 400 spectrometer operating at a B_0 field of 9.4 T. All experiments were performed at room temperature, using a 4 mm double resonance MAS probe and a spinning rate of 12 kHz. The ^{1}H and ^{13}C Larmor frequency were 400.1 and 100.6 MHz, respectively. ^{13}C chemical shifts are quoted in ppm from TMS and were referenced using glycine (C=O at 176.03 ppm). ^{13}C cross polarization MAS (CPMAS) spectra were recorded using a contact time of 2.0 ms with ^{1}H radio-frequency (RF) field strength of 90 kHz (50−100% RAMP-CP shape) and 62.5 kHz for ^{13}C. The ^{1}H 90° pulse was set to 3.0 μs corresponding to RF field strength of 83 kHz; a recycle delay of 5 s was employed. TPPM-15 decoupling was employed during the signal acquisition using a 6.75 μs pulse length for the basic TPPM pulse unit along the ^{1}H channel, employing a ^{1}H RF field strength of 70 kHz.

^{1}H NMR spectra were obtained on a Varian Unity Plus spectrometer at an operating frequency of 300 MHz using the solvent peak as internal reference at 25 °C, chemical shifts of protons being given in ppm using δ_H Me_4Si = 0 ppm as reference.

The release studies were carried out by Shimadzu UV/2501PC spectrophotometer using quartz cells at room temperature. The data were collected in the 600−200 nm range.

The loadings of SA in the samples were determined by thermogravimetric analysis in a STA 409 PC/4/H Luxx Netzsch thermal analyzer. The atmosphere used was high purity air (99.99% minimum purity) with a flow rate of 50 mL min^{-1}. The sample holders used were crucibles of aluminum oxide, supplied by Netzsch. The samples were heated between 50 and 700 °C at 10 °C min^{-1} to evaluate the thermal stability.

2.1.2.4. CELL CULTURE CONDITIONS AND CELL VIABILITY ASSAYS

The human breast cancer cell lines Hs 578T and MDA-MB-468 were obtained from ATCC or from collections developed by Dr. Elena Moisseva (Cancer Biomarkers and Prevention Group, Departments of Biochemistry and Cancer Studies, University of Leicester, UK), Dr.

Marc Mareel (Laboratory of Experimental Cancerology, Ghent University Hospital, Belgium), and Dr. Eric Lam (Imperial College School of Medicine, Hammersmith Hospital, London, UK).

Cell lines were routinely cultured in DMEM (Dulbecco's Modified Eagle Medium, Gibco), containing D-glucose (4.5 g $L^{-}1$) (Invitrogen), supplemented with 10% of fetal bovine serum (FBS, Invitrogen) and 1% penicillin−streptomycin (Invitrogen), at 37 °C in a humidified atmosphere with 5% CO_2. For the cellular viability assays, the DDS were prepared as stock suspensions of 1 mg mL^{-1} in culture medium without FBS. The suspensions dilutions were prepared from this stock also in DMEM without FBS, and the suspensions were submitted to ultrasonic dispersion for 2 min prior to use. The viability assay cells were plated in 96-well plates and allowed to adhere overnight in a complete DMEM medium before incubation with a culture medium without FBS containing the different parent materials and the DDS. The effect of DDS on total biomass was measured by the Sulforhodamine B assay (TOX-6, Sigma-Aldrich), after 48 h of treatment, as previously described.[18] All conditions were examined for statistical significance using Graph Pad Prism 5 Software two-tailed Student's t test for mean comparison, the threshold for significance being *P* values ≤ 0.05. All assays were performed in triplicate at least two times.

2.1.3. RESULTS AND DISCUSSION

2.1.3.1. LOADING AND CHARACTERIZATION OF DDS

Three different DDS were prepared with NaY (microporous) and MCM-41 and SBA-15 (mesoporous), and their effects on the viability of two breast cancer cell lines were compared.

The nitrogen adsorption-desorption isotherms results show the different capacity of the parent micro- and mesoporous structures to encapsulate the salicylic acid (SA). The equilibrium isotherms measured at -196 °C of NaY (a), MCM-41 (b), and SBA-15 (c) are illustrated in Figure 2.1.1.

Textural properties obtained by N_2 adsorption data for both mesoporous structures show that the isotherms are of type IV with a hysteresis loop-typical of solids with a mesoporous structure according to the IUPAC classification.[27] The hysteresis loop is evident in SBA-15. The pore condensation typical of mesoporous materials was reflected in the adsorption isotherms, which present a characteristic sharp inflection at relative pressures lower than 0.35 and 0.70 for MCM-41 and SBA-15, respectively. As expect, NaY exhibits a type I isotherm, which is typical of solids with a mesoporous structure.[18,19]

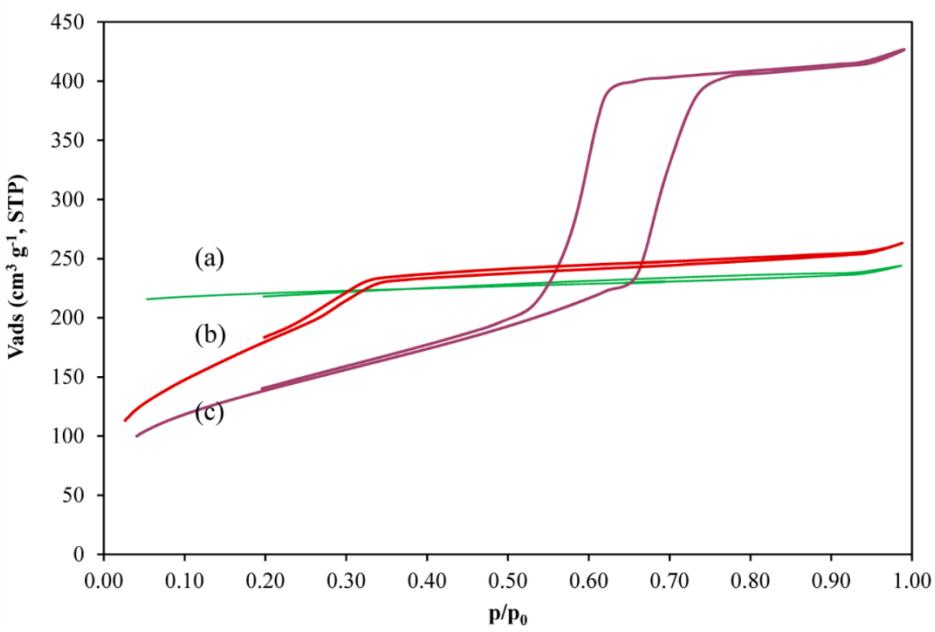

Figure 2.1.1: Nitrogen adsorption-desorption isotherms of NaY (a), MCM-41 (b) and SBA-15 (c).

The micropore volumes (V_{micro}) and mesoporous surface areas (S_{meso}) were calculated by the t-method and the BET surface areas (S_{BET}) by the BET equation. The difference calculated between the total pore volume for $P/P_0 = 0.987$ (V_P) and the micropore volume provide the mesopore volume (V_{meso}). These values are summarized in Table 2.1.1.

Table 2.1.1: Nitrogen adsorption-desorption isotherms of NaY (a), MCM-41 (b) and SBA-15 (c).

Structure	S_{BET} ± 10 (m^2/g)	V_{micro}[a] ± 0.005 (cm^3/g)	S_{ext}[b] ± 5 (m^2/g)	V_p[c] ± 0.005 (cm^3/g)	V_{meso} ± 0.005 (cm^3/g)
NaY	792	0.340	19	0.378	0.038
MCM-41	669	0	669	0.410	0.410
SBA-15	494	0.041	399	0.660	0.619

[a]Micropore volume obtained by the *t*-method. [b]Area different of micropores (area of mesopores + macropores) obtained by the *t*-method. [c]Total pore volume for $P/P_0 = 0.987$.

Pore size distributions were obtained using the non-local density functional theory (NLDFT) kernel available in the Quantachrome package software developed for N2 adsorption at -196 °C assuming silica materials with cylindrical pores. The results obtained are presented in Figure 2.1.2, where the different pore size distributions of the materials tested are evident:

micropores with radius below 10 Å, mesopores with radius between 10 and 20 Å and between 26 and 36 Å for NaY, MCM-41, and SBA-15, respectively.

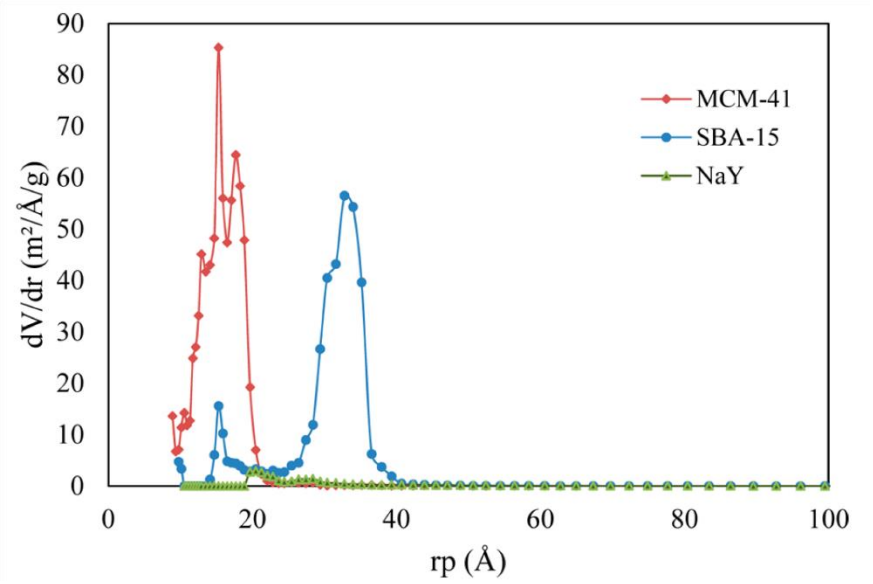

Figure 2.1.2: Pore size distribution obtained by DFT analysis.

The SA was encapsulated into the host structures by adsorption in liquid phase. From our experience, the preparation method of the DDS used in this work does not affect the molecular integrity of the drug as well as the host structures.[16–18]

The presence of SA in the solutions after loading in host structures was confirmed by 1H NMR spectroscopy. Data were obtained with the supernatant solution and compared with pure SA. The ^{1}H NMR spectra of SA and the residue obtained from supernatant solution were recorded at 300 MHz in $CDCl_3$. The carboxylic proton is shifted more downfield than the hydroxyl protons, 13.40 and 11.50 ppm, respectively. In the structure of the acid, the peaks of the aromatic protons present chemical shifts, H−H coupling constants, and splitting patterns as expected: C_3−H (6.95, d, ^{3}J = 7.7), C_4−H (7.50, t, ^{3}J = 7.5), C_5−H (6.91, t, ^{3}J = 7.4), C_6−H (7.82, d, ^{3}J = 7.7). These proton chemical shifts are the same observed for the SA pure molecule.[28] ^{1}H NMR analysis confirms the integrity of the molecular structure of SA after loading in the host structures.

Thermogravimetric analysis (TGA) was carried out to determine the loading of SA into the porous structures. All DDS present the same weight loss profile in the studied temperature range. TGA data of pure SA show two distinct weight changes around 170 and 280 °C, attributed to the onset of melting followed by decomposition of the SA molecule.[19] In the case of DDS, the weight change is extended over the entire temperature range up to 700 °C. The weight loss up to 150 °C was also observed in all DDS, which can be attributed to the removal

of physisorbed water in the structures: 19 weight losses of 24.7, 9.0, and 10.7% are ascribed to SA@NaY, SA@MCM-41, and SA@SBA-15, respectively. The TGA curves for the parent micro- and mesoporous structures show the same weight loss profile around 120-140 °C. The other weight changes observed in DDS were similar to the ones of pure SA with weight losses of 50.1, 45.3, and 43.6% to SA@NaY, SA@MCM-41, and SA@SBA-15, respectively. The SA loadings calculated from the TGA data are provided in Table 2.1.2.

Table 2.1.2: Loading of SA in the DDS determined by TGA.

DDS	SA (mmol)[a]	SA (mmol)[b]	Yield (%)[c]
SA@NaY	2.17	0.74	34.1
SA@MCM-41	2.17	1.23	56.7
SA@SBA-15	2.17	1.07	49.3

[a]Initial SA amount in the solution. [b]SA loading in host structure determined by TGA. [c]Encapsulation efficiency of SA in the host structures.

The TGA data indicate that the highest SA loadings are achieved for the mesoporous structures, MCM-41, followed by SBA-15. As expected, the mesoporous structures are more efficient in the encapsulation of SA than the zeolite NaY. The reason for the difference of the loading between the three DDS might be related to the geometry of the porous structures. NaY possesses cavities interconnected by small pores (0.73 nm) which can accommodate lower amounts of SA molecules. In contrast, MCM-41 and SBA-15 have long cylindrical channels with large diameter (∼3 nm for MCM-41 and ∼7 nm for SBA-15 (see Figure 2.1.2)) in which small SA molecules can diffuse and accommodate easily.

IR spectroscopic data display the evidence of the interaction between SA molecules and the porous structures. FTIR spectra of SA, DDS, and parent host structures are shown in parts (A) NaY, (B) MCM-41, and (C) SBA-15 of Figure 2.1.3.

Figure 2.1.3c shows the characteristic vibrational modes of the drug molecule. A peak at 1660 cm^{-1} is observed for pure SA and is attributed to the carboxyl acid ν(C=O) vibrational mode. Additional bands attributed to ν(C−C) stretching appear at 1578, 1444, 1325, 1295, 1155, and 1030 cm^{-1}. Also, a peak observed at 3238 cm^{-1} is assigned to ν(O−H) vibrational mode from the hydroxyl group.[29]

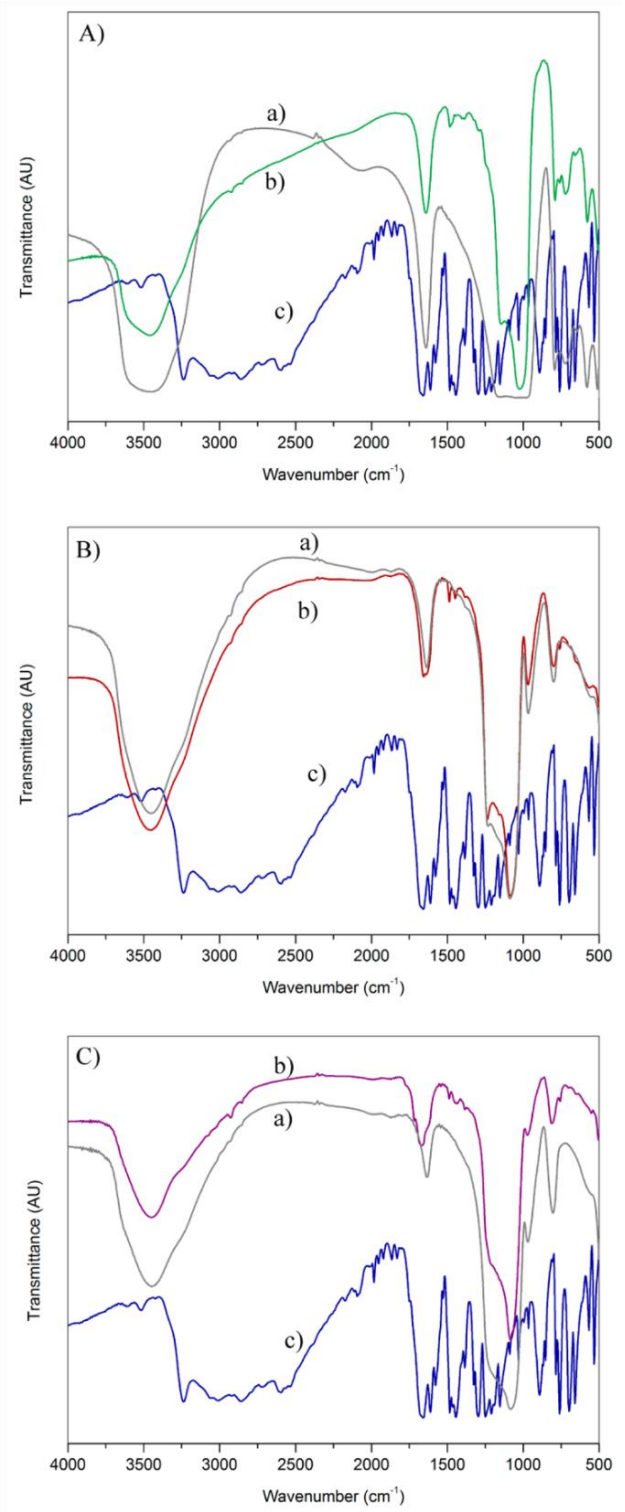

Figure 2.1.3: FTIR spectra of (a) porous structures, (b) SA@porous, and (c) SA molecule in (A) NaY, (B) MCM-41, and (C) SBA-15.

FTIR spectra of SA@porous (Figure 2.1.3b) are dominated by the strong bands assigned to the vibrational modes arising from the porous structures. In all parent structures, the bands at 3500 and 1650 cm^{-1} attributed to the ν(O−H) stretching and the δ(O−H) deformation vibrations,

respectively, were observed and are due to the presence of physisorbed water. In the spectral region between 1250 and 500 cm^{-1}, the bands corresponding to the lattice vibrations are depicted.[17,28,29] In addition to these strong bands caused by the hosts, the FTIR spectra of DDS (Figure 2.1.3b) show bands in the 1600−1200 cm^{-1} region where the porous structures do not absorb and are thus attributed to the presence of the encapsulated drug molecule. In this region, at 1488, 1447, and 1381 cm^{-1}, weaker bands attributed to SA phenyl group vibrations are observed. Furthermore, the principal vibrational bands of the host structures after drug encapsulation do no shift or broaden, further substantiating that the porous frameworks remain unchanged. The spectra of the DDS display the bands attributed to SA, with slight shifts indicating that SA is present and presents host−guest interactions with the porous frameworks.

Figure 2.1.4 presents the ^{13}C CPMAS NMR spectra of SA, SA@ MCM-41, and SA@SAB-15.

The characteristic peaks of the drug molecule with the resonances at δ_{13C} = 175.8 (C7), 161.9 (C2), 138.2 (C4), 132.8 (C6), 120.9 (C5), 118.1 (C3), and 111.7 ppm (C1) are depicted in the ^{13}C NMR spectrum of SA.[28] All observed peaks were assigned to the corresponding ^{13}C moiety in SA, in accordance with previous studies.[28] The peaks ascribed to C4, C6, C5, and C3 appear in the same spectral region in all spectra: SA and SA@porous, indicating the presence and the integrity of the drug inside the pores of the host. In contrast, the resonances due to the carbonyl carbon C7 do not appear in the CPMAS NMR spectra of the encapsulated drug systems (SA@MCM-41 and SA@SBA- 15).

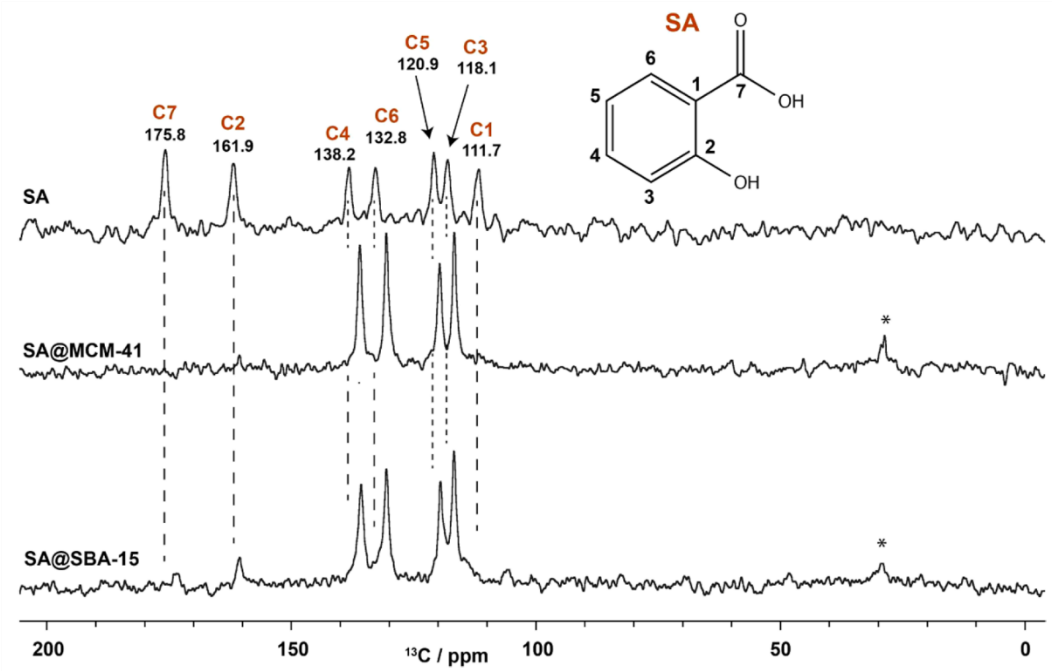

Figure 2.1.4: ^{13}C CPMAS NMR spectra of SA, SA@MCM-41, and SA@SBA-15. The asterisk denotes the presence of CH_3 peaks arising from acetone.

The disappearance of the carbonyl carbon peaks was observed in similar work described by Larsen *et al.*[30] These authors attributed the loss of the signal to the high mobility of the aspirin molecules in the MCM-41 structure, leading to a decreased efficiency of the CPMAS technique due to a decrease in the $^{13}C-^{1}H$ dipolar coupling.[30] The interactions of the SA molecule with the host structures were evidenced by the shift observed in the phenyl ring carbon peaks for all DDS compared to the SA pure molecule. The differences between the spectra of the SA@porous systems and pure SA are attributed to drug interactions with the host structures, consistent with the FTIR analysis (see Figure 2.1.3).

Despite the SA interactions with the parent host structures, the drug can be released out from the structures. The *in vitro* release studies were performed in simulated body fluid at pH 7.4 and 37 °C to mimic the *in vitro* conditions of the breast cancer cell viability assays performed in this study. According to UV/vis analysis the SA molecule was not degraded. Figure 2.1.5 shows the *in vitro* release profiles of SA from the NaY, MCM-41, and SBA-15 systems.

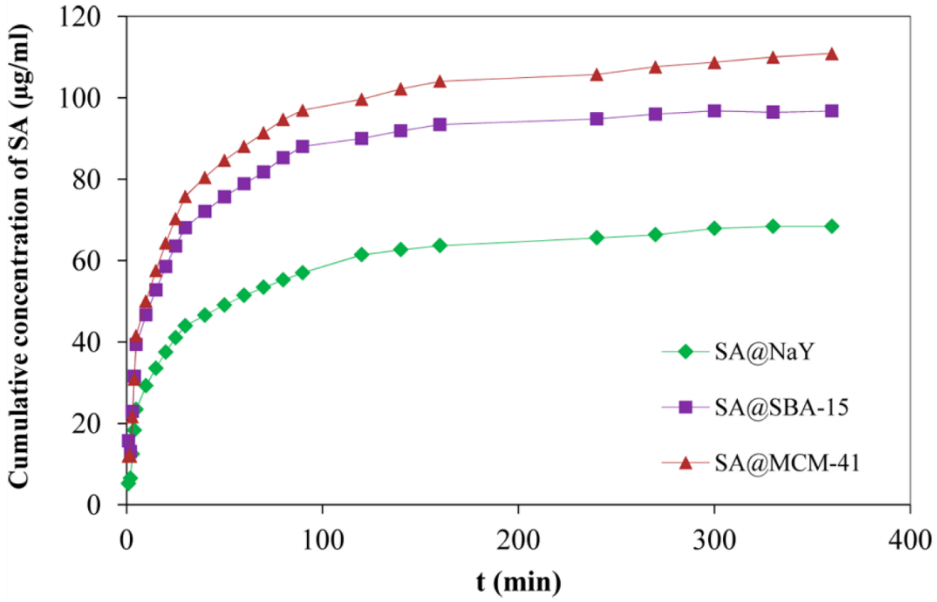

Figure 2.1.5: SA release from NaY, MCM-41, and SBA-15 at PBS pH 7.4 medium.

In the first 15 min, there was an initial burst rate with ca. 50% release of SA observed for all DDS. As expected, the dissolution rate of SA released from the mesoporous carriers was approximately 1.5-1.6-fold faster than the dissolution rate of SA from the microporous carrier. The cumulative concentration of SA at typical sampling times of 15, 60, and 120 min were 34, 51, and 61 µm mL^{-1} for NaY. Accordingly, the cumulative concentrations were 53, 79, and 90 µm mL^{-1} for SBA-15 and 58, 88, and 100 µm mL^{-1} for MCM-41. The cumulative concentrations of SA from all DDS stabilize after 120 min until the end of the dissolution assay (360 min). The

total amount of SA released at the end of the assay was 68.4, 97, and 111 μg mL^{-1} for NaY, SBA-15, and MCM-41, respectively.

The kinetics of the *in vitro* release of drugs from porous carrier materials is frequently described using the zero-order, Higuchi, Korsmeyer-Peppas, and Weibull models.[18,31–33] The validation of the model to describe the release profile was determined by the best correlation coefficient taking into account the conditions of the application of the kinetic models.[31] In our studies, the Korsmeyer-Peppas model fits the SA from the microporous carrier with $R^2 = 0.973$, while the Higuchi model was the best to describe SA release from the mesoporous carriers ($R^2 = 0.944$ and 0.940 for SBA-15 and MCM-41, respectively). These kinetic models describe the drug release mechanism by a process based on Fickian diffusion.[31–33] These results indicate a clear influence of the pore size of the carriers on the diffusion behavior of the drug molecules. Nevertheless, also the nature of the drug is important when choosing the best kinetic model.[18]

2.1.3.2. DRUG BIOACTIVITY STUDIES

The cytotoxicity studies were carried out in two different breast cancer cell lines, Hs 578T and MDA-MB-468. The drug bioactivity studies were performed by preparing three working DDS concentrations by diluting a stock suspension (1.0 mg mL^{-1}) in culture medium. For better homogenization, all suspensions were submitted to ultrasonic dispersion for 2 min prior to use. The best results were achieved with 0.025 mg mL^{-1} of the DDS concentration which has 0.044 mM of SA (4.4×10^{-5} mmol) for SA@NaY, 0.066 mM of SA (6.6×10^{-5} mmol) for SA@MCM-41, and 0.079 mM of SA (7.9×10^{-5} mmol) for SA@SBA-15.

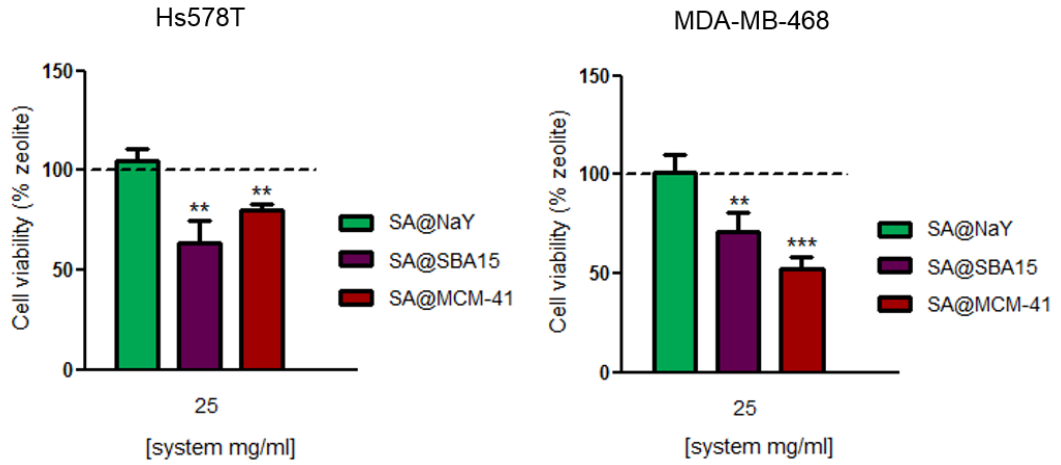

Figure 2.1.6: Cell viability of breast cancer cell lines was measured by Sulforhodamine B assay after cell incubation with 0.025 mg mL^{-1} concentrations of DDS for 48 h. Values are expressed as mean ± S.E.M of at least two independent assays. $^{**}p < 0.01$, $^{***}p < 0.001$ compared to control (0 mg mL^{-1} of DDS, considered as 100% of viability, dashed line).

The ability of SA released from each DDS to affect cell viability is shown in Figure 2.1.6. SBA-15 and MCM-41 as hosts were able to decrease cell viability in both cell lines; however, the MDA-MB-468 cell line was more sensitive than Hs 578T, presenting a reduction of 30% (SA@SBA-15) and 50% (SA@MCM-41) comparing with the respective control (parent porous materials, dashed line). In the Hs 578T cell line the decrease in cell viability was approximately 35% and 20% for SA@SBA-15 and SA@MCM-41, respectively. The DDS based on NaY zeolite did not show any effect on cell viability, remaining similar to the control. The large effect demonstrated by the DDS based on SBA-15 and MCM-41 is due to the enhanced ability in loading SA and a better encapsulation efficiency (Table 2.1.2). Also, the amount of released SA was much higher in these DDS (Figure 2.1.5), which makes them better DDS than NaY, presenting better results in the decrease of cell viability.

Chronic inflammation has been associated with neoplasia, and anti-inflammatory drugs have potential as anticancer agents.[34] The reduction of breast cancer cell viability by SA encapsulated in porous materials highlights their potential to support the activity of anti-inflammatory drugs in cancer therapy.

2.1.4. CONCLUSIONS

The SA molecule was successfully encapsulated into different porous materials and retains its molecular integrity. The parent structures after the encapsulation of the drug molecule do not show any structural modifications or loss of crystallinity. The mesoporous materials SBA-15 and MCM-41 proved to be more efficient in loading SA than microporous zeolite NaY. The release rate of SA increases with increasing pore size for materials with pore diameters in the range 2.5-3.6 nm and follows a Higuchi model to describe the release of SA. The cytotoxicity studies show that the selected porous materials are nontoxic with regard to two different breast cancer cell lines: Hs 578T and MDA-MB-468. Only the DDS prepared with the mesoporous structures revealed a cell viability reduction in both breast cancer cell lines. These results indicate the potential of using SA encapsulated in porous structures for drug loading and delivery to cancer cells. However, further studies are necessary for a better understanding of the drug delivery process.

2.1.5. REFERENCES

1 K. Zitta, P. Meybohm, B. Bein, Y. Huang, C. Heinrich, J. Scholz, M. Steinfath and M. Albrecht, Salicylic acid induces apoptosis in colon carcinoma cells grown in-vitro: Influence of oxygen and salicylic acid concentration, *Exp. Cell Res.*, 2012, **318**, 828–834.

2 X.-L. Tan, K. M. Reid Lombardo, W. R. Bamlet, A. L. Oberg, D. P. Robinson, K. E. Anderson and G. M. Petersen, Aspirin, nonsteroidal anti-inflammatory drugs (NSAID), acetaminophen, and pancreatic cancer risk: A clinic-based case-control study, *Cancer Prev. Res. (Phila).*, 2011, **4**, 1835–1841.

3 J. Cuzick, F. Otto, J. A. Baron, P. H. Brown, J. Burn, P. Greenwald, J. Jankowski, C. La Vecchia, F. Meyskens, H. J. Senn and M. Thun, Aspirin and non-steroidal anti-inflammatory drugs for cancer prevention: an international consensus statement, *Lancet Oncol.*, 2009, **10**, 501–507.

4 P. M. Rothwell, J. F. Price, F. G. R. Fowkes, A. Zanchetti, M. C. Roncaglioni, G. Tognoni, R. Lee, J. F. F. Belch, M. Wilson, Z. Mehta and T. W. Meade, Short-term effects of daily aspirin on cancer incidence, mortality, and non-vascular death: analysis of the time course of risks and benefits in 51 randomised controlled trials, *Lancet*, 2017, **379**, 1602–1612.

5 P. M. Rothwell, M. Wilson, J. F. Price, J. F. F. Belch, T. W. Meade and Z. Mehta, Effect of daily aspirin on risk of cancer metastasis: a study of incident cancers during randomised controlled trials, *Lancet*, 2017, **379**, 1591–1601.

6 A. Bardia, J. E. Olson, C. M. Vachon, D. Lazovich, R. A. Vierkant, A. H. Wang, P. J. Limburg, K. E. Anderson and J. R. Cerhan, Effect of Aspirin and other NSAIDs on Postmenopausal Breast Cancer Incidence by Hormone Receptor Status: Results from a Prospective Cohort Study, *Breast Cancer Res. Treat.*, 2011, **126**, 149–155.

7 E. A. Coleman, Taking aspirin daily for at least 4 years reduces long-term risk of cancer death., *Evid. Based. Nurs.*, 2011, **14**, 71.

8 M. D. Holmes, W. Y. Chen, L. Li, E. Hertzmark, D. Spiegelman and S. E. Hankinson, Aspirin Intake and Survival After Breast Cancer, *J. Clin. Oncol.*, 2010, **28**, 1467–1472.

9 J. C. Wilson, L. A. Anderson, L. J. Murray and C. M. Hughes, Non-steroidal anti-inflammatory drug and aspirin use and the risk of head and neck cancer: a systematic review., *Cancer Causes Control*, 2011, **22**, 803–810.

10 G. D'Arrigo, G. Navarro, C. Di Meo, P. Matricardi and V. Torchilin, Gellan gum nanohydrogel containing anti-inflammatory and anti-cancer drugs: a multi-drug delivery system for a combination therapy in cancer treatment, *Eur. J. Pharm. Biopharm.*, 2014, **87**, 208–216.

11 G. D'Arrigo, C. Di Meo, E. Gaucci, S. Chichiarelli, T. Coviello, D. Capitani, F. Alhaique and P. Matricardi, Self-assembled gellan-based nanohydrogels as a tool for prednisolone delivery, *Soft Matter*, 2012, **8**, 11557–11564.

12 S. Dreve, I. Kacso, A. Popa, O. Raita, F. Dragan, A. Bende, G. Borodi and I. Bratu, Structural investigation of chitosan-based microspheres with some anti-inflammatory drugs, *J. Mol. Struct.*, 2011, **997**, 78–86.

13 M. Danilczuk, K. Długopolska, T. Ruman and D. Pogocki, Molecular sieves in medicine., *Mini Rev. Med. Chem.*, 2008, **8**, 1407–17.

14 D. G. Fatouros, D. Douroumis, V. Nikolakis, S. Ntais, A. M. Moschovi, V. Trivedi, B. Khima, M. Roldo, H. Nazar and P. A. Cox, *In vitro* and in silico investigations of drug delivery via zeolite BEA, *J. Mater. Chem.*, 2011, **21**, 7789–7794.

15 S.-W. Song, K. Hidajat and S. Kawi, Functionalized SBA-15 Materials as Carriers for Controlled Drug Delivery: Influence of Surface Properties on Matrix−Drug Interactions, *Langmuir*, 2005, **21**, 9568–9575.

16 N. Vilaça, R. Amorim, O. Martinho, R. M. Reis, F. Baltazar, A. M. Fonseca and I. C. Neves, Encapsulation of α-cyano-4-hydroxycinnamic acid into a NaY zeolite, *J. Mater. Sci.*, 2011, **46**, 7511–7516.

17 R. Amorim, N. Vilaça, O. Martinho, R. M. Reis, M. Sardo, J. Rocha, A. M. Fonseca, F. Baltazar and I. C. Neves, Zeolite structures loading with an anticancer compound as drug delivery systems, *J. Phys. Chem. C*, 2012, **116**, 25642–25650.

18 N. Vilaça, R. Amorim, A. F. Machado, P. Parpot, M. F. R. Pereira, M. Sardo, J. Rocha, A. M. Fonseca, I. C. Neves and F. Baltazar, Potentiation of 5-fluorouracil encapsulated in zeolites as drug delivery systems for *in vitro* models of colorectal carcinoma, *Colloids Surfaces B Biointerfaces*, 2013, **112**, 237–244.

19 A. Datt, D. Fields and S. C. Larsen, An Experimental and Computational Study of the Loading and Release of Aspirin from Zeolite HY, *J. Phys. Chem. C*, 2012, **116**, 21382–21390.

20 G. J. de A. A. Soler-Illia, C. Sanchez, B. Lebeau and J. Patarin, Chemical Strategies To Design Textured Materials: from Microporous and Mesoporous Oxides to Nanonetworks and Hierarchical Structures, *Chem. Rev.*, 2002, **102**, 4093–4138.

21 A. Sayari and S. Hamoudi, Periodic Mesoporous Silica-Based Organic−Inorganic Nanocomposite Materials, *Chem. Mater.*, 2001, **13**, 3151–3168.

22 A. Galarneau, H. Cambon, F. Di Renzo and F. Fajula, True Microporosity and Surface Area of Mesoporous SBA-15 Silicas as a Function of Synthesis Temperature, *Langmuir*, 2001, **17**, 8328–8335.

23 X. Wang, K. S. K. Lin, J. C. C. Chan and S. Cheng, Direct Synthesis and Catalytic Applications of Ordered Large Pore Aminopropyl-Functionalized SBA-15 Mesoporous Materials, *J. Phys. Chem. B*, 2005, **109**, 1763–1769.

24 A. L. Doadrio, E. M. B. Sousa, J. C. Doadrio, J. Perez Pariente, I. Izquierdo-Barba and M. Vallet-Regi, Mesoporous SBA-15 HPLC evaluation for controlled gentamicin drug delivery., *J. Control. Release*, 2004, **97**, 125–132.

25 T. Ukmar, T. Čendak, M. Mazaj, V. Kaučič and G. Mali, Structural and Dynamical Properties of Indomethacin Molecules Embedded within the Mesopores of SBA-15: A Solid-State NMR View, *J. Phys. Chem. C*, 2012, **116**, 2662–2671.

26 O. Karvan, A. Sirkecioğlu and H. Atakül, Investigation of nano-CuO/mesoporous SiO2 materials as hot gas desulphurization sorbents, *Fuel Process. Technol.*, 2009, **90**, 1452–1458.

27 C. Simons, U. Hanefeld, I. W. C. E. Arends, R. A. Sheldon and T. Maschmeyer, Noncovalent anchoring of asymmetric hydrogenation catalysts on a new mesoporous aluminosilicate: application and solvent effects., *Chemistry*, 2004, **10**, 5829–5835.

28 M. Jadrijevic-Mladar Takac and D. Vikic Topic, FT-IR and NMR spectroscopic studies of salicylic acid derivatives. II. Comparison of 2-hydroxy- and 2,4- and 2,5-dihydroxy derivatives., *Acta Pharm.*, 2004, **54**, 177–191.

29 B. Imelik and C. J. Vedrine, *Catalyst Characterization: Physical Techniques for Solid Materials*, Springer US, New York, 1994.

30 A. Datt, I. El-Maazawi and S. C. Larsen, Aspirin Loading and Release from MCM-41 Functionalized with Aminopropyl Groups via Co-condensation or Postsynthesis Modification Methods, *J. Phys. Chem. C*, 2012, **116**, 18358–18366.

31 P. Costa and J. M. Sousa Lo, Modeling and comparison of dissolution profiles, *Eur. J. Pharm. Sci.*, 2001, **13**, 123–133.

32 J. Andersson, J. Rosenholm, S. Areva and M. Lindén, Influences of Material Characteristics on Ibuprofen Drug Loading and Release Profiles from Ordered Micro- and Mesoporous Silica Matrices, *Chem. Mater.*, 2004, **16**, 4160–4167.

33 F. Rehman, P. L. O. Volpe and C. Airoldi, The applicability of ordered mesoporous SBA-15 and its hydrophobic glutaraldehyde-bridge derivative to improve ibuprofen-loading in releasing system, *Colloids Surfaces B Biointerfaces*, 2014, **119**, 82–89.

34 D. Hanahan and R. A. Weinberg, Hallmarks of cancer: The next generation, *Cell*, 2011, **144**, 646–674.

SUBCHAPTER 2.2

COMPARISON OF DIFFERENT SILICA MICROPOROUS STRUCTURES AS DRUG DELIVERY SYSTEMS FOR *IN VITRO* MODELS OF SOLID TUMORS[2]

Several silica microporous structures have been studied for their potential as drug delivery systems (DDS) over the last years. However, systematic studies comparing host structures with different topologies and particle sizes, and toxicity studies to human cancer cells, are scarce. In the present work, 3D crystalline structures, three different zeolites (large, medium and small pore size) and one titanosilicate (large pore size) were used as hosts for loading 5-fluorouracil (5-FU), an anticancer drug currently used to treat several malignant tumors. Here, we (i) compared the loading capacity and drug release profiles of the different hosts in simulated body fluid conditions, including host structure stability studies; (ii) established the kinetic parameters for the release of 5-FU and (iii) studied the effect of 5-FU encapsulation in the viability of human breast and colon cancer cells, with determination of the potentiation factor. The loading capacity and the release profile of the DDS were revealed to be dependent on the porous framework of the host structures. Decrease in pH to 2.0 (simulation of gastro-intestinal fluid), showed stability of the host structures, with minimal leaching of Al^{3+} and no Ti^{4+} for long periods of time (up to 72 h). All DDS drug release profiles fitted the Weibull model. These silica microporous structures were revealed to be non-toxic to the cancer cells, while all DDS endorsed the important 5-FU potentiation effect on cell viability (see graphical abstract below).

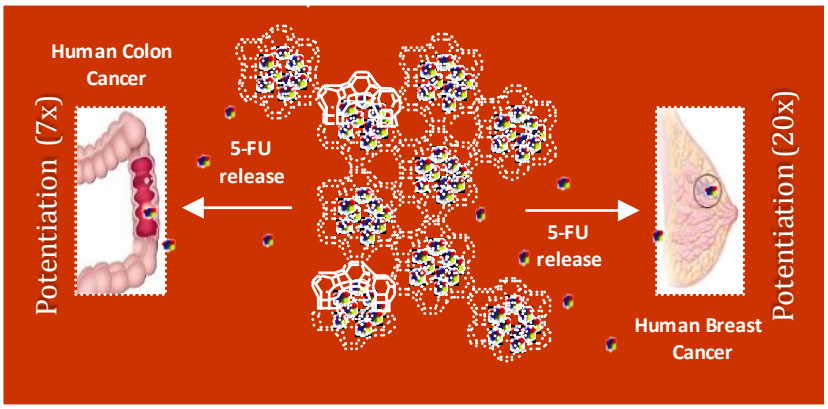

[2] **N. Vilaça**, A. F. Machado, F. Morais-Santos, R. Amorim, A. Patrícia Neto, E. Logodin, M. F. R. Pereira, M. Sardo, J. Rocha, P. Parpot, A. M. Fonseca, F. Baltazar and I. C. Neves, Comparison of different silica microporous structures as drug delivery systems for *in vitro* models of solid tumors, *RSC Adv.*, 2017, **7**, 13104–13111.

2.2.1. INTRODUCTION

The development and selection of drug delivery systems (DDS) is a yield of vital importance in medicine and healthcare. The first commercial DDS was approved by FDA (U.S. Food and Drug Administration) in 1990, containing an antifungal drug, amphotericin B, and after that more than 10 DDS became commercially available.[1]

An ideal DDS is a system that should improve drug bioavailability, prevent its premature degradation, also potentiating its effect. Importantly, the systems must maintain drug concentrations within their therapeutic window, by controlling the drug release rates, and target the pharmacological site at effective concentrations, but with low cytotoxicity.[1,2]

In this context, inorganic nanomaterials have a range of structural and physical properties that are suitable for therapeutic delivery systems. The sizes, topologies, and surfaces of inorganic nanomaterials can be tailored to produce distinct interactions with both *in vitro* and in vivo biological systems.[3] In this class of materials, silica-based structures, such as microporous crystalline titanosilicates and zeolites, mesoporous silica and amorphous or/and crystalline silica particles, are important materials with a wide range of applications.

Thus, zeolites and titanosilicate materials are porous nanomaterials with many potential applications in the biomedical field. There are several examples of zeolite application reported in the literature, including for drug delivery[4–6] and imaging.[7–9] These examples show that different zeolite structures can be exchanged with cations, functionalized or loaded with drug molecules for specific biomedical applications.[10] In the case of the microporous titanosilicate materials, recent studies show that these materials have potential as drug carriers, with low cytotoxicity.[11–13]

The goal of this work is to study the potential of several silica microporous structures as hosts for 5-fluorouracil (5-FU) as drug delivery systems for *in vitro* models of colorectal and breast cancers. 5-FU is a pyrimidine analog antimetabolite, with a general spectrum of activity against solid tumors, such as breast, colorectal, liver and brain cancer, alone or in combination with other chemotherapeutic agents.[14–16] Due to its structure, 5-FU interferes with nucleoside metabolism and can be incorporated into RNA and DNA, leading to cytotoxicity and tumor cell apoptosis, by inhibiting thymidylate synthase.[14] There are several limitations to the use of 5-FU, including its erratic oral bioavailability, with variable gastrointestinal absorption and rapid degradation, its short plasma half-life, development of resistance and important cytotoxicity to normal cells.[15,17,18] Thus, preparation of DDS containing 5-FU could improve its oral bioavailability, preventing its premature degradation and decrease its side effects, increasing concentrations at the target cell site, with lower cytotoxicity for normal cells.

2.2.2. EXPERIMENTAL

2.2.2.1. PREPARATION AND CHARACTERIZATION OF THE SILICA MICROPOROUS STRUCTURES AS HOST FOR THE DDS

Several powder silica microporous structures: three zeolites, FAU (NaY, Si/Al = 2.83, CBV100, Zeolyst International); MFI ((NH_4)ZSM5, Si/Al = 15.0, CBV 3024E, Zeolyst International) and Linde Type A (NaA, Si/Al = 1.24, BCR-705, Sigma-Aldrich), and one titanosilicate, Engelhard Titano Silicate (ETS-10) were used as host for preparing DDS with 5-fluoro-1H-pyrimidine-2,4-dione usually 5-fluorouracil (5-FU, Sigma-Aldrich, 99%). ETS-10 was synthesized according to the procedure previously published.[19] The pentasil structure was subjected to the treatments used before in order to obtain NaZSM5. NaZSM5 was prepared by ion exchange of NH^{4+} from (NH_4)ZSM5 by Na^+ with $NaNO_3$ solution.[20] Briefly, sample was prepared by exchanging 5 g of (NH_4)ZSM5 with 125 mL (25 mL of solution per g zeolite) of 0.50 M $NaNO_3$ solution in an Erlenmeyer flask with a stirrer at room temperature during 24 h. The suspension was separated by filtration, washed with deionized water and dried in an oven at 60 °C for 8 h. The same procedure was performed with a fresh 0.50 M $NaNO_3$ solution. After the two ion exchange treatments, NaZSM5 was dried in an oven at 60 °C for 8 h and calcined at 500 °C during 8 h under a dry air stream.

The morphology and the particle size of the hosts were carried out by scanning electron microscopy (SEM) (JOEL JSM-6010LV/Braga). Textural characterization of the hosts was based on the analysis of N_2 adsorption isotherms, measured at -196 °C with a Nova 4200e (Quantachrome Instruments) equipment.

2.2.2.2. DDS PREPARATION

Before use, all powder silica microporous structures were dehydrated at 120 °C overnight in order to remove the water from the pores. All DDS were prepared by the established encapsulation method.[4,21] So, 5-FU was encapsulated into the host structures by mixing 100 mg of each host with a solution of 5-FU (130 mg, 0.99 mmol) in acetone (15 mL, Aldrich P.A.) as a solvent and was stirred for 48 h at room temperature. The suspensions were filtered off and dried in an oven at 60 °C for 24 h. Finally, the resulting DDS were stored in a desiccator. The pH of the suspensions was monitored during the DDS preparation. Throughout the manuscript, the obtained DDS were identified to as 5-FU@porous where porous represents the silica host structure used in DDS.

The amount of loaded 5-FU was measured using thermogravimetric analysis (TGA) in a STA 409 PC/4/H Luxx Netzsch thermal analyzer. The atmosphere used was high purity air (99.99%

minimum purity) with a low rate of 50 cm^3 min^{-1}. The sample holders used were crucibles of alumina oxide, supplied by Netzsch. The samples were heated between 50 and 700 °C at 10 °C min^{-1} to evaluate the thermal stability.

2.2.2.3. DRUG RELEASE STUDIES OF 5-FU@POROUS AND STABILITY OF THE HOSTS STRUCTURES

The drug release studies were performed according to the procedure describe elsewhere.[4,22] Briefly, the studies were carried out with 10 mg of DDS mixed in 50 mL of specific solutions in order to mimic body fluid conditions (BF) at different pHs and 37 °C: pH 7.4 obtained with a solution of Na_2HPO_4/NaH_2PO_4; pH 5.8 obtained with a solution of KH_2PO_4/NaOH and pH 2.0 with a solution of KCl/HCl. The samples were stirred at ca. 60 rpm and 5 mL aliquots of DDS/BF solution were removed at regular intervals and an equal amount of fresh dissolution medium was added to keep the volume of the mixture constant (50 mL). Aliquots were filtered through a 0.20 µm filter (Whatman). Quantification of the release of 5-FU was carried out by UV/vis spectroscopy using a UV/vis Recording Spectrophotometer UV-2501PC from Shimadzu with software UVProbe 2.10. From the withdrawn aliquots, 0.5 mL were placed in quartz cuvette and added to 2.5 mL of each BF solution and the absorbance of 5-FU was monitored at 260 nm. From the withdraw aliquots, 0.5 mL of this solution was placed in quartz cuvette and added with 2.5 mL of each BF solution and the absorbance of 5-FU was monitored at 260 nm. A calibration curve was constructed using solutions of 5-FU with concentrations from 0.0005 to 0.1000 mg mL^{-1}. The amount of released 5-FU was calculated using the equation previously described.[4,23] Experiments were conducted in triplicate and the values were averaged. The release studies were carried out for 6 h.

The stability of the host structures was evaluated by FTIR and XRD analyses. In these studies, 15 mL of pH 2.0 BF solution was added to 10 mg of NaY or ETS-10 during 72 h under stirring at room temperature. The suspensions were filtered off and dried in an oven at 60 °C for 24 h and stored in a desiccator. The pH of the suspensions was monitored during the assay. Room temperature Fourier Transform Infrared (FTIR) spectra of the parent structures in KBr pellets (2/100 mg) were measured using a ABB FTLA2000 spectrometer in the range 4000–500 cm^{-1} by averaging 32 scans at a maximum resolution of 8 cm^{-1}. Powder X-ray diffraction analysis (XRD) was carried out using a Philips Analytical X-ray model PW1710 BASED diffractometer system equipped with a Cu X-ray tube (selected wavelength λ_{CuKa} = 1.54056 °A). Scans were taken at room temperature in a 2θ range between 5 and 70° with a step of 0.02°.

2.2.2.4. CELL VIABILITY STUDIES

The cell viability studies were performed with two human colon cancer cell lines and one breast cancer cell line. The human breast cancer cell line, MDA-MB-468, was obtained from ATCC (American Type Culture Collection). The human colon cancer derived cell lines HCT-15 and RKO were kindly provided by Dr Raquel Seruca (IPATIMUP, Porto, Portugal). HCT-15 colon cancer cells were maintained in RPMI 1640 medium (Gibco), RKO colon cancer cells and MDA-MB-468 breast cancer cells were maintained in DMEM medium (Gibco). Both cell lines were supplemented with 10% (v/v) fetal bovine serum (FBS) (Gibco, Invitrogen, USA) and 1% (v/v) penicillin–streptomycin solution (P/S) (Invitrogen, USA) and incubated at 37 °C in a 5% CO_2 humidified atmosphere. Cells were subcultured approximately every three days and maintained in a log-phase growth.

Cell viability was assessed using the *in vitro* Toxicology Assay Kit. Sulforhodamine B (SRB) based (Sigma-Aldrich, St. Louis, MO, USA). HCT-15 (7500 cells per 100 mL per well), RKO (6000 cells per 100 mL per well) and MDA-MB-468 (10 000 cells per 100 mL per well) cells were seeded in 96-well plates and incubated at 37 °C in a 5% CO_2 humidified atmosphere for 24 h. In order to assess the effects of the parent structures, 5-FU and DDS used and cells were incubated with increasing concentrations of the systems in culture medium. Controls were performed with culture medium alone. After an incubation period of 48 h, the spent media were removed and the plate wells were washed with 1× phosphate-buffered solution, pH 7.4 (PBS). After a fixation step with cold 10% trichloroacetic acid (TCA), cells were stained with 0.4% SRB and the incorporated dye was solubilized with 10 mM of Tris. Absorbance was monitored with a microplate reader at 570 nm with a background absorbance of 655 nm. Cell viability was determined as percentage of viability: (OD experiment/OD control) × 100 (%). One-way ANOVA, followed by Dunnett post-test were used to perform cell viability assay statistical analysis. The previous tests and 50% growth inhibition (IC_{50}) were determined using the Graphpad Prism 5® software. The level of significance in all the statistical analysis was set at $***p < 0.001$ compared to host alone. All assays were performed in triplicate from three independent experiments. The results were expressed as mean value ± SD of the triplicate assays.

2.2.3. RESULTS AND DISCUSSION

DDS were prepared using silica microporous structure hosts with different topologies and pore sizes, containing aluminum or titanium in the framework.

The chosen 3D zeolites belong to the FAU (large pores), MFI (medium pores) and LTA (small pores) structures.[24] ETS-10 is a 3D large pore structure with titanium in the framework.[11]

The hosts NaY (FAU) and NaA (LTA) were commercially available. However, the parent ETS-10 structure was synthesized and the parent (NH_4)ZSM5 (MFI) was modified in order to obtain HZSM5 and NaZSM5. The modifications in ZSM5 host were performed to study the pore aperture effect in the loading of 5-FU. NaY was already used in a previous publication to encapsulate 5-FU and it is used here for comparison with the remaining structures.[4]

SEM and nitrogen adsorption analyses were performed for evaluating the average particle size and the surface area of the hosts, respectively. Figure 2.2.1 display the SEM micrographs of some silica microporous structures. The average of the particle size obeys the following sequence, larger particles (>100 nm): NaY 700 nm,[4] ZSM5 880 nm, NaA 2700 nm and ETS-10 with 2600 nm and smaller particles (<100 nm): LTL 80 nm.[4]

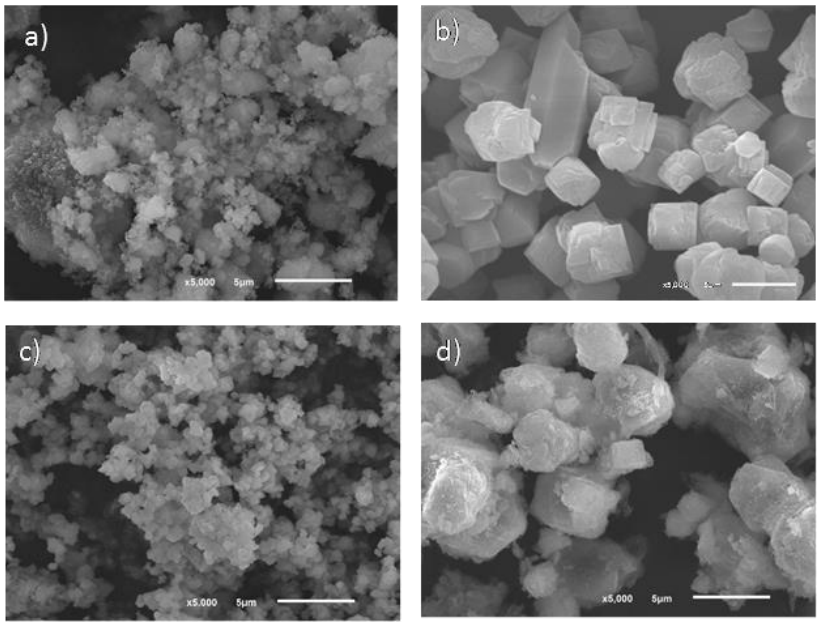

Figure 2.2.1: SEM micrographs of (a) ZSM5, (b) ETS-10, (c) NaY e (d) NaA with same resolution.

The nitrogen adsorption measurements show different surface areas for the zeolite hosts. The BET surface areas (S_{BET}) was determined by the BET equation and the values obtained were: NaY 792 $m^2\ g^{-1}$, LTL 566 $m^2\ g^{-1}$, ZSM5 395 $m^2\ g^{-1}$ and NaA 290 $m^2\ g^{-1}$.

The 5-FU release studies were carried out with all DDS at different pH media simulating blood and gastrointestinal body fluids,[25] and the stability of the host structure at pH = 2.0 was studied with NaY and ETS-10. Besides, cell viability studies were performed on HCT-15 and RKO human colon cancer cells for all hosts and DDS. However, the viability on MDA-MB-468 human breast cancer cell was tested only with the DDS based in NaY, ETS-10 (large pores) and compared with NaA (small pores).

Table 2.2.1 shows the loading of 5-FU in the silica microporous structures obtained by thermogravimetric analysis. TGA profile results are similar for all DDS with two weight losses

observed; the first weight loss was related to the removal of physisorbed water of the host structure and the other one was attributed to the presence of 5-FU in the DDS.[4] The presence of acetone was not detected by TGA analysis since the temperature used in the preparation of the DDS is sufficient to evaporate the solvent.[26] It is evident that loading of 5-FU in the DDS is related to the porous framework of the hosts. The large pore structures, NaY and ETS-10, have higher 5-FU loading capacity than the remaining microporous structures. The medium pore structure HZSM5 presents intermediate 5-FU loading and the introduction of sodium in (NH_4)ZSM5 by ion exchange, enhances a decrease in the loading of 5-FU with 6.8 mmol per g_{host} for NaZSM5, followed by the small pore structure NaA (3D) with 5.8 mmol per g_{host}.

Table 2.2.1: Loading of 5-FU in DDS

Host	DDS	R_{Theo}[a]	R_{Exp}[a]	5-FU (mmol/g_{host})[b]
NaY	5-FU@NaY	1.30	0.98	7.5
HZSM5	5-FU@HZSM5	1.30	0.97	7.4
NaZSM5	5-FU@NaZSM5	1.30	0.89	6.8
NaA	5-FU@NaA	1.30	0.75	5.8
ETS-10	5-FU@ETS-10	1.30	0.99	7.6

[a]R_{Theo} and R_{Exp}. is the ratio of [5-FU]/[host] (wt/wt). [b]5-FU loading in host determined by TGA.

In order to mimic the *in vitro* conditions of the cancer cell viability assays, 5-FU release studies from the silica microporous structures were performed in culture medium at different pH values and 37 °C, by UV/vis analysis. The release was recorded for 360 min, however the concentration remained constant after 60 min.

These studies have been conducted at pH 7.4, 5.8 and 2.0 in order to simulate the blood, intestinal and stomach fluids, respectively.[25] As expected, 5-FU can be easily released from the different microporous hosts due to its small size.[4] As an example, the UV/vis spectra of 5-FU release from 5-FU@NaY (Figure 2.2.2) and the release profiles versus time at pH 7.4 of the prepared DDS are shown in Figure 2.2.3.

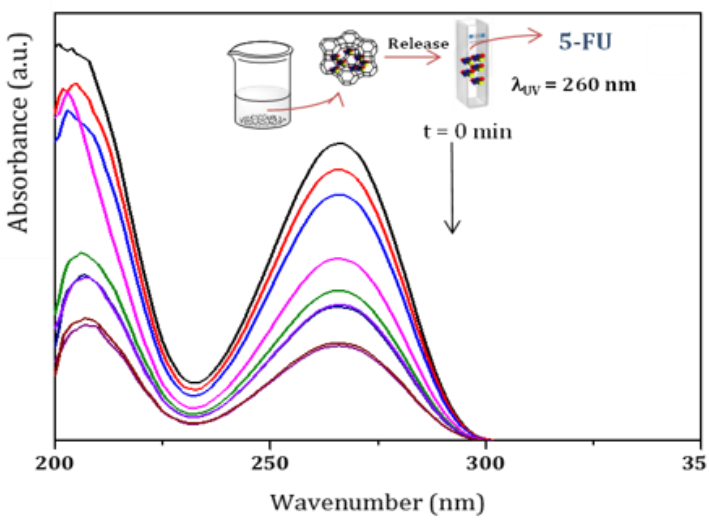

Figure 2.2.2: UV/vis spectra of 5-FU release from 5-FU@NaY up to 60 min.

The results from UV/vis spectra show that, after release from the DDS, 5-FU molecule maintain the characteristic wavelength of the drug (λ = 260 nm).[27] All DDS release profiles show similar behavior, with almost complete release of the adsorbed 5-FU after 40 min, as a consequence of the rapid desorption of the drug.

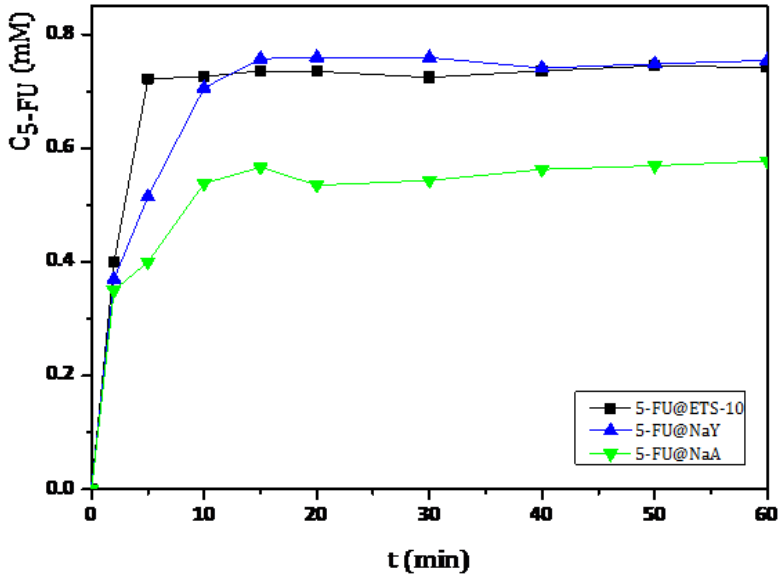

Figure 2.2.3: Release profiles of DDS obtained in BF solution at pH = 7.4 and 37 ºC, followed during 60 min. Release measurements were conducted in triplicate and the concentration values were averaged.

The cumulative concentrations for all DDS stabilize after this time and display approximately the same value until the end of the dissolution assays (360 min). However, some differences were observed between ETS-10 and the zeolites. The release of 5-FU appears to be

dependent on the 5-FU loading capacity of the host. From the large pore 3D structures, ETS-10 and NaY display the highest 5-FU release rates due to the higher amount of adsorbed drug, being ETS-10 release slightly faster (Table 2.2.1). The DDS based on NaA show the slowest rates compared to the large pore structures. The same behavior was observed for HZSM5 and NaZSM5, with the last one presenting the lowest release rates due to the introduction of sodium in the structure (Figure 2.2.4).

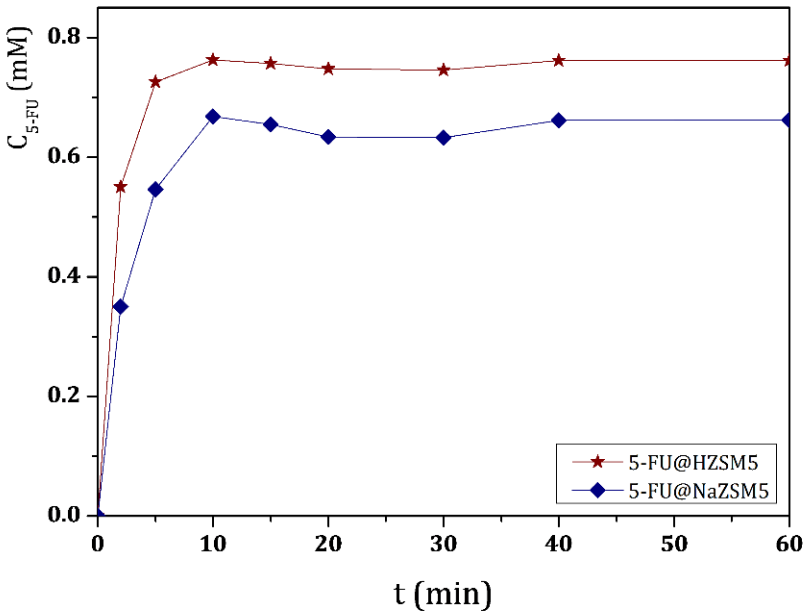

Figure 2.2.4: Release profiles of 5-FU@HZSM5 and 5-FU@NaZSM5 obtained in BF solution at pH = 7.4 and 37 ºC, followed during 60 min. Release measurements were conducted in triplicate and the concentration values were averaged.

These results are in line with those reported in the literature, which show that silica materials are an important class of controlled release matrices.

In the work of Larsen *et al*. the effect of different Si/Al ratio of Y zeolite as hosts for loading and release of 5-fluorouracil were studied and they observed a similar behavior.[28] Also, the DDS based on mesoporous organo-silica nanoparticles with different drugs present the same profile of drug release[29] and the mesoporous silica material SBA-15 was used to achieve immediate release of poorly soluble drug compounds such as itraconazole.[30] However, the studies stated by Martens *et al.* show that the release of the antiseptic chlorhexidine, a large molecule with antibacterial activity, from amorphous microporous silica was fine-tuned by adapting particle size and pore diameter.[31] Recently, our group also showed that the release of salicylic acid from mesoporous and microporous silica hosts is dependent of the pore size of the carriers.[26]

There are several mathematical kinetic models used to describe *in vitro* drug dissolution and drug release from particles.[32–34] Weibull, first-order, Higuchi and Korsmeyer–Peppas are some of the major applied and best describing drug release models.[32–34] The release profiles at pH 7.4 were fitted to these models and the Weibull model shows the best fitting (Figure 2.2.5). In this kinetic model two parameters were determined, the shape ("*b*") and scale ("*a*") parameters. The "*b*" parameter describe the shape of the dissolution curve and the "*a*" parameter represents the time dependence of the system.[32–34] These parameters obtained with this model are listed in Table 2.2.2.

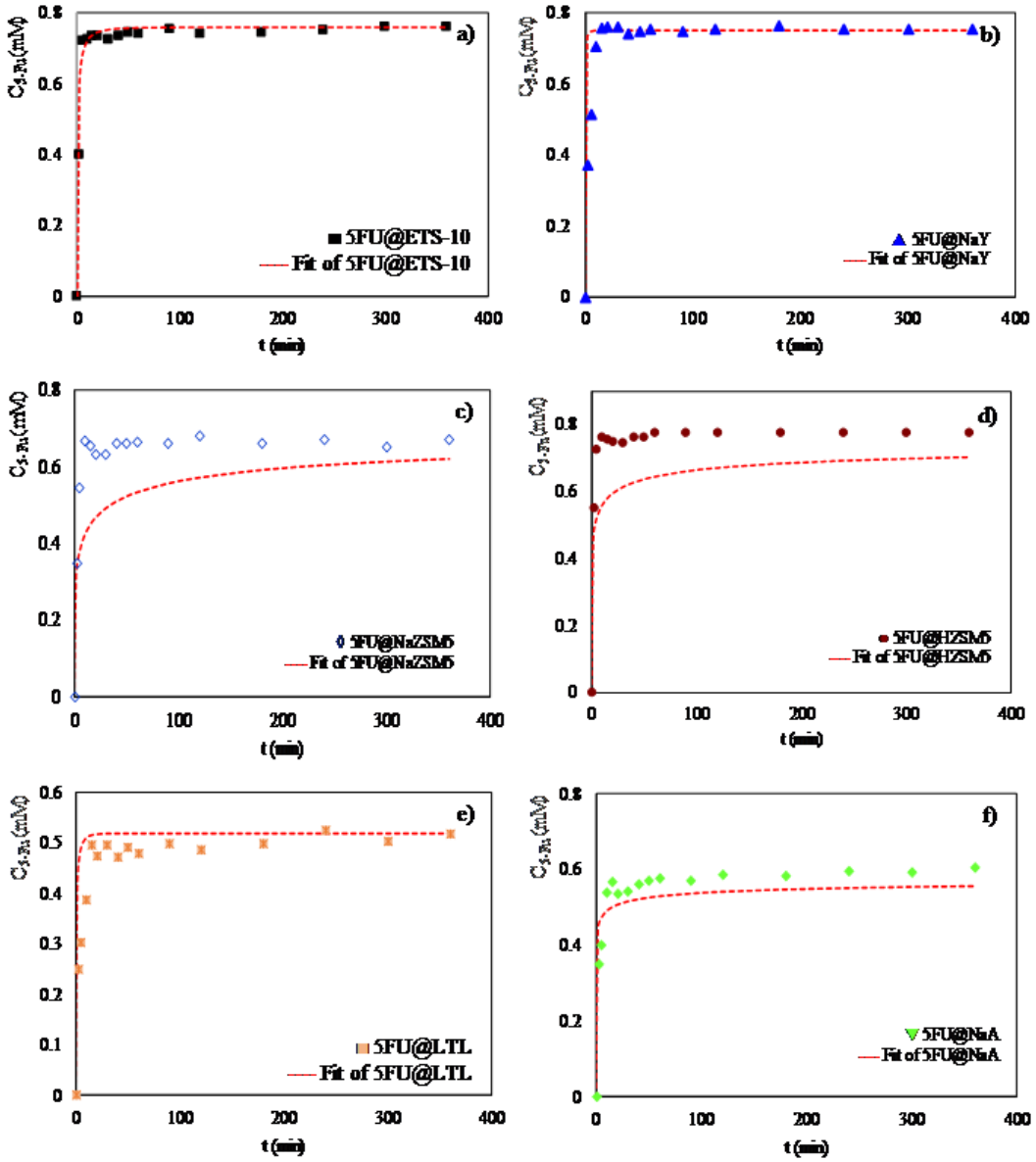

Figure 2.2.5: Release profiles of a) 5-FU@ETS-10, b) 5-FU@NaY, c) 5-FU@NaZSM5, d) 5-FU@HZSM5, e) 5-FU@LTL and d) 5-FU@NaA in buffer solution at pH = 7.4 and 37 ºC. Release measurements were conducted in triplicate and the concentration values were averaged. The solid points and dotted lines show the Weibull model fits to the respective data sets with fit parameters listed in Table 2.2.2.

Table 2.2.2: Fitted kinetic parameters for the release of 5-FU from DDS according to the Weibull model

DDS	*"b"*[a]	*"a"*[a]	R[b]
5-FU@NaY	0.35	0.08	0.9986
5-FU@HZSM5	0.21	0.49	0.9996
5-FU@NaZSM5	0.26	0.65	0.9975
5-FU@NaA	0.15	0.41	0.9699
5-FU@ETS-10	0.40	0.16	0.9842

[a] *"b"* is the shape parameter and *"a"* is the scale parameter of the Weibull model.[32] [b] Correlation coefficient.

The "*b*" parameter calculated for all DDS seems to be dependent on the microporous structures of the hosts. The large pore structures, NaY and ETS-10, have the highest values with 0.35 and 0.40, respectively; followed by the medium pores with similar values and the small pores with 0.15. This parameter describes the shape of the curve as exponential ($b = 1$, case 1), sigmoid, S-shaped, ($b > 1$, case 2), or parabolic, with a higher initial slope and after that consistent with the exponential ($b < 1$, case 3).[32–34] The obtained values are in accordance to case 3 where the release profiles of all DDS present in Figures 2.2.3 and 2.2.4 show this behavior.

The effect of pH on drug release was also evaluated at pH 5.8 and 2.0. The lower pH medium is more likely to affect the stability of the DDS since 5-FU is a weak acid (pK_a of 7.93) and the pH influences the interaction of the molecule with the surface.[27] For these studies, all DDS were submitted to these different pH media, and Figure 2.2.6 shows the results obtained for 5-FU@NaA, as an example.

As expected from 5-FU structure, even at low pH, the 5-FU molecule is not degraded since, we did not observe any shift of the characteristic wavelength of the drug. The results show that the variation of pH does not affect the release of 5-FU in the pH range of 2.0 to 7.4. The effect of pH was also studied for evaluation of the stability of the host microporous structures since the host is important in the protection of the drug in the DDS.

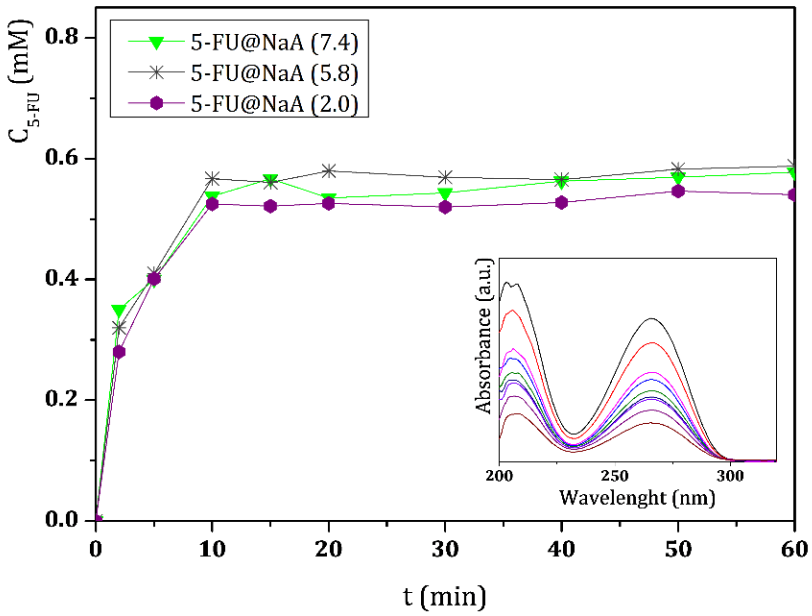

Figure 2.2.6: Release profiles of 5-FU@NaA DDS obtained in different BF solutions at pH = 7.4, 5.8 and 2.0 and 37 ºC, followed during 60 min. Release measurements were conducted in triplicate and the concentration values were averaged. (Inset) UV/vis spectra up to 60 min of the release of 5-FU from the DDS at pH = 2.0.

For this study, the large pore structures NaY and ETS-10 were selected and tested at lower pH. Besides, we also aimed to check if there was any leaching of Al^{3+} from NaY or Ti^{4+} from ETS-10. These hosts were incubated to pH 2.0 BF solution for 72 h under stirring, at room temperature. After the filtration and drying steps, the resulting solids were analyzed by FTIR and XRD. Figure 2.2.7 displays the FTIR spectra obtained before and after NaY and ETS-10 treatment, respectively.

FTIR spectra obtained after treatment for both host structures show the fingerprint bands of the parent structures.[35,36] Also, the principal vibrational bands of the host structures after treatment do not shift or broaden, which confirms that the pore frameworks remain unchanged. So, in all FTIR spectra, a very intense broad band at ca. 3500 cm^{-1} attributed to the hydroxyl groups, the ν(O–H) deformation band at 1650 cm^{-1} characteristic of the absorbed water and in the spectral region between 1250 and 500 cm^{-1}, the bands corresponding to the lattice vibrations of the structures are observed.[35,36] In the case of NaY zeolite, FTIR analysis allows to determine the framework Si/Al ratio using the characteristic band of the zeolite specific double ring vibration mode between 570-600 cm^{-1}.[37] From both spectra in Figure 2.2.7a, bands at 577.1 cm^{-1} and 577.7 cm^{-1} for NaY and NaY (pH = 2.0) were identified, respectively. From these values, the calculated framework Si/Al ratio was 2.66 for NaY and 2.71 for NaY (pH = 2.0). The increase in Si/Al ratio observed is related to partial desalumination due to the contact of the zeolite structure with the lower pH solution.

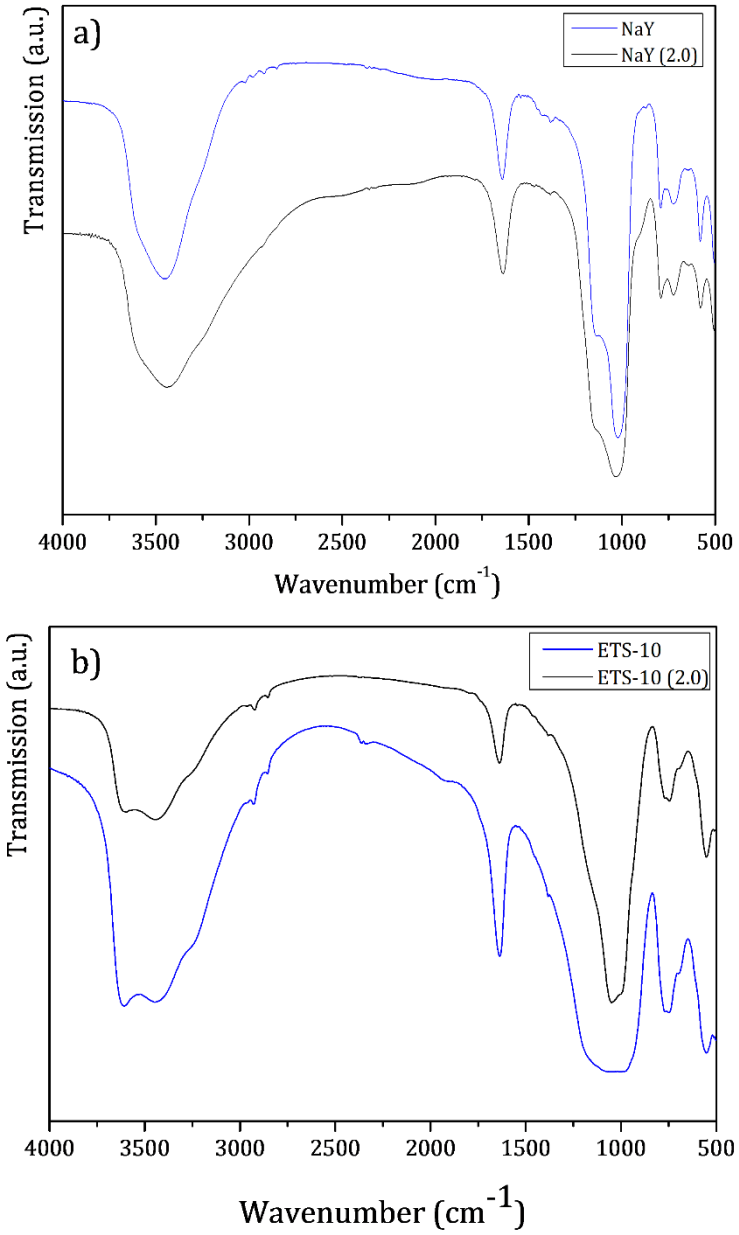

Figure 2.2.7: FTIR spectra before and after treatment with pH = 2.0 BF solution of (a) NaY and (b) ETS-10, for 72h.

XRD analysis confirms these results. The powder X-ray diffraction patterns endorses that the crystalline structure of NaY or ETS-10 does not change after the treatment. In both XRD patterns after treatment, the characteristic Miller peaks corresponding to NaY or ETS-10 were observed indicating that the host structures are not severely affected by low pH (pH 2.0). Figure 2.2.8 displays the XRD patterns of ETS-10 and ETS-10 at pH = 2.0. From Figure 2.2.8, the XRD patterns of both samples ETS-10 and ETS-10 (2.0) are similar and in good accordance with those reported in the literature.[38,39]

The relative crystallinity was estimated by the intensity of the characteristic diffraction peaks of the host structures after treatment, compared to the pattern of the parent structures, which was set to be 100% crystalline. The crystallinity obtained was 100% for ETS-10 (pH = 2.0) and 85% for NaY (pH = 2.0). These results confirm that ETS-10 is not affected by pH 2.0 and NaY is slight affected by the treatment, which is in agreement with the FTIR results.

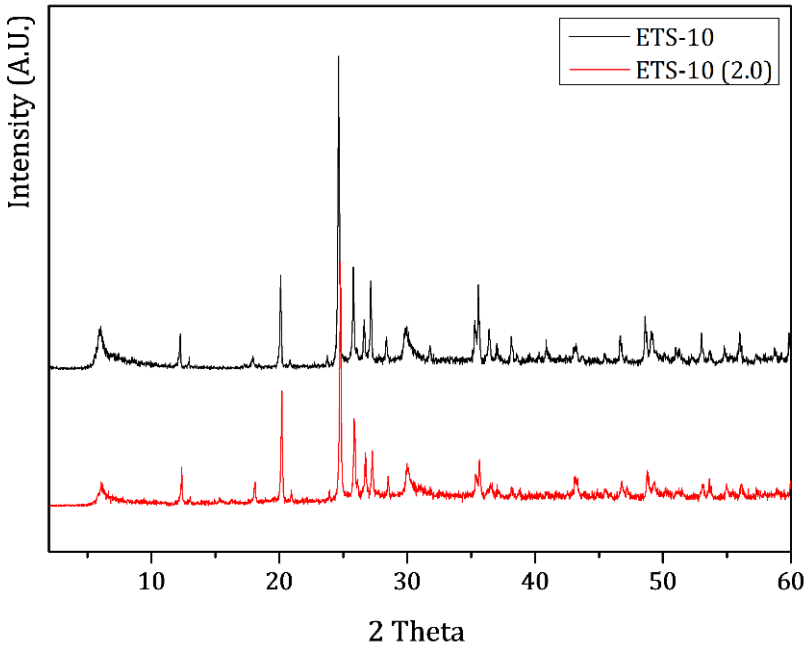

Figure 2.2.8: XRD patterns before and after treatment with pH = 2.0 BF solutions of ETS-10 for 72 h.

2.2.3.1. CELL VIABILITY STUDIES

Cell viability assays were performed with all parent silica microporous to compare their feasibility as host for DDS using different human cell lines, RKO and HCT-15 as colon cancer models and MDA-MB-468 as breast cancer model. These cell lines represent important human carcinomas and they were chosen as extrapolative models to test the potentiation of the chemotherapeutic agent 5-FU when encapsulated in the silica microporous structures. The large pore structures, NaY and ETS-10, and the corresponding DDS were used and compared with the small pore structure NaA in the viability study with the human cell line MDA-MB-468, as breast cancer model.

The viability assays with microporous structures were optimized in our previous work.[26] So, from a stock suspension (1.0 mg DDS per mL), sequential dilutions were made with free serum culture medium in order to get several working DDS concentrations (0.005 to 0.100 mg mL^{-1}). The alterations in cell biomass were evaluated by the sulforhodamine B (SRB) method and were assessed after 48 h of incubation with DDS and the parent hosts.

The parent hosts did not induce reduction in cell viability in any of the cell lines studied. As an example, the ability of 5-FU released from 5-FU@ETS-10 and 5-FU@NaA to affect RKO cell viability is shown in Figure 2.2.9. The other DDS cell viability are shown in Figure 2.2.10.

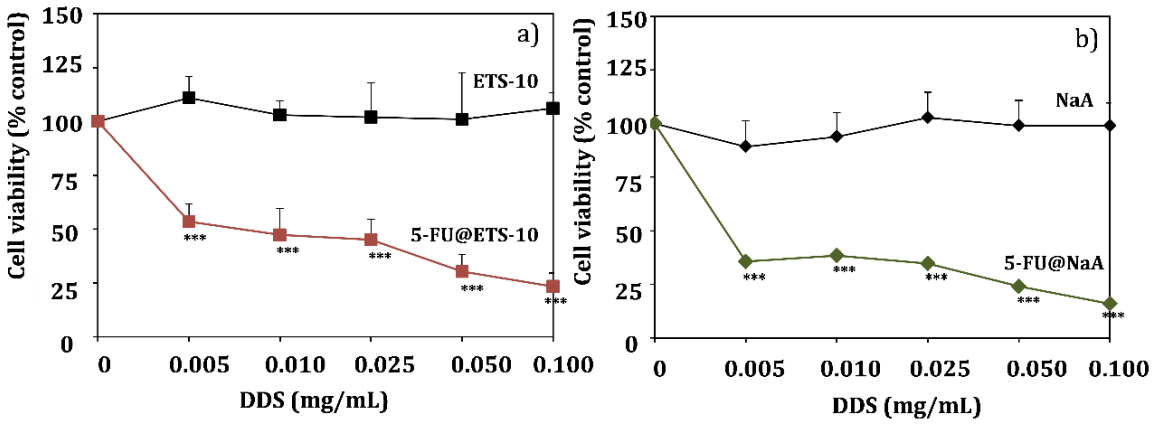

Figure 2.2.9: Effect of ETS-10 (a) and NaA (b) hosts and DDS systems on RKO colon carcinoma cell viability. RKO cells were incubated with hosts and different DDS concentrations for 48 h. Cell viability was measured by the SRB assay. Values are means ± SD of three independent experiments, each performed in triplicate. *$p < 0.05$, ***$p < 0.001$ compared to host alone.

The hosts titanosilicate (ETS-10) and NaA do not show cytotoxicity to the colorectal cancer cell lines studied. The results are in accordance with what we have found for in the DDS prepared with different zeolite structures as hosts with the anticancer drugs α-cyano-4-hydroxycinnamic acid (CHC) and 5-fluorouracil (5-FU), and we also studied their *in vitro* efficacy against colorectal carcinoma cells.[4,26,40] These results are also in line with several toxicity studies which suggest that the internal surface of zeolites does not interact with the biological systems.[41] However, the acidic surface characteristics could be also associated with some toxicity for specific cells. In fact, we showed that NaY zeolite induces toxicity in glioblastoma cells in all range of concentrations studied, but NaMOR zeolite did not show any toxicity to these cells. These results confirm that the zeolite toxicity is dependent on the cell type and the properties of the carrier structure. Also, in the same study, our results show that the DDS prepared with NaMOR are capable of reducing tumor size, using the in vivo chick chorioallantoic membrane (CAM) model.[21]

From Figure 2.2.9, we can also see that there is an evident reduction in cell viability with 5-FU containing DDS, compared to ETS-10 or NaA (controls), with increasing concentrations of 5-FU in both DDS, for RKO cells.

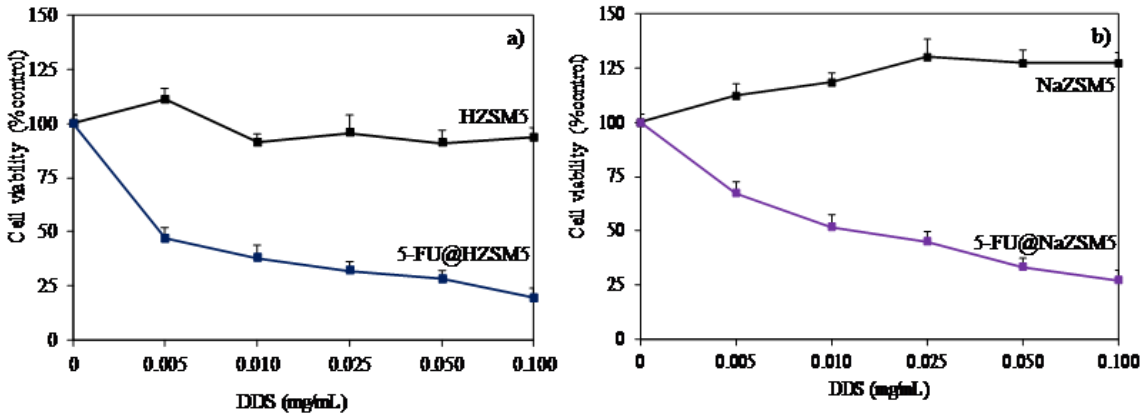

Figure 2.2.10: Effect of HZSM5 a) and NaZSM5 b) hosts and DDS systems on RKO colon carcinoma cell viability. RKO cells were incubated with hosts and different DDS concentrations for 48 h. Cell viability was measured by the SRB assay. Values are means ± SD of three independent experiments, each performed in triplicate. **p* < 0.05, ****p* < 0.001 compared to host alone.

Table 2.2.3 shows the IC_{50} values for RKO and HCT-15 cell viability after treatment with the DDS systems, compared with the drug alone.

Table 2.2.3: IC_{50} values for RKO and HCT-15 cell viability with 5-FU and DDS systems containing 5-FU.

Cell line	**RKO**		**HCT-15**	
	IC_{50} (mM)	**Potentiation**	**IC_{50} (mM)**	**Potentiation**
5-FU	0.13	-	0.61	-
5-FU@NaY	0.02	6.5	0.10	6.1
5-FU@HZSM5	0.02	6.5	0.09	6.8
5-FU@NaZSM5	0.08	1.6	0.20	3.1
5-FU@NaA	0.11	1.2	0.11	5.5
5-FU@ETS-10	0.02	6.5	0.12	5.1
5-FU@LTL[a4]	0.03	4.3	0.31	1.9

[a]LTL DDS results were from ref.4.

It is clear from the results that there is a potentiation of the 5-FU when is encapsulated into the silica microporous structures in both colorectal cancer cell lines. This potentiation is dependent on the capacity of 5-FU loading, as well as on the porous framework of the hosts. For RKO cells, there is an increase in efficiency of the drug between 1.2 and 6.5-fold. The

highest potentiation (6.5-fold) was obtained with the 3D structures, (ETS-10 and NaY, large pores) and HZSM5 (medium pores) hosts, which correspond to 5-FU assay concentrations of 0.02 mM.

Concerning ZSM5 structure, the reduction in pore aperture in NaZSM5 decreases 5-FU potentiation in about 4-fold when compared to 5-FU@HZSM5. The lowest potentiation obtained was for NaA host (1.2-fold), which contains 0.11 mM of 5-FU. Likewise, treatment of HCT-15 cells with the encapsulated 5-FU resulted in a potentiation of the effect of the drug from 3.1 to 6.8-fold, corresponding to 5-FU assay concentrations of 0.20 and 0.09 mM, respectively. For this cell line, the 3D structures seem to favor the potentiation of the drug, rather than the loading of 5-FU in the hosts.

The viability assays were also performed on MDA-MB-468 human breast cancer cells with the DDS based on NaY and ETS-10 (large pores) and compared with NaA (small pore). In addition, these hosts are not toxic for this cell line (Figure 2.2.11) and the DDS based in these hosts were very efficient in the decrease of the cell viability (Table 2.2.4). Importantly, inclusion of 5-FU in the DDS, increased substantially the sensitivity of the breast cancer cells to 5-FU, which are more resistant than the colon cancer cells.

For MDA-MB-468 cells, the best DDS was obtained with ETS-10 with higher 5-FU loading. The potentiation obtained is double compared to the zeolite systems, which display the same potentiation among them, despite different loadings (Table 2.2.1).

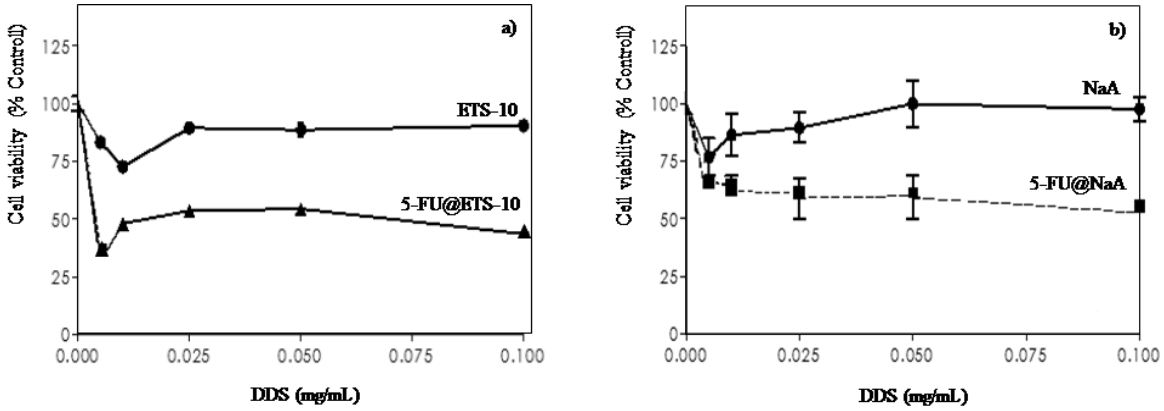

Figure 2.2.11: Effect of ETS-10 a) and NaA b) hosts and DDS systems on MDA-MB-468 breast carcinoma cell viability. MDA-MB-468 cells were incubated with hosts and different DDS concentrations for 48 h. Cell viability was measured by the SRB assay. Values are means ± SD of three independent experiments, each performed in triplicate. *$p < 0.05$, ***$p < 0.001$ compared to host alone.

Table 2.2.4: IC_{50} values for MDA-MB-468 cell viability for 5-FU and DDS systems containing 5-FU.

Cell line	**MDA-MB-468**	
	IC_{50} (mM)	**Potentiation**
5-FU	3.80	-
5-FU@NaY	0.38	10.0
5-FU@NaA	0.37	10.2
5-FU@ETS-10	0.19	19.9

The potential of these host structures will depend on the design and delivery route to be used. While smaller particles (<100 nm, LTL zeolite) would be suitable for systemic administration, e.g. intra venous or inhalation delivery, larger particles (>100 nm, NaY, NaA and ZSM5 zeolites, and ETS-10) will have potential for topical delivery (Figure 2.2.1). Besides systemic treatment, 5-FU is also used topically for the treatment of non-melanoma skin cancer (e.g. superficial basal cell carcinoma) or even other skin pathological conditions such as actinic or solar keratosis.[42,43]

2.2.4. CONCLUSIONS

The hosts selected for this work show potential to be used in the future design and development of DDS for biomedical applications. The silica microporous structures were selected due to the combination of non-cytotoxic effects to the cells, wide and accessible pore expected to be favorable for enhancement of the activity of 5-fuorouracil (5-FU). 5-FU was successfully loaded into the host structures and 5-FU loading was found to be highest in 3D large pores (NaY and ETS-10) followed by ZSM5 (3D, medium pore) and NaA (3D, small pore). All structures are not toxic to the colon and breast cancer cell lines studied and they preserved the integrity of 5-FU even at lower pH, before the contact with the cells. Moreover, 5-FU loaded into the host structures can be at least six times more effective in colon cancer cell death induction than the free 5-FU administered *in vitro* (5-FU@NaY and 5-FU@HZSM5 systems) and twenty times more effective for the breast cancer cells (5-FU@ETS-10).

2.2.5. REFERENCES

1 Y. Zhang, H. F. Chan and K. W. Leong, Advanced materials and processing for drug delivery: The past and the future, *Adv. Drug Deliv. Rev.*, 2013, **65**, 104–120.

2 N. A. Peppas, Historical perspective on advanced drug delivery: How engineering design and mathematical modeling helped the field mature, *Adv. Drug Deliv. Rev.*, 2013, **65**, 5–9.

3 C. S. Kim, G. Y. Tonga, D. Solfiell and V. M. Rotello, Inorganic nanosystems for therapeutic delivery: Status and prospects, *Adv. Drug Deliv. Rev.*, 2013, **65**, 93–99.

4 N. Vilaça, R. Amorim, A. F. Machado, P. Parpot, M. F. R. Pereira, M. Sardo, J. Rocha, A. M. Fonseca, I. C. Neves and F. Baltazar, Potentiation of 5-fluorouracil encapsulated in zeolites as drug delivery systems for *in vitro* models of colorectal carcinoma, *Colloids Surfaces B Biointerfaces*, 2013, **112**, 237–244.

5 I. Braschi, S. Blasioli, L. Gigli, C. E. Gessa, A. Alberti and A. Martucci, Removal of sulfonamide antibiotics from water: Evidence of adsorption into an organophilic zeolite Y by its structural modifications, *J. Hazard. Mater.*, 2010, **178**, 218–225.

6 H. Zhang, Y. Kim and P. K. Dutta, Controlled release of paraquat from surface-modified zeolite Y, *Microporous Mesoporous Mater.*, 2006, **88**, 312–318.

7 M. Norek, I. C. Neves and J. A. Peters, 1H Relaxivity of Water in Aqueous Suspensions of Gd3+-Loaded NaY Nanozeolites and AlTUD-1 Mesoporous Material: the Influence of Si/Al Ratio and Pore Size, *Inorg. Chem.*, 2007, **46**, 6190–6196.

8 W.-S. Li, Z.-F. Li, F.-Y. Jing, X.-G. Yang, X.-J. Li, F.-K. Pei, X.-X. Wang and H. Lei, *Zeolites Mn2+-nay as oral gastrointestinal tract contrast agents in magnetic resonance imaging*, 2007, vol. 65.

9 C. Platas-Iglesias, L. Vander Elst, W. Zhou, R. N. Muller, C. F. G. C. Geraldes, T. Maschmeyer and J. A. Peters, Zeolite GdNaY Nanoparticles with Very High Relaxivity for Application as Contrast Agents in Magnetic Resonance Imaging, *Chem. - A Eur. J.*, 2002, **8**, 5121–5131.

10 I. Braschi, G. Gatti, G. Paul, C. E. Gessa, M. Cossi and L. Marchese, Sulfonamide Antibiotics Embedded in High Silica Zeolite Y: A Combined Experimental and Theoretical Study of Host−Guest and Guest−Guest Interactions, *Langmuir*, 2010, **26**, 9524–9532.

11 M. L. Pinto, A. C. Fernandes, F. Antunes, J. Pires and J. Rocha, Storage and delivery of nitric oxide by microporous titanosilicate ETS-10 and Al and Ga substituted analogues, *Microporous Mesoporous Mater.*, 2016, **229**, 83–89.

12 M. L. Pinto, J. Rocha, J. R. B. Gomes and J. Pires, Slow Release of NO by Microporous Titanosilicate ETS-4, *J. Am. Chem. Soc.*, 2011, **133**, 6396–6402.

13 M. L. Pinto, A. C. Fernandes, J. Rocha, A. Ferreira, F. Antunes and J. Pires, Microporous titanosilicates Cu2+- and Co2+-ETS-4 for storage and slow release of therapeutic nitric oxide, *J. Mater. Chem. B*, 2014, **2**, 224–230.

14 D. B. Longley, D. P. Harkin and P. G. Johnston, 5-Fluorouracil: Mechanisms of Action and Clinical Strategies, *Nat Rev Cancer*, 2003, **3**, 330–338.

15 N. Zhang, Y. Yin, S.-J. Xu and W.-S. Chen, 5-Fluorouracil: Mechanisms of Resistance and Reversal Strategies, *Molecules*, 2008, **13**, 1551–1569.

16 K. Yoneda, T. Yamamoto, E. Ueta and T. Osaki, The inhibitory action of BOF-A2, a 5-fluorouracil derivative, on squamous cell carcinoma, *Cancer Lett.*, 1999, **137**, 17–25.

17 J. L. Arias, M. A. Ruiz, M. López-Viota and Á. V Delgado, Poly(alkylcyanoacrylate) colloidal particles as vehicles for antitumour drug delivery: A comparative study, *Colloids Surfaces B Biointerfaces*, 2008, **62**, 64–70.

18 J. L. Arias, M. López-Viota, Á. V Delgado and M. A. Ruiz, Iron/ethylcellulose (core/shell) nanoplatform loaded with 5-fluorouracil for cancer targeting, *Colloids Surfaces B Biointerfaces*, 2010, **77**, 111–116.

19 J. Rocha, A. Ferreira, Z. Lin and M. W. Anderson, Synthesis of microporous titanosilicate ETS-10 from TiCl3 and TiO2: a comprehensive study, *Microporous Mesoporous Mater.*, 1998, **23**, 253–263.

20 B. Silva, H. Figueiredo, O. S. G. P. Soares, M. F. R. Pereira, J. L. Figueiredo, A. E. Lewandowska, M. A. Bañares, I. C. Neves and T. Tavares, Evaluation of ion exchange-modified Y and ZSM5 zeolites in Cr(VI) biosorption and catalytic oxidation of ethyl acetate, *Appl. Catal. B Environ.*, 2012, **117–118**, 406–413.

21 O. Martinho, N. Vilaça, P. J. G. Castro, R. Amorim, A. M. Fonseca, F. Baltazar, R. M. Reis and I. C. Neves, *In vitro* and in vivo studies of temozolomide loading in zeolite structures as drug delivery systems for glioblastoma, *RSC Adv.*, 2015, **5**, 28219–28227.

22 N. Vilaça, F. Morais-Santos, A. F. Machado, A. Sirkecioğlu, M. F. R. Pereira, M. Sardo, J. Rocha, P. Parpot, A. M. Fonseca, F. Baltazar and I. C. Neves, Micro- and mesoporous structures as drug delivery carriers for salicylic acid, *J. Phys. Chem. C*, 2015, **119**, 3589–3595.

23 K. A. Fisher, K. D. Huddersman and M. J. Taylor, Comparison of Micro- and Mesoporous Inorganic Materials in the Uptake and Release of the Drug Model Fluorescein and Its Analogues, *Chem. – A Eur. J.*, 2003, **9**, 5873–5878.

24 Database of Zeolite Structures from the International Zeolite Association, http://www.iza-structure.org/databases/, (accessed 10 January 2017).

25 M. R. C. Marques, R. Loebenberg and M. Almukainzi, Simulated biologic fluids with possible application in dissolution testing, *Dissolution Technol.*, 2011, 15–28.

26 R. Amorim, N. Vilaça, O. Martinho, R. M. Reis, M. Sardo, J. Rocha, A. M. Fonseca, F. Baltazar and I. C. Neves, Zeolite structures loading with an anticancer compound as drug delivery systems, *J. Phys. Chem. C*, 2012, **116**, 25642–25650.

27 S. Farquharson, A. Gift, C. Shende, F. Inscore, B. Ordway, C. Farquharson and J. Murren, *Molecules*, 2008, 13, 2608–2627.

28 A. Datt, E. A. Burns, N. A. Dhuna and S. C. Larsen, Loading and release of 5-fluorouracil from HY zeolites with varying SiO2/Al2O3 ratios, *Microporous Mesoporous Mater.*, 2013, **167**, 182–187.

29 L. Maggini, I. Cabrera, A. Ruiz-Carretero, E. A. Prasetyanto, E. Robinet and L. De Cola, Breakable mesoporous silica nanoparticles for targeted drug delivery, *Nanoscale*, 2016, **8**, 7240–7247.

30 R. Mellaerts, R. Mols, J. A. G. Jammaer, C. A. Aerts, P. Annaert, J. Van Humbeeck, G. Van den Mooter, P. Augustijns and J. A. Martens, Increasing the oral bioavailability of the poorly water soluble drug itraconazole with ordered mesoporous silica, *Eur. J. Pharm. Biopharm.*, 2008, **69**, 223–230.

31 E. Verraedt, M. Pendela, E. Adams, J. Hoogmartens and J. A. Martens, Controlled release of chlorhexidine from amorphous microporous silica, *J. Control. Release*, 2010, **142**, 47–52.

32 P. Costa and J. M. Sousa Lo, Modeling and comparison of dissolution profiles, *Eur. J. Pharm. Sci.*, 2001, **13**, 123–133.

33 S. Dash, P. Murthy, L. Nath and P. Chowdhury, Review Kinetic Modeling On Drug Release From Controlled Drug Delivery Systems, 2010, **67**, 217–223.

34 I. Kuźniarska-Biernacka, P. Parpot, C. Oliveira, A. R. Silva, M. J. Alves, A. M. Fonseca and I. C. Neves, Norbornene Oxidation by Chiral Complexes Encapsulated in NaY Zeolite, *J. Phys. Chem. C*, 2014, **118**, 19042–19050.

35 K. Thelen, K. Coboeken, S. Willmann, J. B. Dressman and J. Lippert, Evolution of a detailed physiological model to simulate the gastrointestinal transit and absorption process in humans, part II: Extension to describe performance of solid dosage forms, *J. Pharm. Sci.*, 2012, **101**, 1267–1280.

36 M. Guo, E. A. Pidko, F. Fan, Z. Feng, J. P. Hofmann, B. M. Weckhuysen, E. J. M. Hensen and C. Li, Structure and Basicity of Microporous Titanosilicate ETS-10 and Vanadium-Containing ETS-10, *J. Phys. Chem. C*, 2012, **116**, 17124–17133.

37 G. F. Ghesti, J. L. de Macedo, V. C. I. Parente, J. A. Dias and S. C. L. Dias, Investigation of pyridine sorption in USY and Ce/USY zeolites by liquid phase microcalorimetry and thermogravimetry studies, *Microporous Mesoporous Mater.*, 2007, **100**, 27–34.

38 M. W. Anderson, J. Rocha, Z. Lin, A. Philippou, I. Orion and A. Ferreira, Isomorphous substitution in the microporous titanosilicate ETS-10, *Microporous Mater.*, 1996, **6**, 195–204.

39 Z. Lin, J. Rocha, A. Ferreira and M. W. Anderson, Synthesis of microporous titano-alumino-silicate ETAS-10 with different framework aluminum contents, *Colloids Surfaces A Physicochem. Eng. Asp.*, 2001, **179**, 133–138.

40 N. Vilaça, R. Amorim, O. Martinho, R. M. Reis, F. Baltazar, A. M. Fonseca and I. C. Neves, Encapsulation of a-cyano-4-hydroxycinnamic acid into a NaY zeolite., *J. Mater. Sci.*, 2011, **46**, 7511–7516.

41 A. Petushkov, N. Ndiege, A. K. Salem and S. C. Larsen, in *Advances in Molecular Toxicology*, ed. J. C. Fishbein, Elsevier, 2010, vol. 4, pp. 223–266.

42 P. Herranz, C. Morton, T. Dirschka, R. R. Azeredo and R. Roldan-Marin, Low-Dose 0.5% 5-Fluorouracil/10% Salicylic Acid Topical Solution in the Treatment of Actinic Keratoses, *J. Cutan. Med. Surg.*, 2016, **20**, 555–561.

43 B. T. Nguyen, S. D. Gan, N. Konnikov and C. A. Liang, Treatment of superficial basal cell carcinoma and squamous cell carcinoma in situ on the trunk and extremities with ablative fractional laser-Assisted delivery of topical fluorouracil, *J. Am. Acad. Dermatol.*, 2015, **72**, 558–560.

SUBCHAPTER 2.3

5-FU DRUG DELIVERY SYSTEMS BASED ON ZEOLITES FOR CANCER THERAPY: *IN VITRO* AND *IN VIVO* STUDIES[3]

Zeolites have features that make them attractive as carriers for drug delivery systems (DDS). Herein, we loaded the anticancer drug 5-fluorouracil (5-FU) into two different zeolite structures, faujasite (FAU) and linde type L (LTL), to obtain DDS with different properties. The prepared DDS were tested *in vitro* using breast cancer (Hs 578T), colorectal carcinoma (RKO) and melanoma (A375) cell lines and *in vivo* using the chick embryo chorioallantoic membrane as model (CAM), which allows to study angiogenesis, and tumor growth. The results from the *in vitro* assays show that the prepared DDS were able to release the anticancer drug, significantly decreasing cell viability in all cell lines. In the *in vivo* CAM assay, there was a reduction in tumor perimeter for Hs 578T cells, while no reduction was detected for RKO tumors. Thus, after further optimization of the use of these DDS *in vivo*, they might prove to be promising in the treatment of cancer, specially breast cancer (see graphical abstract below).

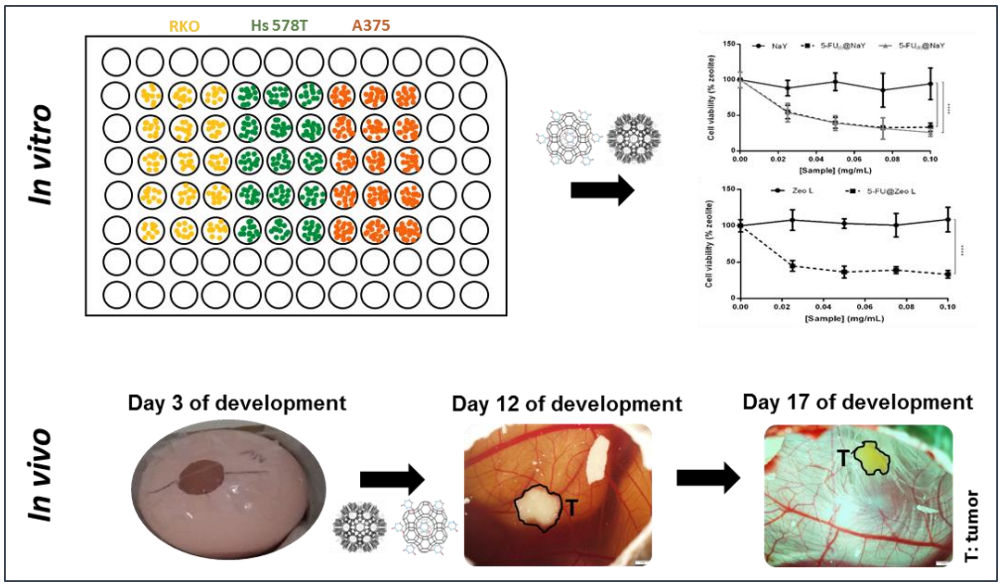

[3] **N. Vilaça**, S. Granja, E. A. Prasetyanto, A. M. Fonseca, L. De Cola, F. Baltazar, I. C. Neves, 5-FU drug delivery systems based on zeolites for cancer therapy: *in vitro* and *in vivo* studies, *submitted*.

2.3.1. INTRODUCTION

Despite the recent advances and improvements in healthcare, cancer incidence has increased over the years, being the leading cause of death worldwide.[1,2] In 2012, it affected 8.2 million of people worldwide and it is estimated that in 2030 will lead to more than 13 million deaths per year, without discrimination between social economic state, gender or age.[3,4] There are many factors that can contribute to the high number of new cases of cancer such as, life style, genetic predisposition, environmental factors, high-fat diet, smoking, and others.[5–9]

In the midst of the different types of cancers, breast cancer is the second most common cancer worldwide, and the most frequent in women[10,11] and colorectal cancer is the third most common in men and the second in women in the world, with special occurrence in developed countries with an estimated 60% of all cases,[12,13] In European Union (EU-28), there are 193.000 new cases of colorectal cancer and 83.000 deaths in men and 152.000 new cases and 69.000 deaths in women. In turn, breast cancer had 362.000 new cases and was responsible for 92.000 of deaths in 2012.[14] Because of that, scientists have been looking for new therapies that can reduce these numbers and contribute for a better quality of life of the patients.[15] One of these strategies are the drug delivery systems (DDS). These systems have great advantages, comparing with the traditional routes of administration of drugs, namely, protecting normal tissues from the undesirable side effects of the drugs, delivery of the drugs on the tumor site, delivering drugs in controlled rates, enhancing the therapeutic index of drugs.[16–19]

To assess the efficacy and toxicity of DDS, these are tested in *in vitro* models, since these provide a simple, safe and efficient way to evaluate DDS effects.[20] However, *in vitro* models do not mimic the complexity of the tumor features, including the tumor environment and, sometimes, drugs that seem promising *in vitro*, fail *in vivo.*[21] Because of that, it is important perform *in vivo* assays that can better simulate the features of the tumor.[20] Among the different types of *in vivo* models, the chick embryo is a simple, rapid and low-cost model that allows the study of tumor growth, angiogenesis and metastasis. This model is capable to sustain grafted tissues and cells without species-specific restrictions since the lymphatic system of the chick is only fully developed at the later stages of incubation.[22,23] The use of chick embryo as a *in vivo* model, which uses the chorioallantoic membrane (CAM), is a well-known experimental model suitable to evaluate the effect of the DDS.[24,25] The CAM is a highly vascularized extraembryonic membrane, formed in the chicken egg[26] by partial fusion of chorion and allantois at 3-5 days of embryo development.[24,27] It is composed by three layers, the ectoderm, mesoderm and endoderm and contains extracellular matrix proteins which mimics the physiological cancer cell environment.[28] The formed tumor on the CAM is exposed to the drugs or carriers to be studied and the perimeter of tumor and angiogenesis can be evaluated.[29]

There are many studies using the CAM model to study the effect of drugs and materials on tumor development and angiogenesis.[26,29–31] In this work, as continuation of your line of research, we prepared DDS using two different types of zeolite structures - hydrated aluminosilicate materials with a regular framework, which can entrap organic molecules on their pores[32,33] – with different amounts of 5-fluorouracil (5-FU) a chemotherapeutic drug used in the treatment of several solid cancers: head and neck, pancreatic, colon, breast, skin cancer (basal cell and keratosis), and others.[34] It is possible to find many studies in the literature reporting the assessment of *in vitro* efficacy of zeolites as DDS. However, to the best of our knowledge, the evaluation of the efficiency of DDS based in zeolites using *in vivo* models, is scarce.[35] Understanding the behavior of these DDS *in vivo* is essential to improve their efficacy and to optimize concentration of these systems for *in vivo* applications. Hence, in order to explore the potential of these DDS for theranostic strategies, we compared the effects of DDS in *in vitro* models using breast, colorectal and melanoma cancer cell lines and *in vivo* CAM model for implanted breast and colorectal microtumors.

2.3.2. EXPERIMENTAL

2.3.2.1. MATERIALS

All reagents and materials were used without any further purification. Zeolite NaY (CVB100, faujasite (FAU) structure) was obtained from Zeolyst International. Zeolite L, (Linde Type L (LTL) structure) was synthetized as previously described.[36] 5-fluorouracil (5-fluoro-1H-pyrimidine-2,4-dione) was purchased from Sigma-Aldrich.

2.3.2.2. PREPARATION AND CHARACTERIZATION OF THE DRUG DELIVERY SYSTEMS

Two different zeolite structures, faujasite, FAU (NaY) and Linde Type L, LTL (Zeo L), capable of hosting 5-FU, were used to prepare the DDS. The preparation of the DDS was performed previously described, with some modifications.[37,38] Prior to the preparation of the DDS, the water in the zeolites pores was removed by dehydration at 120 °C during 12 h. Afterwards, solutions with different amounts of 5-FU (75 mg (0.577 mmol) designated by I and 130 mg (0.999 mmol) by II) were dissolved in 10 mL of water, and 200 mg of NaY was added and mixed during 48 h at room temperature (RT). For Zeo L, 130 mg (0.999 mmol) of 5-FU dissolved in 10 mL of water was added to 200 mg of zeolite and it was also mixed during 48 h at RT. After, the solvent was evaporated at 65 °C by agitation 60 rpm, for all procedures. The obtained DDS was designated by 5-FU$_{(I)}$@NaY and 5-FU$_{(II)}$@NaY, where the subscript number refers to the number of moles of 5-FU used to prepare the DDS, 0.577 and 0.999 mmol, respectively, and 5-FU@Zeo L for the DDS prepared with zeolite LTL.

The prepared DDS were characterized by thermogravimetric analysis (TGA) and Fourier transform infrared (FTIR). TGA was performed to calculate the amount of drug loaded into the zeolitic structure. The conditions of the TGA analysis were described in.[38] FTIR was carried out using 2 mg of sample mixed with 98 mg of KBr and the obtained pellets were measured with a AFT spectrometer between 4000-500 cm^{-1} by averaging 32 scans at a resolution of 4 cm^{-1}.

2.3.2.3. CELL LINES AND GROWTH CONDITIONS

For the *in vitro* cellular viability assays three different model cell lines were used: Hs 578T of breast cancer, RKO of colorectal cancer and A375 of melanoma. Hs 578T cells and A375 cells were obtained from ATCC and RKO was kindly provided by Dr. Raquel Seruca (IPATIMUP, Porto, Portugal). The three cell lines were maintained at 37 °C in 5% CO_2 in DMEM medium (Gibco), supplemented with 10% fetal bovine serum (FBS) (Gibco, Invitrogen, USA) and 1% (v/v) penicillin–streptomycin solution (P/S) (Invitrogen, USA).

2.3.2.4. *IN VITRO* CELL VIABILITY ASSAYS

Cell viability assays were performed as described before.[37,38] Fleetingly, cells where plated in 96-well plates at density of 7000 cells per well for Hs 578T, 6000 cells per well for RKO and 10000 cells per well for A375 and were left to adhere overnight. Stock suspensions of DDS and parent zeolites of 0.5 mg mL^{-1} were prepared in DMEM without FBS. From stock suspensions, diluted suspensions from 0.025 to 0.100 mg mL^{-1} were prepared, once again with DMEM without FBS. The resulting suspensions were sonicated for 2 min to avoid aggregates and get a better homogenization. Subsequently, the cell medium was removed from the wells and the cells were treated with the increasing solutions of DDS or zeolite for 48 h. After this time, cell viability was quantified using the sulforhodamine B (SRB) assay[37] and the obtained results were expressed as mean ± SD viable cells, comparing to the conditions with the parent zeolite.

For IC_{50} determination cells were plated as described above, and the incubated with culture medium containing 0.01 - 10 mM of 5-FU for 48h. The effect of 5-FU was also measured by SRB assay. The IC_{50} values were calculated with Graphpad Prism 6® software, using a sigmoidal dose-response (variable slope) nonlinear regression, next to logarithmic transformation.[39]

2.3.2.5. CHICK CHORIOALLANTOIC MEMBRANE (CAM) ASSAY

This assay was performed to test the effect of the DDS *in vivo* on the tumor growth and angiogenesis. For this purpose, eggs were incubated at 37 °C (day 0), then, on day 3 of chick embryo development, a small window was made in the shell of the egg to detach the CAM membrane from the egg shell and eggs were incubated again at 37 °C. On day 9 of chick embryo development, 1×10^6 Hs 578T breast cancer cells and RKO colorectal cells were mixed with 10 µL of Matrigel to form a gel and graft the cells on top of the CAM, and incubated again at 37 °C. On day 13 of chick embryo development, the windows on the shell were opened and the formed tumor photographed *in ovo,* then 20 µL of the materials suspensions (0.5 mg mL^{-1}) to be tested were placed over the tumor and the shell window closed again. On 17 day of development, the eggs were opened and the tumors were photographed (*in ovo)*. After that, the chick embryos were sacrificed at -80 °C for 10 min and the CAM membrane was removed from the egg and photographed (*ex ovo)*. Tumors perimeters were measured using ImageJ at day 13 (corresponding day 0) and 17 (corresponding day 4). The results were expressed as mean perimeter ± SD of tumor growth for each group.

The percentage of blood vessels density was measured in ImageJ using vessel analysis plugin.

2.3.2.6. IMMUNOHISTOCHEMISTRY

The CAMs collected from the eggs were fixed in formalin and embedded in paraffin. The paraffin blocks were cut into thin sections from immunohistochemistry was performed for Ki-67 (clone MIB-1, DAKO AP10243CM). Slides containing the paraffin sections of tumors, were deparaffinized and rehydrated and heat-induced for the antigen retrieval using a microwave oven during 15 min with 10 mM citrate buffer at pH 6.0. Endogenous peroxidases were inactivated using a 3% solution of hydrogen peroxide and UVblock (LabVision, Thermo Scientific) was added to the slides and incubated for 10 min. Incubation with the primary antibody (dilution 1:200) was done during 2 h at RT. After that, slides were washed twice with PBS for 5 min each and the secondary antibody (kit LabVision, Thermo Scientific) was incubated for 10 min at RT, and the slides washed again with PBS. Then, streptavidine peroxidase (kit LabVision, Thermo Scientific) was added for 10 min (RT), washed, and slides were incubated with the chromogen 3,3'-diamonobenzidine (DAB and Substrate System, Dako) for 10 min to allow the visualization of the immune reaction. After washing with PBS and water, the slides were counterstained with hematoxylin and analyzed under the light microscope. Cells presenting brown nuclear labeling were considered positive for Ki67 staining. For Ki67 quantification tumor slides were observed under microscope (Olympus

BX61), and the areas stained for ki67 were photographed at 20× objective in five different fields. Then, negative and positive cells for Ki67 staining were counted and the percentage of Ki67 positive cells calculated based on the obtained data using the formula: (Ki67 positive cells/(Ki67 positive cells+Ki67 negative cells))×100.[40,41]

2.3.2.7. STATISTICAL ANALYSIS

Differences between the *in vitro* cell viability assay results and the differences between Ki67 positive cells and blood vessel density were analysed by one-way ANOVA, followed by Dunnett's test. The differences between tumor perimeters, were assessed by two-way ANOVA with Sidak's post-test. All results were analysed using GraphPad Prism 6® and are expressed as mean ± standard deviation (SD). Differences were considered statistically significant for $*p < 0.05$, $**p < 0.01$, $***p < 0.001$ and $****p < 0.0001$.

2.3.3. RESULTS AND DISCUSSION

2.3.3.1. PREPARATION AND CHARACTERIZATION OF DDS

Preparation of DDS based on zeolite structures NaY and LTL for delivery 5-FU was based in our previous stablished protocols,[32,37] using water as solvent in this work. The main advantage of this approach is related to the fact of water being non-toxic to cells and if some solvent stays entrapped into zeolite structures, it is guaranteed that the solvent will not cause toxicity to cells.

The prepared DDS were characterized by means of FTIR and TGA (Figure 2.3.1). FTIR was used to prove the molecular interactions of 5-FU with the zeolite structures, the results are shown in Figure 2.3.1A and 2.3.1B. The spectra of Zeo L (Figure 2.3.1A-c) and NaY (Figure 2.3.1B-d) show the characteristic framework bands of some groups such as: 3410 cm^{-1} for O-H bond, between 1300-900 cm^{-1} for the asymmetric T-O-T stretching vibration, where T is Si or Al and at around 719 cm^{-1} related to the surface aluminium species, which are in according to the literature.[42,43] The spectrum corresponding to the 5-fluorouracil, show bands at 2750-3200 cm^{-1} characteristic of C-H and N-H bonds, a band for the imide at 1722 cm^{-1} assigned to the C double O bond, another one at 1374 cm^{-1} for C-N bond, and a peak at 1254 cm^{-1} related with the C-F stretching vibrations, according to the literature.[44] Regarding the DDS spectra prepared with zeolite L (Figure 2.3.1A-b) and prepared with zeolite NaY (Figures 2.3.1B-b and 2.3.1B-c), it is possible to observe the bands characteristic of the groups corresponding to both 5-FU and zeolites. So, characteristics bands of O-H and Si-O-Si groups of the zeolites at 3410 cm^{-1} and 1300-900 cm^{-1} respectively, are detected simultaneously. New bands at 3300-2800 cm^{-1} for the C-H and N-H bonds, at 1731 cm^{-1} for the C=O and at 1259-1253 cm^{-1} for the C-F

are observed. These bands are not observed in the zeolite spectra and they are characteristic of the 5-FU spectrum, confirming the presence of 5-FU on DDS which once again is in line with the literature.[44]

Loading of 5-FU into the zeolites was determined by thermogravimetric analysis (TGA) (Figure 2.3.1C and Table 2.3.1). From the 5-FU TGA curve (Figure 2.3.1C-a), it can be seen that the drug molecule melts around 200 - 300 ºC and decomposes totally around 300 - 400 ºC. The TGA curves for the zeolites (Figure 2.3.1C-c for Zeo L and 2.3.1C-f for NaY) shows weight loss around 50 - 150 ºC, which can be attributed to the removal of water from the zeolite. TGA curves for the DDS (Figure 2.3.1C-b for DDS prepared with Zeo L and Figures 2.3.1C-d and 2.3.1C-e for DDS prepared with NaY) show weight changes corresponding to the 5-FU and the zeolites, which are in accordance with Larsen *et al.*[45]

As expected, DDS prepared with NaY obtained the highest loading of 5-FU (Table 2.3.1). For this zeolite, the loading of 5-FU was 0.46 mmol and 0.55 mmol for 5-FU$_{(I)}$@NaY and 5-FU$_{(II)}$@NaY, respectively. From these results, it is also possible to verify that Zeo L has lower loading capacity than zeolite NaY. This can be related with structural features of the zeolites, Zeo L present mono-dimensional nanochannels and NaY have a tridimensional structure and facilitate the introduction of 5-FU in its channels.[32,46]

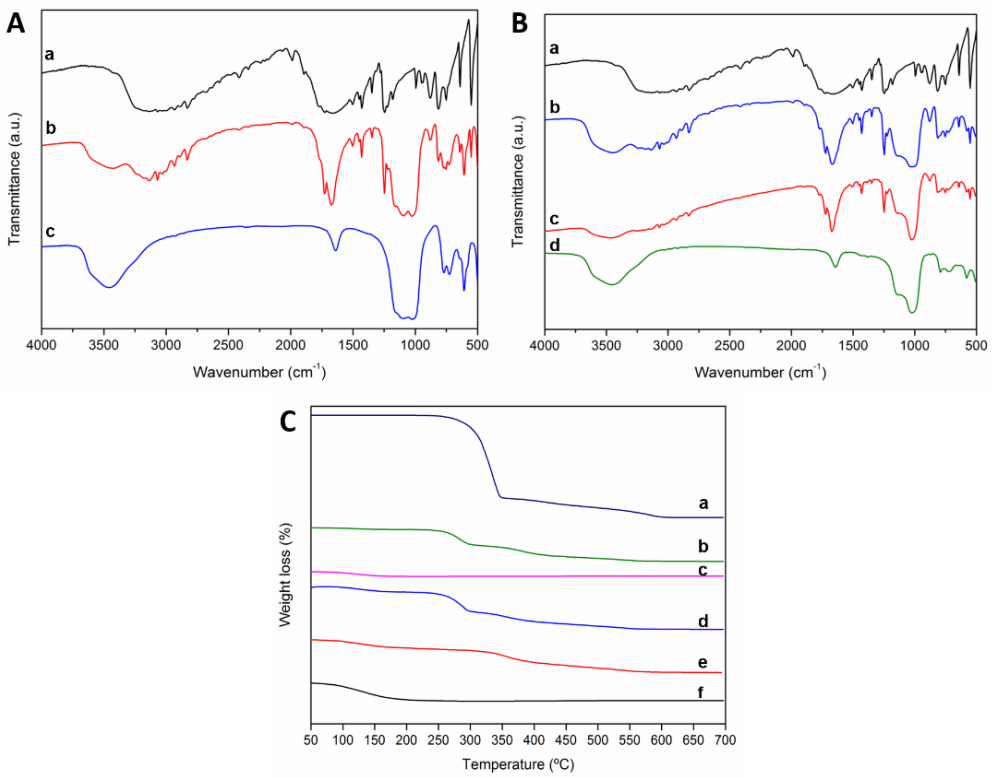

Figure 2.3.1: DDS characterization: A) FTIR spectra of DDS prepared with zeolite LTL: a: 5-FU, b: 5-FU@Zeo L and c: Zeo L. B) FTIR spectra of DDS prepared with zeolite NaY: a: 5-FU, b: 5-FU$_{(II)}$@NaY, c: 5-FU$_{(I)}$@NaY and d: NaY. C) TGA curves of a: 5-FU, b: 5-FU@Zeo L, c: Zeo L, d: 5-FU$_{(II)}$@NaY e: 5-FU$_{(I)}$@NaY, and f: NaY.

Table 2.3.1: Loading of 5-FU in the DDS determined by TGA

DDS	5-FU (mmoles)[a]	5-FU (mmoles)[b]
5-FU$_{(I)}$@NaY	0.58	0.46
5-FU$_{(II)}$@NaY	1.00	0.55
5-FU@ Zeo L	1.00	0.42

[a]Initial amount of 5-FU in the solution. [b]5-FU loading in zeolite structures determined by TGA.

2.3.3.2 ASSESSMENT OF DRUG BIOACTIVITY

Breast and colorectal cancer are the most common types of cancer worldwide.[10,47] Despite of all advances in their treatment, they continue to cause high number of deaths every year. Because of that, it is important to look for new therapeutic approaches. In the current study, DDS based on zeolites were prepared to convey the chemotherapeutic agent 5-FU in different types of cancer models. In our previous work, we already reported the efficacy of DDS based on zeolite in colon, glioma and breast cancer.[35,37,38] However, in the present study we performed various experiments in order to give further insights into the therapeutic effect of 5-FU@zeolite on colorectal, breast and melanoma cancer *in vitro* and, importantly, the therapeutic effect on colorectal and breast cancer *in vivo* using the CAM model.

Firstly, DDS were tested *in vitro* using for this purpose colorectal, breast and melanoma cancer cells. Then, *in vivo* studies using CAM model were carried out to determine whether the DDS are also effective in the reduction of 3D tumor size. Below we demonstrated our findings from these studies.

Evaluation of DDS efficacy *in vitro*

The main focus of this work was to evaluate the *in vitro* and *in vivo* efficacy of these DDS on breast and colorectal cancer.

The *in vitro* cytotoxicity of NaY, 5-FU$_{(I)}$@NaY, 5-FU$_{(II)}$@NaY, Zeo L and 5-FU@Zeo L was assessed on breast (Hs 578T), colorectal (RKO) and melanoma (A375) cancer cells. Hs 578T cell line was chosen as a model of breast cancer which is representative of a triple-negative breast cancer (TNBC),[11,48,49] RKO cells were chosen as model of colorectal cancer and A375 was used as model of melanoma (skin cancer). 5-FU was chosen due its efficiency in the treatment of different types of cancers.[50,51]

The effect of the parent zeolites and respective DDS on Hs 578T, RKO and A375 cell lines is shown in Figure 2.3.2. We exposed cells to parent zeolites and DDS in the range of 0.025 -

0.100 mg mL^{-1} of concentrations. The incubation time was 48 h based on our previous studies showing that the highest reduction in cell viability was achieved at this time. The results demonstrated that NaY and Zeo L were nontoxic to any of the cell lines even for the highest tested concentrations. From our previous study, we know that the morphology and size of zeolite nanoparticles might play an important role in cell internalization. We showed that Zeo L (400 nm) is internalized faster than NaY (700 nm) by breast cancer cells.[36] Sahu *et al.* demonstrated that SiO_2 nanoparticles induced more toxicity than micron particles on L-132 cells,[52] as well as, Kihara *et al.* reported that nanozeolites with different sizes have different toxicity on HeLa cells.[53] They also, reported that LTL zeolites (50 nm and 90 nm) were toxic for HeLa cells from 50 µg mL^{-1}.[53] However, our results demonstrate that there was no direct relation between the size of zeolite nanoparticles and their cytotoxicity, since both zeolites were nontoxic to the cells even in the highest concentrations tested. These results are in accordance to the reports by Deng and coworkers, where it was demonstrated that zinc oxide particles had the same toxicity on neural stem cell (NSC) independently of the size.[54] Similar cytotoxicity of NaY and Zeo L observed in this work, might be related with the different cell lines used, which corroborate the premise that the cytotoxicity of the nanoparticles is dependent of the cell type where they are tested.[55] Grund *et al.* have found that mitoxantrone-loaded zeolite beta nanoparticles exhibit different cytotoxic activities depending the cell type and concentration.[56]

The results of our study, demonstrate that treatment of the cells with all DDS resulted in a significant reduction of cell viability in a concentration-dependent manner ($p < 0.05$), compared to the parent zeolites (control group), with exception for 5-FU@Zeo L in Hs 578T cells at the lowest concentration (0.025 mg mL^{-1}) (Figure 2.3.2). 5-$FU_{(I)}$@NaY reduced Hs 578T cell viability in 10.5%, 61% for RKO and 76% for A375 cells in the highest DDS concentration (0.100 mg mL^{-1}), compared to the same concentration of NaY. The highest concentration of 5-$FU_{(II)}$@NaY decreased cell viability in 16.6% for Hs 578T cells, 68.3% for RKO cells and 83.3% for A375 cells. In turn, 5-FU@Zeo L, reduced cell viability in 21% for Hs 578T cells, 75.4% for RKO cells and 70.1% for A375 cells. Also, at lower concentrations, a decrease in cell viability for all cell lines and all tested DDS was observed. Despite the inhibition of cell growth in all cell lines, it is clear that this inhibition is cell type-dependent since higher reduction is observed in RKO and A375 cell lines, than Hs 578T, denoting once again the importance of the cell type.

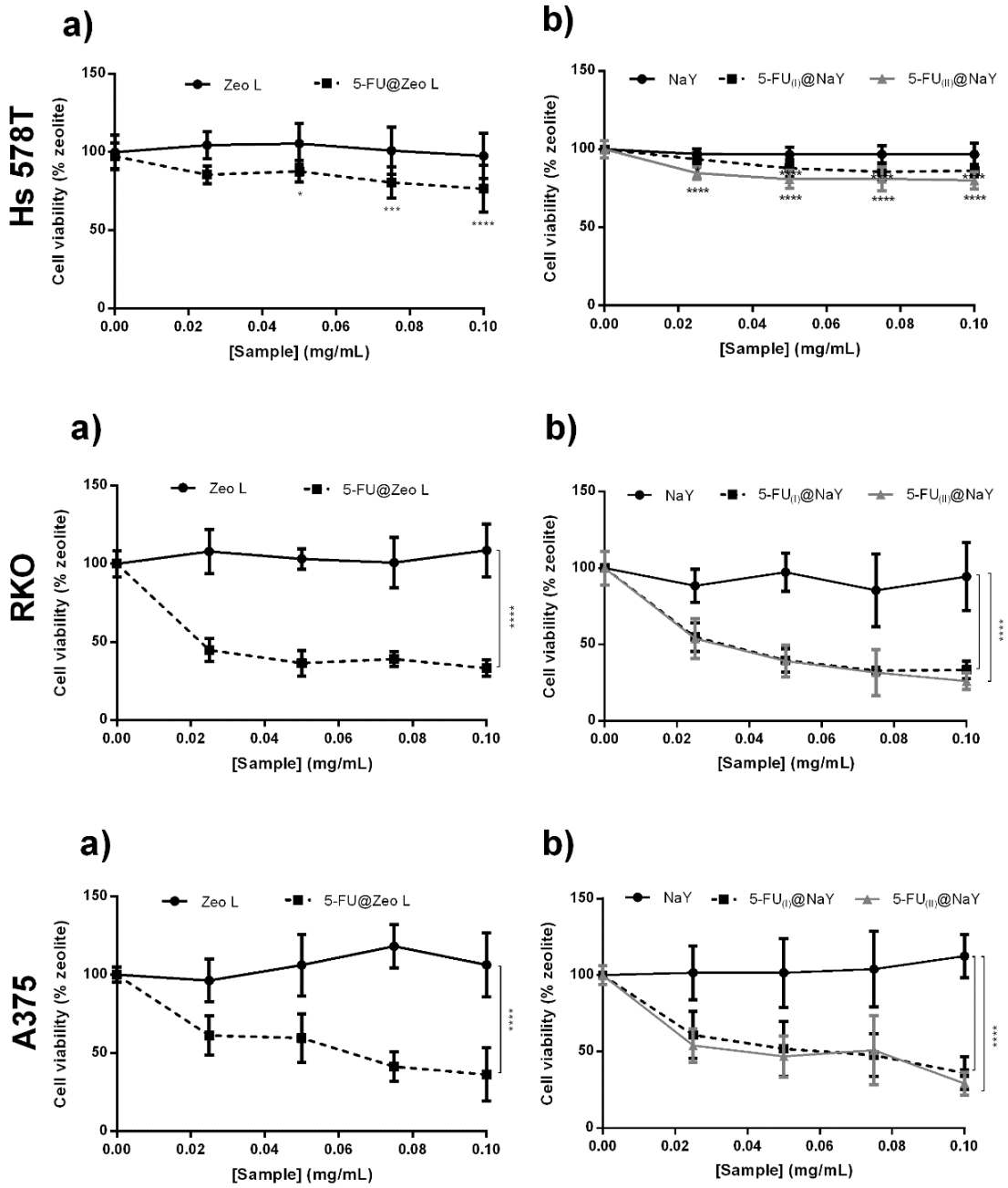

Figure 2.3.2: Effect of Zeo L and 5-FU@Zeo L (a) and NaY and 5-FU$_{(I)}$@NaY and 5-FU$_{(II)}$@NaY (b) on Hs 578T breast cancer, RKO colon carcinoma and A375 melanoma cell viability. Cells were incubated with zeolites and different DDS concentrations for 48 h. Cell viability was measured by the SRB assay. Values are means ± SD of at least three independent experiments, each performed in triplicate. *p < 0.05, ***p < 0.001 and ****p < 0.0001 compared to parent zeolite.

The concentrations of 5-FU (mM) present in DDS suspensions used in *in vitro* drug bioactivity studies are shown in Table 2.3.2 and the IC_{50} values (for cell viability) for 5-FU and DDS are demonstrated in Table 2.3.3.

Table 2.3.2: Final concentrations of 5-FU (mM) in the different DDS suspensions.

DDS (mg mL^{-1})	0.500 (stock)	0.025	0.050	0.075	0.100
5-$FU_{(I)}$@NaY (mM 5-FU)	0.88	0.04	0.09	0.13	0.18
5-$FU_{(II)}$@NaY (mM 5-FU)	1.02	0.05	0.10	0.15	0.20
5-FU@ Zeo L (mM 5-FU)	0.83	0.04	0.08	0.12	0.17

The IC_{50} values for 5-$FU_{(I)}$@NaY in Hs 578T cells are 5.55 mM, 0.05 mM for RKO and 0.09 mM for A375, and for 5-$FU_{(II)}$@NaY are 0.66 mM for Hs 578T, 0.06 mM for RKO and 0.08 mM for A375. The IC_{50} values of 5-FU@Zeo L are 1.99 mM for Hs 578T, 0.02 mM for RKO and 0.09 mM for A375. Bearing in mind the 5-FU concentration in each DDS (Table 2.3.2) and comparing the IC_{50} values of free 5-FU with the DDS, a potentiation of 5-FU is observed when loaded into zeolite structures (Table 2.3.3). Despite the apparent lower effect of the DDS on Hs 578T cells, displaying higher IC_{50}, the sensitivity of these cells to free 5-FU is much lower than for the other cells. Thus, the resulting potentiation is actually higher for Hs 578T cells than for RKO and A375. Data from literature demonstrate that the encapsulation of 5-FU into nanoparticles is a good approach to improve its efficacy and reduce toxicity.[57–59] The presented results indicate that the prepared DDS have inhibitory effect on the tested cell lines and have a higher effect than the free 5-FU, thus demonstrating the potential of these systems for cancer treatment, supporting our previous findings.[37,38]

Table 2.3.3: Viability IC_{50} values for 5-FU and DDS for Hs 578T, RKO and A375 cell lines. *For the calculation of 5-FU potentiation in Hs 578T cell line, was considered 10 mM as value of IC_{50} of free 5-FU.

	Hs 578T		RKO		A375	
	IC_{50} (mM)	**Potentiation***	**IC_{50} (mM)**	**Potentiation**	**IC_{50} (mM)**	**Potentiation**
5-FU	> 10	-	0.13	-	0.17	-
5-$FU_{(I)}$@NaY	5.55	1.8	0.05	2.6	0.09	1.9
5-$FU_{(II)}$@NaY	0.60	16.7	0.06	2.2	0.08	2.1
5-FU@Zeo L	1.99	5.0	0.02	6.5	0.09	1.9

In vivo anti-tumor activity

From the *in vitro* results, exposure to DDS appears to affect cell viability significantly. Thus, we evaluated the potential of these DDS *in vivo* using the chicken CAM assay. CAM is a simple and cost-effective model that allows the fast development of tumors when compared to mammal models.[24] Several authors have been using this model for *in vivo* studies. Özcetin *et al.*[26] used the CAM model to study the antiangiogenic effects of imatinib a tyrosine kinase inhibitor used in the treatment of myeloid leukemia[60] while Katrancioglu *et al.*[30] studied the antiangiogenic effects of an levosimendan, an inodilator used for the treatment of severe chronic heart failure.[61] Also, the angiogenic and inflammatory effect of biomaterials was demonstrated by Valdes et *al.* and Zwadlo-Klarwasser et *al.* using CAM model.[29,31]

In vivo CAM experiments were carried out using Hs 578T and RKO cells. At day 9 of embryo development, cells were mixed with Matrigel and placed onto the CAM membrane. After four days, the formed tumors were treated with 0.5 mg mL^{-1} suspensions of DDS and respective parent zeolites. Four days later, the effect of the materials on tumor growth was assessed.

It was verified by Breslin *et al.* that the efficacy of docetaxel was reduced in 3D compared to 2D cultures.[62] Taking this finding in account, in our studies, we used higher concentrations of DDS for *in vivo* studies, since the *in vivo* drug response was expected to be different from the *in vitro* studies. It is known that the toxicity of the systems tested in the CAM could be evaluated in terms of embryo viability, inflammation and neovascularization of the CAM.[63] Thus, from our observations during the time of the assay, it was possible to infer that the concentrations used were nontoxic to the chick embryos, as almost all of them were alive until the end of the treatment and no inflammation was observed in the CAM (Figures 2.3.3 to 2.3.6).

Hs 578T cells formed smaller tumors than RKO cells, as can be observed in Figures 2.3.3 and 2.3.4 for Hs 578T, and Figures 2.3.5 and 2.3.6 for RKO. The mean perimeter of Hs 578T tumors at day 0 (13-day-old of embryo) and day 4 (17-day-old of embryo) show differences between control, parent zeolites and DDS (Figures 2.3.3B and 2.3.4B). From Figures 2.3.3B

and 2.3.4B, as expected, is was observed that untreated tumors (control (CTR) and zeolite conditions) have grown between day 0 and day 4. In the case of the tumors treated with DDS, a difference was observed in the mean perimeter between day 0 and day 4, presenting a decrease in the mean tumor perimeter at day 4, however this difference is not significant when compared with control ($p > 0.05$).

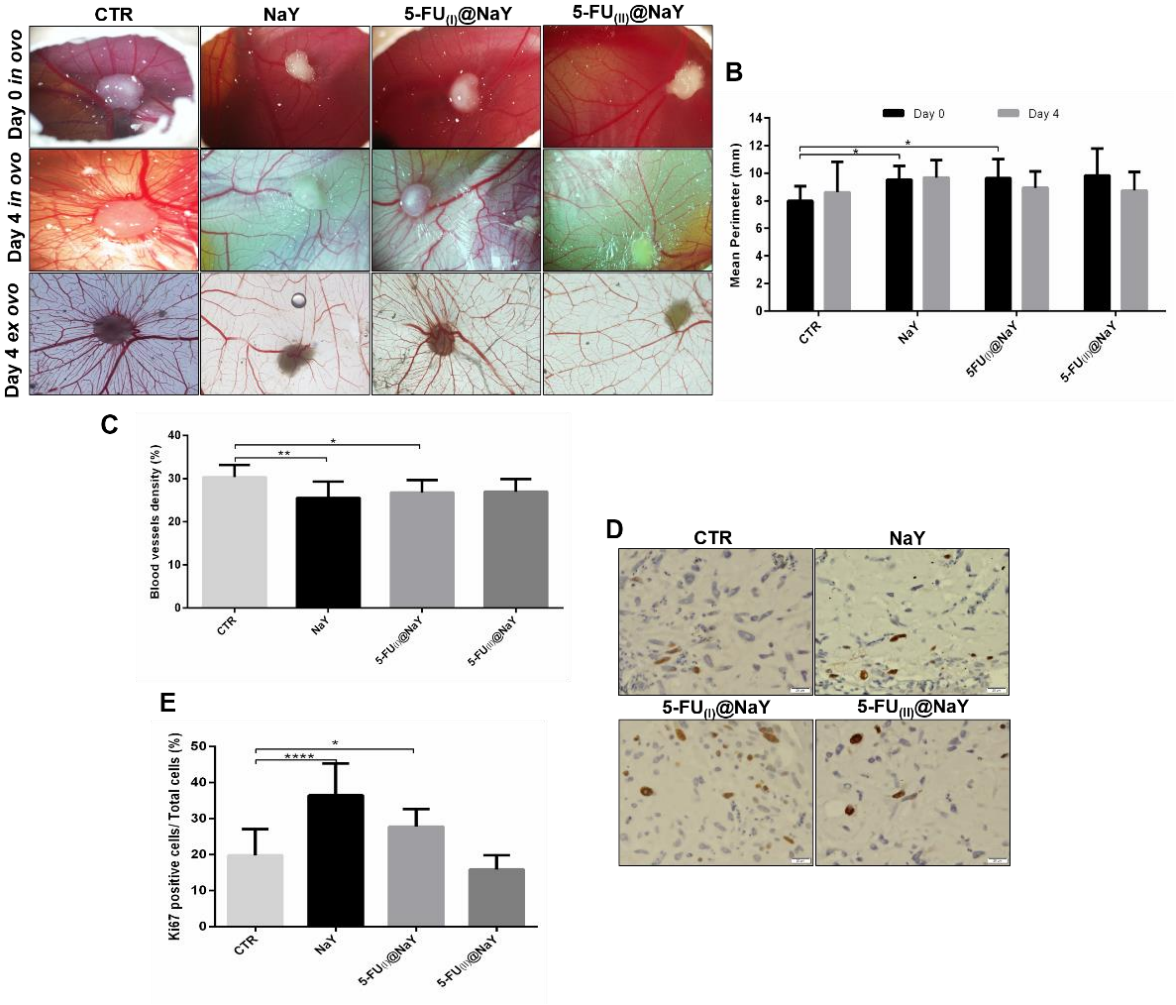

Figure 2.3.3: *In vivo* effect of NaY and DDS in Hs 578T tumor growth and angiogenesis. A) Representative photos of CAM assay *in ovo* (10× magnification) and *ex ovo* (10× magnification) at days 13 and 17 of development. B) Tumor perimeter at different conditions. The results are expressed as mean ± SD of tumor perimeter in day 0 (13 days of development) of treatment and in day 4 (17 days of development) of treatment with zeolite and DDS (0.5 mg mL^{-1}) (NaY group n=9, 5-$FU_{(I)}$@NaY n=12, 5-$FU_{(II)}$@NaY n=11) C) Blood vessel density around the tumors counted *ex ovo* using ImageJ. *$p < 0.05$ and ** $p < 0.01$. D) Representative pictures (400× magnification) of immunohistochemical analysis of Ki67 expression in tumors. E) Percentage of Ki67 positive cells of control compared with zeolite and DDS; data are the mean ± SD. *$p < 0.01$, ****$p < 0.0001$.

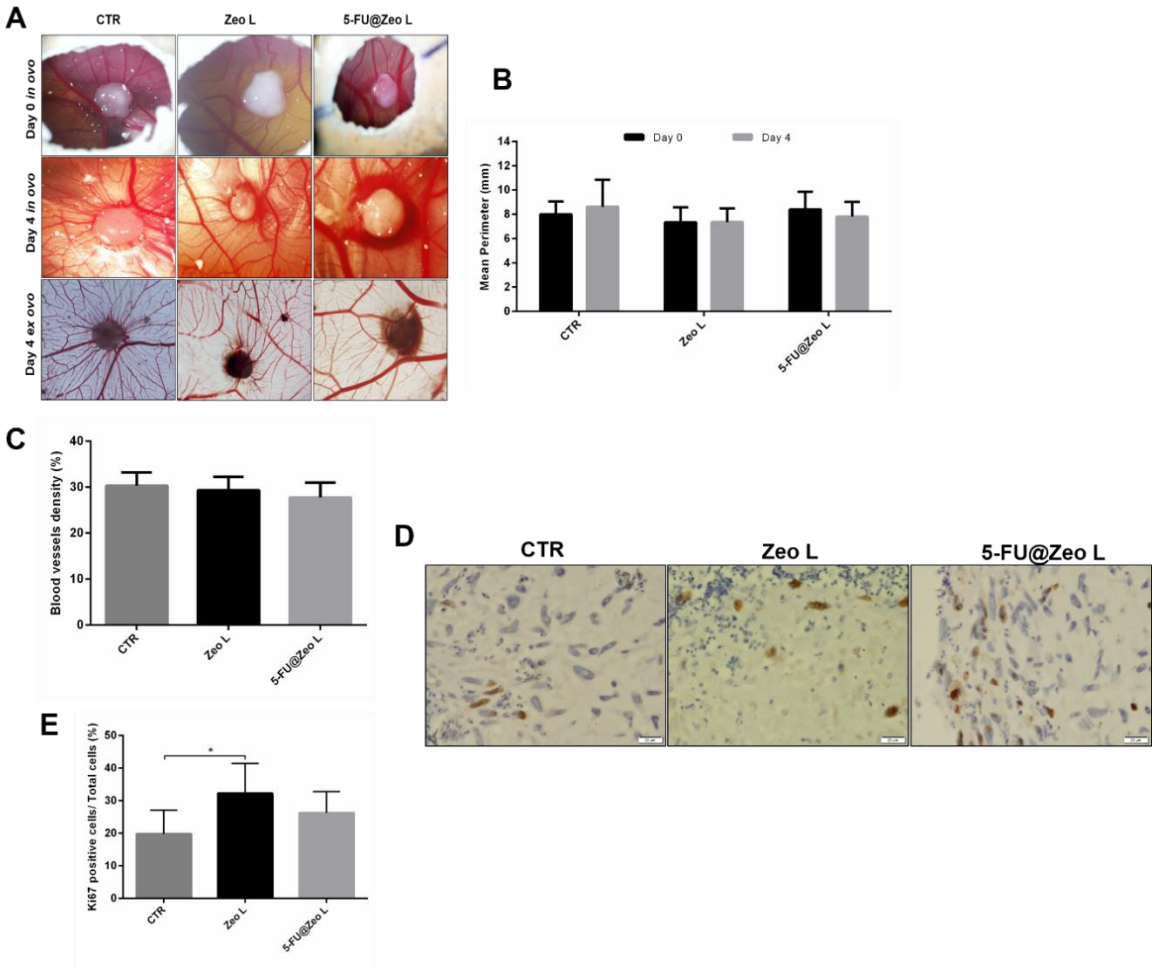

Figure 2.3.4: *In vivo* effect of Zeo L and DDS in Hs 578T tumor growth and angiogenesis. A) Representative photos of CAM assay *in ovo* (10× magnification) and *ex ovo* (10× magnification) at days 13 and 17 of development. B) Tumor perimeter at different conditions. The results are expressed as mean ± SD of tumor perimeter in day 0 (13 days of development) of treatment and in day 4 (17 days of development) of treatment with zeolite and DDS (0.5 mg mL-1) (Zeo L group n=11, and 5-FU@Zeo L group n=10). C) Blood vessel density around the tumors counted *ex ovo* using ImageJ. *p < 0.05 and **p < 0.01. D) Representative pictures (400× magnification) of immunohistochemical analysis of Ki67 expression in tumors. E) Percentage of Ki67 positive cells of control compared with DDS; data are expressed as mean ± SD. ***p < 0.001.

In the case of RKO cells (Figures 2.3.5 and 2.3.6), the mean perimeter at day 0 is in the range of 12.8-14.1 mm and at day 4 is in the range of 14.7-16.9 mm (Figures 2.3.5B and 2.3.6B). For this cell line, there was no apparent reduction in the tumor perimeter after treatment with DDS, even there is an increase in tumor perimeter in some of the conditions between day 0 to day 4 (Figures 2.3.5B and 2.3.6B). From these results, it is observed that there is some effect of the DDS on tumor perimeter only for Hs 578T cells, despite the small reduction observed.

Regarding the blood vessel density in Hs 578T tumors compared with control (Figures 2.3.3C and 2.3.4C), there is a significant decrease for both NaY and 5-FU$_{(l)}$@NaY compared

to control (untreated). In turn, for in RKO tumors (Figure 2.3.5C and 2.3.6C), there was no significant reduction in the density of blood vessels sorrounding the formed tumors upon exposure to the DDS.

Bearing in mind the *in vitro* results, it was expected that the DDS would have some effect in *in vivo* tumor growth since there was a significant effect on cell viability *in vitro*. It is known, that *in vitro* assays are substantially different from the *in vivo* assays since 2D cell culture does not mimic the 3D tumor characteristics in a perfect way, such the interaction with stromal cells and vasculature.[64] This could explain the differences found between *in vitro* and *in vivo* results.

Ki67 is a cell proliferation marker that indicates the proliferation level of a tumor and its sensitivity to certain treatments.[65] The results of the immunohistochemical analysis of Ki67 expression could also explain the different findings for *in vitro* and *in vivo* results (Figures 2.3.3D-E to 2.3.6D-E). Hs 578T cells have a low percentage of Ki67 positive cells, presenting 36.4% in the NaY control group (n=10), 27.8% in 5-FU$_{(I)}$@NaY group (n=11), 15.9% in 5-FU$_{(II)}$@NaY group (n=10), 32.2% in Zeo L control group (n=9) and 26.2% in 5-FU@Zeo L group (n=18) (Figures 2.3.3E and 2.3.4E). Comparing with control (only cells), treatment of the tumor with the DDS seems to not result in a significant reduction of Ki67 positive cells. However, when Ki67 positive cells were compared with the zeolite group, a significant reduction was observed (ANOVA, $p < 0.01$ for 5-FU$_{(I)}$@NaY and $p < 0.0001$ for 5-FU$_{(II)}$@NaY), demonstrating the effect of these DDS on the tumor cell proliferation. On the other hand, treatment with 5-FU@Zeo L did not produce a significant reduction when compared with zeolite group (t-test, $p > 0.05$). The reduction in Ki67 positive cells between zeolite groups and DDS groups could explain the slight differences between the perimeter of Hs 578T tumors at day 0 and day 4 of treatment.

In turn, RKO cells present higher percentage of Ki67 positive cells even in the groups treated with DDS: 73.7% in NaY control group (n=20), 79.3% in 5-FU$_{(I)}$@NaY group (n=17), 66.4% in 5-FU$_{(II)}$@NaY group (n=18), 59.0% in Zeo L control group (n=20) and 63.4% in 5-FU@Zeo L group (n=15) (Figure 2.3.5E and 2.3.6E). Here, there was no reduction observed in the tumor perimeter (Figure 2.3.5B and 2.3.6B). Thus, the results show that RKO cells have higher proliferative activity than Hs 578T cells, with higher Ki67 index. The higher proliferative activity of RKO cells resulted in larger, and probably more dense tumors which might explain the lower response of these tumors to the treatment with DDS. Au *et al*. showed in their work that the penetration of drugs such as paclitaxel and doxorubicin in tumors, is dependent of the drug concentration and cell density, being higher in tumor with low cell density.[66]

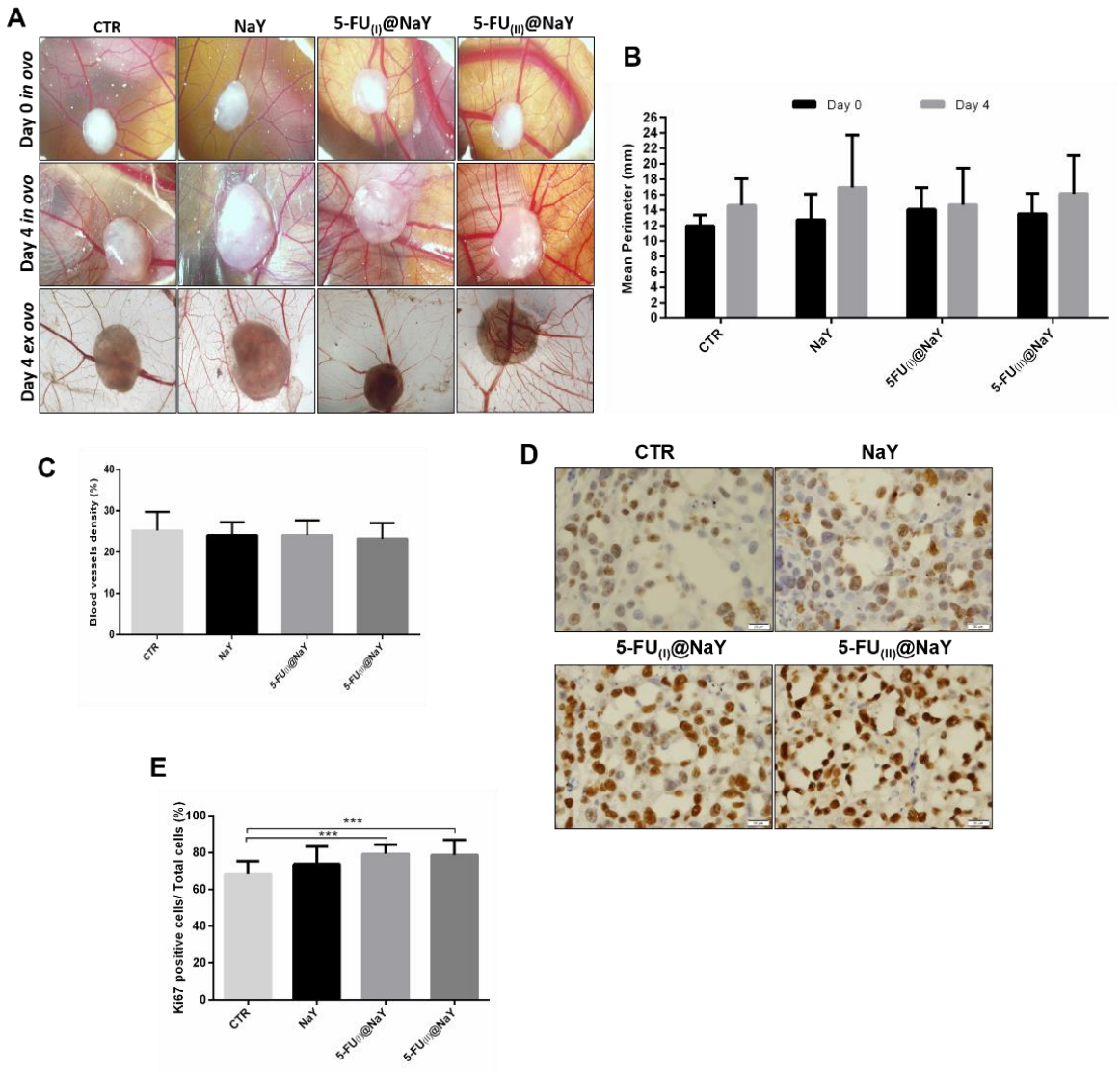

Figure 2.3.5: *In vivo* effect of NaY and DDS in RKO tumor growth and angiogenesis. A) Representative photos of CAM assay *in ovo* (10× magnification) and *ex ovo* (10× magnification) at days 13 and 17 of development. B) Tumor perimeter at different conditions. The results are expressed as mean ± SD of tumor perimeter in day 0 (13 days of development) of treatment and in day 4 (17 days of development) of treatment with zeolites and DDS (0.5 mg/mL) (CTR n=11, NaY n=10, 5-FU$_{(I)}$@NaY n=10, 5-FU$_{(II)}$@NaY n=13). C) Blood vessel density around the tumors counted *ex ovo* using ImageJ. *p < 0.05 and **p < 0.01. D) Representative pictures (400× magnification) of immunohistochemical analysis of Ki67 expression in tumors. E) Percentage of Ki67 positive cells of control compared with DDS; data are expressed as mean ± SD. ***p < 0.001.

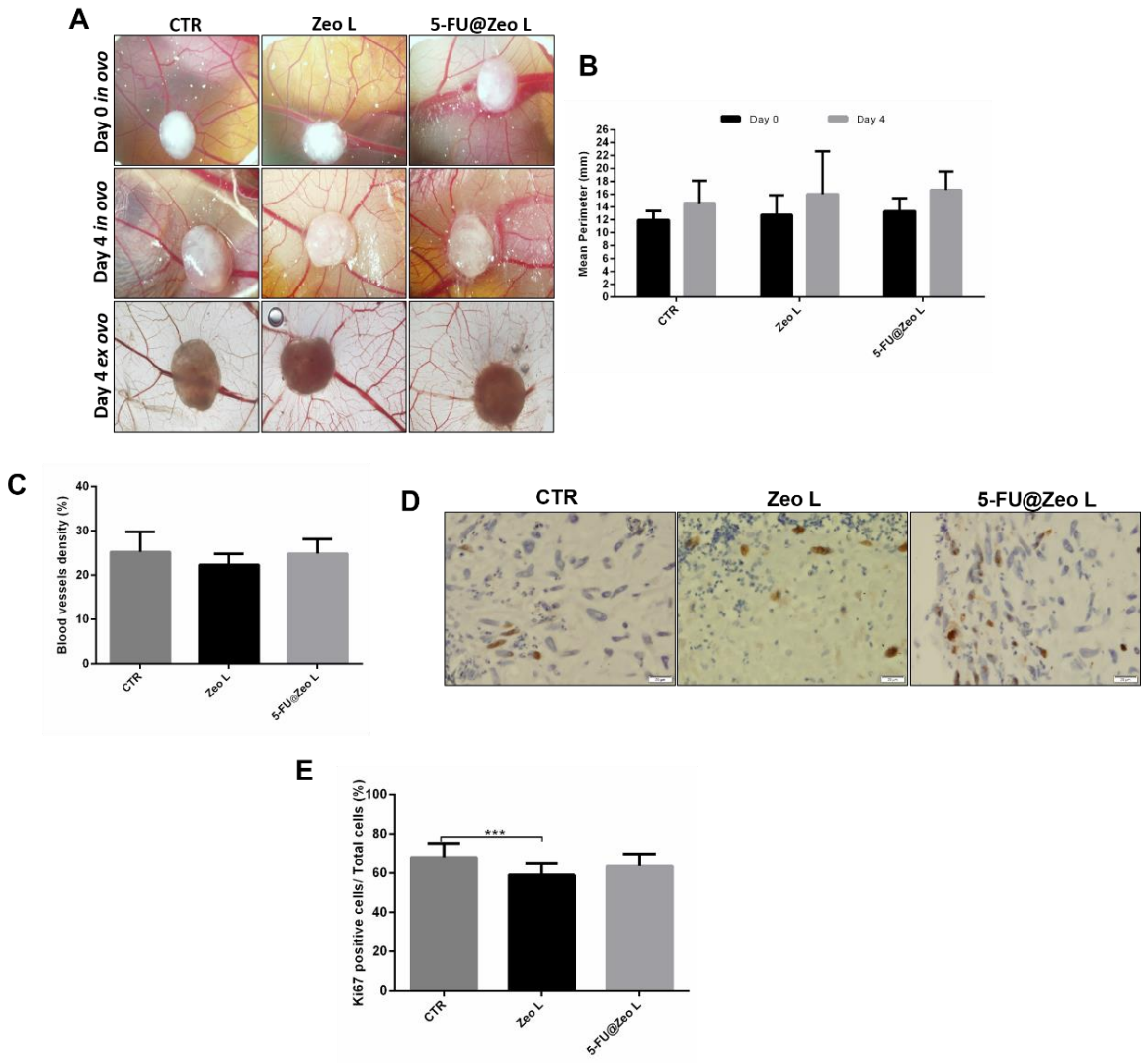

Figure 2.3.6: *In vivo* effect of Zeo L and DDS in RKO tumor growth and angiogenesis. A) Representative photos of CAM assay *in ovo* (10× magnification) and *ex ovo* (10× magnification) at days 13 and 17 of development. B) Tumor perimeter at different conditions. The results are expressed as mean ± SD of tumor perimeter in day 0 (13 days of development) of treatment and in day 4 (17 days of development) of treatment with zeolites and DDS (0.5 mg mL^{-1}) (CTR *n*=11, Zeo L *n*=11, and 5-FU@Zeo L group *n*=9). C) Blood vessel density around the tumors counted *ex ovo* using ImageJ. D) Representative pictures (400× magnification) of immunohistochemical analysis of Ki67 expression in tumors. E) Percentage of Ki67 positive cells of control compared with DDS. Data are expressed as mean ± SD. **p* < 0.05 and ***p* < 0.01. ****p* < 0.001.

The *in vivo* results are not totally in accordance with the *in vitro* results, since the effect of the DDS on cell viability *in vitro* was not confirmed in the *in vivo* model. *In vitro* studies demonstrated higher reduction in cell viability in RKO cells than in Hs 578T cells. However, in the *in vivo* studies some effect of the DDS on Hs 578T tumors was observed, but no effect in RKO tumors. This supports the knowledge that *in vivo* and *in vitro* systems are different and sometimes the results obtained in *in vitro* experiments are not confirmed *in vivo*.[21] It is known that cell cultures do not mimic the biological environment and *in vivo* tumors are more resistant

to drugs than 2D cell cultures, with drug diffusion being around 5- to 10-fold faster in cell cultures than in solid tumors.[66–68] For example, in the work of Sayes *et al.* on silica toxicity *in vitro* and *in vivo*, demonstrated that the toxicity of silica is different *in vitro* and *in vivo*.[69] The extracellular matrix (ECM) present in *in vivo* tumors supports cancer cells and affects cellular functions, being involved in the tumor cell response to different stimuli.[68] The presence of ECM in 3D tumors could influence the effect of drug treatment since it can prevent the diffusion of the drug into cancer cells.[70] The lack of effect of DDS in RKO tumors in the CAM model could be due to the tumor microenvironment and by preventing the capacity of DDS to penetrate deeper into the tumors. It might also be related with the tested concentrations, zeolite structure and cell line used. In a previous study from our group, the effect of DDS based on NaMOR zeolite structure was assessed in glioblastoma cells and the results showed a reduction in tumor size.[35] In the study here reported, were NaY and LTL were used in colorectal and breast cancer cells, which could explain the different results. Thus, results show that the cell type and zeolitic structure influence the effect of the DDS *in vivo*. Thus, the *in vivo* experiments require optimization to ensure that the DDS is able to penetrate the tumor mass.

2.3.4. CONCLUSIONS

In this work, we confirmed that zeolite structures are good carriers for DDS. The obtained DDS show very promising results *in vitro*, with 5-FU potentiation when loaded into zeolites. Additionally, we found that DDS efficacy was lower in CAM model compared to the *in vitro* studies, showing the innate differences between *in vitro* and *in vivo* models. The CAM model revealed to be a good *in vivo* system to be used as a transition between *in vitro* experiments and a more complex *in vivo* model, since it can be used to evaluate of both effect of DDS on tumor growth and angiogenesis. However, there was no significant effect of the DDS in the *in vivo* model, which requires further optimization of the DDS for *in vivo* studies which reflects the complexity of the physiological environment.

2.3.5. REFERENCES

1 S. Zununi Vahed, R. Salehi, S. Davaran and S. Sharifi, Liposome-based drug co-delivery systems in cancer cells, *Mater. Sci. Eng. C*, 2016, **71**, 1327–1341.

2 L. A. Torre, F. Bray, R. L. Siegel, J. Ferlay, J. Lortet-tieulent and A. Jemal, Global Cancer Statistics, 2012, *CA a cancer J. Clin.*, 2015, **65**, 87–108.

3 A. Wicki, D. Witzigmann, V. Balasubramanian and J. Huwyler, Nanomedicine in cancer therapy: Challenges, opportunities, and clinical applications, *J. Control. Release*, 2015, **200**, 138–157.

4 B. B. S. Cerqueira, A. Lasham, A. N. Shelling and R. Al-Kassas, Nanoparticle therapeutics: Technologies and methods for overcoming cancer, *Eur. J. Pharm. Biopharm.*, 2015, **97**, 140–151.

5 M. Estanqueiro, M. H. Amaral, J. Conceição and J. M. Sousa Lobo, Nanotechnological carriers for cancer chemotherapy: The state of the art, *Colloids Surfaces B Biointerfaces*, 2015, **126**, 631–648.

6 Y. S. R. Krishnaiah, V. Satyanarayana, B. Dinesh Kumar and R. S. Karthikeyan, *In vitro* drug release studies on guar gum-based colon targeted oral drug delivery systems of 5-fluorouracil, *Eur. J. Pharm. Sci.*, 2002, **16**, 185–192.

7 M. M. Center, A. Jemal, R. A. Smith and E. Ward, Worldwide Variations in Colorectal Cancer, *CA. Cancer J. Clin.*, 2009, **59**, 366–378.

8 K. Esposito, P. Chiodini, A. Capuano, G. Bellastella, M. I. Maiorino, C. Rafaniello, D. B. Panagiotakos and D. Giugliano, Colorectal cancer association with metabolic syndrome and its components: a systematic review with meta-analysis, *Endocrine*, 2013, **44**, 634–647.

9 S. Hossein Hassanpour and M. Dehghani, Review of cancer from perspective of molecular, *J. Cancer Res. Pract.*, 2017, **4**, 127–129.

10 A. Di Leo, G. Curigliano, V. Diéras, L. Malorni, C. Sotiriou, C. Swanton, A. Thompson, A. Tutt and M. Piccart, New approaches for improving outcomes in breast cancer in Europe, *The Breast*, 2015, **24**, 321–330.

11 L. Hutchinson, Breast cancer: Challenges, controversies, breakthroughs, *Nat. Rev. Clin. Oncol.*, 2010, **7**, 669–670.

12 A. Farinetti, V. Zurlo, A. Manenti, F. Coppi and A. V. Mattioli, Mediterranean Diet and Colorectal Cancer: a systematic review, *Nutrition*, 2017, **43**–**44**, 83–88.

13 A. Goulart, A. Varejão, F. Nogueira, S. Martins, A. Mesquita-Rodrigues, N. Sousa and P. Leão, The influence of metabolic syndrome in the outcomes of colorectal cancer patients, *Diabetes Metab. Syndr. Clin. Res. Rev.*, 2017, **11**, S867–S871.

14 GLOBOCAN, Estimated Cancer Incidence, Mortality and Prevalence Worldwide in 2012, http://globocan.iarc.fr/Pages/fact_sheets_cancer.aspx, (accessed 27 July 2017).

15 L. Bregoli, D. Movia, J. D. Gavigan-Imedio, J. Lysaght, J. Reynolds and A. Prina-Mello, Nanomedicine applied to translational oncology: A future perspective on cancer treatment, *Nanomedicine Nanotechnology, Biol. Med.*, 2016, **12**, 81–103.

16 A. Sousa, K. C. Souza and E. M. B. Sousa, Mesoporous silica/apatite nanocomposite: Special synthesis route to control local drug delivery, *Acta Biomater.*, 2008, **4**, 671–679.

17 Park John W, Liposome-based drug delivery in breast cancer treatment, *Breast Cancer Res.*, 2002, **4**, 95–99.

18 D. A. LaVan, T. McGuire and R. Langer, Small-scale systems for in vivo drug delivery, *Nat. Biotechnol.*, 2003, **21**, 1184–1191.

19 J. I. Hare, T. Lammers, M. B. Ashford, S. Puri, G. Storm and S. T. Barry, Challenges and strategies in anti-cancer nanomedicine development: An industry perspective, *Adv. Drug Deliv. Rev.*, 2017, **108**, 25–38.

20 D. A. Khan, A. Banerji, J. Greiwe and J. A. Bernstein, in *Drug Allergy Testing*, 2018, pp. 85–95.

21 D. Van Den Brand, L. F. Massuger, R. Brock and W. P. R. Verdurmen, Mimicking Tumors: Toward More Predictive *In vitro* Models for Peptide-and Protein-Conjugated Drugs, *Bioconjug. Chem.*, 2017, **28**, 846–856.

22 E. I. Deryugina and J. P. Quigley, Chick embryo chorioallantoic membrane model systems to study and visualize human tumor cell metastasis, *Histochem Cell Biol*, 2008, **130**, 1119–1130.

23 C. Siang Kue, K. Y. Tan, M. L. Lam and H. B. Lee, Chick embryo chorioallantoic membrane (CAM): an alternative predictive model in acute toxicological studies for anti-cancer drugs, *Exp. Anim.*, 2015, **64**, 129–138.

24 D. Ribatti, The chick embryo chorioallantoic membrane as a model for tumor biology, *Exp. Cell Res.*, 2014, **328**, 314–324.

25 A. Vargas, M. Zeisser-Labouèbe, N. Lange, R. Gurny and F. Delie, The chick embryo and its chorioallantoic membrane (CAM) for the in vivo evaluation of drug delivery systems, *Adv. Drug Deliv. Rev.*, 2007, **59**, 1162–1176.

26 A. Özcetin, A. Aigner and U. Bakowsky, A chorioallantoic membrane model for the determination of anti-angiogenic effects of imatinib, *Eur. J. Pharm. Biopharm.*, 2013, **85**, 711–715.

27 D. Ribatti, The chick embryo chorioallantoic membrane (CAM) assay, *Reprod. Toxicol.*, 2017, **70**, 97–101.

28 N. A. Lokman, A. S. F. Elder, C. Ricciardelli and M. K. Oehler, Chick chorioallantoic membrane (CAM) assay as an in vivo model to study the effect of newly identified molecules on ovarian cancer invasion and metastasis, *Int. J. Mol. Sci.*, 2012, **13**, 9959–9970.

29 T. I. Valdes, D. Kreutzer and F. Moussy, The chick chorioallantoic membrane as a novel in vivo model for the testing of biomaterials, *J. Biomed. Mater. Res.*, 2002, **62**, 273–282.

30 N. Katrancioglu, O. Karahan, A. T. Kilic, A. Altun, O. Katrancioglu and Z. A. Polat, The antiangiogenic effects of levosimendan in a CAM assay, *Microvasc. Res.*, 2012, **83**, 263–266.

31 G. Zwadlo-Klarwasser, K. Görlitz, B. Hafemann, D. Klee and B. Klosterhalfen, The chorioallantoic membrane of the chick embryo as a simple model for the study of the angiogenic and inflammatory response to biomaterials, *J. Mater. Sci. Mater. Med.*, 2001, **12**, 195–199.

32 N. Vilaça, A. F. Machado, F. Morais-Santos, R. Amorim, A. Patrícia Neto, E. Logodin, M. F. R. Pereira, M. Sardo, J. Rocha, P. Parpot, A. M. Fonseca, F. Baltazar and I. C. Neves, Comparison of different silica microporous structures as drug delivery systems for *in vitro* models of solid tumors, *RSC Adv.*, 2017, **7**, 13104–13111.

33 I. Braschi, S. Blasioli, L. Gigli, C. E. Gessa, A. Alberti and A. Martucci, Removal of sulfonamide antibiotics from water: Evidence of adsorption into an organophilic zeolite Y by its structural modifications, *J. Hazard. Mater.*, 2010, **178**, 218–225.

34 A. M. Tomoiaga, B. I. Cioroiu, V. Nica and A. Vasile, Investigations on nanoconfinement of low-molecular antineoplastic agents into biocompatible magnetic matrices for drug targeting, *Colloids Surfaces B Biointerfaces*, 2013, **111**, 52–59.

35 O. Martinho, N. Vilaça, P. J. G. Castro, R. Amorim, A. M. Fonseca, F. Baltazar, R. M. Reis and I. C. Neves, *In vitro* and in vivo studies of temozolomide loading in zeolite structures as drug delivery systems for glioblastoma, *RSC Adv.*, 2015, **5**, 28219–28227.

36 N. Vilaça, R. Totovao, E. A. Prasetyanto, V. Miranda-Gonçalves, F. Morais-Santos, R. Fernandes, F. Figueiredo, M. Banõbre-López, A. M. Fonseca, L. De Cola, F. Baltazar and I. C. Neves, Internalization studies on zeolite nanoparticles using human cells, *J. Mater. Chem. B*, 2018, **6**, 469–476.

37 N. Vilaça, R. Amorim, A. F. Machado, P. Parpot, M. F. R. Pereira, M. Sardo, J. Rocha, A. M. Fonseca, I. C. Neves and F. Baltazar, Potentiation of 5-fluorouracil encapsulated in zeolites as drug delivery systems for *in vitro* models of colorectal carcinoma, *Colloids Surfaces B Biointerfaces*, 2013, **112**, 237–244.

38 R. Amorim, N. Vilaça, O. Martinho, R. M. Reis, M. Sardo, J. Rocha, A. M. Fonseca, F. Baltazar and I. C. Neves, Zeolite structures loading with an anticancer compound as drug delivery systems, *J. Phys. Chem. C*, 2012, **116**, 25642–25650.

39 F. Morais-Santos, V. Miranda-Goncalves, S. Pinheiro, A. F. Vieira, J. Paredes, F. C. Schmitt, F. Baltazar and C. Pinheiro, Differential sensitivities to lactate transport inhibitors of breast cancer cell lines., *Endocr. Relat. Cancer*, 2014, **21**, 27–38.

40 M. D. Reid, P. Bagci, N. Ohike, B. Saka, I. Erbarut Seven, N. Dursun, S. Balci, H. Gucer, K.-T. Jang, T. Tajiri, O. Basturk, S. Y. Kong, M. Goodman, G. Akkas and V. Adsay, Calculation of the Ki67 index in pancreatic neuroendocrine tumors: a comparative analysis of four counting methodologies, *Mod. Pathol.*, 2014, **28**, 686.

41 A. Laurinavicius, B. Plancoulaine, A. Laurinaviciene, P. Herlin, R. Meskauskas, I. Baltrusaityte, J. Besusparis, D. Dasevicius, N. Elie, Y. Iqbal, C. Bor and I. O. Ellis, A methodology to ensure and improve accuracy of Ki67 labelling index estimation by automated digital image analysis in breast cancer tissue, *Breast Cancer Res.*, 2014, **16**, R35.

42 I. Braschi, G. Gatti, G. Paul, C. E. Gessa, M. Cossi and L. Marchese, Sulfonamide Antibiotics Embedded in High Silica Zeolite Y: A Combined Experimental and Theoretical Study of Host−Guest and Guest−Guest Interactions, *Langmuir*, 2010, **26**, 9524–9532.

43 M. A. and R. F.-P. and S. I. and J. A. and M. R. I. and J. Santamaría, Sustained release of doxorubicin from zeolite–magnetite nanocomposites prepared by mechanical activation, *Nanotechnology*, 2006, **17**, 4057–4064.

44 S. Egodawatte, S. Dominguez and S. C. Larsen, Solvent effects in the development of a drug delivery system for 5-fluorouracil using magnetic mesoporous silica nanoparticles, *Microporous Mesoporous Mater.*, 2017, **237**, 108–116.

45 A. Datt, E. A. Burns, N. A. Dhuna and S. C. Larsen, Loading and release of 5-fluorouracil from HY zeolites with varying SiO2/Al2O3 ratios, *Microporous Mesoporous Mater.*, 2013, **167**, 182–187.

46 Z. Li, J. Hüve, C. Krampe, G. Luppi, M. Tsotsalas, J. Klingauf, L. De Cola and K. Riehemann, Internalization pathways of anisotropic disc-shaped zeolite L nanocrystals with different surface properties in HeLa cancer cells, *Small*, 2013, **9**, 1809–1820.

47 P. Zhu, N. Zhao, D. Sheng, J. Hou, C. Hao, X. Yang, B. Zhu, S. Zhang, Z. Han, L. Wei and L. Zhang, Inhibition of Growth and Metastasis of Colon Cancer by Delivering 5-Fluorouracil-loaded Pluronic P85 Copolymer Micelles, *Sci. Rep.*, 2016, **6**, 20896–20906.

48 H. Jeon, J. H. Kim, E. Lee, Y. J. Jang, J. E. Son, J. Y. Kwon, T.-G. Lim, S. Kim, J. H. Y. Park, J.-E. Kim and K. W. Lee, Methionine deprivation suppresses triple-negative breast cancer metastasis *in vitro* and in vivo, *Oncotarget*, 2016, **7**, 67223–67234.

49 Z. J. Deng, S. W. Morton, E. Ben-Akiva, E. C. Dreaden, K. E. Shopsowitz and P. T. Hammond, Layer-by-Layer Nanoparticles for Systemic Codelivery of an Anticancer Drug and siRNA for Potential Triple-Negative Breast Cancer Treatment, *ACS Nano*, 2013, **7**, 9571–9584.

50 S. P. Chandran, S. B. Natarajan, S. Chandraseharan and M. S. B. Mohd Shahimi, Nano drug delivery strategy of 5-fluorouracil for the treatment of colorectal cancer, *J. Cancer Res. Pract.*, 2017, **4**, 45–48.

51 L. Nair K, S. Jagadeeshan, S. A. Nair and G. S. V. Kumar, Biological evaluation of 5-fluorouracil nanoparticles for cancer chemotherapy and its dependence on the carrier, PLGA, *Int. J. Nanomedicine*, 2011, **6**, 1685–1697.

52 D. Sahu, G. M. Kannan, M. Tailang and R. Vijayaraghavan, *In vitro* Cytotoxicity of Nanoparticles: A Comparison between Particle Size and Cell Type, *J. Nanosci.*, 2016, **2016**, 1–9.

53 T. Kihara, Y. Zhang, Y. Hu, Q. Mao, Y. Tang and J. Miyake, Effect of composition, morphology and size of nanozeolite on its *in vitro* cytotoxicity, *J. Biosci. Bioeng.*, 2011, **111**, 725–730.

54 X. D. and Q. L. and W. C. and Y. W. and M. W. and H. Z. and Z. Jiao, Nanosized zinc oxide particles induce neural stem cell apoptosis, *Nanotechnology*, 2009, **20**, 115101.

55 I.-Y. Kim, E. Joachim, H. Choi and K. Kim, Toxicity of silica nanoparticles depends on size, dose, and cell type, *Nanomedicine Nanotechnology, Biol. Med.*, 2015, **11**, 1407–1416.

56 S. Grund, T. Doussineau, D. Fischer and G. J. Mohr, Mitoxantrone-loaded zeolite beta nanoparticles: Preparation, physico-chemical characterization and biological evaluation, *J. Colloid Interface Sci.*, 2012, **365**, 33–40.

57 C. Murugan, K. Rayappan, R. Thangam, R. Bhanumathi, K. Shanthi, R. Vivek, R. Thirumurugan, A. Bhattacharyya, S. Sivasubramanian, P. Gunasekaran and S. Kannan, Combinatorial nanocarrier based drug delivery approach for amalgamation of anti-tumor agents in breast cancer cells: an improved nanomedicine strategy, *Sci. Rep.*, 2016, **6**, 34053.

58 S. Tummala, M. N. Satish Kumar and A. Prakash, Formulation and characterization of 5-Fluorouracil enteric coated nanoparticles for sustained and localized release in treating colorectal cancer, *Saudi Pharm. J.*, 2015, **23**, 308–314.

59 M. N. Patel, S. Lakkadwala, M. S. Majrad, E. R. Injeti, S. M. Gollmer, Z. A. Shah, S. H. S. Boddu and J. Nesamony, Characterization and Evaluation of 5-Fluorouracil-Loaded Solid Lipid Nanoparticles Prepared via a Temperature-Modulated Solidification Technique, *AAPS PharmSciTech*, 2014, **15**, 1498–1508.

60 M. Miura, Therapeutic drug monitoring of imatinib, nilotinib, and dasatinib for patients with chronic myeloid leukemia., *Biol. Pharm. Bull.*, 2015, **38**, 645–654.

61 M. S. Nieminen, S. Fruhwald, L. M. A. Heunks, P. K. Suominen, A. C. Gordon, M. Kivikko and P. Pollesello, Levosimendan: current data, clinical use and future development, *Hear. Lung Vessel.*, 2013, **5**, 227–245.

62 S. Breslin and L. O'Driscoll, The relevance of using 3D cell cultures, in addition to 2D monolayer cultures, when evaluating breast cancer drug sensitivity and resistance, *Oncotarget*, 2016, **7**, 45745–45756.

63 D. Ribatti, The chick embryo chorioallantoic membrane (CAM). A multifaceted experimental model, *Mech. Dev.*, 2016, **141**, 70–77.

64 M. A. Skowron, A. Sathe, A. Romano, M. J. Hoffmann, W. A. Schulz, G. A. van Koeveringe, P. Albers, R. Nawroth and G. Niegisch, Applying the chicken embryo chorioallantoic membrane assay to study treatment approaches in urothelial carcinoma, *Urol. Oncol. Semin. Orig. Investig.*, 2017, **35**, 544.e11-544.e23.

65 T. Scholzen and J. Gerdes, The Ki-67 protein: From the known and the unknown, *J. Cell. Physiol.*, 2000, **182**, 311–322.

66 J. L.-S. Au, S. H. Jang, J. Zheng, C.-T. Chen, S. Song, L. Hu and M. G. Wientjes, Determinants of drug delivery and transport to solid tumors, *J. Control. Release*, 2001, **74**, 31–46.

67 L. G. Griffith and M. A. Swartz, Capturing complex 3D tissue physiology *in vitro*, *Nat. Rev. Mol. Cell Biol.*, 2006, **7**, 211–224.

68 V. Stankevicius, G. Vasauskas, R. Noreikiene, K. Kuodyte, M. Valius and K. Suziedelis, Extracellular Matrix-dependent Pathways in Colorectal Cancer Cell Lines Reveal Potential Targets for Anticancer Therapies., *Anticancer Res.*, 2016, **36**, 4559–4567.

69 C. M. Sayes, K. L. Reed and D. B. Warheit, Assessing Toxicity of Fine and Nanoparticles: Comparing *In vitro* Measurements to In Vivo Pulmonary Toxicity Profiles, *Toxicol. Sci.*, 2007, **97**, 163–180.

70 R. Januchowski, P. Zawierucha, M. Ruciński, M. Nowicki and M. Zabel, Extracellular Matrix Proteins Expression Profiling in Chemoresistant Variants of the A2780 Ovarian Cancer Cell Line, *Biomed Res. Int.*, 2014, **2014**, 365867.

CHAPTER 3

SYNTHESIS, CHARACTERIZATION AND *IN VITRO* VALIDATION OF MAGNETIC NaY ZEOLITE WITH T_2-MRI PROPERTIES[4]

Magnetic nanoparticles (MNPs) have been gaining a significant importance as building blocks to form more complex nanostructures due to the multifunctional performance enabled by their magnetic character, i.e. magnetic resonance imaging (MRI) and magnetic hyperthermia (MH). This study focusses on the development of a magnetic zeolite nanocomposite (MZNC) as a suitable platform towards the design of a theranostic system. In addition to the well-known drug encapsulation properties of the zeolite structures, in this work we explored their ability to act as T_2-MRI contrast agents in magnetic resonance imaging (MRI) when magnetic nanoparticles are incorporated in their structure. MZNC was prepared by a simple one-pot colloidal chemistry route based on the co-precipitation of Fe(II) and Fe(III) salts in an aqueous solution containing NaY zeolite (see graphical abstract below).

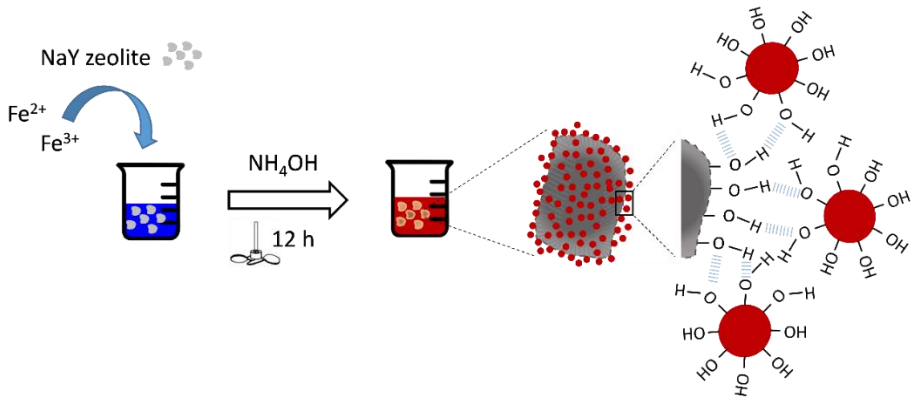

The as-synthesized samples were carefully characterized in terms of morphological, structural and magnetic properties. Results confirm the formation of magnetic assemblies with microporous structure and superparamagnetic behavior, based on the combination of the structural properties from the zeolite and the magnetic performance of the magnetite

[4] **N. Vilaça**, J. Gallo, R. Fernandes, F. Figueiredo, A. M. Fonseca, F. Baltazar, I. C. Neves, M. Bañobre-López, Synthesis, characterization and *in vitro* validation of magnetic NaY zeolite with T_2-MRI properties, *submitted*.

nanoparticles. TEM analysis evidenced the cell internalization of MZNC particles by human breast cancer cells and their accumulation in the cytoplasm, whereas cytotoxicity assays in both tumoral breast and non-tumoral mammary cell lines showed that MZNC was non-toxic at the highest concentration tested. Finally, the capability of MZNC to act as imaging probe in MRI was confirmed and validated *in vitro* at a clinical field of 3T, resulting in an enhanced dark contrast compared to control cells. The combination of the well-known high load encapsulation efficiency of NaY zeolite structures and the additional MRI contrast enhancement provided by their innovative assembly with biocompatible magnetite nanoparticles constitutes a step forward towards the design of inorganic hybrids as image-drug delivery systems combining thermo- and chemotherapeutic effects.

3.1. INTRODUCTION

The application of nanotechnology to medicine, nanomedicine, is expected to bring many advances to health by improving diagnostics and therapeutics of cancer.[1–3] Nanomaterials can be used in many applications such as bioimaging, diagnostic technology, and drug delivery.[4–8] So far, numerous nanomaterials have been exploited in cancer nanomedicine including, polymers,[9,10] lipids,[11,12] mesoporous silica nanoparticles,[13–16], zeolite nanoparticles[17–19] and magnetic nanoparticles (MNPs).[20–23] In particular, superparamagnetic iron oxide nanoparticles (SPIONs) are especially interesting in biomedicine due to their unique properties, such as biocompatibility and non-toxicity, tunable particle sizes and morphologies, ability to be functionalized with biological ligands and excellent magnetic properties that enable multiple diagnosis and therapy applications, such as magnetic resonance imaging (MRI), targeted drug delivery and alternating magnetic field (AMF)-based hyperthermia treatments.[24,25]

The combination of MNPs with other materials to obtain hybrid composites that possess the advantages of both materials counterparts has been recently explored. In this sense, magnetic hybrid nanocomposites and inorganic assemblies have been found to open new perspectives for biomedical and environmental applications.[26] For example, iron oxides nanoparticles were combined with polymeric or lipidic structures to obtain multifiunctional materials with therapeutic and/or imaging properties. Bañobre-López and co-workers[27] incorporated magnetite nanoparticles into different biocompatible and bioresorbable materials to fabricate magnetic scaffolds for magnetic hyperthermia-based bone tissue engineering, whereas Grillo *et al*[28] fabricated polycaprolactone nanocapsules containing SPIONs that provided the final sub-micrometer nanocomposites with both MRI and magnetic hyperthermia (MH) performance. On the other hand, zeolite-type structures (crystalline microporous aluminosilicates) have been widely studied as adsorbents and catalyst carriers due to their unique adsorption properties and their ion exchange capacity. Several synthesis procedures have been proposed to incorporate an extra iron framework into zeolites, i.e. liquid/solid ion exchange or chemical vapor deposition, which led to the coexistence of several ion species inside the pores or on the surface (i.e. Fe ions, Fe_xO_y clusters, Fe_2O_3 nanoparticles).[29,30] Iron-containing zeolites have been extensively studied for their outstanding catalytic activity (selective reduction of nitrogen oxides by NH_3,[30] low-temperature methane hydroxylation,[31] and chemical oxidation of methyl tert-butyl ether (MTBE) in water with H_2O_2.[32,33]). This excellent catalytic activity is mainly attributed to the activation of the extra Fe-lattice attached to the ion-exchange sites derived from a constrained coordination geometry enforced by the zeolite lattice.[31,33] The extrapolation of zeolites structures to the biomedical field has been recently arisen from their ability to physically adsorb hydrophobic molecules and their stability in biological environments. Zeolites present high surface areas and regular channels or cages,

forming a network of pores. In this framework, a high variety of biomolecules can be entrapped, such as fluorescent dyes or drugs, making zeolites good candidates as drug encapsulation and delivery carriers.[34–37] As an example, hydrophobic chemotherapeutic drugs like 5-fluorouracil, temozolomide and alpha-cyano-4-hydroxy-cinnamic acid have been successfully encapsulated in different zeolite structures in previous works from Vilaça *et al*.[18,19,38] The incorporation of MNPs in zeolites has been already explored to develop magnetically controllable composites with optical properties.[39] Also, the effect of this magnetic functionalization on the catalytic activity of zeolites has been also explored in environmental applications.[40–42] However, the translation of these achievements and the applicability of magnetic zeolites in the biomedical field is still in a very early stage. To the best of our knowledge, there are only a few recent works dealing with the incorporation of MNPs in zeolites for biomedical application, mainly focused on the drug encapsulation properties of the zeolite structures[36] and the capability of the MNPs to act as magnetic actuators and trigger a drug release by MH.[43]

In this work we intend to provide the NaY zeolite with extra biomedical capabilities by assembling *in situ* synthesized magnetite nanoparticles, thus profiting from the drug encapsulation properties of the microporous zeolite structure and the magnetic properties of the superparamagnetic iron oxide nanoparticles (SPIONs). The inorganic assembly of these two materials in one single hybrid nanocomposite constitutes a step forward towards the design of suitable novel biomaterials with theranostic properties, enabling diagnosis and therapy technologies such as MRI, MH and drug delivery. Special focus was particularly paid on the ability of the final magnetic assemblies to generate a MRI contrast enhancement. SPIONs emerged as a safer alternative to the Gd chelates, which still exclusively constitute the contrast agents (CAs) used in the clinic nowadays. Unlike Gd-based CAs that offer a bright contrast (T_1-CAs), SPIONs induce a dark contrast (T_2-CAs) and are the gold star materials in nanoparticulated T_2-CAs development for clinical MRI. With this purpose, we developed a simple wet-chemistry approach for the magnetization of NaY zeolite. The resultant magnetic zeolite nanocomposite (MZNCs) were thoroughly characterized, and their effect on breast cancer (MCF-7 and Hs 578T) and normal (MCF-10) cells was studied. On the one hand, the physiochemical characterization results showed that the magnetization of the zeolite structure was successfully achieved, whereas cell viability assays indicated that the as-synthesized MZNCs were non-toxic to the cells. Most of these nanoparticles were observed to be internalized by cells and accumulate in the cytoplasm. On the other hand, the capability of MZNCs to act as T_2-MRI probes and generate a dark contrast enhancement was validated *in vitro*. These results are highly promising and invite to the design and optimization of this new generation of theranostic materials as an approach towards image-guided therapy and monitoring of the response to treatment.

3.2. EXPERIMENTAL

3.2.1. CHEMICAL AND BIOLOGICAL REAGENTS

The reagents used in this work were analytical grade and used as received without further purification. NaY zeolite (CBV100, faujasite structure, Si/Al = 2.83 and 700 nm)) in powder form was acquired from Zeolyst International. Iron(III) chloride hexahydrate ($FeCl_3.6H_2O$), iron(II) chloride tetrahydrate ($FeCl_2.4H_2O$) and ammonium hydroxide (NH_4OH, 28%) were obtained from Sigma Aldrich.

Dulbecco's Modified Eagle's Medium (DMEM (1x)), Dulbecco's Modified Eagle's Medium F12 (DMEM/F12 (1:1)), Fetal Bovine Serum (FBS), Penicillin-Streptomycin (P/S) were purchased from Gibco. Human insulin solution, cholera toxin and hydrocortisone were acquired from Sigma Aldrich and epidermal growth factor (EGF) from Peprotech. The human breast cancer cell lines MCF-7 and Hs 578T were obtained from ATCC (American Type Culture Collection) and the MCF-10 epithelial mammary cell line was kindly provided by Dra. Lígia Rodrigues (CEB, University of Minho, Portugal).

3.2.2. PREPARATION OF MZNCS

MZNCs were synthetized by basic co-precipitation of Fe(II) and Fe(III) ions in the presence of commercial NaY zeolite nanoparticles. First, magnetite (Fe_3O_4) nanoparticles were prepared by slight modification of an elsewhere reported procedure.[44] Briefly, water (20 mL, milliQ, 18 MΩ cm) was purged by bubbling nitrogen (N_2) gas for 30 min. Then, aqueous solutions of $FeCl_3.6H_2O$ (1.74 g) and $FeCl_2.4H_2O$ (0.64 g) were prepared and mixed. Next, NaY zeolite (0.50 g) was added to the resulting ferrous solution and mixed vigorously under mechanical stirring for 10 min. Then, 40 mL of NH_4OH was added to the dispersion, which immediately turned into brown-black, and magnetic stirring was kept overnight. After, the dispersion was left to settle for 1 h, purified twice with water and three times with water/acetone (1:1) and recovered by magnetically separation and centrifugation. Finally, the sample was dried at 65 °C for 24 h.

3.2.3. CHARACTERIZATION OF MZNCS

The structural phase of the magnetic zeolite nanocomposite was analyzed by X-ray diffraction (XRD) using a PANanalytical X Pert PRO MRD diffractometer with a PIXcel 3D detector, set at accelerating voltage of 45 kV, and tube current of 40 mA at room temperature (RT). Fourier transform infrared (FTIR) analysis was performed using an ABB-FLTA 2000

covering 4000-500 cm^{-1} range at RT. For each sample, 32 scans were collected with a wavenumber resolution of 8 cm^{-1}. Morphological analysis of the samples was performed by transmission electron microscopy (TEM) using a JEOL 2100 working at 200 keV and scanning electron microscopy (SEM) using a Quanta FEG 650 (FEI). For TEM analysis, a drop of an aqueous dispersion of the nanocomposite was placed onto a 400-mesh copper grid coated with carbon film and dried under vacuum before being visualized into the microscope. For SEM analysis, a drop of material dispersion was placed onto a silicon wafer and left to dry under vacuum before being observed. Iron concentration in the sample was determined by inductively coupled plasma optical emission spectrometry (ICP-OES) (ICPE-9000, Shimadzu). For this, 7.4 µL of sample dispersion were digested with 1 mL of 37% HCl overnight. Then, the total volume was adjusted to 100 mL by adding MilliQ water prior to ICP analysis. The magnetic properties of MZNCs were characterized using a superconducting quantum interference device (SQUID) magnetometer (Quantum Design, USA). Surface areas and pore volumes of the samples were measured with an autosorb iQ2 equipment (Quantachrome) using N_2 as the adsorbate at -196 °C. For each sample, approximately 60 mg of sample was degasified overnight at 120 °C. After this first step, an adsorption-desorption isotherm was measured, and values were used to calculate the surface area.

3.2.4. CELL CULTURE AND CELL VIABILITY ASSESSMENT

MCF-7 breast cancer cells and MCF-10 epithelial mammary cells were cultivated at 37 °C with 5 % CO_2 in DMEM (1x) supplemented with 10 % of FBS and 1 % of P/S, and in DMEM/F12 (1:1) containing 5 % FBS, 1 % P/S and supplemented with 20 ng mL^{-1} of EGF, 100 ng mL^{-1} of cholera toxin, 0.01 mg mL^{-1} of insulin and 500 ng mL^{-1} of hydrocortisone, respectively.

Cell toxicity of MZNCs was evaluated measuring the cellular protein content by the sulforhodamine B (SRB) assay.[45,18] To this end, MCF-7 and Hs 578T cells (7000 cells per well) and MCF-10 cells (5000 cells per well) were plated in 96-well plates and allowed to adhere for 24 h prior to use. The cells were incubated for 24 and 48 h with increasing concentrations of MZNCs solutions (25 – 100 µg mL^{-1}), which were prepared in fresh medium without FBS.

Statistical significance for each treatment compared to the control was done using one-way analysis of variance (ANOVA) followed by Dunnett's test (GraphPad Prism 6® software) where *p*-value < 0.05 was considered as statistically significant. All results are expressed as mean ± SD of at least three independent assays.

3.2.5. MZNCS INTERNALIZATION

Hs 578T and MCF-10 cells were plated in 12-well plates at a density of 1.5×10^5 and 1.7×10^5, respectively and allowed to adhere for 24 h. Then, the cells were exposed to 50 µg mL^{-1} of MZNCs for 4 h. Cells were washed 3 times with PBS, harvested by trypsinization, centrifuged and resuspended in fresh medium. Subsequently, cells were fixed using 2.5% glutaraldehyde (Electron Microscopy sciences, Hatfield, USA) and 2% paraformaldehyde (Merck, Darmstadt, Germany) in cacodylate buffer 0.1 M (pH 7.4), dehydrated and then embedded in epon resin (TAAB, Berks, England). The resulting blocks were cut using a RMC Ultramicrotome (PowerTome, USA) in ultrathin sections and stained with uranyl acetate substitute and lead citrate and then observed with a JEOL JEM 1400 TEM (Tokyo, Japan), equipped with a CCD digital camera Orious 1100W.

3.2.6. MAGNETIC RESONANCE IMAGING

Magnetic resonance imaging (MRI) was performed in a 3T horizontal bore MR Solutions Benchtop MRI system equipped with 48 G/cm actively-shielded gradients. To image the samples, a 56-mm diameter quadrature birdcage coil was used in transmit/receive mode. For the phantom imaging, different samples at a concentration of 50 µg mL^{-1} were incubated with Hs 578T cells for 4 h. After incubation, the cells were washed 3 times with PBS 1x, trypsinized and centrifuged to form a pellet. This pellet was resuspended in 50 µL of warm 2 % agar and pipetted into PCR microtubes. These microtubes were immediately immersed in ice/water for 30 min to solidify the gel, and then were stored in the fridge until imaging analysis. MRI images of the phantoms were acquired with an image matrix 256 x 248, FOV 60 x 60 mm, 3 slices with a slice thickness of 1 mm and 0.1 mm slice gap. For T_2-weighted imaging, fast spin echo (FSE) sequences with the following parameters were used: T_E = 68 ms, T_R = 4800 ms, N_A = 5, A_T = 12m 24s. Image analysis was performed using ImageJ software (http://imagej.nih.gov/ij).

3.3. RESULTS AND DISCUSSION

3.3.1. PREPARATION AND CHARACTERIZATION OF MZNCS

The hybrid MZNCs were prepared through the chemical coprecipitation of an aqueous mixture of Fe(II) and Fe(III) chloride salts (Fe^{2+}/Fe^{3+} molar ratio equal to 0.5) at basic pH containing commercial zeolite NaY nanoparticles. The faujasite structure choice was based on previous results that proved the biocompatibility and non-toxicity of the NaY zeolite against human cells, as well as on their excellent properties to encapsulate and deliver hydrophobic

anti-cancer drugs.[17,36,46] NaY zeolite was used in order to avoid batch-to-batch irreproducibility issues[47] and guarantee the same physicochemical properties in all the materials replicas prepared.

The *in situ* synthesized magnetic nanoparticles were characterized by powder XRD (Figure 3.1A). The position and relative intensity of the reflections indicated the formation of a single phase of magnetite (Fe_3O_4) with inverse spinel structure (crystallographic open database – COD–, pattern code 96-900-2318). The D_{hkl} was calculated by the Debye-Scherrer formula from the full width at half-maximum of the two most intense peaks in the whole measured range of 2θ, indicating an average crystallite size of 6.6 ± 0.9 nm. This value was close to the particle size measured from TEM observations (d = 4.7 ± 0.2 nm, see Figure 3.2) and confirmed the magnetite nanoparticles as small single crystals. The inorganic assembly between the NaY zeolite structure and the *in situ* synthesized magnetite nanoparticles relies on the electrostatic attraction mediated by intermolecular hydrogen-bond formation between the hydroxyl groups at the surface of the iron oxide nanoparticles and those in the NaY zeolite particles. The grafting of MNPs onto the surface of a zeolite structure has been also observed in pristine L zeolites.[39]

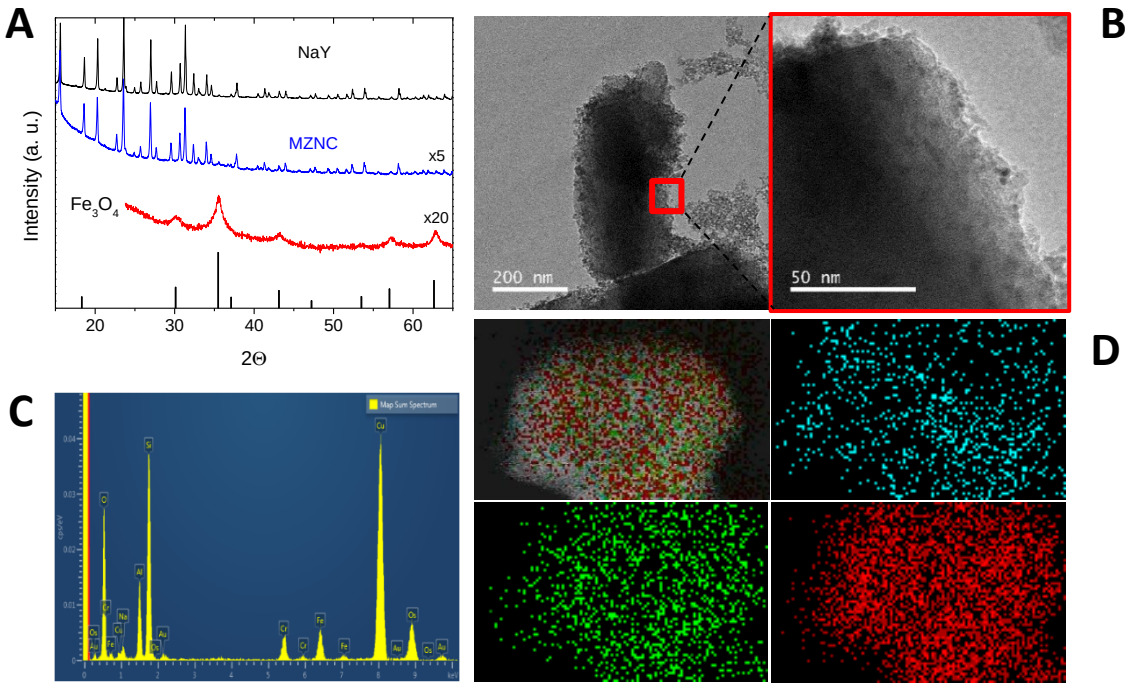

Figure 3.1: A) Powder XRD patterns of magnetite nanoparticles (red), NaY zeolite crystals (black) and MZNC particles (blue); B) TEM images of a MZNC particles; C) Energy-dispersive X-ray spectroscopy (EDS) microanalysis on the MZNC particle shown in B; D) EDS compositional maps of a MZNC crystal.

Figure 3.1A also shows the XRD patterns from the NaY zeolite and the magnetic zeolite, MZNC. The diffraction pattern of the NaY zeolite showed the main characteristic peaks at 2θ angles in the range from 11 to 35º typical of the Miller peaks of the faujasite crystal structure.[48] After co-precipitation of the iron salts in presence of the NaY zeolite and the subsequent assembly between the *in situ* formed magnetite nanoparticles and the NaY zeolite particles, the XRD pattern of the resulting magnetic nanocomposite showed the main characteristic peaks at exactly the same position and with the same intensity as those observed in the parent zeolite pattern. This discards the presence of secondary phases as impurities and confirms the preservation of the faujasite crystal structure of the NaY zeolite during the magnetic nanocomposite formation. However, the presence of magnetite nanoparticles in the final magnetic zeolite is not clearly evidenced by XRD, as the diffraction intensity coming from the relative amount of the magnetite phase is too low compared to that of the zeolite and the corresponding reflections were not distinguished. This has been also observed in magnetic imidazolate frameworks and was attributed to the stronger XRD intensity of the hetero-nanostructures than that of nanocrystals by several orders of magnitude.[42] Additionally, in this particular nanocomposite the main reflections of NaY zeolite overlap the most intense diffractions peaks of magnetite, which coincide at the same 2θ positions.

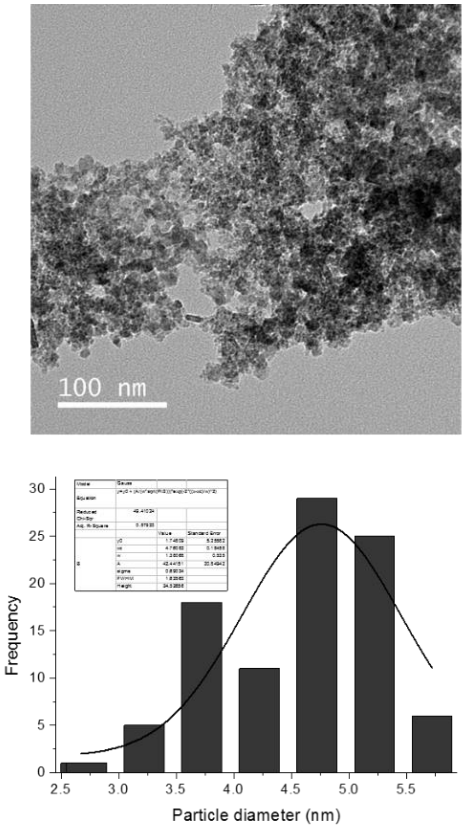

Figure 3.2: (Upper) TEM micrograph of the as-synthesized magnetite nanoparticles; (lower) Particle size distribution obtained from the TEM picture above and fitted to a Gaussian function.

The presence of magnetite nanoparticles in the final magnetic zeolite nanocomposite was evidenced by TEM analysis (Figure 3.1B). TEM images clearly show the presence of magnetic nanoparticles as dark spots grafted to the zeolite nanoparticles' surface. Both morphology and average particle size of the magnetite nanoparticles remained unchanged after their assembly with the zeolite structure. Despite the number of washings carried out during the sample purification protocol, still some small amount of isolated magnetite nanoparticles can be observed. Images also evidence a homogenous and significant coverage of the zeolite nanoparticles' surface with magnetite nanoparticles. However, although the porous structure of the zeolite particles is clearly distinguished (mainly close to the surface, see Figures 3.1B and 3.3A) and the presence of some dark spots could presumably be attributed to the internal rather than superficial localization of magnetite nanoparticles, the presence of magnetite nanoparticles inside the porous is not conclusive from the images.

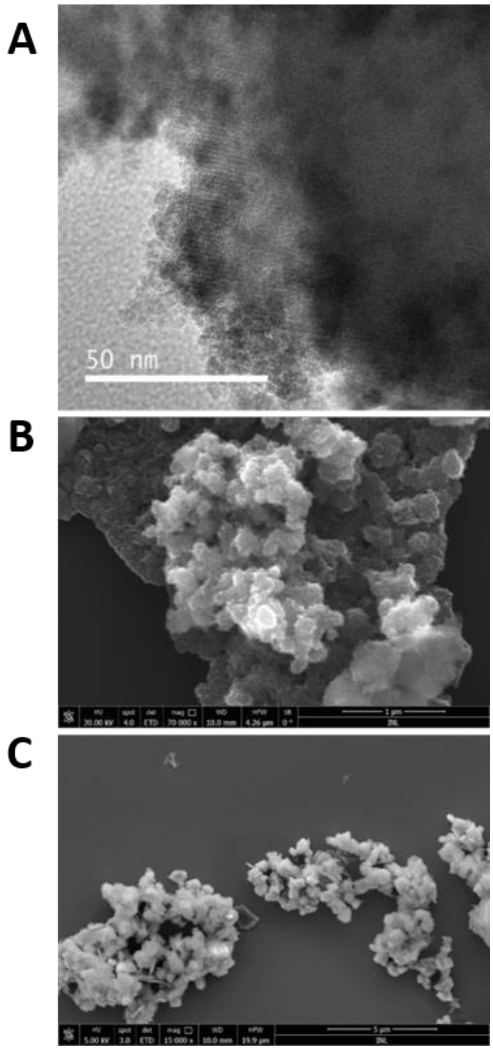

Figure 3.3: A) TEM image of a MZNC particle in which the porous structure is clearly observed. Fe_3O_4 NPs are also observed to be grafted to the zeolite particle surface B) SEM image of MZNC particles. C) SEM image of non-magnetic NaY zeolite particles.

SEM images also confirmed a homogenous distribution of magnetite nanoparticles around the zeolite particles, as deduced by the overall observed rough particle surface of the magnetic nanocomposite crystals, which is very likely indicative of the grafting of magnetic nanoparticles on the zeolite surface and which is not appreciated in the SEM image corresponding to the parent NaY zeolite (see Figures 3.3B and 3.3C). Energy-dispersive X-ray spectroscopy (EDS) microanalysis unequivocally detected the presence or Fe on the NaY zeolite particles' surface and the compositional elemental maps further proved a random distribution of Fe around the NaY zeolite particles (Figures 3.1C and 3.1D, respectively), evidencing a homogeneous coating with magnetite nanoparticles. A high density of Al and Si is also observed, as they constitute the main compositional elements in the zeolite structure.

The FTIR spectra of magnetite, NaY zeolite and MZNCs were recorded between 4000 and 500 cm^{-1} (Figure 3.4). The formation of magnetite nanoparticles and their anchoring to the NaY zeolite structure was mainly evidenced by the band appearing at 600 cm^{-1} in the MZNCs spectrum, observed in the region where the zeolite does not absorb and that is ascribed to the intrinsic stretching vibration of the characteristic Fe-O bond of magnetite. In the magnetite spectrum this absorption band is slightly shifted to lower wavenumbers 580 cm^{-1}, thereby confirming the presence of magnetite nanoparticles and their interaction with the zeolite structure.[36,49] The additional bands at 1633 and 3400 cm^{-1} in the magnetite spectrum were assigned to the stretching vibration of the O-H hydroxyl groups.[50] MZNCs spectrum presents characteristic bands of the zeolite structure at 547 cm^{-1} and 970 cm^{-1}, which are related to the double ring and TO_4 asymmetric stretch (T= Si, Al).[36] In the same MZNCs spectrum, the ν(O–H) stretching vibration at 3410 cm^{-1} and the δ(O–H) deformation band at 1650 cm^{-1} are attributed to the surface hydroxyl groups (terminal silanol groups) and the physisorbed water, while bands in the spectral region between 1250 and 500 cm^{-1} correspond to the lattice vibrations.[45] Importantly, new bands at 3200 and 1400 cm^{-1} are observed in the MZNCs (not visible in the NaY zeolite spectrum) that could be attributed to inter and intramolecular hydrogen bonding, pointing to the formation of hydrogen bonds as the main driving force that governs the interaction between the *in situ* formed magnetite nanoparticles and the zeolite particles.[36] Figure 3.5 show a scheme of the MZNCs preparation and the mechanism of interaction proposed between the *in situ* formed MNPs and zeolite nanoparticles' surface.

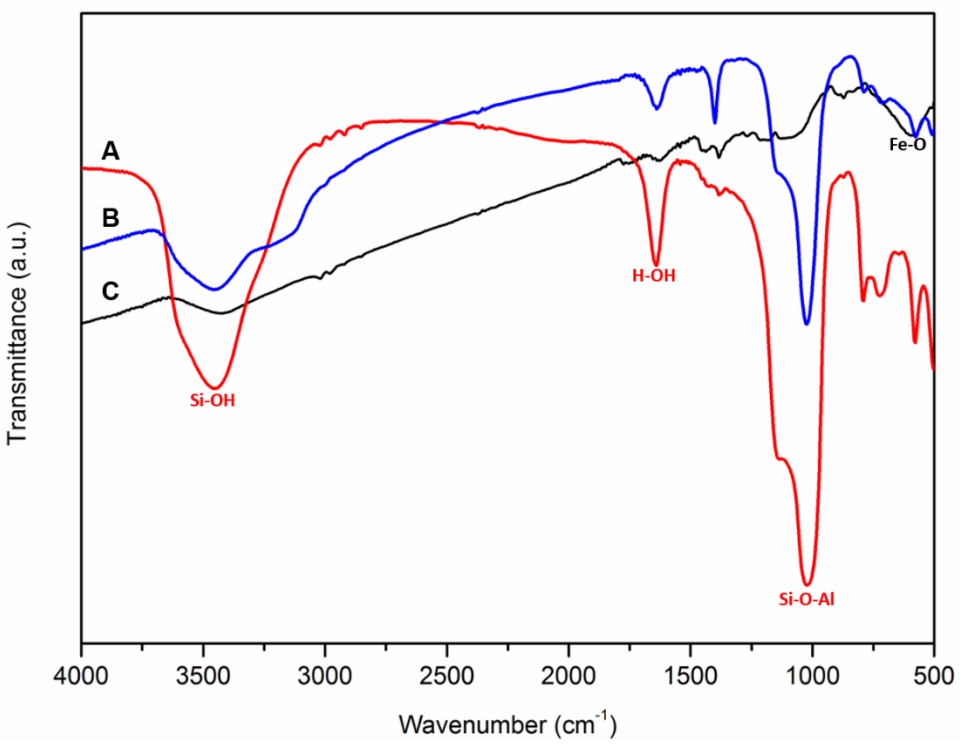

Figure 3.4: FTIR spectrum of Fe_3O_4 nanoparticles (C - black), NaY zeolite (A - red) and MZNC (B - blue). The IR-active chemical groups attributed to the main bands are indicated.

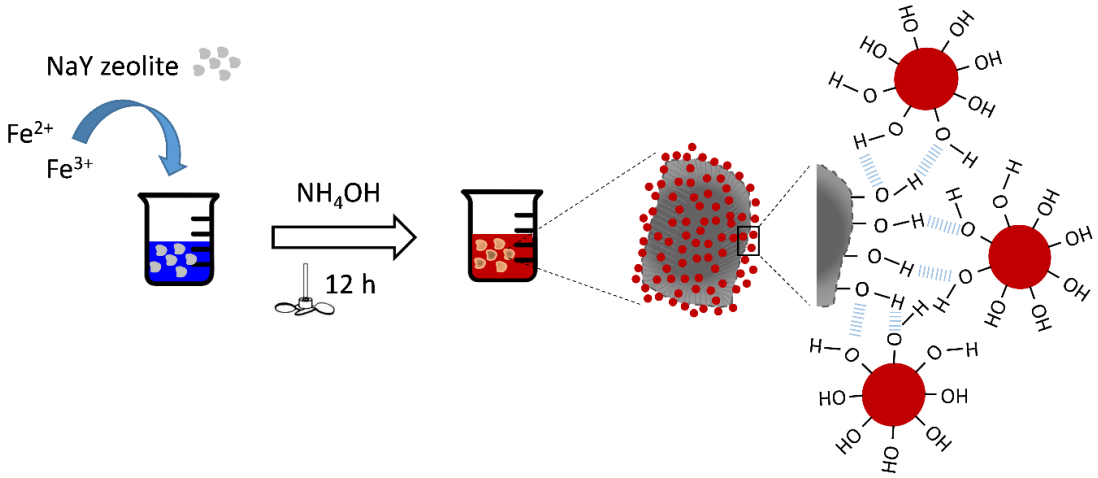

Figure 3.5: Scheme of the MZNCs preparation and the mechanism of interaction proposed between the *in situ* formed MNPs and zeolite particles.

Hysteresis loops of the MZNCs were measured with a SQUID magnetometer in the applied magnetic field range from –20 kOe to +20 kOe at 2 and 300 K (Figure 3.6C). The M *vs* H curves at 300 K showed the typical superparamagnetic (SPM) behaviour for small magnetite nanoparticles of around 5 nm (Figure 3.6D). No coercive forces or remanence were observed due to the small average nanoparticle size, which was well below the single-to-multi domain

limit (around 20 nm for magnetite nanoparticles). The high surface-to-volume contribution in small magnetite nanoparticles is responsible of the observed non-saturated magnetization at the maximum field tested (20 kOe), as consequence of the atomic disorder and spin frustration at the surface (spin-glass like behaviour) and opposite to the spin-ordered magnetic core. In fact, a linear paramagnetic (PM) component is clearly over imposed to the classic SPM behaviour due to the small particle size of the magnetite nanoparticles. In an attempt to compare the saturation magnetization (*Ms*) of our MZNCs with data from other magnetized zeolites from the literature, the *Ms* was calculated by the extrapolation of the M *vs* H^{-1} curve for $H^{-1} \rightarrow 0$. The *Ms* value obtained was 2.8 emu g^{-1} and contrasts with the ~65 emu g^{-1} of 10-20 nm magnetite nanoparticles and with the ~92 emu g^{-1} of bulk magnetite.[51,52] A low value of *Ms* is expected, as the amount of magnetite nanoparticles in the final hybrid is very low. Previously reported *Ms* data in zeolites magnetized with similar magnetite nanoparticles oscillate between 2.1 and 8.35 emu g^{-1} at room temperature.[36,39,43] According to the value of *Ms* found for our MZNCs compared to that measured for our ~5 nm SPM magnetite nanoparticles (Ms ≈ 60 emu g^{-1}, Figure 3.6A), the mass of magnetite nanoparticles only took up about 1/23 in the MZNC. However, even though the total magnetic moment in the sample was apparently low, the powder sample was still attracted by the magnetic field generated by a portable external magnet (see inset in Figure 3.6C). At low temperature (2 K), the hysteresis loop showed a ferromagnetic (FM)-like behaviour as consequence of the magnetite nanoparticles to be in a magnetically blocked state, showing hysteresis, remanence and higher *Ms* than that observed at room temperature (Figure 3.6C), as predicted by the Bloch's law.[53] For a further magnetic analysis, the temperature dependent zero-field-cooled (ZFC) and field-cooled (FC) magnetization curves of MZNCs were measured from the 2 to 300 K under an applied magnetic field of 100 Oe (Figure 3.6D). As the temperature decreases from room temperature the magnetization increases until a maximum in the ZFC curve at ~70 K, which represents the blocking temperature (T_B), at which the thermal energy becomes comparable to the anisotropy energy barrier.[54] T_B is strongly dependent on the surface state, interparticle interactions, particle size and particle size distribution of the grafted magnetite nanoparticles. A wide range of T_B in the range 20 - 170 K has been reported as a function of different surface coatings and particle sizes for magnetite nanoparticles in the 5 - 11 nm size range.[55–57] The observed value of T_B for MZNCs is in agreement with that of uncoated magnetite nanoparticles between 4 and 11 nm prepared by the co-precipitation method, what supports the XRD and TEM data that indicated a particle size for the as-synthesized magnetite nanoparticles around 5 nm. It is also worth mentioning the thermal irreversibility feature observed in the ZFC-FC bifurcation temperature region below T_{irr} = 250 K. Large differences between the T_B and T_{irr} are ascribed to a distribution of magnetic anisotropy in the sample, most likely due to the

polydispersity in the particle size.[58] This is also in agreement with the broad peak observed at T_B in the ZFC curve. Furthermore, the gap $T = T_B - T_{irr}$ is on the order of 180 K, indicating strong magnetic couplings between the NPs. In a more detailed inspection of the shape of the FC curve we can observe that the magnetization monotonically increases as the temperature decreases until ~T_B, below which it keeps increasing down to 2 K, with a small plateu between 35 and 20 K. This feature points to a strong interacting magnetite nanoparticles system and highlights the presence of significant dipolar magnetic interactions. This magnetically strong interacting-like behaviour differs from the collective behaviour observed in other MNPs-based magnetic systems, such as magnetite nanoparticles arrays and magnetic zeolites,[39,59] where both ZFC and FC magnetization decrease below T_B. In the case of previous reported MNPs-based magnetized zeolites, both the higher weight ratio of the nanoparticles to the zeolite and the degree of coverage of the zeolite crystals were higher than that of this work, meaning shorter inter-particle distances and higher dipolar magnetic interactions. On the other hand, if we compare the temperature dependence of the magnetization *M(T)* under ZFC and FC conditions of MZNCs and magnetite nanoparticles separately, we observe a significant decrease from ~160 to ~40 K once the magnetite nanoparticles are grafted and homogenously distributed on the zeolite nanoparticles' surface (see Figures 3.6B and 3.6D). This hydrogen bonds-mediated interaction between magnetite nanoparticles and zeolites can decrease the interparticle aggregation and lead to the formation of smaller, but still interacting, magnetic aggregates. An opposite effect was found in magnetite nanoparticles coated with 3-aminopropyl-triethoxysilane (APTES), where an increase of T_B was observed when compared to that of uncoated nanoparticles. In this case, the effect was ascribed to the alkosylanes condensation, which increases the interparticle aggregation, leading to the formation of larger aggregates particles.[60]

In our case, magnetic results are consistent with the morphological characterization of MZNCs by TEM, where a coverage of the zeolite nanoparticles' surface is observed, resulting in short-particle distances and presence of small particle aggregates.

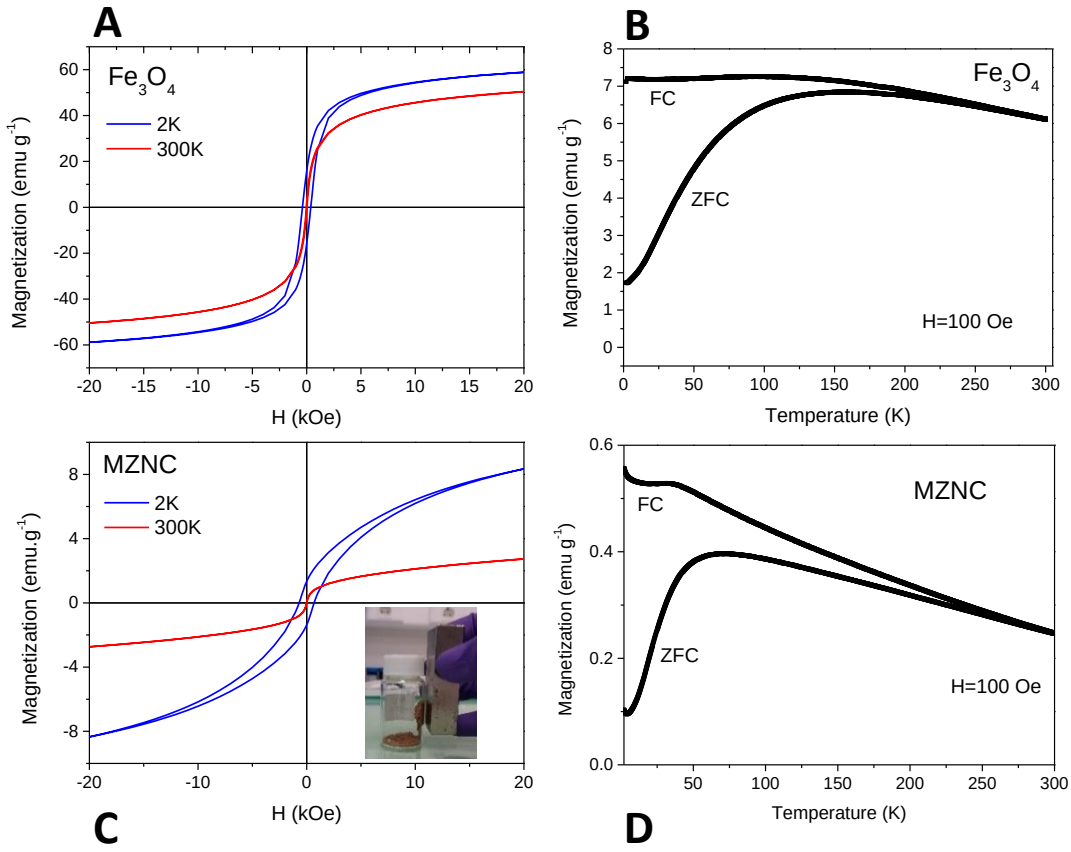

Figure 3.6: A) Hysteresis loops of the Fe_3O_4 nanoparticles at 300 and 2 K; B) Temperature dependence of the magnetization under ZFC and FC conditions at an applied field of H=100 Oe; C) Hysteresis loops of the MZNCs at 300 and 2 K; D) Temperature dependence of the magnetization of MZNCs under ZFC and FC conditions at an applied field of H=100 Oe.

N_2 absorption analysis were performed in both NaY zeolite and MZNCs samples (Figure 3.7). From the shape of the curves obtained, we verified that both samples showed a I-type isotherm according to the IUPAC classification, as they did not exhibit the hysteresis loop characteristic from microporous solids.[61] Moreover, MZNCs retained the same isotherm profile as that of the parent NaY zeolite, although a significant reduction of the surface area from 792 to 527 $m^2\ g^{-1}$ was observed after the inorganic assembly between the magnetite nanoparticles and the zeolite particles. This reduction of the surface area strongly suggests the partial occlusion of the microporous network of the zeolite structure. On the one hand, this could be provoked by the incorporation of magnetic nanoparticles into the micropores and it has been already observed by different authors.[62–64] The Fe^{2+} and Fe^{3+} metal ion precursors in the original solution could penetrate into the open pores of the zeolite particles, giving rise to the formation of magnetite nanoparticles inside the micropores once the coprecipitation is induced by the base addition. However, by comparing the NaY zeolite microporous channels diameter (0.73 nm) and the particle size distribution calculated from TEM data, seems unlikely that the

formation of magnetite nanoparticles takes place inside the pores. On the other hand, it is well known that the zeolite structure present also a degree of the mesoporosity.[18] However, although the incorporation of magnetite nanoparticles in the mesoporous channels (< 2 nm) cannot be completely discarded, since the particle size distribution of the magnetite nanoparticles determined by TEM shows the presence of very small magnetite nanoparticles of similar size, the observed magnetite nanoparticles distribution on the zeolite surface rather points to a blockage of the micro/meso porous by particle accumulation at the pore entrance as the main reason for the surface area reduction. This effect was also observed in bimetallic catalysts by Freitas *et al,* where this obstruction was caused by the incorporation of Cu and Pd metal species affected the amount of available acid sites and therefore the catalytic activity of the designed catalysts.[65]

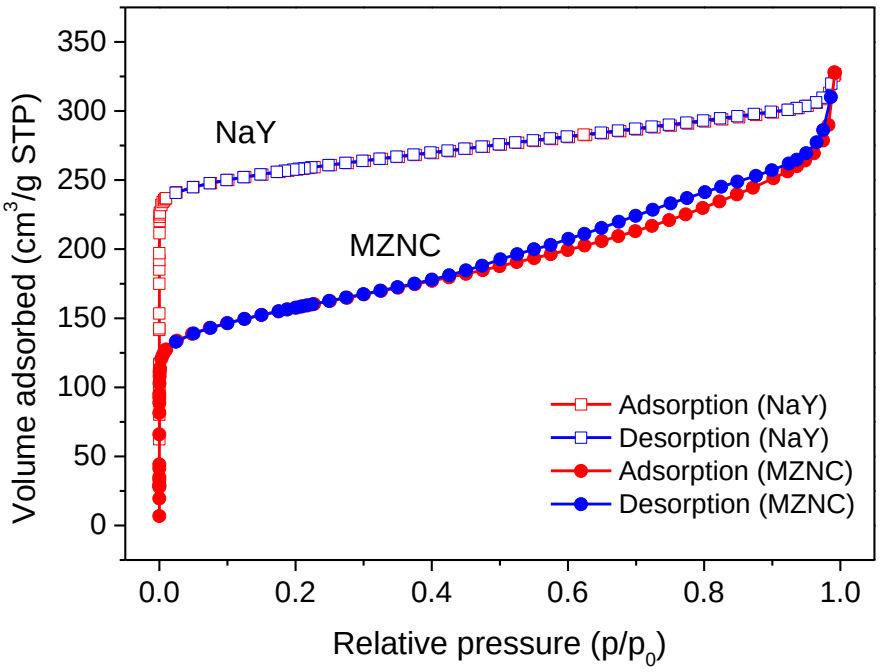

Figure 3.7: N_2 adsorption-desorption isotherms of NaY zeolite (open symbols) and MZNC (closed symbols) particles.

3.3.2. *IN VITRO* STUDIES

3.3.2.1. MZNCS CYTOTOXICITY AND INTERNALIZATION STUDIES.

The *in vitro* effect of MZNCs was evaluated on three different human cell lines: Hs 578T and MCF-7 breast cancer cells, and MCF-10 normal breast epithelial cells. Different concentration of MZNCs from 0.025 to 0.100 mg mL^{-1} were incubated with the cells in serum-free medium. The effect of this incubation on the cell viability was studied after 24 and 48 h by means of the

SRB assay for cytotoxicity screening. From the analysis of the results showed in the Figure 3.8, we can deduce that there is not a cytotoxicity effect after 24 h of incubation induced either by NaY or MZNCs in any of the cell lines and concentrations tested. However, from the results obtained after 48 h of cell-samples exposure time, a slight reduction on the cell viability was observed for both Hs 578T and MCF-7 cells at high concentrations of NaY zeolite. This reveals a dose- and time-dependent toxicity in the case of NaY, which interestingly disappears when magnetite nanoparticles attach to NaY zeolite nanoparticles' surface to yield the MZNC sample. For MCF-10 cells treated with these samples, no decrease in cell viability was observed both for NaY and MZNCs, which may be explained by the fact that normal cells display lower endocytosis activity than cancer cells.[66]

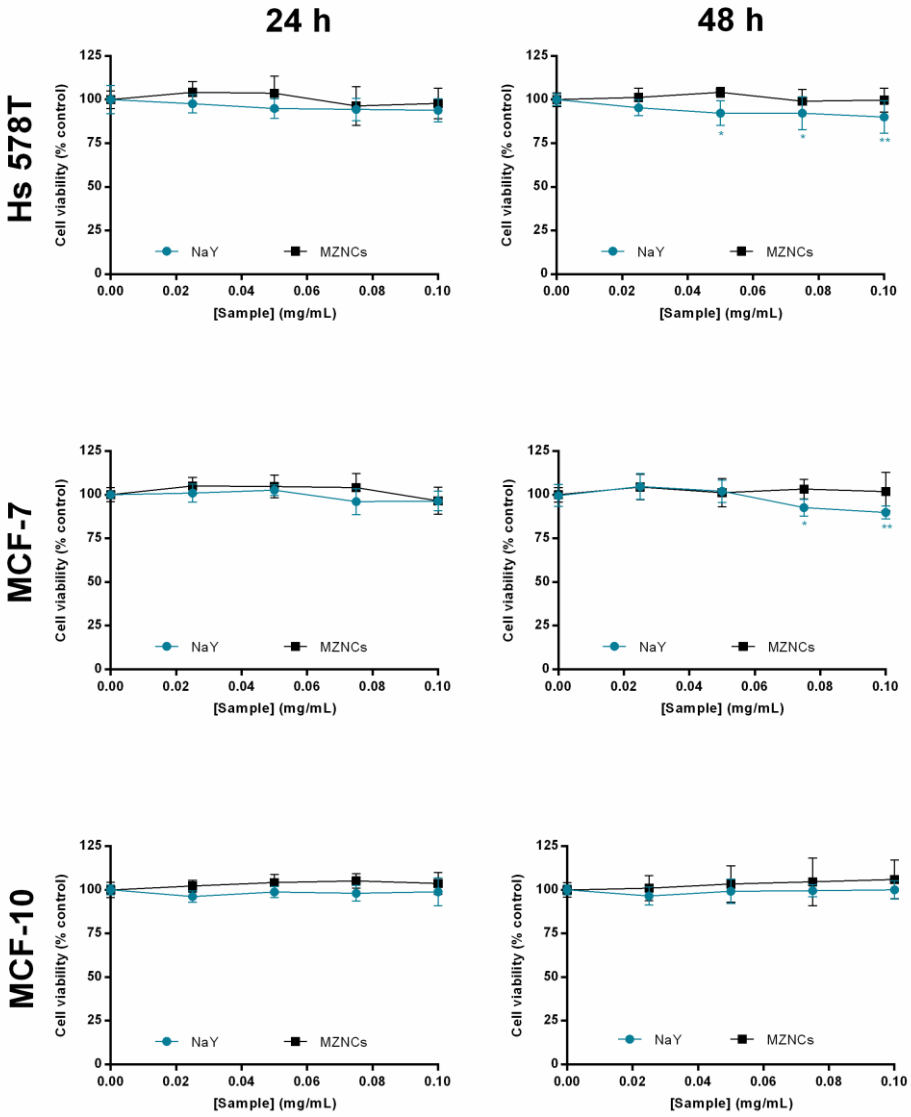

Figure 3.8: Hs 578T, MCF-7 and MCF-10 cell viability after incubation with NaY and MZNCs at 24 and 48 h of incubation. The data are given as mean ± SD (*n*=3).

In order to study the cell internalization of the MZNC particles, 50 µg mL^{-1} of this sample were incubated with Hs 578T breast cancer cells and MCF-10 epithelial mammary cells for 4 h. After the incubation, the resulting cells were washed several times with fresh medium and processed as described in the experimental section to obtain a thin enough cross section of the cells for TEM analysis. A set of TEM images are shown in Figure 3.9 that confirm the internalization of MZNC particles by both cellular types, clearly distinguishable as dark stains within the cellular compartments (Figures 3.9B and 3.9D). Both cell lines incubated with MZNC particles showed filopodia, with nanoparticles located in cytoplasmic vesicles, without any apparent localization in the cellular organelles. A safe and efficient localization of MNPs into the cytosol is of utmost importance in applications such as phototherapy, intracellular imaging, cell tracking or targeting or in gene or intracellular drug delivery.[67]

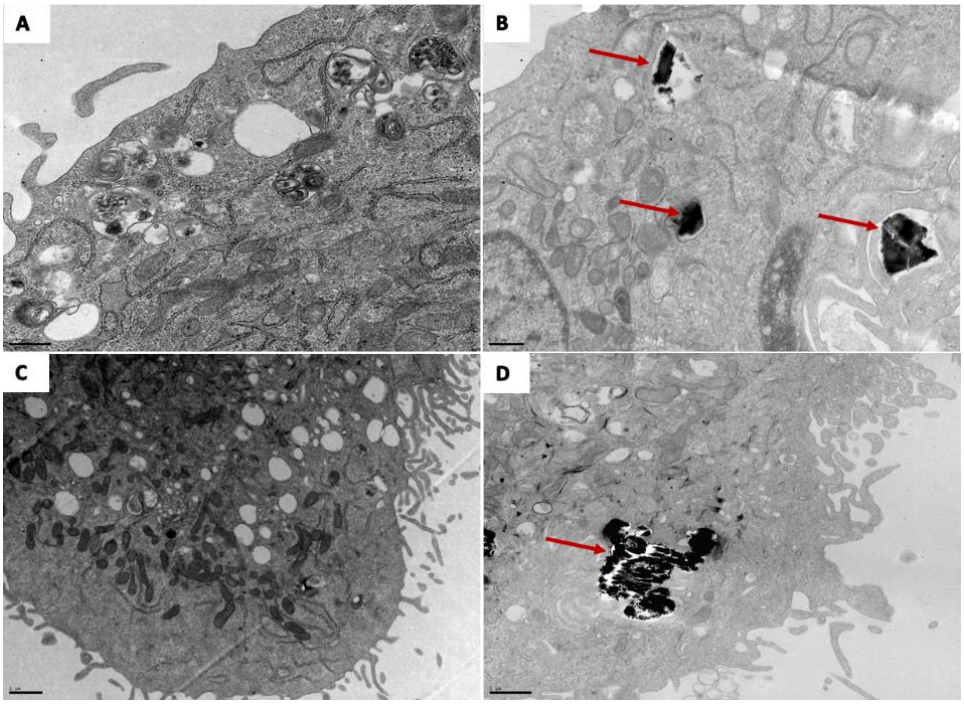

Figure 3.9: TEM images of Hs 578T and MCF-10 cells incubated with 50 µg mL^{-1} of MZNC particles for 4 h: A) Hs 578T cells control; B) Hs 578T with MZNC particles; C) MCF-10 cells control and D) MCF-10 with MZNC particles.

MRI

Given the excellent cell internalization of MZNC particles by tumor cells, their capability as T_2-CA for MRI was assessed *in vitro* at a clinical field of 3 T and 37 ºC. An agarose-gel cell phantom was prepared containing purified Hs 578T breast cells after 4 h incubation with both non-magnetic and magnetic zeolite samples (Figure 3.10A). The rational choice of agarose as supporting medium of the cells was based on an attempt to mimic as much as possible the

solid morphology and structure of a human tissue, so that the results would better approach a relevant clinical application. The tissue-equivalent MRI phantom including a control (only cells) was imaged under T_2-weighted conditions. As expected, the magnetite nanoparticles present in the MZNC act as T_2 effectors and induce a darker contrast in the MRI image of the Hs 578T cancer cells, compared to that provided by non-incubated control cells or cells incubated with non-magnetic NaY zeolite. The quantitative analysis of the MRI image shows a clear reduction of the T_2 signal intensity for those cells containing MZNC particles (Figure 3.10B). This observed T_2-MRI contrast enhancement confirms their cell internalization and render these magnetic zeolites suitable T_2-imaging probes in MRI applications, enabling new opportunities such as cell labeling and tracking and image-guided drug delivery.

The development of zeolite structures for applications in the biomedical field is still in its early stage. The attachment of MNPs on the zeolite surface adds an interesting imaging functionality to the system. This is especially interesting in NaY zeolite, since in addition to their proved drug encapsulation ability, the herein demonstrated T_2-MRI enhancement suggests their further optimization towards the design of more efficient theranostic agents, enabling new opportunities for these inorganic hybrids in the biomedical field.

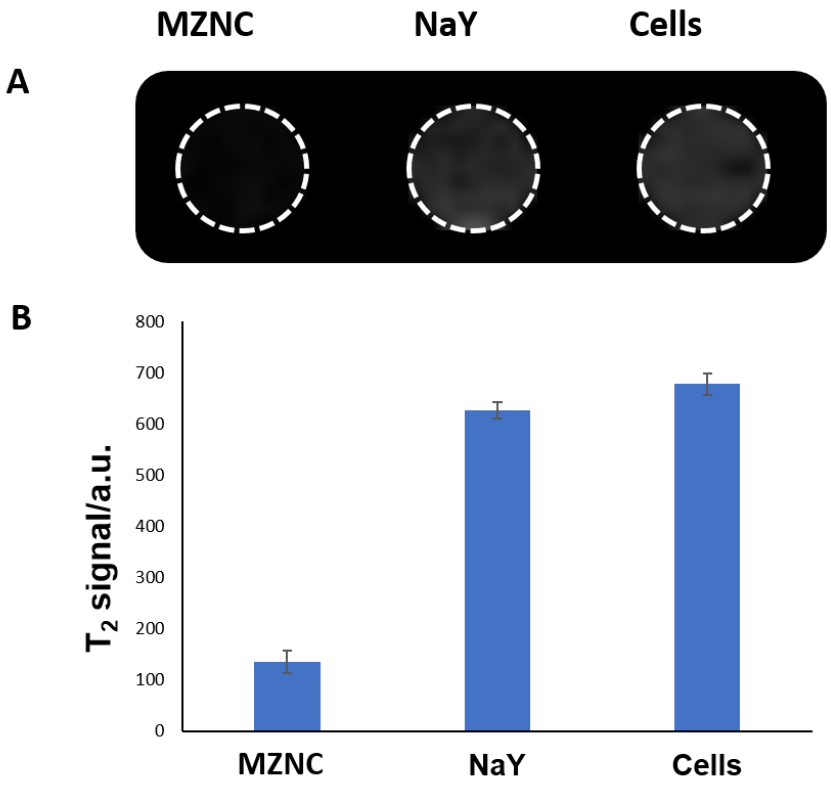

Figure 3.10: A) T_2-weighted MRI images of an agarose cell phantom of MZNC and NaY particles internalized by Hs 578T cells. T_2-weighted fast spin echo (FSE): TE = 68 ms; TR = 4800 ms; FOV = 60 x 60 mm; NA = 4; At = 9'55''; NS = 6; SG = 0.1 mm; ST = 1 mm. Agarose gel only with cells was taken as a control. B) Quantitative analysis of the MRI signal measured in the T_2-weighted image shown in (A).

3.4. CONCLUSIONS

Biocompatible and non-toxic magnetic NaY zeolite have been achieved by simple basic coprecipitation of Fe(II) and Fe(III) salts in an aqueous solution containing zeolite nanoparticles. The formation of small ~5 nm magnetite nanoparticles and their grafting to the zeolite nanoparticles' surface have been confirmed by XRD, SQUID, EDS, IR and TEM. MZNC particles showed a non-saturated superparamagnetic behavior and presence of dipolar magnetic interactions, in agreement with a fully coverage of the zeolites' surface and formation of small aggregates (short interparticle distances). Also, the N_2 adsorption-desorption profile of the MZNC particles pointed to an obstruction of the porous network, which was attributed to the magnetite nanoparticles accumulation at the zeolite surface rather than inside the pores. *In vitro* studies evidenced an excellent cell internalization of MZNCs by human breast tumor cells. The MRI properties of MZNC-labeled cells were studied in a tissue-equivalent agarose gel and rendered magnetic zeolites suitable T_2-MRI contrast enhancers at a clinical field of 3 T. These results constitute a step forward towards the design and optimization of zeolite structures as multifunctional systems for theranostic applications in biomedicine. The demonstrated cell labeling efficiency and capability to enhance the T_2-MRI contrast, together with the previously proved drug encapsulation efficacy, make magnetic zeolites promising candidates for further development, which currently is in an early stage.

3.5. REFERENCES

1 E. H. Chang, J. B. Harford, M. A. W. Eaton, P. M. Boisseau, A. Dube, R. Hayeshi, H. Swai and D. S. Lee, Nanomedicine: Past, present and future - A global perspective, *Biochem. Biophys. Res. Commun.*, 2015, **468**, 511–517.

2 L. Wang, L. L. Li, Y. S. Fan and H. Wang, Host-guest supramolecular nanosystems for cancer diagnostics and therapeutics, *Adv. Mater.*, 2013, **25**, 3888–3898.

3 M. Bañobre-López, A. Teijeiro and J. Rivas, Magnetic nanoparticle-based hyperthermia for cancer treatment, *Reports Pract. Oncol. Radiother.*, 2013, **18**, 397–400.

4 J. S. Kim, T. J. Yoon, K. N. Yu, S. N. Mi, M. Woo, B. G. Kim, K. H. Lee, B. H. Sohn, S. B. Park, J. K. Lee and M. H. Cho, Cellular uptake of magnetic nanoparticle is mediated through energy-dependent endocytosis in A549 cells, *J. Vet. Sci.*, 2006, **7**, 321–326.

5 A. G. Arranja, V. Pathak, T. Lammers and Y. Shi, Tumor-targeted nanomedicines for cancer theranostics, *Pharmacol. Res.*, 2017, **115**, 87–95.

6 F. ud Din, W. Aman, I. Ullah, O. S. Qureshi, O. Mustapha, S. Shafique and A. Zeb, Effective use of nanocarriers as drug delivery systems for the treatment of selected tumors., *Int. J. Nanomedicine*, 2017, **12**, 7291–7309.

7 C. Fornaguera and M. J. García-Celma, Personalized Nanomedicine: A Revolution at the Nanoscale, *J. Pers. Med.*, 2017, **7**, 12.

8 C. Von Roemeling, W. Jiang, C. K. Chan, I. L. Weissman and B. Y. S. Kim, Breaking Down the Barriers to Precision Cancer Nanomedicine, *Trends Biotechnol.*, 2017, **35**, 159–171.

9 R. Gupta, J. Shea, C. Scafe, A. Shurlygina and N. Rapoport, Polymeric micelles and nanoemulsions as drug carriers: Therapeutic efficacy, toxicity, and drug resistance, *J. Control. Release*, 2015, **212**, 70–77.

10 K. Avgoustakis, PLGA–mPEG nanoparticles of cisplatin: *in vitro* nanoparticle degradation, *in vitro* drug release and in vivo drug residence in blood properties, *J. Control. Release*, 2002, **79**, 123–135.

11 I. Singh, R. Swami, M. K. Jeengar, W. Khan and R. Sistla, p-Aminophenyl-α-d-mannopyranoside engineered lipidic nanoparticles for effective delivery of docetaxel to brain, *Chem. Phys. Lipids*, 2015, **188**, 1–9.

12 N. Akhtar and R. A. Khan, Liposomal systems as viable drug delivery technology for skin cancer sites with an outlook on lipid-based delivery vehicles and diagnostic imaging inputs for skin conditions', *Prog. Lipid Res.*, 2016, **64**, 192–230.

13 L. Maggini, I. Cabrera, A. Ruiz-Carretero, E. A. Prasetyanto, E. Robinet and L. De Cola, Breakable mesoporous silica nanoparticles for targeted drug delivery, *Nanoscale*, 2016, **8**, 7240–7247.

14 B. Tian, S. Liu, S. Wu, W. Lu, D. Wang, L. Jin, B. Hu, K. Li, Z. Wang and Z. Quan, pH-responsive poly (acrylic acid)-gated mesoporous silica and its application in oral colon targeted drug delivery for doxorubicin, *Colloids Surfaces B Biointerfaces*, 2017, **154**, 287–296.

15 Y. Wang, J. Wang, Y. Yang, Y. Sun, Y. Yuan, Y. Li and C. Liu, In situ biodegradable crosslinking of cationic oligomer coating on mesoporous silica nanoparticles for drug delivery, *Colloids Surfaces B Biointerfaces*, 2017, **153**, 272–279.

16 Z. Tian, Y. Xu and Y. Zhu, Aldehyde-functionalized dendritic mesoporous silica nanoparticles as potential nanocarriers for pH-responsive protein drug delivery, *Mater. Sci. Eng. C*, 2017, **71**, 452–459.

17 R. Amorim, N. Vilaça, O. Martinho, R. M. Reis, M. Sardo, J. Rocha, A. M. Fonseca, F. Baltazar and I. C. Neves, Zeolite structures loading with an anticancer compound as drug delivery systems, *J. Phys. Chem. C*, 2012, **116**, 25642–25650.

18 N. Vilaça, R. Amorim, A. F. Machado, P. Parpot, M. F. R. Pereira, M. Sardo, J. Rocha, A. M. Fonseca, I. C. Neves and F. Baltazar, Potentiation of 5-fluorouracil encapsulated in zeolites as drug delivery systems for *in vitro* models of colorectal carcinoma, *Colloids Surfaces B Biointerfaces*, 2013, **112**, 237–244.

19 O. Martinho, N. Vilaça, P. J. G. Castro, R. Amorim, A. M. Fonseca, F. Baltazar, R. M. Reis and I. C. Neves, *In vitro* and *in vivo* studies of temozolomide loading in zeolite structures as drug delivery systems for glioblastoma, *RSC Adv.*, 2015, **5**, 28219–28227.

20 T. K. Jain, J. Richey, M. Strand, D. L. Leslie-Pelecky, C. A. Flask and V. Labhasetwar, Magnetic nanoparticles with dual functional properties: Drug delivery and magnetic resonance imaging, *Biomaterials*, 2008, **29**, 4012–4021.

21 S. Natesan, C. Ponnusamy, A. Sugumaran, S. Chelladurai, S. S. Palaniappan and R. Palanichamy, Artemisinin loaded chitosan magnetic nanoparticles for the efficient targeting to the breast cancer, *Int. J. Biol. Macromol.*, 2017, **104**, 1853–1859.

22 K. Lee, A. E. David, J. Zhang, M. C. Shin and V. C. Yang, Enhanced accumulation of theranostic nanoparticles in brain tumor by external magnetic field mediated in situ clustering of magnetic nanoparticles, *J. Ind. Eng. Chem.*, 2017, **54**, 389–397.

23 M. Moskvin, M. Babič, S. Reis, M. M. Cruz, L. P. Ferreira, M. D. Carvalho, S. A. C. Lima and D. Horák, Biological evaluation of surface-modified magnetic nanoparticles as a platform for colon cancer cell theranostics, *Colloids Surfaces B Biointerfaces*, 2018, **161**, 35–41.

24 Q. A. P. and J. C. and S. K. J. and J. Dobson, Applications of magnetic nanoparticles in biomedicine, *J. Phys. D. Appl. Phys.*, 2003, **36**, R167.

25 C. Sun, J. Lee and M. Zhang, Magnetic nanoparticles in MR imaging and drug delivery, *Adv. Drug Deliv. Rev.*, 2008, **60**, 1252–1265.

26 C. Sanson, O. Diou, J. Thévenot, E. Ibarboure, A. Soum, A. Brûlet, S. Miraux, E. Thiaudière, S. Tan, A. Brisson, V. Dupuis, O. Sandre and S. Lecommandoux, Doxorubicin Loaded Magnetic Polymersomes: Theranostic Nanocarriers for MR Imaging and Magneto-Chemotherapy, *ACS Nano*, 2011, **5**, 1122–1140.

27 M. Banõbre-Lopez, Y. Pineiro-Redondo, M. Sandri, A. Tampieri, R. De Santis, V. A. Dediu and J. Rivas, Hyperthermia Induced in Magnetic Scaffolds for Bone Tissue Engineering, *IEEE Trans. Magn.*, 2014, **50**, 1–7.

28 R. Grillo, J. Gallo, D. G. Stroppa, E. Carbó-Argibay, R. Lima, L. F. Fraceto and M. Bañobre-López, Sub-Micrometer Magnetic Nanocomposites: Insights into the Effect of Magnetic Nanoparticles Interactions on the Optimization of SAR and MRI Performance, *ACS Appl. Mater. Interfaces*, 2016, **8**, 25777–25787.

29 R. Joyner and M. Stockenhuber, Preparation, Characterization, and Performance of Fe−ZSM-5 Catalysts, *J. Phys. Chem. B*, 1999, **103**, 5963–5976.

30 G. Delahay, D. Valade, A. Guzmán-Vargas and B. Coq, Selective catalytic reduction of nitric oxide with ammonia on Fe-ZSM-5 catalysts prepared by different methods, *Appl. Catal. B Environ.*, 2005, **55**, 149–155.

31 B. E. R. Snyder, P. Vanelderen, M. L. Bols, S. D. Hallaert, L. H. Böttger, L. Ungur, K. Pierloot, R. A. Schoonheydt, B. F. Sels and E. I. Solomon, The active site of low-temperature methane hydroxylation in iron-containing zeolites, *Nature*, 2016, **536**, 317–321.

32 R. Gonzalez-Olmos, U. Roland, H. Toufar, F.-D. Kopinke and A. Georgi, Fe-zeolites as catalysts for chemical oxidation of MTBE in water with H2O2, *Appl. Catal. B Environ.*, 2009, **89**, 356–364.

33 R. Gonzalez-Olmos, F.-D. Kopinke, K. Mackenzie and A. Georgi, Hydrophobic Fe-Zeolites for Removal of MTBE from Water by Combination of Adsorption and Oxidation, *Environ. Sci. Technol.*, 2013, **47**, 2353–2360.

34 D. Brühwiler and G. Calzaferri, Selective functionalization of the external surface of zeolite L, *Comptes Rendus Chim.*, 2005, **8**, 391–398.

35 M. G. Rimoli, M. R. Rabaioli, D. Melisi, A. Curcio, S. Mondello, R. Mirabelli and E. Abignente, Synthetic zeolites as a new tool for drug delivery, *J. Biomed. Mater. Res. - Part A*, 2008, **87**, 156–164.

36 M. Huysal, Z. Durmus, B. Zengin, M. Senel and S. Is, Preparation and *in vitro* evaluation of 5- flourouracil loaded magnetite–zeolite nanocomposite (5-FU-MZNC) for cancer drug delivery applications, *Biomed. Pharmacother.*, 2016, **77**, 182–190.

37 S. Mintova, J.-P. Gilson and V. Valtchev, Advances in nanosized zeolites, *Nanoscale*, 2013, **5**, 6693–703.

38 N. Vilaça, R. Amorim, O. Martinho, R. M. Reis, F. Baltazar, A. M. Fonseca and I. C. Neves, Encapsulation of a-cyano-4-hydroxycinnamic acid into a NaY zeolite., *J. Mater. Sci.*, 2011, **46**, 7511–7516.

39 S. Fibikar, G. Luppi, V. Martínez-Junza, M. Clemente-León and L. De Cola, Manipulation and orientation of zeolite L by using a magnetic field, *Chempluschem*, 2015, **80**, 62–67.

40 H. Faghihian, M. Moayed, A. Firooz and M. Iravani, Synthesis of a novel magnetic zeolite nanocomposite for removal of Cs+ and Sr2+ from aqueous solution: Kinetic, equilibrium, and thermodynamic studies, *J. Colloid Interface Sci.*, 2013, **393**, 445–451.

41 C. Pizarro, M. A. Rubio, M. Escudey, M. F. Albornoz, D. Muńoz, J. Denardin and J. D. Fabris, Nanomagnetite-zeolite composites in the removal of arsenate from aqueous systems, *J. Braz. Chem. Soc.*, 2015, **26**, 1887–1896.

42 F. Pang, M. He and J. Ge, Controlled synthesis of Fe3O4/ZIF-8 nanoparticles for magnetically separable nanocatalysts, *Chemistry*, 2015, **21**, 6879–6887.

43 J. Fang, Y. Yang, W. Xiao, B. Zheng, Y.-B. Lv, X.-L. Liu and J. Ding, Extremely low frequency alternating magnetic field-triggered and MRI-traced drug delivery by optimized magnetic zeolitic imidazolate framework-90 nanoparticles, *Nanoscale*, 2016, **8**, 3259–3263.

44 S. García-Jimeno and J. Estelrich, Ferrofluid based on polyethylene glycol-coated iron oxide nanoparticles: Characterization and properties, *Colloids Surfaces A Physicochem. Eng. Asp.*, 2013, **420**, 74–81.

45 N. Vilaça, A. F. Machado, F. Morais-Santos, R. Amorim, A. Patrícia Neto, E. Logodin, M. F. R. Pereira, M. Sardo, J. Rocha, P. Parpot, A. M. Fonseca, F. Baltazar and I. C. Neves, Comparison of different silica microporous structures as drug delivery systems for *in vitro* models of solid tumors, *RSC Adv.*, 2017, **7**, 13104–13111.

46 N. Vilaça, F. Morais-Santos, A. F. Machado, A. Sirkecioǂlu, M. F. R. Pereira, M. Sardo, J. Rocha, P. Parpot, A. M. Fonseca, F. Baltazar and I. C. Neves, Micro- and mesoporous structures as drug delivery carriers for salicylic acid, *J. Phys. Chem. C*, 2015, **119**, 3589–3595.

47 S. P. Zhdanov, in *Molecular Sieve Zeolites-I*, American Chemical Society, 1974, vol. 101, pp. 2–20.

48 T. F. Mastropietro, E. Drioli and T. Poerio, Low temperature synthesis of nanosized NaY zeolite crystals from organic-free gel by using supported seeds, *RSC Adv.*, 2014, **4**, 21951.

49 H. Faghihian, M. Moayed, A. Firooz and M. Iravani, Evaluation of a new magnetic zeolite composite for removal of Cs+ and Sr2+ from aqueous solutions: Kinetic, equilibrium and thermodynamic studies, *Comptes Rendus Chim.*, 2014, **17**, 108–117.

50 K. Petcharoen and A. Sirivat, Synthesis and characterization of magnetite nanoparticles via the chemical co-precipitation method, *Mater. Sci. Eng. B Solid-State Mater. Adv. Technol.*, 2012, **177**, 421–427.

51 D. H. Han, J. P. Wang and H. L. Luo, Crystallite size effect on saturation magnetization of fine ferrimagnetic particles, *J. Magn. Magn. Mater.*, 1994, **136**, 176–182.

52 P. Guardia, B. Batlle-Brugal, A. G. Roca, O. Iglesias, M. P. Morales, C. J. Serna, A. Labarta and X. Batlle, Surfactant effects in magnetite nanoparticles of controlled size, *J. Magn. Magn. Mater.*, 2007, **316**, e756–e759.

53 F. Bloch, Zur Theorie des Ferromagnetismus, *Zeitschrift für Phys.*, 1930, **61**, 206–219.

54 B. D. Cullity and C. . Graham, *Introduction to Magnetic Materials*, Addison-Wesley, MA, 2nd edn., 1972.

55 K. C. and M. T. and Y. C. and J. M. H. and S. J. S. and R. G. Harrison, Particle size effects on the magnetic behaviour of 5 to 11 nm Fe3O4 nanoparticles coated with oleic acid, *J. Phys. Conf. Ser.*, 2014, **521**, 12004.

56 M. Mikhaylova, D. K. Kim, N. Bobrysheva, M. Osmolowsky, V. Semenov, T. Tsakalakos and M. Muhammed, Superparamagnetism of Magnetite Nanoparticles: Dependence on Surface Modification, *Langmuir*, 2004, **20**, 2472–2477.

57 G. F. Goya, T. S. Berquó, F. C. Fonseca and M. P. Morales, Static and dynamic magnetic properties of spherical magnetite nanoparticles, *J. Appl. Phys.*, 2003, **94**, 3520–3528.

58 A. Lopez-Cruz, C. Barrera, V. L. Calero-DdelC and C. Rinaldi, Water dispersible iron oxide nanoparticles coated with covalently linked chitosan, *J. Mater. Chem.*, 2009, **19**, 6870–6876.

59 M. Knobel, W. C. Nunes, H. Winnischofer, T. C. R. Rocha, L. M. Socolovsky, C. L. Mayorga and D. Zanchet, Effects of magnetic interparticle coupling on the blocking temperature of ferromagnetic nanoparticle arrays, *J. Non. Cryst. Solids*, 2007, **353**, 743–747.

60 R. A. Bini, R. F. C. Marques, F. J. Santos, J. A. Chaker and M. Jafelicci, Synthesis and functionalization of magnetite nanoparticles with different amino-functional alkoxysilanes, *J. Magn. Magn. Mater.*, 2012, **324**, 534–539.

61 L. Zhang, A. N. C. van Laak, P. E. de Jongh and K. P. de Jong, in *Zeolites and Catalysis: Synthesis, Reactions and Applications*, Wiley-VCH Verlag GmbH & Co. KGaA, Weinheim, Germany, 2010, pp. 237–282.

62 C. J. Ronhovde, J. Baer and S. C. Larsen, Effects of pore topology and iron oxide core on doxorubicin loading and release from mesoporous silica nanoparticles, *J. Nanoparticle Res.*, 2017, **19**, 215–225.

63 D. Li, S. Egodawatte, D. I. Kaplan, S. C. Larsen, S. M. Serkiz and J. C. Seaman, Functionalized magnetic mesoporous silica nanoparticles for U removal from low and high pH groundwater, *J. Hazard. Mater.*, 2016, **317**, 494–502.

64 A. M. Tomoiaga, B. I. Cioroiu, V. Nica and A. Vasile, Investigations on nanoconfinement of low-molecular antineoplastic agents into biocompatible magnetic matrices for drug targeting, *Colloids Surfaces B Biointerfaces*, 2013, **111**, 52–59.

65 C. M. A. S. Freitas, O. S. G. P. Soares, J. J. M. Orfao, A. M. Fonseca, M. F. R. Pereira and I. C. Neves, Highly efficient reduction of bromate to bromide over mono and bimetallic ZSM5 catalysts, *Green Chem.*, 2015, **17**, 4247–4254.

66 Y. Han, S. Li, X. Cao, L. Yuan, Y. Wang, Y. Yin, T. Qiu, H. Dai and X. Wang, Different inhibitory effect and mechanism of hydroxyapatite nanoparticles on normal cells and cancer cells *in vitro* and in vivo., *Sci. Rep.*, 2014, **4**, 7134.

67 A.- Rahman and S. Anjum, *Frontiers in Stem Cell and Regenerative Medicine Research (Volume 7)*, Bentham eBooks, 2017.

CHAPTER 4

CHARACTERIZATION OF THE MECHANISMS INVOLVED IN THE UPTAKE OF ZEOLITE NANOCARRIERS BY HUMAN CELLS

This chapter will focus on the work about the internalization and uptake of zeolite nanoparticles by human cells, as well as on the effect of the outer surface functionalization on the uptake of zeolite nanoparticles uptake. Since this type of studies are scarce, this work represents an important endorsement to the understanding of the endocytic mechanisms involved in zeolite nanoparticle internalization.

Subchapter 4.1, describes the results of the study on the internalization of zeolite NaY and L nanoparticles by breast cancer cells and epithelial mammary cells. This study enabled the understanding how human cells interact with zeolite nanoparticles. The endocytic pathway for the internalization of these materials was also identified.

In turn, subchapter 4.2 includes the results of the endorsement of the endocytic pathways, using six pharmacological inhibitors and also the uptake of positively and negatively charged zeolite L nanoparticles by breast cancer and epithelial mammary cells.

SUBCHAPTER 4.1

INTERNALIZATION STUDIES ON ZEOLITE NANOPARTICLES BY HUMAN CELLS[5]

Zeolites are crystalline porous materials with a regular framework which have non-toxic effects on a variety of human cell lines and have been explored for cell imaging and drug delivery. Understanding the interaction between zeolite nanoparticles and cells is imperative for improving their potentialities, since the process of internalization of these particles is still poorly understood. In this study, the intracellular trafficking and internalization kinetics of zeolite L into breast cancer cells and normal epithelial mammary cells were analysed using scanning electron microscopy (SEM), confocal microscopy and transmission electron microscopy (TEM) (see graphical abstract below). We also studied the involvement of endocytic pathways using two pharmacological inhibitors, chlorpromazine and dynasore. Zeolite nanoparticles were taken up by both cell types and the cellular uptake was fast and started immediately after 5 min of incubation. Interestingly, the uptake was dependent on the cell type since in breast cancer cells it was faster and more efficient, with a higher number of nanoparticles being internalized by cancer cells over time, compared to that in the epithelial mammary cells. TEM results showed that the internalized nanoparticles were mainly localized in the cell vacuoles. The data obtained upon using endocytic pharmacological inhibitors suggest that the zeolite L uptake is mediated by caveolin.

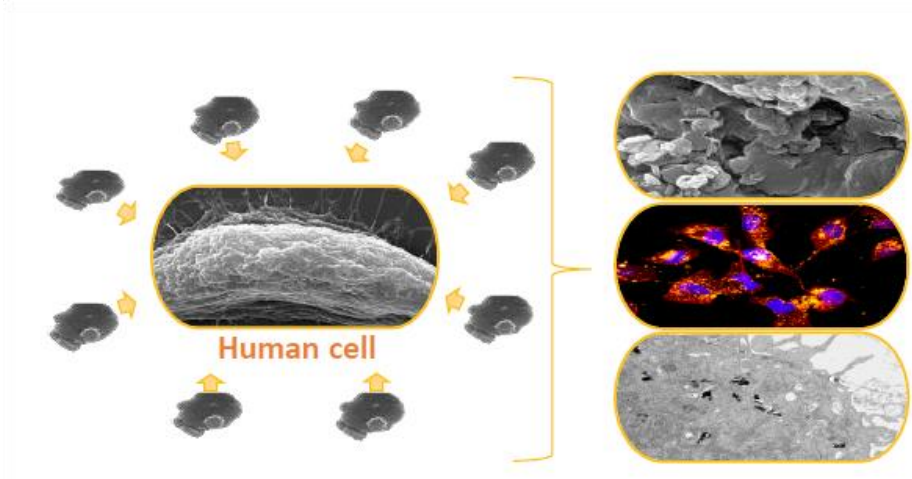

[5] **N. Vilaça**, R. Totovao, E. A. Prasetyanto, V. Miranda-Gonçalves, F. Morais-Santos, R. Fernandes, F. Figueiredo, M. Bañobre-López, A.M. Fonseca, L. De Cola, F. Baltazar, I.C. Neves, Internalization Studies of Zeolite Nanoparticles by Human Cells, *J. Mater. Chem. B*, 2018, **6**, 469-476.

4.1.1. INTRODUCTION

Cancer is currently the leading cause of death worldwide, with 14.1 million new cases, 32.6 million people fighting against cancer (within 5 years of diagnosis) and 8.2 million deaths worldwide, as reported in 2012.[1] Among different types of cancer, breast cancer, just after lung cancer, is the second most common and the most deadly malignancy in women[2–5] with 1.7 million cases diagnosed in 2012 worldwide and about 522 000 deaths.[6] Breast cancer incidence is higher in developed countries but it is increasing in developing countries and is expected to rise in the next few years.[7] Bearing these facts in mind, scientists have been focusing their efforts towards a better understanding of cancer origin and progression and have also been looking for novel nanomaterials for the development of more efficient and less toxic anticancer therapeutic strategies.[8–11] One of these strategies explores drug delivery systems (DDS), which can deliver drugs to the desirable location, reduce side effects and control drug release rates. Furthermore, the use of carriers could improve the bioavailability of the drugs and protect them from degradation in harsh body environments.[11,12] A number of different materials are used to prepare DDS such as metal nanoparticles, metal–organic frameworks (MOF), polymers, liposomes, dendrimers, carbon nanotubes and porous materials.[13]

Amongst porous nanomaterials silica based systems have recently received a lot of attention. Zeolites are microporous crystalline aluminosilicates with three-dimensional frameworks, comprising silicon, aluminum and oxygen, and water molecules featuring a uniform network of channels and pores with regular dimensions.[14–16] The channel size and shape define the structural parameters of a given type of zeolite.[17] Zeolites have been successfully used as hosts for DDS,[15,18–20] but a deep understanding of the uptake mechanisms associated with these structures, in order to design safe and efficient applications for therapeutic purposes, is still lacking. When nanoparticles are in contact with cells, they can be internalized by endocytosis, a mechanism in which a particle is engulfed by the cell membrane, originating intracellular vesicles.[8,21] There are two different types of endocytosis: phagocytosis and pinocytosis. Phagocytosis occurs predominantly in special cells called phagocytes, such as macrophages, neutrophils and monocytes, and pinocytosis refers to the uptake of fluids and solutes.[22,23] The endocytic pathways involved in the internalization of nanoparticles can be studied using endocytic markers to track the location of the nanoparticles, or using pharmacological inhibitors to identify the endocytic mechanism involved in the cellular uptake.[21,23]

The aim of this work is to investigate the internalization mechanism and intracellular localization of zeolite nanoparticles in breast cancer cells and normal epithelial mammary cells. Zeolite L was chosen due to its ordered porous structure where the channels are unidimensional and parallel to each other. Such configuration allows molecules to diffuse in

and out, and the channels can be closed with appropriate stopper molecules. In addition, small sized disc-shaped particles can be prepared, which decrease the tendency to form aggregates compared to zeolite Y. To achieve visualization of biologically related problems, we have used confocal imaging, scanning electron microscopy (SEM) and transmission electron microscopy (TEM). We have examined the cellular uptake of fluorescent labeled zeolite L in Hs 578T breast cancer cells, HMEC and MCF-10 epithelial mammary cells. In addition, pharmacological inhibitors were used to study the internalization mechanism. The results indicate that the internalization of zeolite L is faster in breast cancer cells than in normal cells and the internalization process is aided by a caveolin-mediated process. Our study gives a valuable contribution to the characterization of biological mechanisms involved in the uptake of zeolite nanoparticles by human cells.

4.1.2. EXPERIMENTAL

4.1.2.1. MATERIALS AND CELLS

Sodium hydroxide, aluminum hydroxide, potassium hydroxide and Ludox® HS-40 colloidal silica, were purchased from Merck, Acros Organics and Sigma Aldrich (St. Louis, MO), respectively. NaY zeolite (CBV100) was acquired from Zeolyst International. N,N'-Bis(2,6-dimethylphenyl)perylene-3,4,9,10-tetracarboxylic diimide (DXP) dye was acquired from Fluka.

Dulbecco's Modified Eagle's Medium (DMEM (1x)), Dulbecco's Modified Eagle's Medium F12 (DMEM/F12 (1:1)), HuMEC Ready Medium (HuMEC), Fetal Bovine Serum (FBS), Penicillin-Streptomycin (P/S) were purchased from Gibco. Human insulin solution, cholera toxin and hydrocortisone were acquired from Sigma Aldrich and epidermal growth factor (EGF) from Peprotech. The human breast cancer cell line Hs 587T was obtained from ATCC (American Type Culture Collection), the human mammary epithelial cells (HMEC) were obtained from Gibco™ and the MCF-10 epithelial mammary cells were kindly provided by Dra. Lígia Rodrigues (CEB, University of Minho, Portugal). The pharmacological inhibitors, chlorpromazine and dynasore, were obtained from Sigma Aldrich. α-Tubulin antibody (SC23948) was from Santa Cruz Biotechnology and Alexa Fluor 594 goat anti-mouse (A11032) was purchased from Life Technologies.

4.1.2.2. SYNTHESIS AND CHARACTERIZATION OF ZEOLITE L

Zeolite L was synthetized as previously described with some alterations.[24–26] Briefly, 1.74 g of sodium hydroxide, 2.70 g of potassium hydroxide and 0.65 g of aluminum hydroxide were added to a round-bottom flask containing 17.3 g of distilled water, and refluxed for 3 h at 120 °C until a clear solution was obtained. This solution was allowed to cool down to room

temperature and then the amount of lost water was added. Under mechanic stirring, the solution was added to 17.67 g of Ludox® HS-40 and then the obtained gel was transferred to a PTFE vessel and left at room temperature for 18 h. After that, the PTFE vessel was rotated at 40 rpm, 160 °C, for 48 h. After cooling, the zeolite was recovered by centrifugation (7000 rpm, 5 min) and washed five times with distilled water to obtain neutral pH. Finally, 1 g of zeolite L was dried under vacuum overnight.

The morphology and the particle size of zeolite L was assessed by scanning electron microscopy (SEM) (Quanta Feg 250, FEI Company, USA). The X-ray diffraction (XRD) pattern was studied with a Bruker D2 Phaser (Bruker, USA). Nitrogen adsorption isotherms were obtained with a Micromeritics porosimeter (model ASAP-2020). Fourier transform infrared analysis (FTIR) was performed using ABB-FLTA 2000 covering 4000-500 cm^{-1} range and recorded with a resolution of 8 cm^{-1}. Zeta potential was measured on a DelsaNano C Particle Analyzer, Beckman Coulter.

4.1.2.3. CELL CULTURE

Hs 587T breast cancer cells were cultured in DMEM (1x) with 10% of FBS and 1% of P/S. HMEC cells were cultured in HuMEC Basal Serum Media supplemented with 1% of HuMEC supplement and 70 mg mL^{-1} of bovine pituitary extract and 1% P/S. MCF-10 epithelial mammary cells were cultured in DMEM/F12 (1:1) containing 5% FBS, 1% P/S and supplemented with 20 ng mL^{-1} of EGF, 100 ng mL^{-1} of cholera toxin, 0.01 mg mL^{-1} of insulin and 500 ng mL^{-1} of hydrocortisone. Both cell lines were maintained in a humidified atmosphere of 5% CO_2 at 37 °C.

4.1.2.4. CELL VIABILITY ASSAYS

Sulforhodamine B (SRB) colorimetric assay was used to assess the effect of zeolite L and inhibitors, chlorpromazine and dynasore, on cell viability. For this purpose, Hs 578T (7000 cells per cm^2) and MCF-10 cells (5000 cells per cm^2) were seeded onto 96-well plates and incubated overnight at 37 °C under 5% CO_2 atmosphere. Then the medium was replaced by increasing concentrations of zeolite (10 - 125 µg mL^{-1}), chlorpromazine (2 - 10 µg mL^{-1}) and dynasore (100 - 400 µM) in medium with no FBS and incubated for 48 h with the zeolite solutions and 1 h with the inhibitor solutions. Then, the cells were fixed with cold 10% (w/v) trichloroacetic acid (TCA) for 1 h and washed three times with distilled water. After the fixation step, the cells were stained with SRB for 30 min and washed three times with 1% (v/v) acetic acid and left to dry. Then the dye was solubilized with 10 mM Tris base solution and the absorbance was read at 490 nm in a microplate reader.

4.1.2.5. INTERNALIZATION STUDIES OF ZEOLITE L BY MICROSCOPIC TECHNIQUES

In order to study the cell internalization of zeolites we have used and combined different techniques based on electron and optical microscopies.

SEM microscopy analysis: SEM analysis was performed to assess the surface interactions between zeolite L with Hs 578T breast cancer cells and HMEC human mammary epithelial cells. In addition to the studies with zeolite L, we also performed assays with zeolite Y, to evaluate the influence of particle size and shape in cellular internalization.

For these studies, cells were cultured onto 12 mm coverslips and incubated at 37 °C overnight. Then the culture medium was removed, and the cells were incubated with 50 µg mL^{-1} solution of the zeolites for 5, 10, 15, 20, 30 and 60 min. Afterwards, the used media was removed, and the cells were washed 3 times with PBS. Then the cells were fixed with 2.5% glutaraldehyde in PBS for 45 min at RT and for 1 h at 4 °C, and the fixed cells were also washed 3 times with PBS. After the fixation step, cells were dehydrated with increasing concentration of ethanol from 10% to 100%, for 20 min each. The coverslips were then dried at room temperature overnight. After this procedure, the coverslips were sputter-coated with gold and SEM images were then obtained with a FEI Quanta FEG 250 scanning electron microscope (FEI Company, USA).

Confocal microscopy analysis: The cell uptake of zeolite L into Hs 578T and MCF-10 cells was investigated by confocal microscopy. For this purpose, Hs 578T and MCF-10 cell lines were seeded onto coverslips in 24-well plates with the density of 2.5×10^4 cells per well and incubated at 37 °C in 5% CO_2 atmosphere overnight. Afterwards, 50 µg mL^{-1} zeolite L dispersion was added and incubated for 4 and 24 h. At the end of the incubation period, the cells were rinsed twice with PBS and fixed with cold methanol for 15 min, washed once with PBS Glycine 10 mM, washed again twice with PBS and permeabilized with triton x-100 0.1% for 10 min. Next, after two washes with PBS, the cells were blocked with BSA 5% in PBS during 30 min and then incubated with α-tubulin antibody (SC23948, Santacruz) diluted in 5% BSA in PBS (1:100) during 2 h at room temperature (RT). In the next step, cells were washed twice with PBS (5 min each) and incubated with the secondary antibody Alexa Fluor 594 goat anti-mouse (A11032, Life Technologies) diluted in 5% BSA in PBS (1:250) during 1 h at RT in the dark. Then, the cells were washed twice with PBS and the nuclei were stained with DAPI for 10 min. Finally, after two washes with PBS (5 min each) and one wash with sterile water (very quickly), the cells were mounted in Permafluor (Thermo Scientific).

Confocal images were obtained with an Olympus FV1000 confocal microscope (Olympus). Images were acquired with an LSM UPLSAPO 60.0 × 1.35 N.A. oil immersion objective. The

cells stained with DAPI (excitation/emission wavelength: 405/461 nm), and Alexa Fluor® 594 dye (excitation/emission wavelength: 559/618 nm) were excited independently at 405, and 559 nm, respectively. DXP dye was excited at 488 nm. Images were processed by Fluoview FV1000 software (Olympus). ImageJ software (National Institutes of Health) was used for quantification of the mean intracellular fluorescence.

TEM microscopy analysis: For TEM, Hs 578T and MCF-10 cells were seeded at the density of 1.5×10^5 and 1.8×10^5 cells per well, respectively, and incubated at 37 °C in 5% CO_2 atmosphere for 24 h. Then, the culture medium was removed, and the cells were incubated with 50 µg mL^{-1} dispersion zeolite L for 4 h and 24 h. After incubation, the spent media was removed, and the cells were washed three times with PBS 1x, trypsinized, centrifuged for 5 min at 900 rpm and resuspend in 1 mL of media. Then samples were fixed in 2.5% glutaraldehyde (Electron Microscopy sciences, Hatfield, USA) and 2% paraformaldehyde (Merck, Darmstadt, Germany) in cacodylate buffer 0.1 M (pH 7.4), dehydrated and embedded in Epon resin (TAAB, Berks, England). After that, ultrathin sections (40 - 60 nm thickness) were prepared on a RMC Ultramicrotome (PowerTome, USA) using diamond knives (DDK, Wilmington, DE, USA). The sections were mounted on 200 mesh copper or nickel grids, stained with uranyl acetate substitute and lead citrate for 5 min each, and examined under a JEOL JEM 1400 TEM (Tokyo, Japan). The images were digitally recorded using a CCD digital camera Orious 1100W Tokyo, Japan at the HEMS/i3S (IBMC) of the University of Porto. Recorded images were analysed using ImageJ Software. For quantification of the percentage of zeolite L nanoparticles internalized by cell lines, the images were thresholded leaving only the defined zeolite L nanoparticles and the area occupied by nanoparticles was calculated.[27]

Investigation of endocytosis mechanisms using pharmacological inhibitors: To explore the mechanism of zeolite L uptake, we used two pharmacological inhibitors, chlorpromazine (CPZ) which interferes with clathrin-mediated endocytosis by a translocation of clathrin and adaptor proteins from the plasma membrane to intracellular vesicles blocking the formation of clathrin-coated pit,[28–30] and dynasore which acts on clathrin and caveolin-mediated processes.[31,32] We used two approaches to investigate the effect of these inhibitors: flow cytometry and TEM.

For flow cytometry analysis (FACS), Hs 578T and MCF-10 cells were seeded in 6-well plates at density of 1.25×10^5 for both cell lines and treated with chlorpromazine (10 µg mL^{-1}) and dynasore (400 µM) in free-serum culture medium for 1 h at 37 °C, and incubated for 4 h with 50 µg mL^{-1} of zeolite L. After the incubation time, the cells were washed, detached by trypsinization, centrifuged, resuspended in PBS and analysed by FACS. For TEM analysis, the

cells were also treated with the inhibitors for 1 h and incubated with zeolite L for 4 h. After the incubation time, cells were prepared as described above.

4.1.2.6. STATISTICAL ANALYSIS

Statistically significant differences of the results from cytotoxicity studies were determined by Student's *t* test, and one-way analysis of variance (ANOVA) with the Dunnett's test. Differences between groups of the confocal and TEM results were evaluated by two-way ANOVA followed by Bonferroni post-test. A *p* value lower than 0.05 was considered statistically significant. All statistical analyses were performed with GraphPad Prism 6® software.

4.1.3. RESULTS AND DISCUSSION

4.1.3.1. PREPARATION AND CHARACTERIZATION OF ZEOLITE L

The characterization results of synthesized zeolite L are shown in Figure. 4.1.1. The size and morphology of zeolite particles were obtained by scanning electron microscopy (SEM) (Figure. 4.1.1A). SEM images revealed homogenous disc-shaped particles with an average diameter of 432 ± 7 nm determined by ImageJ. The powder XRD pattern of zeolite L (Figure. 4.1.1B) indicated the crystallinity of the synthesized material and revealed the characteristic XRD peaks of zeolite L at 2θ of 5.5, 19.4, 22.7, 28.0, 29.1 and 30.7.[33] Nitrogen adsorption analysis (Figure 4.1.1C) showed a Langmuir adsorption which is the typical adsorption pattern of microporous materials, with a pore size of 0.7 nm. From FTIR spectrum (Figure 4.1.1D), it is possible to see the characteristic bands of zeolite L. The band in the region between 1098 and 1020 cm^{-1} was assigned to the asymmetric stretch of the structure sensitive vibrations.[34] The bands at 3480-3410 cm^{-1} and 1641-1637 cm^{-1} are attributed to the O-H stretching vibration and O-H deformation, respectively. The bands at 642, 606 and 580 cm^{-1} are the vibrations of the tetrahedron due to the external linkages of the double rings in the framework structure and the bands between 767-721 cm^{-1} are due to the symmetric stretching of the internal tetrahedron of the zeolite structure.[35,36]

The zeta potential of the zeolite particles was measured in water at neutral pH and presented a value of -44 mV, confirming the negatively charged surface of zeolites.

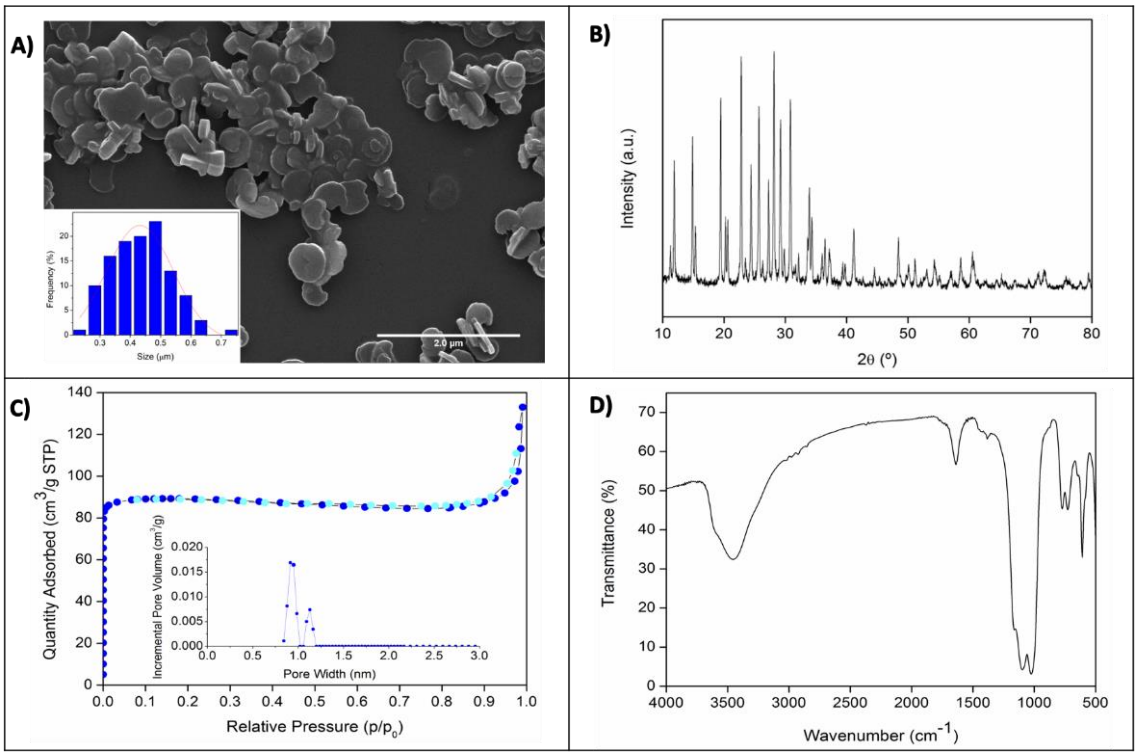

Figure 4.1.1: Characterization of the synthesized zeolite L. A) SEM micrographs of zeolite L dispersed in ethanol. Inset: Histogram representing statistical size distribution of zeolite L nanoparticles. B) XRD pattern of zeolite L. C) Nitrogen adsorption of zeolite L. Inset: pore size distribution. D) FTIR spectrum of zeolite L.

4.1.3.2. CYTOTOXICITY STUDIES

Viability tests were performed to evaluate the toxicity of zeolite L on Hs 578T breast cancer cells and MCF-10 epithelial mammary cells, using SRB assay. This assay is based on the binding of SRB to protein components of cells, allowing determination of cell density.[37]

Six test solutions of zeolite L were prepared according to our previously established procedure.[14,38,39] A stock solution (0.5 mg mL^{-1}) was diluted using culture medium in order to obtain the test concentrations (0.01, 0.025, 0.05, 0.075, 0.1 and 0.125 mg mL^{-1}). As described in our previous study, all suspensions were sonicated for 2 min for homogenization.[38,39]

The effect of zeolite L on Hs 578T breast cancer growth and MCF-10 epithelial cells after 48 h of incubation is shown in Figure 4.1.2. In the range of the tested concentrations, zeolite L did not exhibit any toxicity to normal cells, whereas the viability curve decreases for breast cancer cells from 0.05 mg mL^{-1}. However, reduction in Hs 578T cell growth is only significant at 0.125 mg mL^{-1} compared to the control, as calculated by Dunnett's test.

It was also important to evaluate the *in vitro* cytotoxicity of the endocytic inhibitors to know if the effect of the inhibitors comes from their endocytic inhibition capacity or toxicity to cells. So we investigated the effect of chlorpromazine and dynasore at three different concentrations: 2, 5 and 10 µg mL^{-1} for chlorpromazine and 100, 200 and 400 µM for dynasore. The inhibitors

were diluted in serum-free medium and incubated with the cells for 1 h. Both cell lines were quite insensitive to the tested concentration of chlorpromazine and dynasore, with viability values above 90% (data not shown).

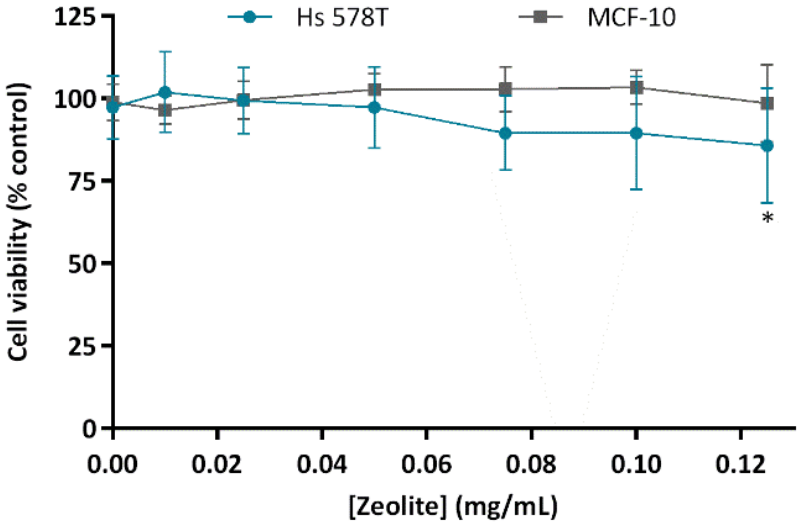

Figure 4.1.2: Cell viability of Hs 578T and MCF-10 cells, evaluated with SRB assay after 48 h incubation time with increasing concentrations of zeolite. Results are expressed in relation to the control (0% of zeolite, considered 100% of viability) as mean ± SD of three independent experiments, each performed in triplicate. Differences with a $p < 0.05$ were considered statistically significant (*).

4.1.3.3. KINETIC STUDIES OF ZEOLITE UPTAKE INTO HS 578T BREAST CANCER CELLS AND MCF-10 EPITHELIAL MAMMARY CELLS

To exploit the potential of zeolite L as drug delivery system, it is important to understand the interactions and internalization of this type of zeolite in living cells. For this purpose, SEM, TEM and confocal microscopy were used in breast cancer cells and epithelial mammary cells. SEM experiments were performed on Hs 578T and HMEC cells. In these assays, the cells were incubated for 60 min with 50 mg mL^{-1} of zeolite solutions. Different studies have demonstrated that the shape and size of particles can influence the uptake process by the cells.[40–42] For instance, Xie X. *et al.*[43] demonstrated that shape can modulate the uptake of nanoparticles into RAW264.7 cells and Liu X. *et al.*[44] have shown that the aspect ratio of bionanorods influences the internalization pathways in different cells. Thus, in the present study, besides SEM studies with zeolite L, we also performed SEM analysis with zeolite NaY which has a different morphology. Both materials have been tested in Hs 578T and HMEC cell lines in order to compare their rate of internalization and evaluate if the size and shape of zeolite nanoparticles have some effect on the kinetic or internalization process. The zeolite NaY used

in this work shows cubic geometry with an average diameter of 700 nm,[14] while zeolite L has disc-shaped particles around 400 nm.

SEM results for zeolite NaY (Figure 4.1.3) show that after 5 min of incubation the cells start to engulf the zeolite particles with their filopodia, but only few of them are inside the cell maybe also due to the formation of aggregates.

This result shows that the uptake of the zeolite particles is very fast, which is consistent with other published studies.[45] Upon increasing the incubation time, it is noteworthy that the particles start to cross the cell membrane and the number of particles that are internalized increased with time. After 1 h of incubation, a large number of particles are completely internalized by the cell membrane. In the case of zeolite L (Figure 4.1.4), it is possible to see that after 5 min of incubation more particles, compared with zeolite NaY, are already internalized. These results could be explained by the fact that this zeolite is smaller and thinner than zeolite NaY, which makes their uptake easier. Once again for zeolite L, the number of internalized particles increases upon increasing the incubation time. These results are in agreement with other studies in which 50 nm and 120 nm nanoparticles are internalized faster, compared to 250 nm particles.[46]

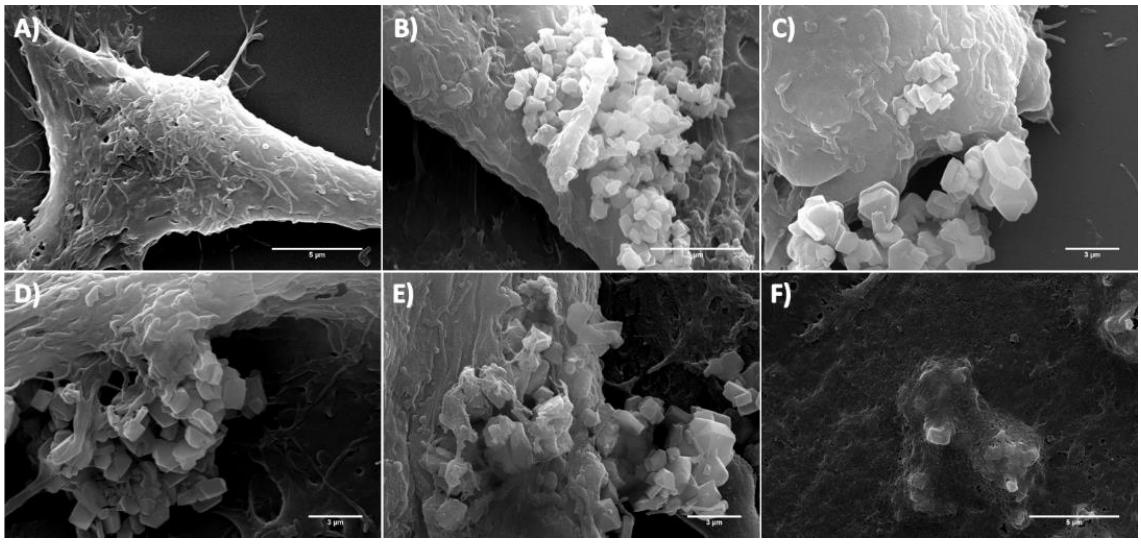

Figure 4.1.3: SEM micrographs showing the uptake of the zeolite NaY by Hs 578T breast cancer cells. (A) Control (without zeolite); cellular uptake observed after: (B) 5 min, (C) 10 min, (D) 15 min, (E) 30 min and (F) 60 min. Scale bar: (A, B and F) 5 µm and (C, D and E) 3 µm.

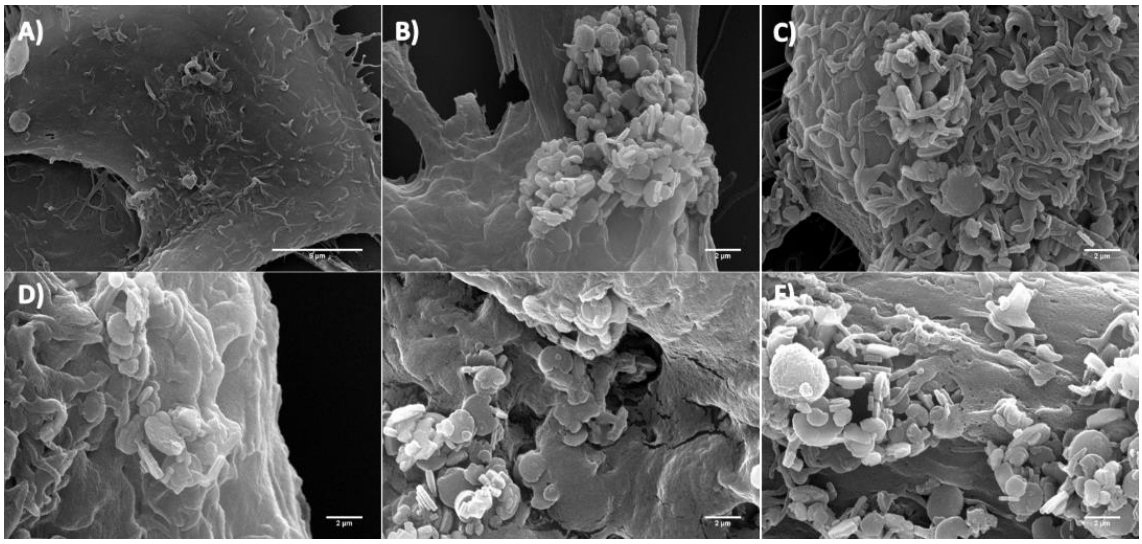

Figure 4.1.4: SEM micrographs showing the uptake of the zeolite L by Hs 578T breast cancer cells. (A) Control (without zeolite); cellular uptake observed after: (B) 5 min, (C) 10 min, (D) 15 min, (E) 30 min and (F) 60 min. Scale bar: (A) 5 µm and (B - F) 2 µm.

The results for HMEC epithelial mammary cells (Figure 4.1.5) show that the internalization of zeolite L is much slower than that for the breast cancer cells. Moreover, even after increasing the incubation time, just a small amount of zeolite nanoparticles is internalized.

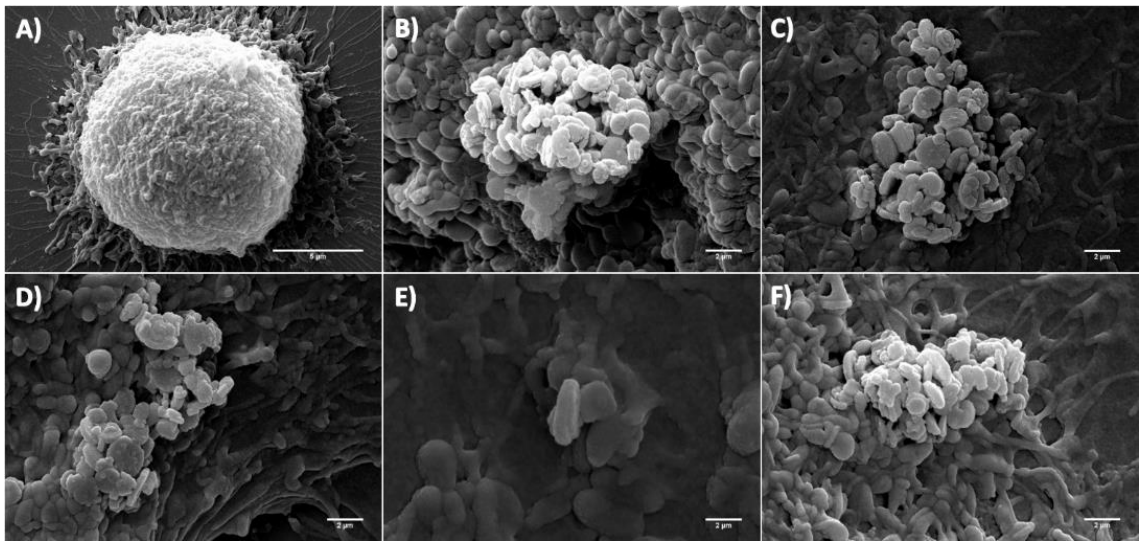

Figure 4.1.5: SEM micrographs showing the uptake of the zeolite L by HMEC epithelial mammary cells. (A) Control (without zeolite); cellular uptake observed after: (B) 5 min, (C) 10 min, (D) 15 min, (E) 30 min and (F) 60 min. Scale bar: (A) 5 µm and (B - F) 2 µm.

The obtained results show that the shape and the size of the particles have an important role in their internalization and that this process is also dependent on the cell type. Cancer cells are able to uptake zeolites at a faster rate due to their higher permeability. Since SEM

only allows the visualization of the cell surface, we also performed confocal microscopy and TEM to support these results. Therefore, zeolite L was loaded with a fluorescent dye, DXP, which is insoluble in aqueous media, and therefore it is not released from the zeolite pores.[47] Intracellular localization of zeolite L was carried out by Hs 578T and MCF-10 cells, incubated with 50 µg mL^{-1} of zeolite nanoparticles during 4 and 24 h. The uptake of the particles was analysed by confocal microscopy upon excitation of the dye at 488 nm and z-stacking analysis confirmed the internalization.

Figure 4.1.6 shows the confocal images and z-stack for Hs 578T cells taken after 4 and 24 h incubation. After 4 h, it is clear that a significant amount of zeolite nanoparticles is already inside the cells and after 24 h the amount of zeolite particles becomes higher, with the particles being predominantly localized in the cytoplasm. This is in line with other studies which have demonstrated that the cellular uptake of nanoparticles is time-dependent.[48]

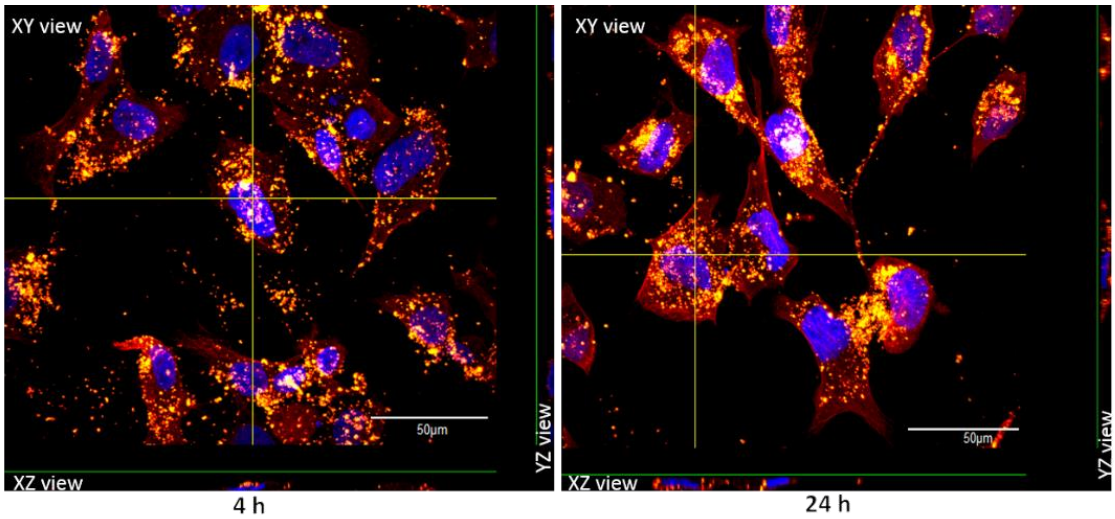

Figure 4.1.6: Confocal images of Hs 578T cells incubated with 50 µg mL^{-1} of zeolite L. Z-stack proving the uptake of zeolite L at 4 and 24 h incubation times. Cells nuclei were stained with DAPI (blue), α-tubulin was immunolabeled with a specific Alexa Fluor 594-coupled antibody (red) and zeolite L nanoparticles were labeled with DXP (yellow). Scale bar: 50 µm.

But unlike, what was observed for Hs 578T cells, the uptake of zeolite L in MCF-10 cells, after the same times of incubation (Figure 4.1.7), is lower. At 4 h of incubation, the fluorescence intensity measured using ImageJ, for Hs 578T cell line was 18.3 (± 0.3) while for MCF-10 cells was 16.1 (± 0.4). For 24 h of incubation the fluorescence intensity was higher in both cell lines, 22.2 (± 1.7) for Hs 578T and 18.2 (± 0.7) for MCF-10 (Figure 4.1.8). Commonly, the attractive forces such as van der Waals and electrostatic forces are responsible for the interaction between the particles and cell membranes and these interactions become more intense with time.[49] Zeolites are negatively charged and it seems that for the MCF-10 cell line, there is some

repulsion between zeolite nanoparticles and cells (Figure 4.1.7, white arrows). This repulsion suggests that the zeolite nanoparticles have low impact on these healthy cells.

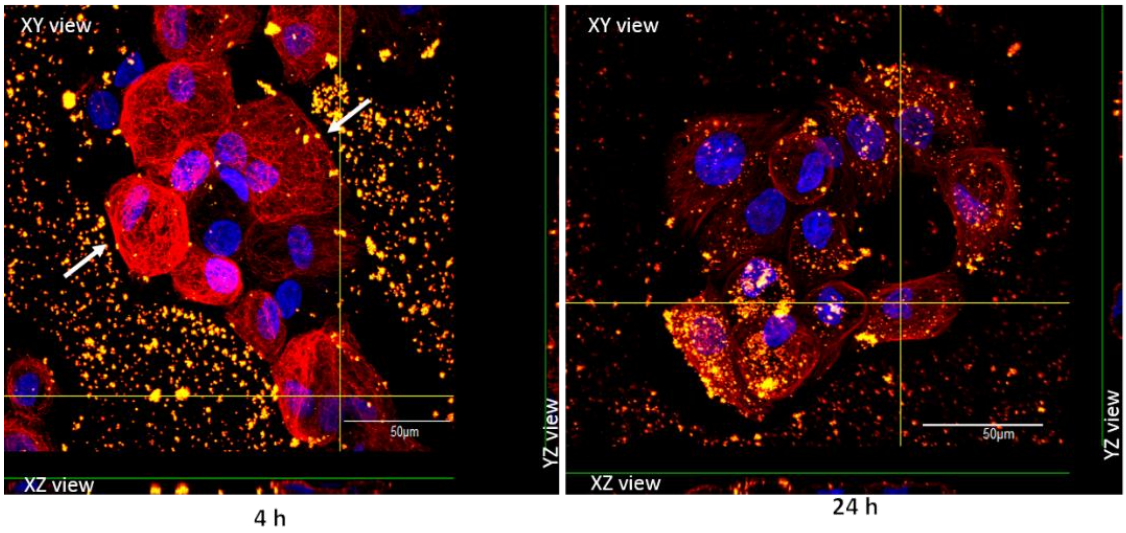

Figure 4.1.7: Confocal images of MCF-10 cells incubated with 50 µg mL^{-1} of zeolite L. Z-stack proves the uptake of zeolite L at 4 and 24 h incubation times. Cells nuclei were stained with DAPI (blue), α-tubulin was immunolabeled with a specific Alexa Fluor 594-coupled antibody (red) and zeolite L nanoparticles were labeled with DXP (yellow). Scale bar: 50 µm.

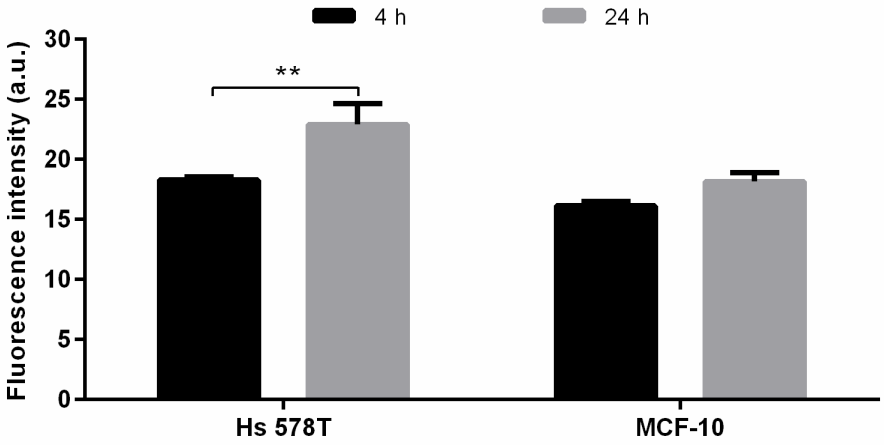

Figure 4.1.8: Percentage of zeolite L nanoparticles internalized by Hs 578T and MCF-10 cells. Cells were incubated with 50 µg mL^{-1} of zeolite L at 4 and 24 h incubation times. Results were analyzed by ImageJ Software. Difference between groups were evaluated by Two-way ANOVA followed by Bonferroni post-test. ***$p < 0.001$. Mean ± SD. n=4 for Hs 578T experiments and n=5 for MCF-10 experiments.

Confocal results confirm the SEM results in which we also observed more internalization in breast cancer cells than in epithelial mammary cells and once again confirm that the internalization of zeolite L nanoparticles is time-dependent. The higher internalization rates of

zeolite L in breast cancer cells than in epithelial mammary cells, due to a higher permeability of the membrane, might explain the lower toxicity of zeolite L on epithelial mammary cells obtained by the cell viability test.

TEM results for Hs 578T cell line for 4 and 24 h of incubation (Figure 4.1.9) clearly shows that the zeolite is internalized by the cells and it is localized mostly in vacuoles. By comparing these results with those for MCF-10 cell line (Figure 4.1.10) for the same incubation time, we observe again that the number of the internalized particles is lower than for Hs 578T cells (Figure 4.1.11). These results also corroborate the confocal data. Our results are not the only ones which show that the internalization of nanoparticles is higher in cancer cells. Other studies showed that ZnAl-HTlc nanoparticles were internalized faster by HeLa cervical cancer cells than in MDCK normal cells, and also demonstrated that the internalization is time-dependent.[50]

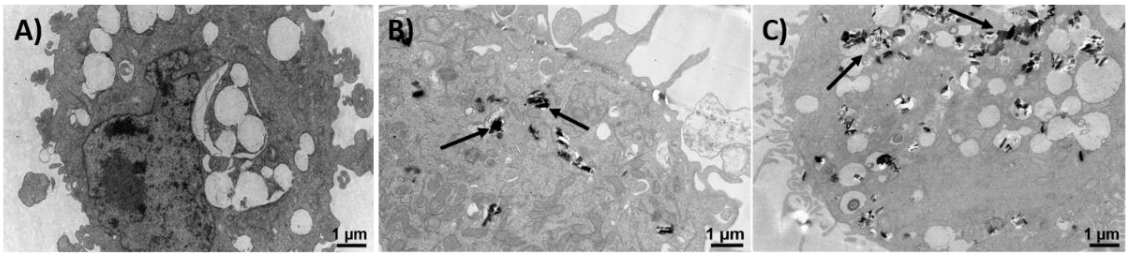

Figure 4.1.9: TEM micrographs of Hs 578T cells incubated with 50 µg mL^{-1} of zeolite L. (A) Control (cells only); (B) the uptake of zeolite L at 4 h of incubation time; (C) the uptake of zeolite L at 24 h of incubation time. The arrows indicate the presence of zeolite L. Scale bar: 1 µm.

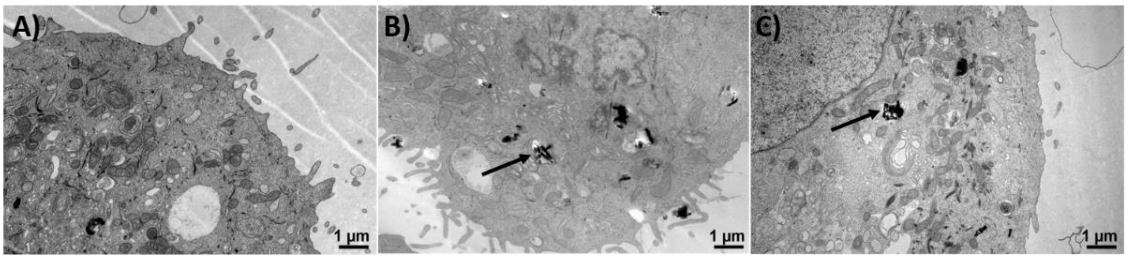

Figure 4.1.10: TEM micrographs of MCF-10 cells incubated with 50 µg mL^{-1} of zeolite L. (A) Control (cells only); (B) the uptake of zeolite L at 4 h of incubation time; (C) the uptake of zeolite L at 24 h of incubation time. The arrows indicate the presence of zeolite L. Scale bar: 1 µm.

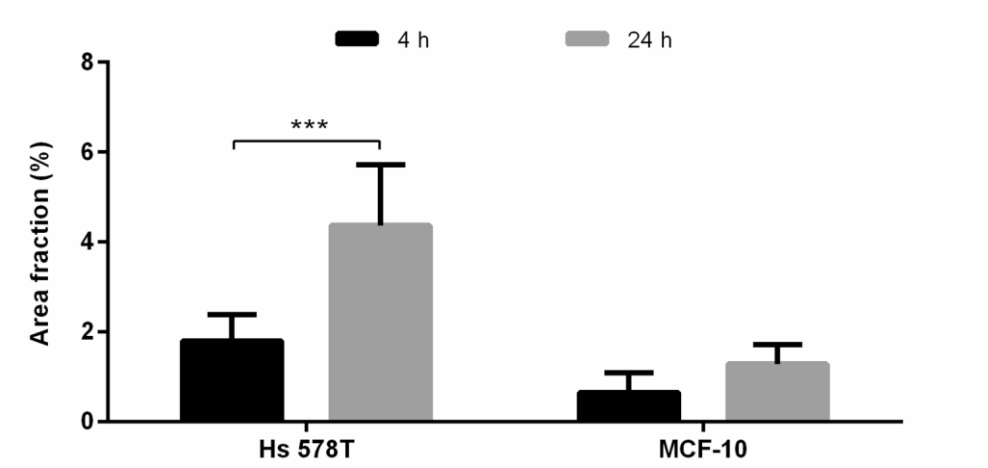

Figure 4.1.11: Percentage of zeolite L nanoparticles internalized by Hs 578T and MCF-10 cells. Cells were incubated with 50 µg mL^{-1} of zeolite L at 4 and 24 h incubation times. Results were analyzed by ImageJ Software. Difference between groups were evaluated by Two-way ANOVA followed by Bonferroni post-test. ***$p < 0.001$. Mean ± SD. n=4 for Hs 578T experiments and n=5 for MCF-10 experiments.

4.1.3.4. THE EFFECTS OF ENDOCYTIC INHIBITORS ON CELLULAR UPTAKE

In order to clarify the mechanism of internalization of zeolite L, we studied the zeolite uptake by Hs 578T and MCF-10 cells in the presence of two inhibitors, chlorpromazine (CPZ) and dynasore, which inhibit clathrin-dependent endocytosis and block GTPase activity of dynamin on clathrin and caveolin-mediated processes, respectively.[51,52] For this propose we used flow cytometry and TEM analyses. The internalization of zeolite L by Hs 578T and MCF-10 cells without any pharmacological inhibitor and in the presence of CPZ or dynasore is shown in Figure 4.1.12. The literature data suggest that the internalization of zeolite L is affected by CPZ and dynasore.[53] However, our results show that the pre-treatment of Hs 578T cells with CPZ, prior to incubation with the zeolite L had no effect on its uptake. In contrast, dynasore caused a significant decrease in the uptake of the zeolite L.

The same behaviour was observed for MCF-10 cells, with no effect of CPZ and with dynasore exerting some inhibition on the internalization of zeolite L. The findings that CPZ had no effect on zeolite L internalization, could be related to the cell lines used in this work, since the internalization of particles is cell type- dependent.[54,55]

Since CPZ inhibits clathrin-dependent endocytosis and dynasore inhibits clathrin and caveolin-mediated processes, the internalization of the zeolite L appears to be mediated by caveolin. These results also show that without any pharmacological inhibitor, Hs 578T cells internalize a bigger amount of zeolite L nanoparticles than MCF-10 cells, which is in accordance with the microscopy results.

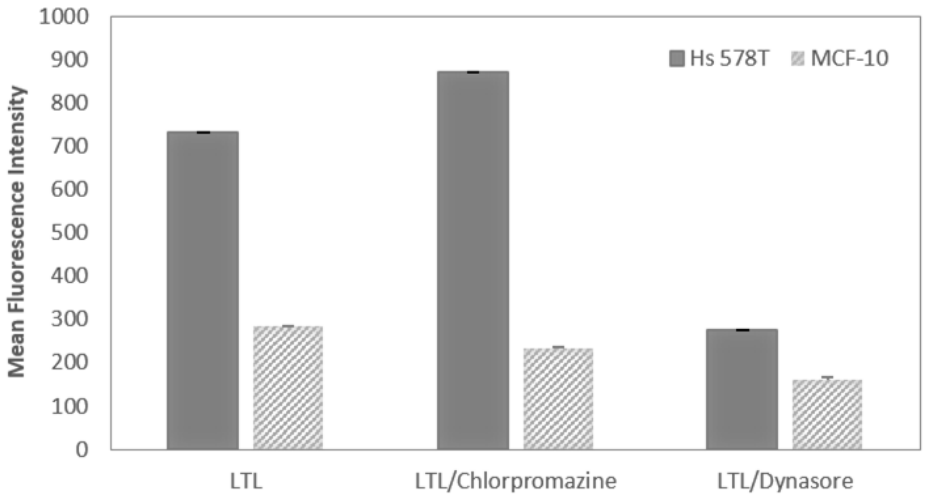

Figure 4.1.12: Effects of the pharmacological inhibitors on the uptake of zeolite L in Hs 578T and MCF-10 cells. Cells were treated with chlorpromazine (10 µg mL^{-1}) and dynasore (400 µM) for 1 h before incubation with 50 µg mL^{-1} of zeolite L for 4 h. After incubation cells were collected and analyzed by flow cytometry.

Flow cytometry results were also confirmed by TEM (Figure 4.1.13), where it is possible to observe the particles inside Hs 578T and MCF-10 cells when CPZ is used (Figure 4.1.13B and E), as opposed to dynasore, where there are no particles inside Hs 578T (Figure 4.1.13C) and only a small amount of zeolites are observed in MCF-10 cells (Figure 4.1.13F).

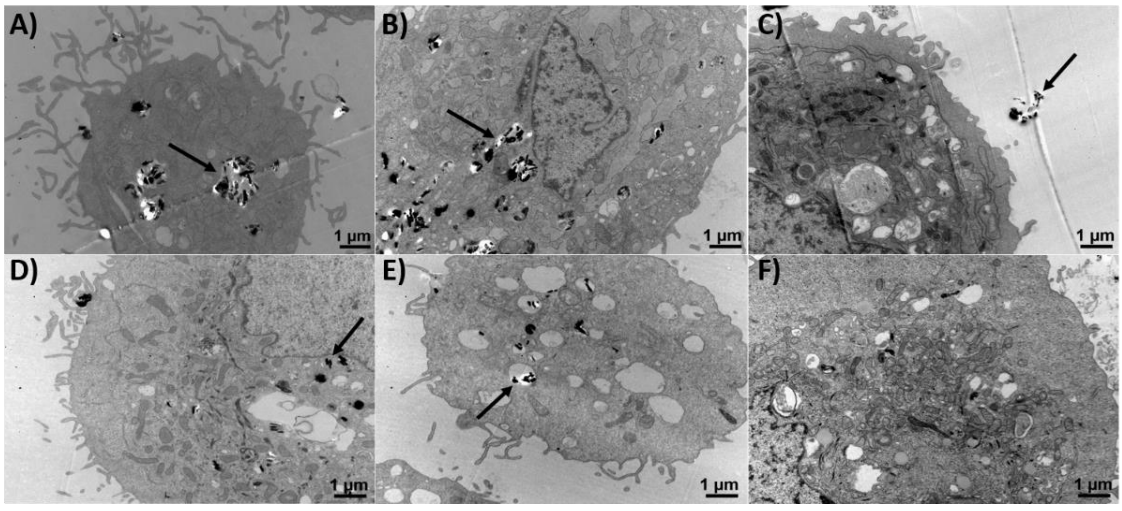

Figure 4.1.13: TEM images of the effect of the pharmacological inhibitors on the uptake of zeolite L in Hs 578T and MCF-10 cells incubated with 50 µg mL^{-1} of zeolite L for 4 h. (A) Hs 578T without inhibitor; (B) Hs 578T treated with 10 µg mL^{-1} of chlorpromazine; (C) Hs 578T treated with 400 µM of dynasore; (D) MCF-10 without inhibitor; (E) MCF-10 treated with 10 µg mL^{-1} of chlorpromazine and (F) MCF-10 treated with 400 µM of dynasore. The arrows indicate the localization of zeolite L. Scale bar: 1 µm.

4.1.4. CONCLUSIONS

In this work, we proved by SEM analysis that cell internalization of the zeolite L was faster in breast cancer cells when compared to normal breast cells, with some particles already internalized after 5 min of incubation. Internalization of zeolite L by the normal epithelial mammary cells was slower and, even after 60 min of incubation, only a small number of nanoparticles were internalized. The same behaviour was observed by confocal and TEM analyses, that evidenced that breast cancer cells internalize a higher number of zeolite nanoparticles than epithelial mammary cells, with the particles mainly localized in the vacuoles in both of the cell lines. The use of endocytic pharmacological inhibitors suggests that zeolite L is internalized by the cells by means of a caveolin-mediated process since dynasore inhibited significantly the uptake. These results may contribute to optimize the uptake of these systems by cancer cells.

4.1.5. REFERENCES

1 J. Ferlay, I. Soerjomataram, R. Dikshit, S. Eser, C. Mathers, M. Rebelo, D. M. Parkin, D. Forman and F. Bray, Cancer incidence and mortality worldwide: Sources, methods and major patterns in GLOBOCAN 2012, *Int. J. Cancer*, 2015, **136**, E359–E386.

2 C. Fitzmaurice, D. Dicker, A. Pain, H. Hamavid, M. Moradi-Lakeh, M. F. MacIntyre, C. Allen, G. Hansen, R. Woodbrook, C. Wolfe, R. R. Hamadeh, A. Moore, A. Werdecker, B. D. Gessner, B. Te Ao, B. McMahon, C. Karimkhani, C. Yu, G. S. Cooke, D. C. Schwebel, D. O. Carpenter, D. M. Pereira, D. Nash, D. S. Kazi, D. De Leo, D. Plass, K. N. Ukwaja, G. D. Thurston, K. Yun Jin, E. P. Simard, E. Mills, E.-K. Park, F. Catalá-López, G. DeVeber, C. Gotay, G. Khan, H. D. Hosgood, I. S. Santos, J. L. Leasher, J. Singh, J. Leigh, J. B. Jonas, J. Sanabria, J. Beardsley, K. H. Jacobsen, K. Takahashi, R. C. Franklin, L. Ronfani, M. Montico, L. Naldi, M. Tonelli, J. Geleijnse, M. Petzold, M. G. Shrime, M. Younis, N. Yonemoto, N. Breitborde, P. Yip, F. Pourmalek, P. A. Lotufo, A. Esteghamati, G. J. Hankey, R. Ali, R. Lunevicius, R. Malekzadeh, R. Dellavalle, R. Weintraub, R. Lucas, R. Hay, D. Rojas-Rueda, R. Westerman, S. G. Sepanlou, S. Nolte, S. Patten, S. Weichenthal, S. F. Abera, S.-M. Fereshtehnejad, I. Shiue, T. Driscoll, T. Vasankari, U. Alsharif, V. Rahimi-Movaghar, V. V. Vlassov, W. S. Marcenes, W. Mekonnen, Y. A. Melaku, Y. Yano, A. Artaman, I. Campos, J. MacLachlan, U. Mueller, D. Kim, M. Trillini, B. Eshrati, H. C. Williams, K. Shibuya, R. Dandona, K. Murthy, B. Cowie, A. T. Amare, C. A. Antonio, C. Castañeda-Orjuela, C. H. van Gool, F. Violante, I.-H. Oh, K. Deribe, K. Soreide, L. Knibbs, M. Kereselidze, M. Green, R. Cardenas, N. Roy, T. Tillmann, Y. Li, H. Krueger, L. Monasta, S. Dey, S. Sheikhbahaei, N. Hafezi-

Nejad, G. A. Kumar, C. T. Sreeramareddy, L. Dandona, H. Wang, S. E. Vollset, A. Mokdad, J. A. Salomon, R. Lozano, T. Vos, M. Forouzanfar, A. Lopez, C. Murray and M. Naghavi, The Global Burden of Cancer 2013., *JAMA Oncol.*, 2015, **1**, 505–527.

3 K. Servick, Breast Cancer: A World of Differences, *Science (80-.).*, 2014, **343**, 1452–1453.

4 L. Hutchinson, Breast cancer: Challenges, controversies, breakthroughs, *Nat. Rev. Clin. Oncol.*, 2010, **7**, 669–670.

5 C. Núñez, J. L. Capelo, G. Igrejas, A. Alfonso, L. M. Botana and C. Lodeiro, An overview of the effective combination therapies for the treatment of breast cancer, *Biomaterials*, 2016, **97**, 34–50.

6 World Health Organization and International Agency for Research on Cancer, Latest world cancer statistics Global cancer burden rises to 14.1 million new cases in 2012: Marked increase in breast cancers must be addressed, http://www.iarc.fr/en/media-centre/pr/2013/pdfs/pr223_E.pdf, (accessed 1 April 2017).

7 J. Cuzick, A. DeCensi, B. Arun, P. H. Brown, M. Castiglione, B. Dunn, J. F. Forbes, A. Glaus, A. Howell, G. von Minckwitz, V. Vogel and H. Zwierzina, Preventive therapy for breast cancer: A consensus statement, *Lancet Oncol.*, 2011, **12**, 496–503.

8 G. Sahay, D. Y. Alakhova and A. V. Kabanov, Endocytosis of nanomedicines, *J. Control. Release*, 2010, **145**, 182–195.

9 S. M. Sagnella, J. A. McCarroll and M. Kavallaris, Drug delivery: Beyond active tumour targeting, *Nanomedicine Nanotechnology, Biol. Med.*, 2014, **10**, 1131–1137.

10 O. M. Koo, I. Rubinstein and H. Onyuksel, Role of nanotechnology in targeted drug delivery and imaging: a concise review, *Nanomedicine Nanotechnology, Biol. Med.*, 2005, **1**, 193–212.

11 T. Sun, Y. S. Zhang, B. Pang, D. C. Hyun, M. Yang and Y. Xia, Engineered nanoparticles for drug delivery in cancer therapy, *Angew. Chemie - Int. Ed.*, 2014, **53**, 12320–12364.

12 Y. Zhang, H. F. Chan and K. W. Leong, Advanced materials and processing for drug delivery: The past and the future, *Adv. Drug Deliv. Rev.*, 2013, **65**, 104–120.

13 R. Gupta, J. Shea, C. Scafe, A. Shurlygina and N. Rapoport, Polymeric micelles and nanoemulsions as drug carriers: Therapeutic efficacy, toxicity, and drug resistance, *J. Control. Release*, 2015, **212**, 70–77.

14 N. Vilaça, R. Amorim, A. F. Machado, P. Parpot, M. F. R. Pereira, M. Sardo, J. Rocha, A. M. Fonseca, I. C. Neves and F. Baltazar, Potentiation of 5-fluorouracil encapsulated in zeolites as drug delivery systems for *in vitro* models of colorectal carcinoma, *Colloids Surfaces B Biointerfaces*, 2013, **112**, 237–244.

15 M. G. Rimoli, M. R. Rabaioli, D. Melisi, A. Curcio, S. Mondello, R. Mirabelli and E. Abignente, Synthetic zeolites as a new tool for drug delivery, *J. Biomed. Mater. Res. - Part A*, 2008, **87**, 156–164.

16 A. Datt, E. A. Burns, N. A. Dhuna and S. C. Larsen, Loading and release of 5-fluorouracil from HY zeolites with varying SiO2/Al2O3 ratios, *Microporous Mesoporous Mater.*, 2013, **167**, 182–187.

17 S. M. Auerbach, K. A. Carrado and P. K. Dutta, *Zeolite Science and Technology*, CRC Press, 2003.

18 E. Khodaverdi, H. A. Soleimani, F. Mohammadpour and F. Hadizadeh, Synthetic Zeolites as Controlled-Release Delivery Systems for Anti-Inflammatory Drugs, *Chem. Biol. Drug Des.*, 2016, **87**, 849–857.

19 A. Szarpak-Jankowska, C. Burgess, L. De Cola and J. Huskens, Cyclodextrin-modified zeolites: host-guest surface chemistry for the construction of multifunctional nanocontainers, *Chemistry*, 2013, **19**, 14925–14930.

20 E. Khodaverdi, R. Honarmandi, M. Alibolandi, R. Rafatpanah Baygi, F. Hadizadeh and G. Zohuri, Evaluation of synthetic zeolites as oral delivery vehicle for anti-inflammatory drugs, *Iran. J. Basic Med. Sci.*, 2014, **17**, 337–343.

21 T.-G. Iversen, T. Skotland and K. Sandvig, Endocytosis and intracellular transport of nanoparticles: Present knowledge and need for future studies, *Nano Today*, 2011, **6**, 176–185.

22 H. Hillaireau and P. Couvreur, Nanocarriers' entry into the cell: Relevance to drug delivery, *Cell. Mol. Life Sci.*, 2009, **66**, 2873–2896.

23 L. Kou, J. Sun, Y. Zhai and Z. He, The endocytosis and intracellular fate of nanomedicines: Implication for rational design, *Asian J. Pharm. Sci.*, 2013, **8**, 1–10.

24 O. Bossart, L. De Cola, S. Welter and G. Calzaferri, Injecting electronic excitation energy into an artificial antenna system through an Ru2+ complex, *Chem. - A Eur. J.*, 2004, **10**, 5771–5775.

25 Z. Li, J. Hüve, C. Krampe, G. Luppi, M. Tsotsalas, J. Klingauf, L. De Cola and K. Riehemann, Internalization pathways of anisotropic disc-shaped zeolite L nanocrystals with different surface properties in HeLa cancer cells, *Small*, 2013, **9**, 1809–1820.

26 N. S. Kehr, B. Ergün, H. Lülf and L. De Cola, Spatially controlled channel entrances functionalization of zeolites l, *Adv. Mater.*, 2014, **26**, 3248–3252.

27 J. J. McDougall, A. K. Barin and C. M. McDougall, Loss of vasomotor responsiveness to the mu-opioid receptor ligand endomorphin-1 in adjuvant monoarthritic rat knee joints., *Am. J. Physiol. Regul. Integr. Comp. Physiol.*, 2004, **286**, 634–641.

28 D. Vercauteren, R. E. Vandenbroucke, A. T. Jones, J. Rejman, J. Demeester, S. C. De Smedt, N. N. Sanders and K. Braeckmans, The use of inhibitors to study endocytic pathways of gene carriers: optimization and pitfalls., *Mol. Ther.*, 2010, **18**, 561–569.

29 H. T. McMahon and E. Boucrot, Molecular mechanism and physiological functions of clathrin-mediated endocytosis, *Nat Rev Mol Cell Biol*, 2011, **12**, 517–533.

30 J. A. Daniel, N. Chau, M. K. Abdel-Hamid, L. Hu, L. von Kleist, A. Whiting, S. Krishnan, P. Maamary, S. R. Joseph, F. Simpson, V. Haucke, A. McCluskey and P. J. Robinson, Phenothiazine-Derived Antipsychotic Drugs Inhibit Dynamin and Clathrin-Mediated Endocytosis, *Traffic*, 2015, **16**, 635–654.

31 T. Kirchhausen, E. Macia and H. E. Pelish, Use of Dynasore, the Small Molecule Inhibitor of Dynamin, in the Regulation of Endocytosis, *Methods Enzymol.*, 2008, **438**, 77–93.

32 J. M. Steinbach, Y.-E. Seo and W. M. Saltzman, Cell penetrating peptide-modified poly(lactic-co-glycolic acid) nanoparticles with enhanced cell internalization., *Acta Biomater.*, 2016, **30**, 49–61.

33 H. R. Aghabozorg, S. S. Hassani and F. Salehirad, in *Modern Aspects of Bulk Crystal and Thin Film Preparation*, ed. Dr. Nikolai Kolesnikov, InTech, 2012, pp. 357–372.

34 Y. Di, Y. Yu, Y. Sun, X. Yang, S. Lin, M. Zhang, L. Shougui and F. S. Xiao, Synthesis, characterization, and catalytic properties of stable mesoporous aluminosilicates assembled from preformed zeolite L precursors, *Microporous Mesoporous Mater.*, 2003, **62**, 221–228.

35 E. M. Flanigen, H. Khatami and H. A. Szymanski, in *Molecular Sieve Zeolites-I*, American Chemical Society, 1974, vol. 101, pp. 16–201.

36 H. G. Karge, in *Verified Syntheses of Zeolitic Materials*, 2001, pp. 69–71.

37 V. Vichai and K. Kirtikara, Sulforhodamine B colorimetric assay for cytotoxicity screening., *Nat. Protoc.*, 2006, **1**, 1112–1116.

38 R. Amorim, N. Vilaça, O. Martinho, R. M. Reis, M. Sardo, J. Rocha, A. M. Fonseca, F. Baltazar and I. C. Neves, Zeolite structures loading with an anticancer compound as drug delivery systems, *J. Phys. Chem. C*, 2012, **116**, 25642–25650.

39 N. Vilaça, R. Amorim, O. Martinho, R. M. Reis, F. Baltazar, A. M. Fonseca and I. C. Neves, Encapsulation of a-cyano-4-hydroxycinnamic acid into a NaY zeolite., *J. Mater. Sci.*, 2011, **46**, 7511–7516.

40 E. C. Cho, L. Au, Q. Zhang and Y. Xia, The Effects of Size, Shape, and Surface Functional Group of Gold Nanostructures on Their Adsorption and Internalization by Cells, *Small*, 2010, **6**, 517–522.

41 W. Jiang, B. Y. S. Kim, J. T. Rutka and W. C. W. Chan, Nanoparticle-mediated cellular response is size-dependent., *Nat. Nanotechnol.*, 2008, **3**, 145–50.

42 S. Zhang, J. Li, G. Lykotrafitis, G. Bao and S. Suresh, Size-Dependent Endocytosis of Nanoparticles, *Adv. Mater.*, 2009, **21**, 419–424.

43 X. Xie, J. Liao, X. Shao, Q. Li and Y. Lin, The Effect of shape on Cellular Uptake of Gold Nanoparticles in the forms of Stars, Rods, and Triangles, *Sci. Rep.*, 2017, **7**, 3827.

44 X. Liu, F. Wu, Y. Tian, M. Wu, Q. Zhou, S. Jiang and Z. Niu, Size Dependent Cellular Uptake of Rod-like Bionanoparticles with Different Aspect Ratios, *Sci. Rep.*, 2016, **6**, 24567.

45 E. A. Prasetyanto, A. Bertucci, D. Septiadi, R. Corradini, P. Castro-Hartmann and L. De Cola, Breakable Hybrid Organosilica Nanocapsules for Protein Delivery, *Angew. Chemie - Int. Ed.*, 2016, **55**, 3323–3327.

46 W.-L. L. Suen and Y. Chau, Size-dependent internalisation of folate-decorated nanoparticles via the pathways of clathrin and caveolae-mediated endocytosis in ARPE-19 cells, *J. Pharm. Pharmacol.*, 2014, **66**, 564–573.

47 A. Bertucci, H. Lülf, D. Septiadi, A. Manicardi, R. Corradini and L. De Cola, Intracellular Delivery of Peptide Nucleic Acid and Organic Molecules Using Zeolite-L Nanocrystals, *Adv. Healthc. Mater.*, 2014, **3**, 1812–1817.

48 J. Davda and V. Labhasetwar, Characterization of nanoparticle uptake by endothelial cells, *Int. J. Pharm.*, 2002, **233**, 51–59.

49 E. Huerta-García, S. G. Márquez-Ramírez, M. del P. Ramos-Godinez, A. López-Saavedra, L. A. Herrera, A. Parra, E. Alfaro-Moreno, E. O. Gómez and R. López-Marure, Internalization of titanium dioxide nanoparticles by glial cells is given at short times and is mainly mediated by actin reorganization-dependent endocytosis, *Neurotoxicology*, 2015, **51**, 27–37.

50 T. Posati, F. Bellezza, L. Tarpani, S. Perni, L. Latterini, V. Marsili and A. Cipiciani, Selective internalization of ZnAl-HTlc nanoparticles in normal and tumor cells. A study of their potential use in cellular delivery, *Appl. Clay Sci.*, 2012, **55**, 62–69.

51 O. Heikkilä, P. Susi, T. Tevaluoto, H. Härmä, V. Marjomäki, T. Hyypiä and S. Kiljunen, Internalization of coxsackievirus A9 is mediated by β2-microglobulin, dynamin, and Arf6 but not by caveolin-1 or clathrin., *J. Virol.*, 2010, **84**, 3666–3681.

52 T. dos Santos, J. Varela, I. Lynch, A. Salvati and K. A. Dawson, Effects of Transport Inhibitors on the Cellular Uptake of Carboxylated Polystyrene Nanoparticles in Different Cell Lines, *PLoS One*, 2011, **6**, e24438.

53 R. Marega, E. A. Prasetyanto, C. Michiels, L. De Cola and D. Bonifazi, Fast Targeting and Cancer Cell Uptake of Luminescent Antibody-Nanozeolite Bioconjugates, *Small*, 2016, **12**, 5431–5441.

54 S. Bhattacharyya, R. D. Singh, R. Pagano, J. D. Robertson, R. Bhattacharya and P. Mukherjee, Switching the Targeting Pathways of a Therapeutic Antibody by Nanodesign, *Angew. Chemie Int. Ed.*, 2012, **51**, 1563–1567.

55 B. D. Grant and J. G. Donaldson, Pathways and mechanisms of endocytic recycling, *Nat. Rev. Mol. Cell Biol.*, 2009, **10**, 597–608.

SUBCHAPTER 4.2

ENDORSEMENT OF ENDOCYTIC PATHWAY INVOLVED IN THE INTERNALIZATION OF ZEOLITE NANOPARTICLES BY HUMAN CELLS[6]

Due to an increasing interest in the biomedical applications of nanocarriers, it becomes more important to better understand their interaction with human cells. To gain further insight in this direction, in this work, studies of internalization of the parent zeolite L, using six pharmacological inhibitors, were performed to unveil the endocytic pathway involved. The results show that the zeolite L nanoparticles were internalized by a caveolin-mediated process, in breast cancer and epithelial mammary human cells. Also, the outer surface of disc-shaped zeolite L was functionalized using different compounds, amino (NH_2) or carboxylic acid (COOH) groups and coated with poly-L-lysine (PLL) in order to assess if the surface charges of the nanoparticles have influence on the cellular uptake and endorse the internalization mechanism. Thus, we investigated the biocompatibility of these modified nanomaterials towards human cells. Subsequently, the uptake of these modified nanomaterials was examined, using confocal microscopy, scanning electron microscopy (SEM) and transmission electron microscopy (TEM) at different temperatures (37 °C and 4 °C). The obtained results show that functionalized nanomaterials are non-toxic to the human cells and that their internalization is fast, being faster for the nanomaterial modified with PLL (see graphical abstract below).

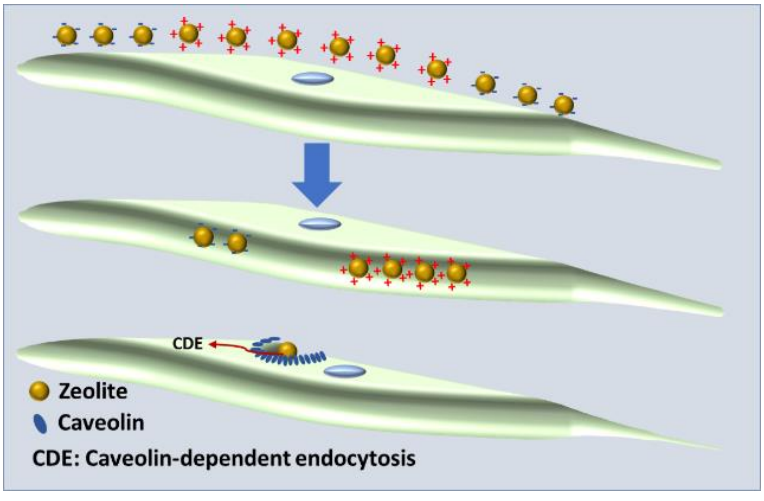

[6] **N. Vilaça**, E. A. Prasetyanto, R. Fernandes, F. Figueiredo, A. M. Fonseca, L. De Cola, F. Baltazar, I. C. Neves, Endorsement of endocytic pathway involved in the internalization of zeolite nanoparticles by human cells, *submitted*.

4.2.1. INTRODUCTION

The application of nanotechnology in medicine is a new and exciting field which can bring powerful progresses in the prevention, diagnosis and treatment of diseases by developing more efficient strategies.[1] Nanocarriers display characteristics that make them interesting for the delivery of drugs, such as, high surface area per unit volume ratio, their small size and easy surface functionalization.[2,3] There are numerous advantages related with drug delivery systems (DDS) using nanocarriers, including transport of the drugs to target tissues, protection of the drug from degradation and increase in drug concentration in the intended local of action, requiring lower doses of drug.[4,5] Thus, it is essential to develop systems with more efficient drug delivery.[6] For that, it is crucial to know the internalization mechanism of the DDS. This mechanism can occur by endocytosis. Endocytosis can be divided into phagocytosis, which refers to the uptake of large particles and is specific of phagocytic cells and pinocytosis, which refers to the uptake of fluids and solutes and are present in all types of cells.[7,8] In turn, pinocytosis can be divided into clathrin-dependent endocytosis (CDE) and clathrin-independent endocytosis (CIE).[9,10] CDE pathway is associated with the internalization of nanoparticles up to 200 nm[11] and in this process there is formation of a partially invaginated membrane structure by the action of the assembly proteins AP-2 and AP180 and then dynamin, a multidomain GTPase, which promotes scission of the invaginated clathrin-coated vesicles (CCV) which, in turn, are then released into the cytosol under cytoskeleton regulation.[7,12] CIE can be divided into caveolin-mediated, caveolin- and clathrin-independent and macropinocytosis, according to the proteins involved in the pathways. In caveolae-mediated endocytosis, caveolin is the main protein involved.[13] In this process, nanoparticles are involved into flask-shaped vesicles and cut off from the membrane by the action of dynamin.[13] Caveolin- and clathrin-independent pathways can be classified in Arf6-dependent, Cdc42-dependent and Rhoa-dependent, depending the type of GTPases involved.[7,13,14] In turn, macropinocytosis can internalize nanoparticles without receptor mediation, but mediated by actin. This route is normally used to internalize particles with an average size below 2 mm.[15] To investigate the endocytic mechanisms involved in the internalization of nanoparticles, specific endocytic pharmacological inhibitors are used.[14]

During the recent years, our research group has focused on the development of DDS based on zeolite nanostructures, for colorectal cancer treatment and more recently for breast cancer treatment.[16–19] However, an important point of the work is elucidating how zeolite nanoparticles enter inside the cells to optimize the design of DDS. Recently, we showed that the zeolite L nanoparticles were internalized faster by breast cancer cells than epithelial mammary cells, with the nanoparticles mainly localized in the vacuoles by means of a caveolin-mediated process.[20] Following these studies, in this work, the internalization mechanism of the parent

zeolite L nanoparticles was investigated using six pharmacological inhibitors unveil the endocytic pathway involved.

One of the strategies to enhance cellular uptake, internalization and avoid aggregation is to modify the outer surface of nanocarriers. Surface modification can be carried out by using functional groups, such as amino (-NH_2), carboxylic (-COOH), sulfhydryl (-SH) groups, by PEGylation or other coatings and targeting ligands, such as antibodies, peptides and aptamers.[5,21] These modifications will enable to increase the cellular uptake, the specificity and the efficiency of the intracellular delivery and endorse the internalization mechanism.[22,23]

Positively-charged nanoparticles can interact with negative cellular membrane proteins, therefore are more efficiently internalized than negatively charged or neutral particles.[24–26] However, in order to design more efficient surface modifications, the endocytic mechanisms used by nanoparticles to entry into cells need to be known. When living cells are exposed to nanoparticles, these latter can enter the cells by endocytosis or through the phospholipid bilayer by a process of direct translocation.[27–29] This latter is an energy-independent process.[27,30] In the endocytosis process, the nanoparticles are firstly engulfed by membrane invaginations, originating endosomes or phagosomes depending on the type of cells. Then, the endosomes deliver the nanoparticles to various specialized vesicular structures and finally they are delivered to various intracellular compartments and recycled to the extracellular milieu or delivered across cells.[79]

Motivated by that, we functionalized the outer surface of disc-shaped zeolite L nanoparticles with different groups, amino or carboxylic acid groups and coated with poly-L-lysine and we assessed the toxicity of these modified nanomaterials toward breast cancer and epithelial mammary cells. Then, the uptake of these modified nanomaterials was studied in the same human cell lines, using confocal microscopy, scanning electron microscopy (SEM) and transmission electron microscopy (TEM) at 37 °C and 4 °C, in order to evaluate if the uptake of these modified nanomaterials is energy-dependent.

4.2.2. EXPERIMENTAL

4.2.2.1. MATERIALS

Dry toluene and (3-Aminopropyl)triethoxysilane (APTES) were acquired from Acros Organics and triethylamine (TEA) from Merck. Succinic anhydride and poly-L-lysine were purchased from Sigma Aldrich and dimethyl sulfoxide (DMSO) from Roth. N,N'-Bis(2,6-dimethylphenyl)perylene-3,4,9,10-tetracarboxylic diimide (DXP) dye was acquired from Fluka.

Dulbecco's Modified Eagle's Medium (DMEM), Dulbecco's Modified Eagle's Medium F12 (DMEM/F12 (1:1)), Fetal Bovine Serum (FBS) and Penicillin-Streptomycin (P/S) were

purchased from Gibco. Human insulin solution, cholera toxin and hydrocortisone were acquired from Sigma Aldrich and epidermal growth factor (EGF) from Peprotech. The human breast cancer cell line, Hs 587T, was obtained from ATCC (American Type Culture Collection) and the epithelial mammary cells, MCF-10, were kindly provided by Dra. Lígia Rodrigues (CEB, University of Minho, Portugal). The pharmacological inhibitors, chlorpromazine, dynasore, LY294002, nystatin, genistein and nocodazole were obtained from Sigma-Aldrich. 4′,6-Diamidine-2′-phenylindole dihydrochloride (DAPI) was purchased from Sigma-Aldrich, α-Tubulin antibody (SC23948) was from Santa Cruz Biotechnology and Alexa Fluor 594 goat anti-mouse (A11032) was purchased from Life Technologies.

4.2.2.2. INHIBITION OF THE ENDOCYTIC PATHWAYS

To identify the endocytic pathways responsible for cellular uptake of zeolite L nanoparticles, were used six pharmacological inhibitors: chlorpromazine, dynasore, nystatin, LY294002, genistein and nocodazole. The cells treated with the inhibitors were observed by TEM to investigate the presence or absence of nanoparticles inside the cells. To achieve this purpose, 1.5×10^5 Hs 578T and 1.8×10^5 MCF-10 cells were cultured on 24-well plates with zeolite L (50 μg mL^{-1}) for 4 h. After the incubation time, the cells were fixed with 2.5% glutaraldehyde (Electron Microscopy sciences, Hatfield, USA) and 2% paraformaldehyde in cacodylate buffer 0.10 M (pH 7.4). Then, the cells were dehydrated and included in Epon resin and ultrathin sections were stained with uranyl acetate. The samples were analyzed in a JEOL JEM 1400 TEM. Images were digitally recorded using a CCD digital camera Orious 1100W Tokyo, Japan at the HEMS/i3S (IBMC) of the University of Porto.

4.2.2.3. ZEOLITE L SURFACE FUNCTIONALIZATION

In this study, we modified the outer surface of synthetized zeolite L obtained by method previously described,[31,32] via attachment of various groups onto the zeolite surface: NH_2 groups, COOH groups and also coated with PLL in order to study if charge surface modification enhances cellular uptake. To functionalize the nanoparticles, we followed previous reported procedures.[33] First, zeolite L was modified with amino groups. For this purpose, the zeolite L was suspended in toluene, followed by addition of (3-Aminopropyl)triethoxysilane (APTES), and triethylamine (TEA) and the mixture was sonicated for 5 min and then refluxed at 120 °C for 2 h. Then, it was left to cool down, centrifuged and washed once with toluene and twice with ethanol and dried under vacuum.

To obtained carboxylic acid-functionalized zeolite L nanoparticles, an amount of amino-modified zeolite L was dispersed in a succinic anhydride solution in DMSO and, after 10 min

of sonication, the mixture was stirred overnight at room temperature (RT). The modified zeolite was then centrifuged and washed three times with water and dried under vacuum.

For coating with poly-L-lysine (PLL), the zeolite L was dispersed in a 1 mg mL^{-1} solution of poly-L-lysine hydrobromide in water and the mixture was stirred overnight at room temperature and then washed three times with water. The obtained modified nanomaterials were dried under vacuum and characterized by zeta potential using a Delsa Nano C Particle Analyzer (Beckman Coulter, Brea, CA, USA) and SEM. The zeta potential values represent a mean of three measurements.

From now on, the obtained modified nanomaterials will be designated as "L-NH_2" for the zeolite L functionalized with amino groups, "L-COOH" for the zeolite L functionalized with carboxylic acid groups and "L-PLL" for the zeolite L coated with poly-L-lysine.

4.2.2.4. DXP DYE LOADING

To perform confocal microscopy studies is necessary to have an emitting fluorescence material; DXP dye was chosen to achieve this purpose. DXP dye loading was performed following a previously reported protocol.[33] Briefly, zeolite L was mixed with 2 mL of DXP in dichloromethane in a glass ampoule. After that, DXP was dehydrated in a vacuum line at 1.0 × 10^{-5} mbar for 6 h and sealed, and the mixture was left at 300 °C overnight in order to obtain dye insertion. The ampoule was then opened and the zeolite with the dye was washed with *n*-butanol until the supernatant did not show any fluorescence. L-NH_2, L-COOH and L-PLL were also loaded with DXP dye using the method described above.

4.2.2.5. CULTURE OF HUMAN CELL LINES

Hs 578T cells were purchased from ATCC (ATCC® HTB126™). This cell line was cultured in DMEM medium supplemented with 10% FBS and 1% Pen/Strep and keep at 37 °C in 5% CO_2 atmosphere. Cells were exposed to 50 µg mL^{-1} of the nanomaterials for 4 and 24 h. MCF-10 epithelial mammary cells were cultured in DMEM/F12 (1:1) containing 5 % FBS, 1 % P/S and supplemented with 20 ng mL^{-1} of EGF, 100 ng mL^{-1} of cholera toxin, 0.01 mg mL^{-1} of insulin and 500 ng mL^{-1} of hydrocortisone. Both cell lines were maintained in a humidified atmosphere of 5 % CO_2 at 37 °C.

4.2.2.6. SULFORHODAMINE B ASSAY

The toxicity of L-NH_2, L-COOH and L-PLL was assessed using sulforhodamine B (SRB) assay as previously described.[18] Briefly, Hs 578T and MCF-10 were seeded at density of 7000 cells per cm^2 and 5000 cells per cm^2, respectively, and left to grow overnight at 37 °C under 5

% CO_2 atmosphere. After that, the medium was replaced by the solutions of the modified nanomaterials (0.01 - 0.125 mg mL^{-1}) in medium FBS-free and incubated for 48 h. Then, cells were fixed for 1 h with cold 10 % (w/v) trichloroacetic acid (TCA), stained with sulforhodamine B for 30 min and the dye was solubilized with 10 mM Tris base solution and the absorbance was read at 490 nm.

4.2.2.7. CELLULAR UPTAKE OF FUNCTIONALIZED ZEOLITE L

Confocal microscopy, transmission electron microscopy (TEM) and scanning electron microscopy (SEM) were used to analyze the internalization and uptake of modified zeolite L in Hs 578T breast cancer cells and epithelial mammary cells.

For the confocal microscopy, 2.5×10^4 cells were seeded in coverslips on 24-well plates overnight. Then the cells were treated with 50 µg mL^{-1} of the nanomaterials and incubated for 4 and 24 h. After the incubation time, cells were washed twice with PBS and fixed with cold methanol during 15 min and the immunoreaction was carried out. After fixation, cells were washed with PBS with 10 mM glycine, washed with PBS 1x, permeabilized with triton X-100 0.1%, washed again and blocked with 5% BSA in PBS. Next, the cells were incubated with α-tubulin antibody (SC23948, Santacruz) diluted in 5% BSA in PBS (1:100) for 30 min, washed with PBS 1x and incubated with secondary antibody Alexa Fluor 594 goat anti-mouse (A11032, Life Technologies) diluted in 5% BSA in PBS (1:250) during 1 h at RT. After washing, cell nuclei were stained with DAPI and mounted in Permafluor. Confocal images were acquired with an Olympus FV1000 confocal microscope (Olympus). Emission profiles were acquired with an LSM UPLSAPO 60.0 × 1.35 N.A. oil immersion objective. Cells stained with DAPI (excitation/emission wavelength: 405/461 nm), and Alexa Fluor® 594 dye (excitation/emission wavelength: 559/618 nm) were excited independently at 405, and 559 nm, respectively. DXP dye was excited at 488 nm. Image processing was done using a Fluoview FV1000 software (Olympus).

For TEM analysis, Hs 578T and MCF-10 cells were plated at the density of 1.5×10^5 and 1.8×10^5 cells per wells, respectively, and incubated at 37 °C in 5% CO_2 atmosphere for 24 h. Then, the cells were incubated with 50 µg mL^{-1} suspension of the modified nanomaterials for 4 h at 4 and 37 °C and 24 h at 37 °C. Afterwards, the cells were washed three times with PBS 1x, trypsinized, centrifuged for 5 min at 900 rpm and resuspended in 1 mL of media. 2.5% glutaraldehyde (Electron Microscopy sciences, Hatfield, USA) and 2% paraformaldehyde (Merck, Darmstadt, Germany) in cacodylate buffer 0.1 M (pH 7.4) were used to fix the cells. After dehydration, the cells were embedded in Epon resin (TAAB, Berks, England), and ultrathin sections (40-60 nm) were prepared on a RMC Ultramicrotome (PowerTome, USA) using diamond knives (DDK, Wilmington, DE, USA). The sections were mounted on 200 mesh

copper or nickel grids, stained with uranyl acetate substitute and lead citrate for 5 min each, and examined under a JEOL JEM 1400 TEM (Tokyo, Japan). Images were digitally recorded using a CCD digital camera Orious 1100W Tokyo, Japan at the HEMS/i3S (IBMC) of the University of Porto.

To performed SEM experiments at 37 °C, Hs 578T cells were seeded at density of 5.0×10^4 on 12-mm coverslips and to experiments at 4 °C both cells, Hs 578T and MCF-10, were seeded at the density of 5.0×10^4. After growing overnight, cells were incubated with 50 µg mL^{-1} solution of the nanomaterials for 5, 10, 15, 20, 30, 60 min and 4 h at 37 °C and 10, 60 min and 4 h at 4 °C. Then, the cells were washed 3 times with PBS 1x and fixed with 2.5% glutaraldehyde in PBS for 45 min at RT and for 60 min at 4 °C, and again washed 3 times with PBS 1x. After these steps, the cells were dehydrated with series graded of ethanol from 10% until 90% for 20 min each and twice with 100% for 20 min. Coverslips were then dried at RT overnight. For visualization, the coverslips were sputter-coated with gold and images were then recorded with a JEOL JSM-6010LV scanning electron microscope (JEOL, Tokyo, Japan).

4.2.2.8. STATISTICAL ANALYSIS

The tests were performed in at least three independent experiments. Results of viability studies are expressed as means ± standard deviation (SD) and the results were analyzed using one-way ANOVA with GraphPad Prism 6® software. A *p*-value of < 0.05 was considered statistically significant.

4.2.2.9. IMAGING DATA ANALYSIS

The images were analyzed by ImageJ software. For TEM quantification, the threshold tool was used, the zeolite L highlighted in red and the area occupied by particles was measured. For fluorescence quantification, was used the freehand-selection tool to select each cell and circularity, area, mean fluorescence measured, along with several adjacent background readings, and the total corrected cellular fluorescence (TCCF) was calculated.[34]

4.2.3. RESULTS AND DISCUSSION

Among the different types of porous materials that can be used to prepare DDS, zeolites are good drug carriers due to their structures that can efficiently load drugs, their biological stability and lack of cell toxicity.[35–37] Thus, as a continuation of our previous work,[20] herein we have gone deeper into the understanding of the internalization mechanisms of the zeolite L nanoparticles, using for this purpose six pharmacological inhibitors: chlorpromazine (CPZ), dynasore, nystatin, LY294002, genistein and nocodazole. Two of them, CPZ and dynasore

inhibitors, were already explored in our previous work.[20] However, our goal here is to further characterize the endocytic pathways involved in the internalization of zeolite L nanoparticles, using different inhibitors. Additionally, we explored the surface functionalization of the zeolite L nanoparticles, *in vitro* biocompatibility and the differences in the cellular uptake.

4.2.3.1. ZEOLITE L ENDOCYTIC PATHWAYS DETERMINATION USING PHARMACOLOGICAL INHIBITORS

We already provided evidences for the internalization of the zeolite L nanoparticles by means of a caveolin-mediated process both in Hs 578T and MCF-10 cells.[20] Thus, in order to further characterize the pathways involved in the zeolite L nanoparticles uptake, we used six pharmacological inhibitors: CPZ that inhibits clathrin-mediated endocytosis;[38,39] dynasore which is a dynamin inhibitor by preventing the closure of the membrane invagination to form free vesicles interfering with both clathrin-mediated and caveolin-mediated endocytosis;[40,41] nystatin that is used to inhibit caveolin-mediated endocytosis by interaction with cholesterol and enhances cell membrane permeability;[42,43] LY294002 which inhibits micropinocytosis;[44] genistein that is a caveolar inhibitor exerting its effect on the receptor-associated tyrosine-specific protein kinase,[6,45] and nocodazole which is a microtubule-depolymerizing agent which binds to β-tubulin and averts the formation of one of the two interchain disulfide linkages, which leads to inhibition of microtubule dynamics and consequently, blocks endocytic vesicle trafficking.[46,47]

For these studies, Hs 578T breast cancer cells and MCF-10 epithelial mammary cells were treated with CPZ (10 μg mL^{-1}), dynasore (400 μM), nystatin (5 μg mL^{-1}), LY294002 (50 μM), genistein (200 μM) and nocodazole (41 μM) in culture media without FBS that were previously tested in terms of cytotoxicity. The effect of these inhibitors was investigated by TEM and Figure 4.2.1 displays the results obtained with Hs 578T breast cancer cells and the parent zeolite L nanoparticles.

In Hs 578T cells, the zeolite L cellular uptake was strongly inhibited by dynasore since in Figure 4.2.1A-d nanoparticles are not observed inside the cell, which was already previously reported in our work.[20] Also, nocodazole displayed an inhibitor effect since only few cells showed internalization of the nanoparticles (Figure 4.2.1A-h). Figure 4.2.1B demonstrates the percentage of zeolite L nanoparticles that are internalized by cells after their treatment with pharmacological inhibitors compared with cells not exposed to any inhibitor. We can see that when cells are not exposed to any inhibitor, a higher percentage of zeolite L nanoparticles (1.25% ± 1.04) is internalized while the presence of inhibitors seems to lower this percentage. In this respect, only dynasore and nocodazole exert significant inhibition in the internalization of zeolite L nanoparticles (ANOVA, $p < 0.0001$ and $p < 0.001$, respectively). The effect of

nocodazole (0.25% ± 0.13) is lower than the effect of dynasore (0.03% ± 0.03) (Figure 4.2.1B). Cells treatment with dynasore inhibited almost completely the internalization of zeolite L nanoparticles. The treatment with nocodazole is not as effective as dynasore, however as already denoted, a lower percentage of nanoparticles is internalized and some zeolite L nanoparticles were located near the cellular membrane, demonstrating the difficulty of nanoparticles to enter into the cells when they were treated with nocodazole (Figure 4.2.1A-g, red arrow).

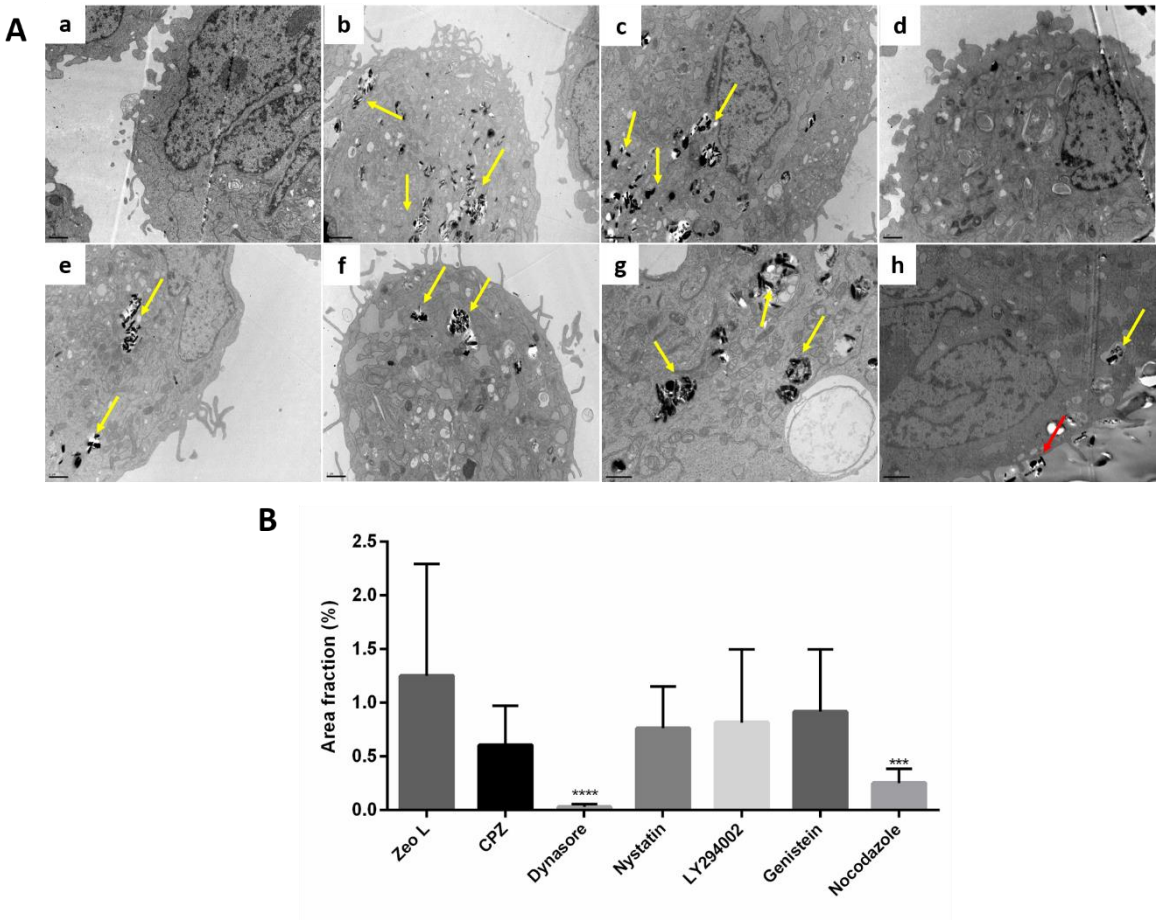

Figure 4.2.1: A) Effect of the endocytic inhibitors on the internalization of zeolite L nanoparticles by Hs 578T breast cancer cells analyzed by TEM. Control (cells were not exposed to pharmacological inhibitors neither to zeolite L nanoparticles) (a); cells exposed only to zeolite L nanoparticles (b); cells were treated with 10 µg mL^{-1} of CPZ (c), 400 µM of dynasore (d), 5 µg mL^{-1} of nystatin (e), 50 µM of LY294002 (f), 200 µM of genistein (g) and 41 µM of nocodazole (h) for 60 min before being exposed to 50 µg mL^{-1} of the zeolite L nanoparticles for 4 h. Images of cells are showed at a magnification of 8.000x (b), 12.000x (a, c, d, e, f) and 15.000× (g and h). Yellow and red arrows point toward some nanoparticles. Scale bar: 1 µm (a, c, d, e, f, g, and h); 2 µm (b). B) Quantification of the percentage of zeolite L nanoparticles internalized by Hs 578T cells after their incubation with pharmacological inhibitors (n=10) related with zeolite L condition (cells not treated with inhibitor).

For the remaining four inhibitors, there was no significant reduction in the zeolite L nanoparticles internalization since in all TEM images it is possible to observe their presence inside cells (Figure 4.2.1A, yellow arrows). By the findings of these experiments, it is possible to conclude that the uptake of the zeolite L nanoparticles by Hs 578T cells is mediated by a caveolin process and it also depends on microtubule dynamics to create the endocytic vesicles.

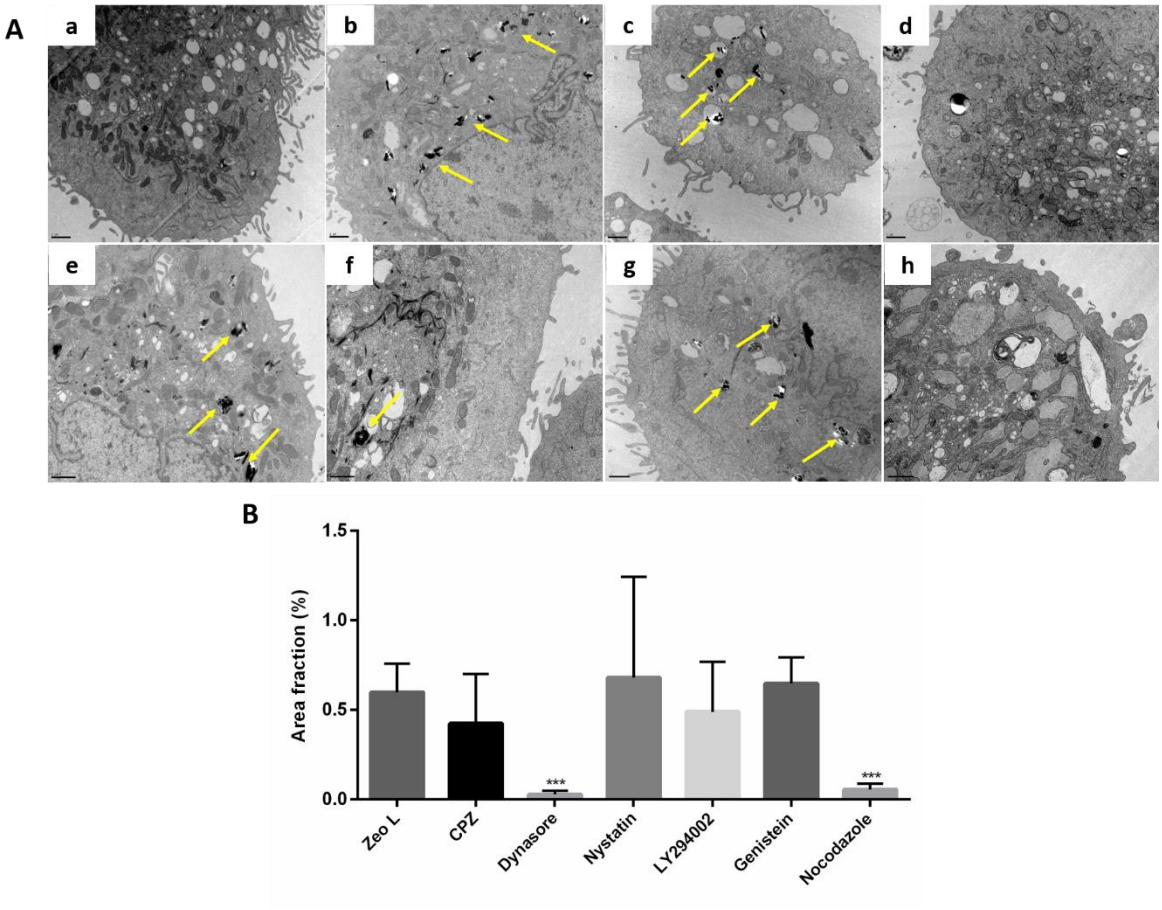

Figure 4.2.2: A) Effect of the endocytic inhibitors on the internalization of zeolite L nanoparticles by MCF-10 cells. Control (cells were not exposed to pharmacological inhibitors neither to zeolite L nanoparticles) (a); cells exposed only to zeolite L nanoparticles (b); cells were treated with 10 µg mL^{-1} of CPZ (c), 400 µM of dynasore (d), 5 µg mL^{-1} of nystatin (e), 50 µM of LY294002 (f), 200 µM of genistein (g) and 41 µM of nocodazole (h) for 60 min before being exposed to 50 µg mL^{-1} of the zeolite L nanoparticles for 4 h. Images of cells are showed at a magnification of 12.000× (a, b, c, d, g and f) and 15.000× (e, h). Yellow arrows point toward some particles. Scale bar: 1 µm. B) Quantification of the percentage of zeolite L nanoparticles internalized by Hs 578T cells after their incubation with pharmacological inhibitors (*n*=10) related with zeolite L condition (cells not treated with inhibitor).

In the case of MCF-10 cell line (Figure 4.2.2), dynasore and nocodazole also strongly inhibited zeolite L uptake since in the TEM images corresponding to these two inhibitors, no or very few zeolite L nanoparticles were observed inside the cells (Figure 4.2.2A-d and 4.2.2A-

h). Once again in this cell line, using CPZ, nystatin, LY294002 and genistein we observed nanoparticles inside the cells (Figure 4.2,2, yellow arrows), which demonstrates no inhibition of cellular uptake by these inhibitors. In Figure 4.2.2B, it is possible to see a significant reduction in the percentage of internalized zeolite L nanoparticles when the cells were treated with dynasore (ANOVA, $p < 0.001$; 0.03% ± 0.02) and also a significant reduction when the cells were treated with nocodazole (ANOVA, $p < 0.001$; 0.05 % ± 0.03). Ricardo Marega *et al.* showed that the internalization of Zeo-NHCO-Ctxb is affected by CPZ, amiloride and genistein and Zeo-NH_2 was influenced by dynasore.[47] Only dynasore effect is in line with our findings. The differences between Ricardo Marega's results and the results presented in this work might be explained by the different cell lines used and the different functionalization of zeolite surface since these characteristics could influence the endocytic pathway.[48]

Overall, the results of these experiments demonstrate that the pathways involved in the internalization of zeolite L are the same for both Hs 578T and MCF-10 cells despite the lower amount of internalized nanoparticles by the latter cell line.

4.2.3.2. SURFACE FUNCTIONALIZATION OF ZEOLITE L NANOPARTICLES

The typical disc-shaped zeolite L nanoparticles were functionalized using different compounds (Figure 4.2.3) in order to verify if the surface charges of the nanoparticles affect the cellular uptake and endorse the internalization mechanism.

Amino-functionalization of zeolite L (L-NH_2) was obtained by silanization with 3-aminopropyltriethoxysilane (APTES, $H_2N(CH_2)_3Si(OC_2H_5)_3$) molecules and carboxyl-functionalization was obtained by ring opening linker elongation reaction of the amine group[49,50] (Figure 4.2.3, reactions 1 and 2); poly-L-lysine coating was obtained by mixing the zeolite L with a solution of poly-l-lysine (Figure 4.2.3, reaction 3).

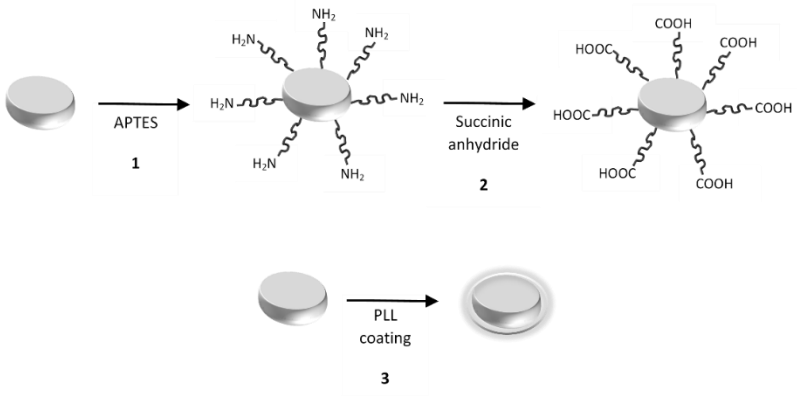

Figure 4.2.3: Schematic representation of the functionalization procedures. 1) Amino-functionalization of zeolite L; 2) Carboxyl-functionalization of zeolite L; 3) Coating of zeolite L with poly-L-lysine (PLL).

After these procedures, it was necessary to confirm if the zeolite L was successfully functionalized. The first approach to investigate that was to measure the zeta potential of the samples. For that, a very diluted solution of the modified nanomaterials was prepared and the zeta potential was measured. The zeta potential of the parent zeolite L was -44 mV, confirming the stability of the surface of the zeolite. After the functionalization with amino groups, the zeta potential value changed to +35 mV, confirming the amino functionalization of the outer surface of zeolite L. Then the amino-groups reacted with succinic anhydride to convert the primary NH_2 to COOH groups (Figure 4.2.3, reaction 2), forming a sample (L-COOH) with -28 mV zeta potential as a result of the formation of carboxylic groups on the outer surface of zeolite L. In turn, poly-L-lysine (PLL), a positively charged polymer, with no toxicity and with good biocompatibility,[51] was used to coat zeolite L surface, originating a positively charged sample with +32 mV zeta potential (Figure 4.2.4).

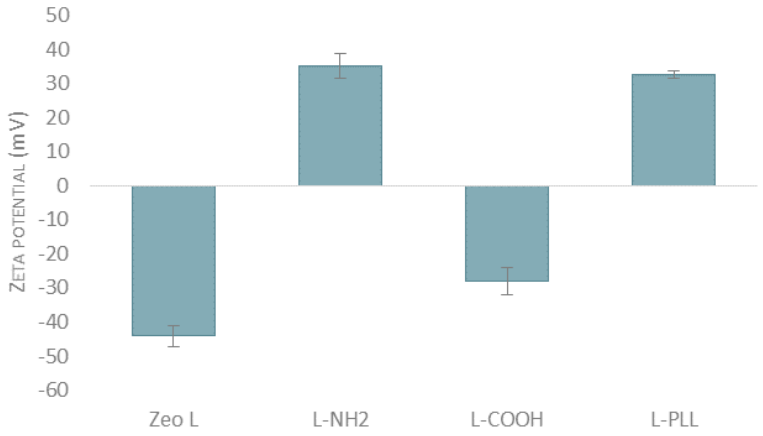

Figure 4.2.4: Zeta potential of unmodified and modified zeolite L in water. The error bars represent the standard deviation for three measurements.

SEM micrographs of the zeolite L (Zeo L) and the modified nanomaterials, L-NH_2, L-COOH and L-PLL (Figure 4.2.5), show that the functionalized samples present the same morphology and similar size of the particles comparing with the parent zeolite L.

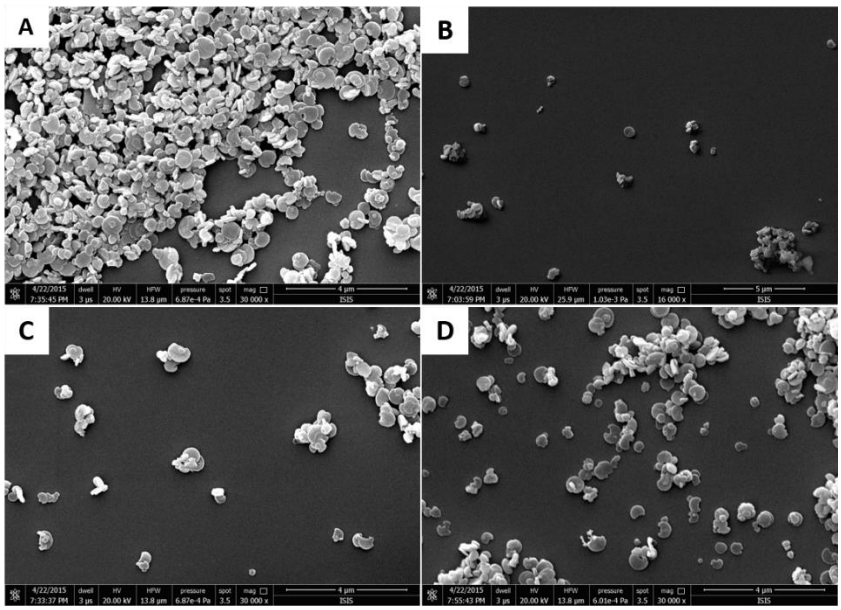

Figure 4.2.5: SEM micrographs of functionalized zeolite L dispersed in ethanol. A) Zeolite L unmodified, scale bar: 4 µm. B) L-NH_2, scale bar: 5 µm; C) L-COOH, scale bar: 4 µm; and D) L-PLL, scale bar: 4 µm.

4.2.3.3. *IN VITRO* TOXICITY STUDIES

The effect of the modified nanomaterials and the parent zeolite L on the viability of Hs 578T and MCF-10 cells was determined by the sulforhodamine B assay. Comparing the materials with control (only cells), the parent zeolite L induced some toxicity on Hs 578T cells for 0.075, 0.100 and 0.125 mg mL^{-1}, reducing cell viability in 15, 14 and 24%, respectively (Figure 4.2.6). In contrast, when cells were treated with L-NH_2, L-COOH and L-PLL nanomaterials, a decrease in cell viability was not evident compared to the control even at higher concentrations, within the tested concentration range (0.010 - 0.125 mg mL^{-1}). Furthermore, there were no significant differences between the amino-functionalized, carboxylic-functionalized and PLL coated zeolites. These results show that the functional groups used on the zeolite L do not increase material cytotoxicity and it even appears to decrease the toxicity observed for the parent zeolite L.

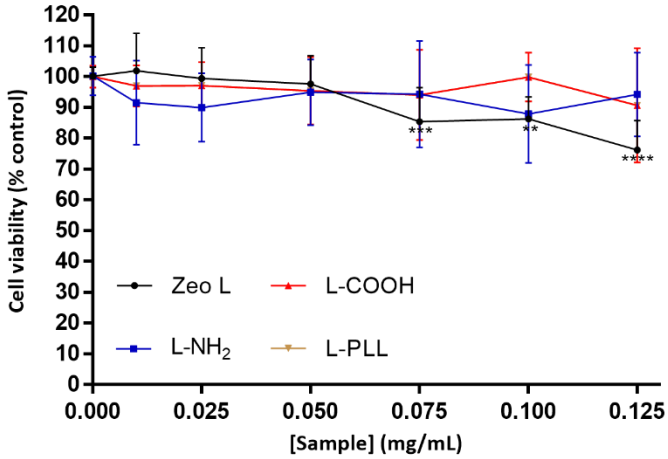

Figure 4.2.6: Cell viability, measured by SRB assay, of Hs 578T cells incubated with different concentrations of Zeo L, L-NH_2, L-COOH e L-PLL after 48 h incubation. Data are expressed in relation to the control (0% of zeolite, considered 100 % of viability) as mean ± SD of five independent experiments, each performed in triplicate. Asterisk represents statistically significant differences from unexposed control, *p < 0.05, **p < 0.01, ***p < 0.001 and ****p < 0.0001.

Contrarily to what happened in Hs 578T cells, treatment of the MCF-10 cells with zeolite L, L-NH_2, L-COOH and L-PLL, did not decrease cell viability after 48 h of incubation (Figure 4.2.7). These results demonstrate that functionalization of zeolite L with amino and carboxylic groups and coating with PLL is non-toxic for both studied cell lines, whereas zeolite L presents some toxicity for Hs 578T cells for higher concentrations.

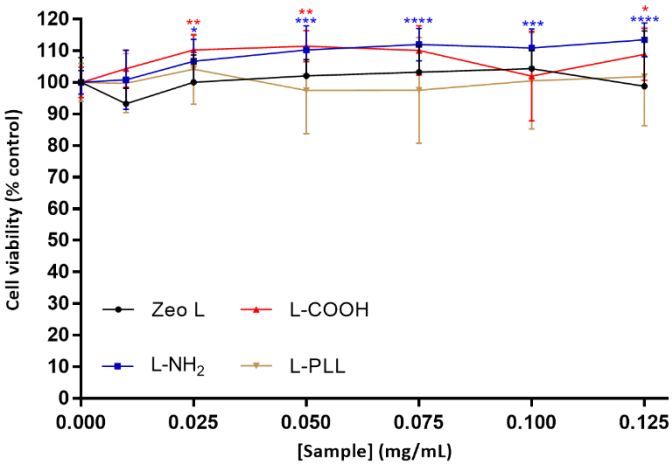

Figure 4.2.7: Cell viability, measured by SRB assay, of MCF-10 cells incubated with different concentrations of Zeo L, L-NH_2, L-COOH e L-PLL after 48 h incubation. Data are expressed in relation to the control (0% of zeolite, considered 100% of viability) as mean ± SD of five independent experiments, each performed in triplicate. Asterisk represents statistically significant differences from unexposed control, *p < 0.05, **p < 0.01, ***p < 0.001 and ****p < 0.0001.

4.2.3.4. CELL INTERNALIZATION OF THE FUNCTIONALIZED ZEOLITE L NANOPARTICLES

Hs 578T and MCF-10 cells were incubated with the parent zeolite L (negatively charged) and the modified nanomaterials, L-NH_2 (positively charged), L-COOH (negatively charged) and L-PLL (positively charged) and confocal microscopy imaging was performed. Figure 4.2.8 illustrates the confocal results for Hs 578T cell line for 4 and 24 h of incubation time at 37 °C. From analysis of Figure 4.2.8A, it is possible to observe a yellow fluorescent signal which corresponds to the nanoparticles accumulated into Hs 578T cells after 4 h of incubation time. This signal is stronger in Figure 4.2.8A-b and Figure 4.2.8A-d, which corresponds to L-NH_2 (34 ± 22) × 10^3 and L-PLL (39 ± 26) × 10^3 nanomaterials. Figure 4.2.8B also shows a yellow fluorescent signal, however this signal is stronger than the images shown in Figure 4.2.8A, which is expected since these results correspond to 24 h of incubation and the uptake of the nanoparticles increased with the time of incubation as has shown by Rosa *et al*.[52] Also in Figure 4.2.8B, it is possible to observe a stronger signal in images corresponding to L-NH_2 (46 ± 19) × 10^3 and L-PLL (64 ± 45) × 10^3. These results show that the cellular internalization of positively charged nanoparticles (L-NH_2 and L-PLL) is higher compared to that of negatively charged nanoparticles (Zeo L and L-COOH), which are in line with the reported in literature.[53]

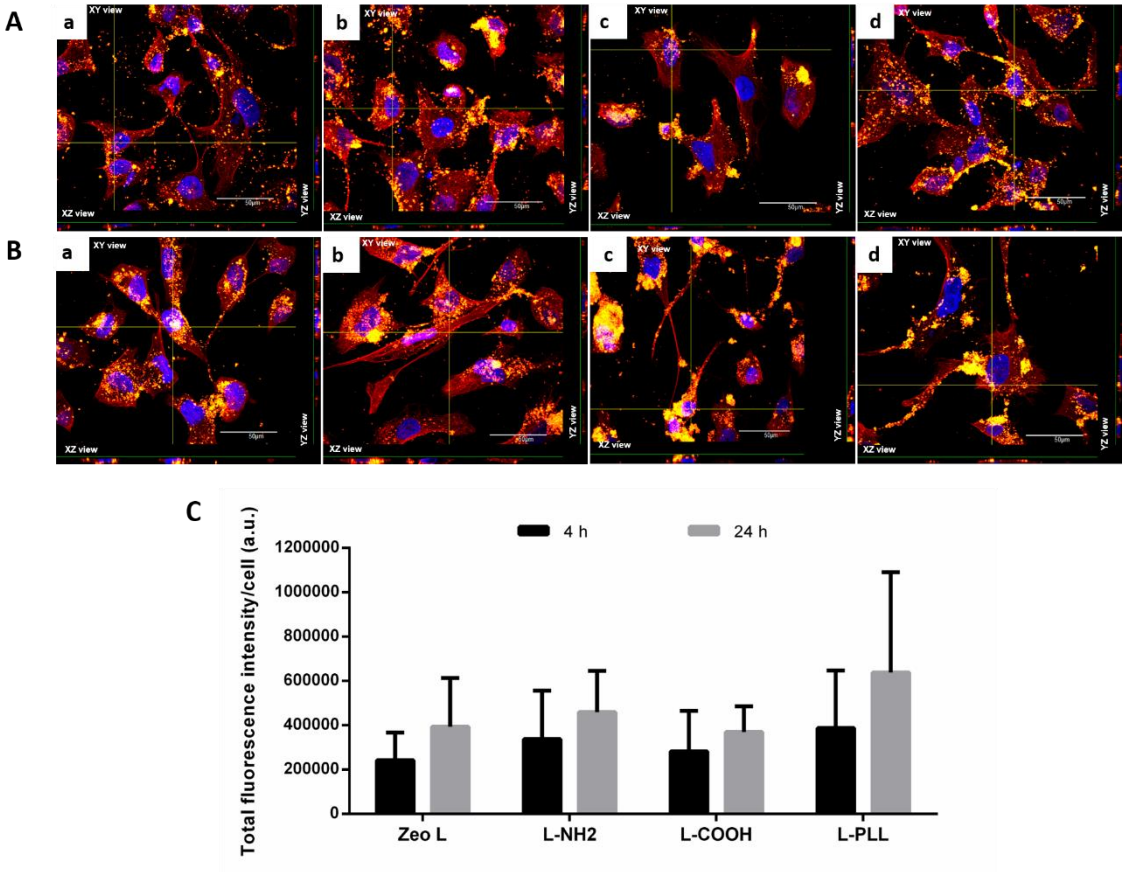

Figure 4.2.8: Confocal microscopy of Hs 578T cells incubated with samples (0.5 mg mL^{-1}) for 4 h (A) and 24 h (B) at 37 °C: a) Zeo L; b) L-NH_2; c) L-COOH; d) L-PLL. Scale bar: 50 µm. Quantitative calculation of total fluorescence intensity per cell (C). Error bar denote standard deviations.

In Figure 4.2.9A and Figure 4.2.9B, it is possible to observe the obtained results for MCF-10 cells after 4 and 24 h of incubation time. The results show the yellow fluorescence signal, however this signal is weaker than in Figure 4.2.8, related to Hs 578T cells, which demonstrate that only a small amount of zeolite nanoparticles, both positively and negatively charged, is internalized. This finding could be explained by the different growth rates of cancer and normal cells. Cancer cells grow faster and have higher metabolic rates than normal ones, which may explain the faster uptake of the nanoparticles by cancer than normal cells whose growth is slower.[54] Another possible explanation for the fact that Hs 578T cells internalize more zeolite nanoparticles than MCF-10 overtime could be related to the fact that cancer cell are more permeable than normal cells, which can enhance the permeability of tumoral cells to particles. Since this effect is not present in normal cells, it is expected that normal cells internalize less particles than tumoral ones.[55–57]

Despite the lower number of accumulated particles in normal cells, once again, the number of internalized nanoparticles is higher for positively charged than for negatively charged ones, as it is demonstrated in Figure 4.2.9C. These results are in accordance with other studies in

the literature, where it is reported that positively charged nanoparticles have higher rates of internalization by cells than those negatively charged, because the cellular membrane is negatively charged and positively charged nanoparticles will allow electrostatic interactions with the cell membrane, favoring cellular uptake.[58–60]

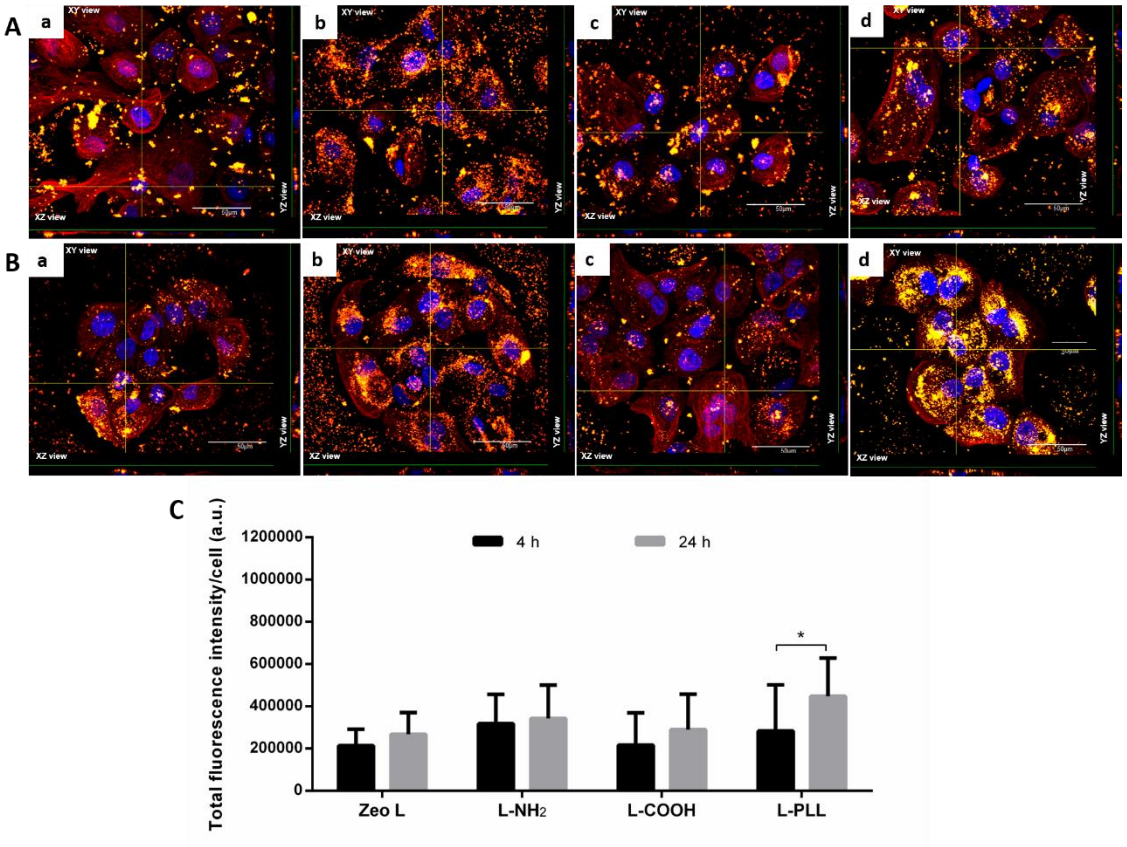

Figure 4.2.9: Confocal microscopy of MCF-10 cells incubated with samples (0.5 mg mL^{-1}) for 4 h (A) and 24 h (B) at 37 °C: a) Zeo L; b) L-NH_2; c) L-COOH; d) L-PLL. Scale bar: 50 µm. Quantitative calculation of total fluorescence intensity per cell (C). Error bar denote standard deviations, *p <0.05.

Confocal results show that Hs 578T and MCF-10 cells are able to internalize the zeolite L nanoparticles. To corroborate the cellular uptake by the nanomaterials, we also performed TEM analysis. To do this, cells were incubated with the zeolite nanoparticles during 4 h. The obtained results are displayed in Figure 4.2.10 for Hs 578T cell line and Figure 4.2.11 for MCF-10 cell line. These are consistent with those results obtained by confocal microscopy; nanoparticles with positively charged surface have a higher rate of internalization by both cells lines than nanoparticles with negatively charged surface. Once again, it is obvious that Hs 578T cells internalize a higher amount of nanoparticles than MCF-10 cells overtime, independently on the surface charge. From the TEM results it is also possible to observe that the nanomaterials were in vesicles inside the cells, likely vacuoles, for both cell lines.

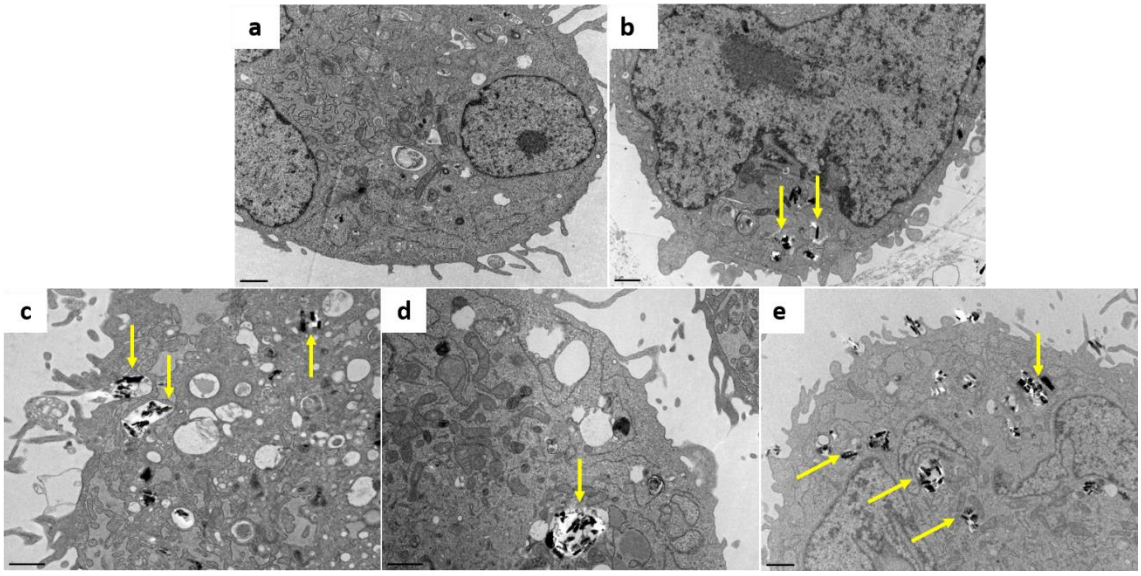

Figure 4.2.10: Internalization of materials by Hs 578T cells evaluated using TEM. The cells were incubated with 50 µg mL^{-1} of each nanomaterial for 4 h at 37 °C. a) Control (only cells); b) Zeo L; c) L-NH_2; d) L-COOH; e) L-PLL. Yellow arrows point toward some particles.

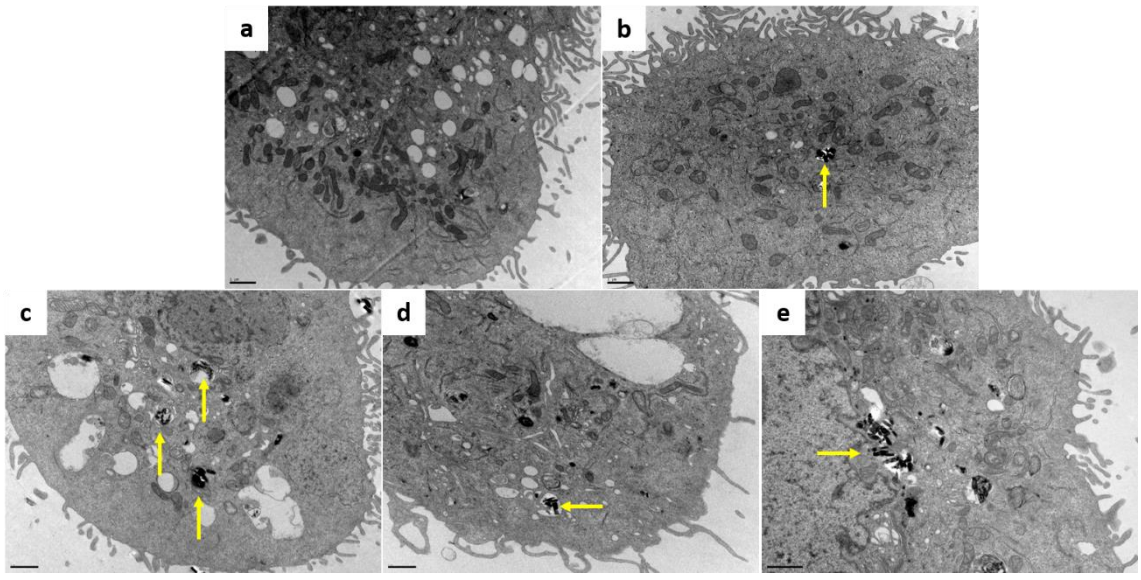

Figure 4.2.11: Internalization of materials by MCF-10 cells evaluated using TEM. The cells were incubated with 50 µg mL^{-1} of each nanomaterial for 4 h at 37 °C. a) Control (only cells); b) Zeo L; c) L-NH_2; d) L-COOH; e) L-PLL. Yellow arrows point toward some particles.

SEM is a superficial technique which demonstrates what is happening on the surface of the cells when they are incubated with the nanomaterials. For SEM analysis, Hs 578T cells where incubated with the parent zeolite L and the modified nanomaterials for different times. Herein, we just present the micrographs corresponding to 4 h of incubation (Figure 4.2.12). The results show that the internalization of the zeolite nanoparticles is fast for both negatively and

positively charged nanoparticles, with internalized particles already at 20 min of incubation. However, the number of internalized nanoparticles is higher for positively charged ones (L-NH_2 and L-PLL). As it was observed by TEM and confocal analyses, also in SEM results it is possible to observe that the number of internalized nanoparticles is time-dependent, with a higher number of internalized particles after 4 h of incubation.

From TEM and SEM results, it is possible to observe the presence of filopodia that engulfed zeolite L nanoparticles and are responsible for the beginning of the internalization process. In TEM images, the formation of vesicles with the particles inside can also be observed, which support the internalization of the zeolite L nanoparticles by endocytosis.

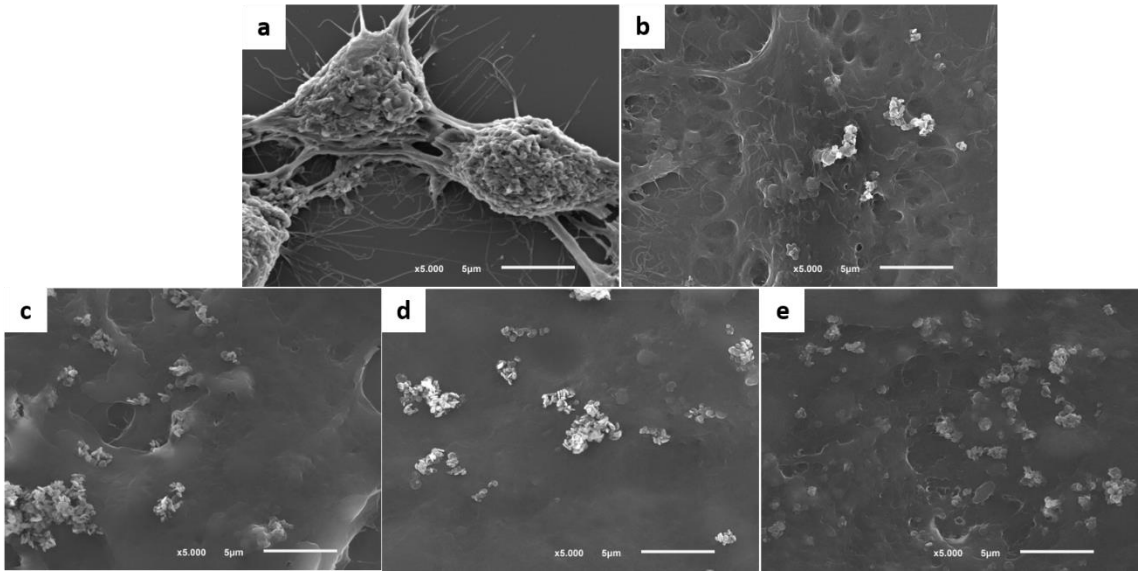

Figure 4.2.12: SEM micrographs of Hs 578T cells incubated with 50 µg mL^{-1} of nanomaterials for 4 h at 37 °C. A) Control (only cells), B) Zeo L, C) L-NH_2, D) L-COOH and E) L-PLL.

4.2.3.4. ENERGY-DEPENDENCE OF THE UPTAKE OF THE MODIFIED NANOMATERIALS

To assess if the uptake of the modified nanomaterials and the parent zeolite L is dependent on energy, we also performed experiments at 4 °C, since this approach inhibits all energy-dependent pathways.[30] When cells are incubated at 4 °C, many proteins and enzymes are inactivated[61] and the membrane become more rigid, which hampers the internalization of particles.[62] Hs 578T and MCF-10 cells were pre-incubated at 4 °C during 1 h with DMEM FBS-free and then incubated with the nanomaterial suspensions for 4 h at 4 °C and then the samples were analyzed by TEM.

From the results, it is possible to observe that when the cells are exposed to the temperature of 4 °C their filopodia is reduced. Filopodia are plasma-membrane filaments rich in actin which have an important role in several processes, including endocytosis[63] and these protrusions are

reduced at 4 °C, it is expected that the rates of internalization decrease. This decrease was observed (Figure 4.2.13 and 4.2.14) especially in cancer cells. Figure 4.2.13 shows a significant decrease on cell filopodia of cancer cells, which is translated in a strong reduction in cell internalization. In normal cells (Figure 4.2.14), a decrease on cellular filopodia formation was also observed, however this is less obvious than in the cancer ones. This observation could be explained by the fact of cancer cells have more abundant filopodia[63,64] than normal ones and the temperature has a more significant effect on cancer cells filopodia formation than in normal cells.

Comparing the obtained results at 37 °C (Figures 4.2.10 and 4.2.11) with the results at 4 °C (Figures 4.2.13 and 4.2.14), a reduction in the number of internalized nanoparticles was observed, which proves that the uptake of the zeolite L is an energy-dependent process. This reduction is proved by the quantification of the percentage of zeolite L nanoparticles which are internalized by both cell lines at 37 and 4 °C (Figure 4.2.13B and 4.2.14B). In Hs 578T cell line (Figure 4.2.13B), comparing the results at 37 and 4 °C it is clearly observed that at 37 °C a higher percentage of nanoparticles is internalized than at 4 °C. For MCF-10 cell line (Figure 4.2.14B), it is observed the same trend than in Hs 578T, with the internalization of zeolite nanoparticles being reduced at 4 °C. A close look on the literature confirmed the effect of the temperature on the nanoparticles internalization. For example, Sandra Vranic *et al.*, showed in their work that the internalized of SiO_2 nanoparticles by pulmonary epithelial cell line (NCI-H292) is reduced at 4 °C.[62] Also, Azzah M. Bannunah *et al.* demonstrated that the trafficking of both positively and negatively charged nanoparticles by intestinal Caco-2 cells is temperature-dependent.[65]

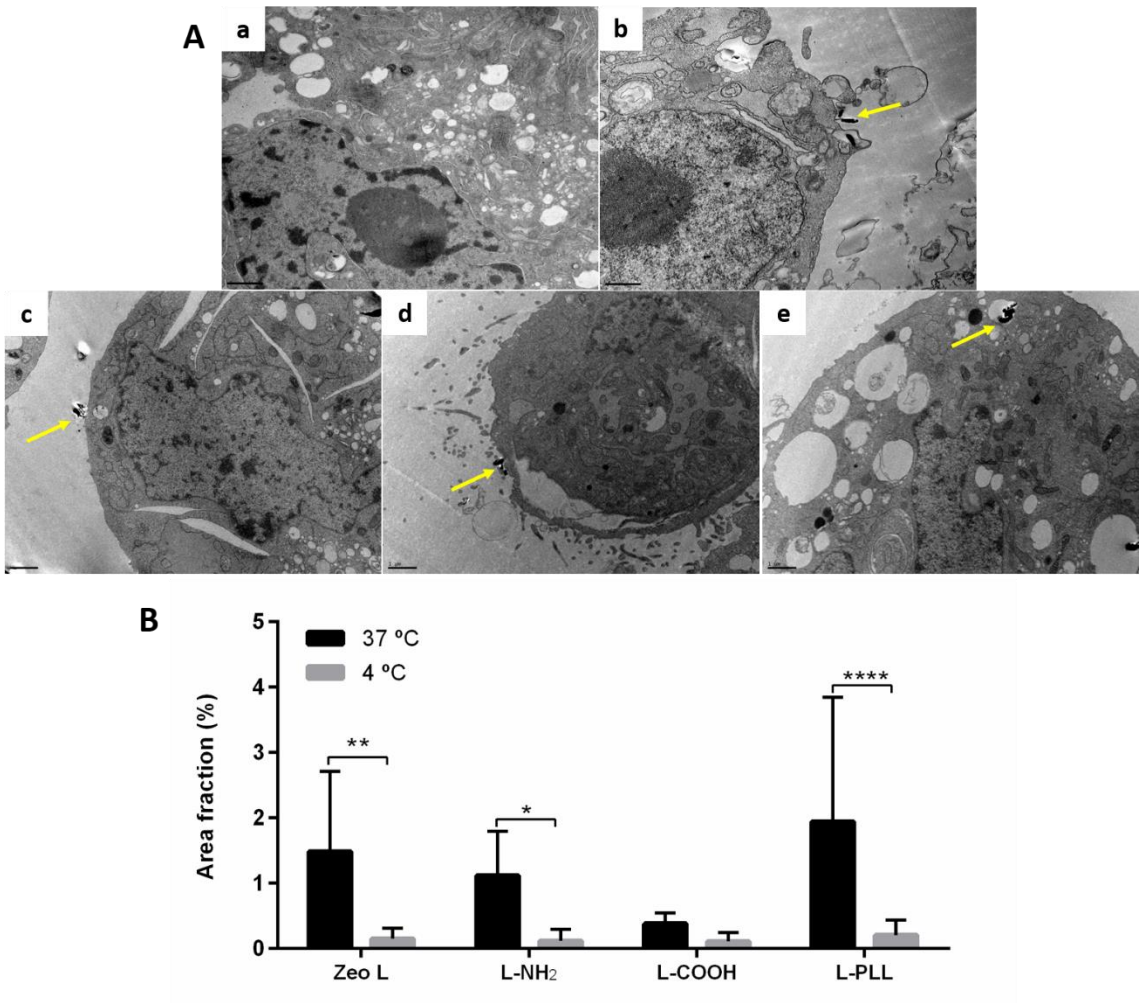

Figure 4.2.13: Effect of temperature on the internalization of materials by Hs 578T cells. Cells were pre-incubated at 4°C for 1 h and then treated with 50 µg mL^{-1} of Zeo L (b), L-NH_2 (c), L-COOH (d) and L-PLL (e) for 4 h. Unexposed cells were used as control (a). Images of cells are showed at a magnification of 12.000× (a, c, d and e) and 15.000× (b). Yellow arrows point toward some particles. Scale bar = 1 µm. B) Quantification of the percentage of zeolite L nanoparticles internalized by Hs 578T cells at 37 and 4 °C. *$p < 0.05$, **$p < 0.01$ and ****$p < 0.0001$ (n=10).

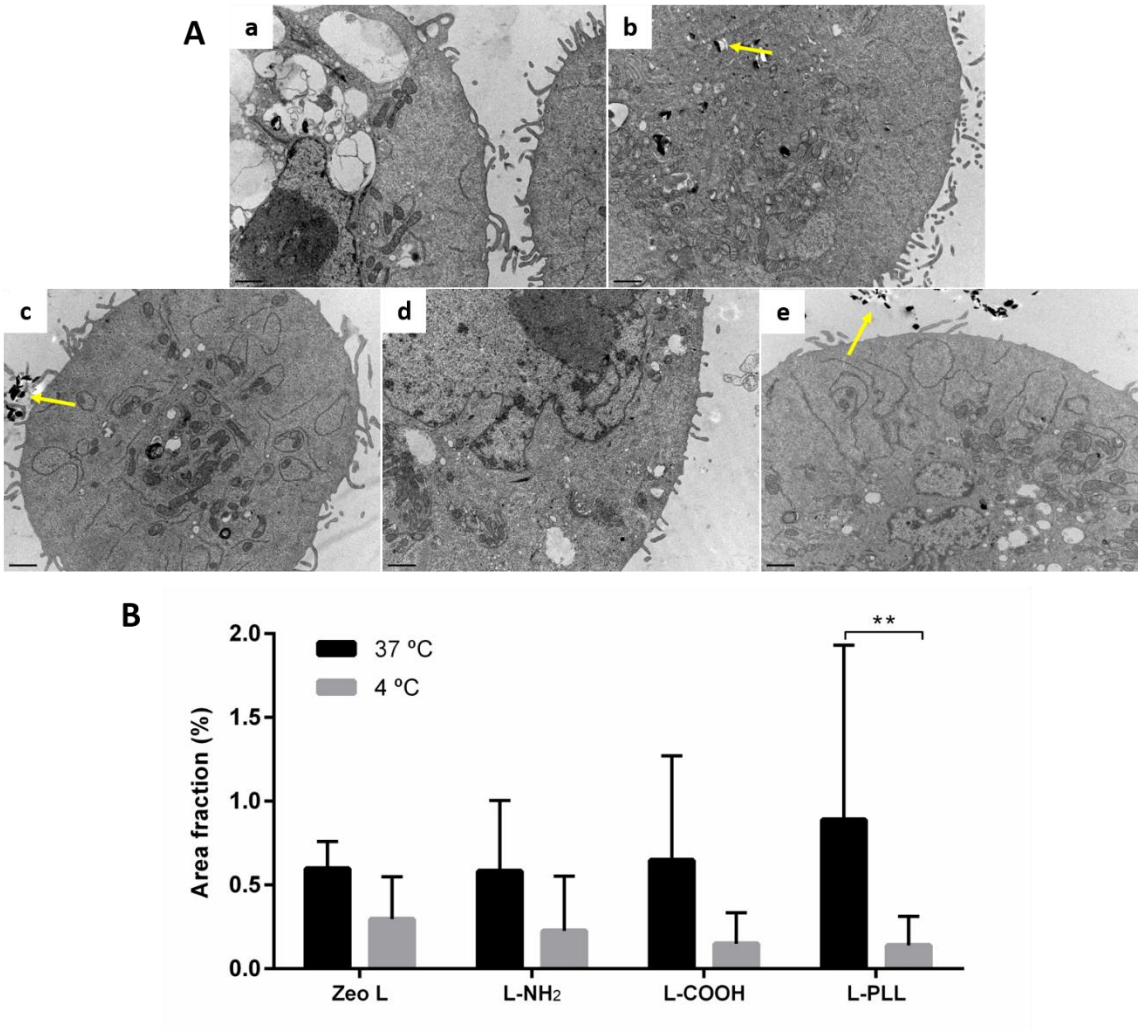

Figure 4.2.14: A) Effect of temperature on the internalization of materials by MCF-10 cells. Cells were pre-incubated at 4 °C for 1 h and then treated with 50 µg mL^{-1} of Zeo L (b), L-NH_2 (c), L-COOH (d) and L-PLL (e) for 4 h. Unexposed cells were used as control (a). Images of cells are showed at a magnification of 12.000× (a, c, d and e) and 15.000× (b). Yellow arrows point toward some particles. Scale bar = 1 µm. B) Quantification of the percentage of zeolite L nanoparticles internalized by MCF-10 cells at 37 and 4 °C. *$p < 0.05$ (n=10).

In SEM results (Figure 4.2.15 and 4.2.16) it is also possible to observe a reduction on cellular filopodia in both cell lines. Some nanoparticles seem to be internalized, however most of them are located around the cellular membrane.

From this study, it is possible to conclude that for the internalization of the parent and the modified zeolite L by Hs 578T and MCF-10 cells, the presence of filopodia and protein activity is needed since at low temperature the internalization is significantly reduced.

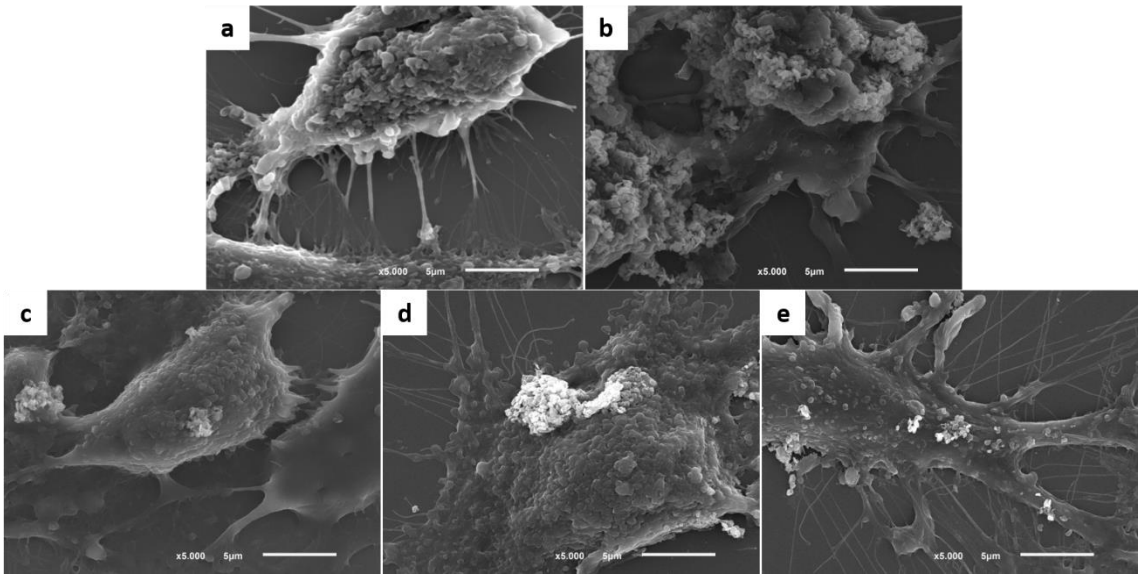

Figure 4.2.15: SEM images of Hs 578T cells incubated for 4 h at 4 °C with 50 µg mL^{-1} of b) Zeo L, c) L-NH_2, d) L-COOH and e) L-PLL. Unexposed cells were used as control (a).

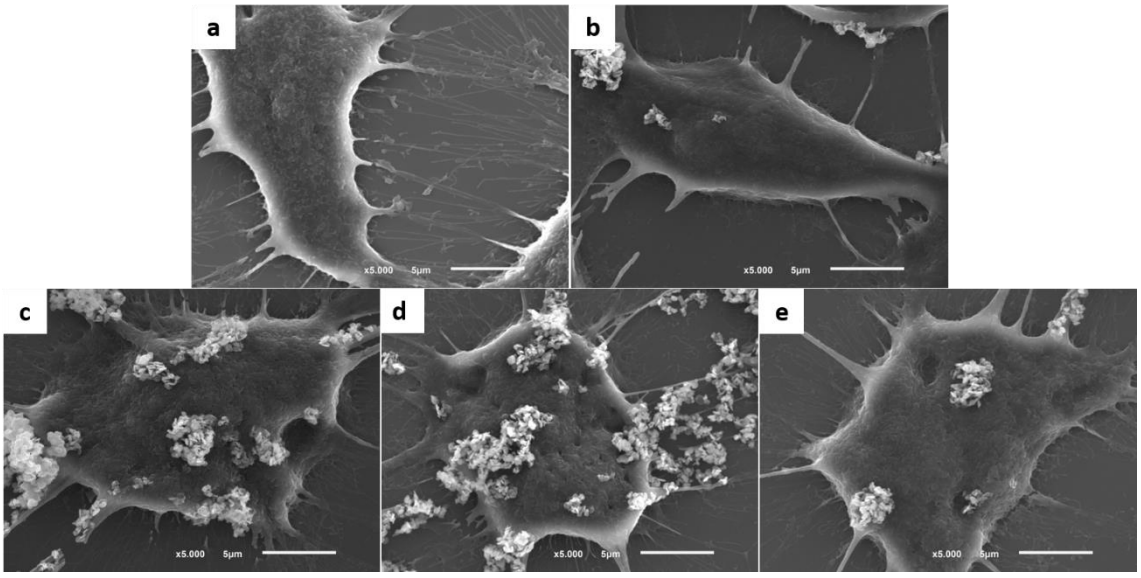

Figure 4.2.16: SEM micrographs of MCF-10 cells incubated for 4 h at 4 °C with 50 µg mL^{-1} of b) Zeo L, c) L-NH_2, d) L-COOH and e) L-PLL. Unexposed cells were used as control (a).

These results are in agreement with the results obtained using the different pharmacological inhibitors for zeolite L internalization which showed that the internalization of zeolite L by both studied cell lines is dependent on caveolin and microtubule polymerization since it was demonstrated that when the cells are exposed to low temperature conditions and the activity of proteins is reduced, the zeolite nanoparticles are less internalized.

Figure 4.2.17 depict the different endocytic pathways. The results of this study are represented by the step 4 highlighted in red.

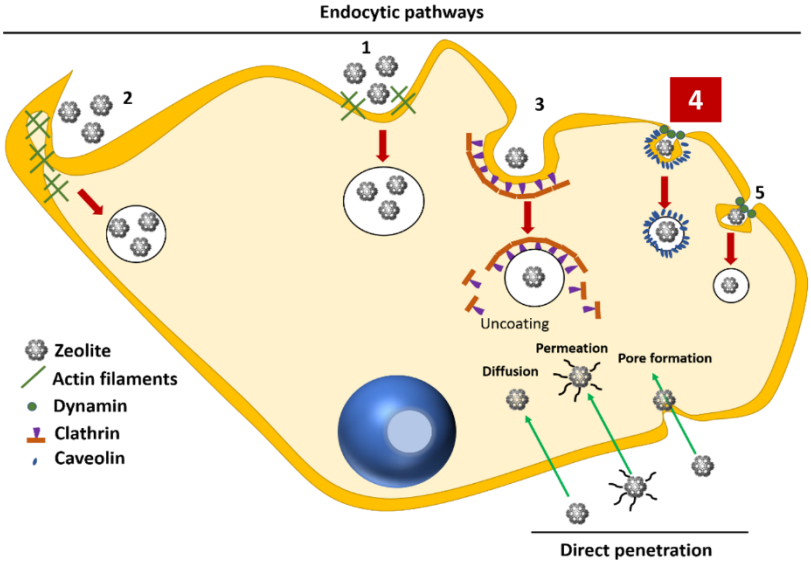

Figure 4.2.17: Different endocytic pathways. 1) Phagocytosis; 2) Macropinocytosis; 3) Clathrin-mediated endocytosis; 4) Caveolin-mediated endocytosis and 5) Clathrin- and caveolin- independent endocytosis.

Our results related to zeolite functionalization show that the different functional groups on zeolite L surface have an effect on the rate of internalization of nanoparticles, with positively charged nanoparticles being more internalized than those negatively charged.

4.2.4. CONCLUSIONS

In the present work, the parent zeolite L was modified by binding different groups to its outer surface and the effect of this functionalization in cultured cancer and normal cells was evaluated. The results demonstrate that the groups chosen for the surface functionalization of the zeolite nanoparticles are quite biocompatible since the nanomaterials are non-toxic to the cells. The uptake efficiency and endocytic pathways of zeolite L were also evaluated. We have shown how the surface charge affects the uptake of zeolite L by cancer and normal cells. The main endocytic pathway involved in the internalization of zeolite L in Hs 578T cells is caveolin-mediated, which confirms our previous results. Nevertheless, in this work we observed that microtubule polymerization also has some importance on zeolite L nanoparticle internalization into Hs 578T cells. From the studies with MCF-10 cells, we observed that there are two main endocytic pathways involved in zeolite L internalization, caveolin-mediated process and microtubule polymerization. Internalization of zeolite L by both Hs 578T and MCF-10 cells appears to be energy-dependent and the differences were more obvious for Hs 578T cancer cells than for MCF-10 cells, which proves that cellular uptake is cell type-dependent.

4.2.5. REFERENCES

1 R. Lehner, X. Wang, S. Marsch and P. Hunziker, Intelligent nanomaterials for medicine: Carrier platforms and targeting strategies in the context of clinical application, Nanomedicine Nanotechnology, Biol. Med., 2017, 9, 742–757.

2 J. I. Hare, T. Lammers, M. B. Ashford, S. Puri, G. Storm and S. T. Barry, Challenges and strategies in anti-cancer nanomedicine development: An industry perspective, Adv. Drug Deliv. Rev., 2017, 108, 25–38.

3 J. H. Lee and Y. Yeo, Controlled drug release from pharmaceutical nanocarriers, Chem. Eng. Sci., 2015, 125, 75–84.

4 A. Z. Wilczewska, K. Niemirowicz, K. H. Markiewicz and H. Car, Nanoparticles as drug delivery systems, Pharmacol. Reports, 2012, 64, 1020–1037.

5 T. Sun, Y. S. Zhang, B. Pang, D. C. Hyun, M. Yang and Y. Xia, Engineered nanoparticles for drug delivery in cancer therapy, Angew. Chemie - Int. Ed., 2014, 53, 12320–12364.

6 I. I. Slowing, B. G. Trewyn, V. S.-Y. S.-Y. Lin, I. I. Slowing, B. G. Trewyn, B. G. Trewyn, V. S.-Y. S.-Y. Lin and V. S.-Y. S.-Y. Lin, Effect of surface functionalization of MCM-41-type mesoporous silica nanoparticles on the endocytosis by human cancer cells., J Am Chem Soc, 2006, 128, 14792–14793.

7 G. Sahay, D. Y. Alakhova and A. V. Kabanov, Endocytosis of nanomedicines, J. Control. Release, 2010, 145, 182–195.

8 N. Oh and J.-H. Park, Endocytosis and exocytosis of nanoparticles in mammalian cells, Int. J. Nanomedicine, 2014, 9, 51–63.

9 B. D. Grant and J. G. Donaldson, Pathways and mechanisms of endocytic recycling, Nat. Rev. Mol. Cell Biol., 2009, 10, 597–608.

10 K. Murugan, Y. E. Choonara, P. Kumar, D. Bijukumar, L. C. du Toit and V. Pillay, Parameters and characteristics governing cellular internalization and trans-barrier trafficking of nanostructures., Int. J. Nanomedicine, 2015, 10, 2191–206.

11 D. Vercauteren, R. E. Vandenbroucke, A. T. Jones, J. Rejman, J. Demeester, S. C. De Smedt, N. N. Sanders and K. Braeckmans, The use of inhibitors to study endocytic pathways of gene carriers: optimization and pitfalls., Mol. Ther., 2010, 18, 561–569.

12 S. Guo, X. Zhang, M. Zheng, X. Zhang, C. Min, Z. Wang, S. H. Cheon, M. H. Oak, S. Y. Nah and K. M. Kim, Selectivity of commonly used inhibitors of clathrin-mediated and caveolae-dependent endocytosis of G protein-coupled receptors, Biochim. Biophys. Acta - Biomembr., 2015, 1848, 2101–2110.

13 L. Kou, J. Sun, Y. Zhai and Z. He, The endocytosis and intracellular fate of nanomedicines: Implication for rational design, Asian J. Pharm. Sci., 2013, 8, 1–10.

14 T.-G. Iversen, T. Skotland and K. Sandvig, Endocytosis and intracellular transport of nanoparticles: Present knowledge and need for future studies, Nano Today, 2011, 6, 176–185.

15 Z. Li, H. Jiang, C. Xu and L. Gu, A review: Using nanoparticles to enhance absorption and bioavailability of phenolic phytochemicals, Food Hydrocoll., 2015, 43, 153–164.

16 N. Vilaça, R. Amorim, A. F. Machado, P. Parpot, M. F. R. Pereira, M. Sardo, J. Rocha, A. M. Fonseca, I. C. Neves and F. Baltazar, Potentiation of 5-fluorouracil encapsulated in zeolites as drug delivery systems for in vitro models of colorectal carcinoma, Colloids Surfaces B Biointerfaces, 2013, 112, 237–244.

17 R. Amorim, N. Vilaça, O. Martinho, R. M. Reis, M. Sardo, J. Rocha, A. M. Fonseca, F. Baltazar and I. C. Neves, Zeolite structures loading with an anticancer compound as drug delivery systems, J. Phys. Chem. C, 2012, 116, 25642–25650.

18 N. Vilaça, A. F. Machado, F. Morais-Santos, R. Amorim, A. Patrícia Neto, E. Logodin, M. F. R. Pereira, M. Sardo, J. Rocha, P. Parpot, A. M. Fonseca, F. Baltazar and I. C. Neves, Comparison of different silica microporous structures as drug delivery systems for in vitro models of solid tumors, RSC Adv., 2017, 7, 13104–13111.

19 N. Vilaça, F. Morais-Santos, A. F. Machado, A. Sirkecioğlu, M. F. R. Pereira, M. Sardo, J. Rocha, P. Parpot, A. M. Fonseca, F. Baltazar and I. C. Neves, Micro- and mesoporous structures as drug delivery carriers for salicylic acid, J. Phys. Chem. C, 2015, 119, 3589–3595.

20 N. Vilaça, R. Totovao, E. A. Prasetyanto, V. Miranda-Gonçalves, F. Morais-Santos, R. Fernandes, F. Figueiredo, M. Banõbre-López, A. M. Fonseca, L. De Cola, F. Baltazar and I. C. Neves, Internalization studies on zeolite nanoparticles using human cells, J. Mater. Chem. B, 2018, 6, 469–476.

21 S. Męczyńska-Wielgosz, A. Piotrowska, A. Majkowska-Pilip, A. Bilewicz and M. Kruszewski, Effect of Surface Functionalization on the Cellular Uptake and Toxicity of Nanozeolite A, Nanoscale Res. Lett., 2016, 11, 123–136.

22 A. K. Gupta and M. Gupta, Cytotoxicity suppression and cellular uptake enhancement of surface modified magnetic nanoparticles, Biomaterials, 2005, 26, 1565–1573.

23 M. R. Lorenz, V. Holzapfel, A. Musyanovych, K. Nothelfer, P. Walther, H. Frank, K. Landfester, H. Schrezenmeier and V. Mailänder, Uptake of functionalized, fluorescent-labeled polymeric particles in different cell lines and stem cells, Biomaterials, 2006, 27, 2820–2828.

24 C. Graf, Q. Gao, I. Schütz, C. N. Noufele, W. Ruan, U. Posselt, E. Korotianskiy, D. Nordmeyer, F. Rancan, S. Hadam, A. Vogt, J. Lademann, V. Haucke and E. Rühl, Surface functionalization of silica nanoparticles supports colloidal stability in physiological media and facilitates internalization in cells, Langmuir, 2012, 28, 7598–7613.

25 T. Xia, M. Kovochich, M. Liong, H. Meng, S. Kabehie, S. George, J. I. Zink, A. E. Nel, J. Z. I, A. E. Nel, S. George, J. I. Zink and A. E. Nel, Polyethyleneimine Coating Enhances the Cellular Uptake of Mesoporous Silica Nanoparticles and Allows Safe Delivery of siRNA and DNA Constructs, ACS Nano, 2009, 3, 3273–3286.

26 T. Posati, F. Bellezza, L. Tarpani, S. Perni, L. Latterini, V. Marsili and A. Cipiciani, Selective internalization of ZnAl-HTlc nanoparticles in normal and tumor cells. A study of their potential use in cellular delivery, Appl. Clay Sci., 2012, 55, 62–69.

27 O. Maniti, E. Blanchard, G. Trugnan, A. Lamazire and J. Ayala-Sanmartin, Metabolic energy-independent mechanism of internalization for the cell penetrating peptide penetratin, Int. J. Biochem. Cell Biol., 2012, 44, 869–875.

28 S. Kumari, S. Mg and S. Mayor, Endocytosis unplugged: multiple ways to enter the cell, Cell Res., 2010, 20, 256–275.

29 S. Mayor and R. E. Pagano, Pathways of clathrin-independent endocytosis, Nat. Rev. Mol. Cell Biol., 2007, 8, 603–612.

30 A. Gräslund, F. Madani, S. Lindberg, Ü. Langel and S. Futaki, Mechanisms of cellular uptake of cell-penetrating peptides, J. Biophys., 2011, 2011, 414729.

31 O. Bossart, L. De Cola, S. Welter and G. Calzaferri, Injecting electronic excitation energy into an artificial antenna system through an Ru2+ complex, Chem. - A Eur. J., 2004, 10, 5771–5775.

32 S. Megelski and G. Calzaferri, Tuning the Size and Shape of Zeolite L-Based Inorganic-Organic Host-Guest Composites for Optical Antenna Systems, Adv. Funct. Mater., 2001, 11, 277–286.

33 A. Bertucci, H. Lülf, D. Septiadi, A. Manicardi, R. Corradini and L. De Cola, Intracellular Delivery of Peptide Nucleic Acid and Organic Molecules Using Zeolite-L Nanocrystals., Adv. Healthc. Mater., 2014, 1–6.

34 R. A. McCloy, S. Rogers, C. E. Caldon, T. Lorca, A. Castro and A. Burgess, Partial inhibition of Cdk1 in G(2) phase overrides the SAC and decouples mitotic events, Cell Cycle, 2014, 13, 1400–1412.

35 A. Petushkov, N. Ndiege, A. K. Salem and S. C. Larsen, in Advances in Molecular Toxicology, ed. J. C. Fishbein, Elsevier, 2010, vol. 4, pp. 223–266.

36 M. Spanakis, N. Bouropoulos, D. Theodoropoulos, L. Sygellou, S. Ewart, A. M. Moschovi, A. Siokou, I. Niopas, K. Kachrimanis, V. Nikolakis, P. A. Cox, I. S. Vizirianakis and D. G. Fatouros, Controlled release of 5-fluorouracil from microporous zeolites, Nanomedicine Nanotechnology, Biol. Med., 2014, 10, 197–205.

37 M. G. Rimoli, M. R. Rabaioli, D. Melisi, A. Curcio, S. Mondello, R. Mirabelli and E. Abignente, Synthetic zeolites as a new tool for drug delivery, J. Biomed. Mater. Res. - Part A, 2008, 87, 156–164.

38 J. A. Daniel, N. Chau, M. K. Abdel-Hamid, L. Hu, L. von Kleist, A. Whiting, S. Krishnan, P. Maamary, S. R. Joseph, F. Simpson, V. Haucke, A. McCluskey and P. J. Robinson, Phenothiazine-Derived Antipsychotic Drugs Inhibit Dynamin and Clathrin-Mediated Endocytosis, Traffic, 2015, 16, 635–654.

39 K. M. Hussain, K. L. J. Leong, M. M.-L. Ng and J. J. H. Chu, The essential role of clathrin-mediated endocytosis in the infectious entry of human enterovirus 71., J. Biol. Chem., 2011, 286, 309–21.

40 M. Forte, G. Iachetta, M. Tussellino, R. Carotenuto, M. Prisco, M. De Falco, V. Laforgia and S. Valiante, Polystyrene nanoparticles internalization in human gastric adenocarcinoma cells, Toxicol. Vitr., 2016, 31, 126–136.

41 Z. Garaiova, S. P. Strand, N. K. Reitan, S. Lélu, S. T. Størset, K. Berg, J. Malmo, O. Folasire, A. Bjørkøy and C. De L. Davies, Cellular uptake of DNA-chitosan nanoparticles: The role of clathrin- and caveolae-mediated pathways, Int. J. Biol. Macromol., 2012, 51, 1043–1051.

42 J. M. Steinbach, Y.-E. Seo and W. M. Saltzman, Cell penetrating peptide-modified poly(lactic-co-glycolic acid) nanoparticles with enhanced cell internalization., Acta Biomater., 2016, 30, 49–61.

43 R. Pan, W. Xu, Y. Ding, S. Lu and P. Chen, Uptake Mechanism and Direct Translocation of a New CPP for siRNA Delivery, Mol. Pharm., 2016, 13, 1366–1374.

44 M. A. E. M. van der Aa, U. S. Huth, S. Y. Häfele, R. Schubert, R. S. Oosting, E. Mastrobattista, W. E. Hennink, R. Peschka-Süss, G. A. Koning and D. J. A. Crommelin, Cellular Uptake of Cationic Polymer-DNA Complexes Via Caveolae Plays a Pivotal Role in Gene Transfection in COS-7 Cells, Pharm. Res., 2007, 24, 1590–1598.

45 J. Dausend, A. Musyanovych, M. Dass, P. Walther, H. Schrezenmeier, K. Landfester and V. Mailänder, Uptake Mechanism of Oppositely Charged Fluorescent Nanoparticles in HeLa Cells, Macromol. Biosci., 2008, 8, 1135–1143.

46 T. H. Chung, S. H. Wu, M. Yao, C. W. Lu, Y. S. Lin, Y. Hung, C. Y. Mou, Y. C. Chen and D. M. Huang, The effect of surface charge on the uptake and biological function of mesoporous silica nanoparticles in 3T3-L1 cells and human mesenchymal stem cells, Biomaterials, 2007, 28, 2959–2966.

47 R. Marega, E. A. Prasetyanto, C. Michiels, L. De Cola and D. Bonifazi, Fast Targeting and Cancer Cell Uptake of Luminescent Antibody-Nanozeolite Bioconjugates, Small, 2016, 12, 5431–5441.

48 L. Henriksen, M. V. Grandal, S. L. J. Knudsen, B. van Deurs and L. M. Grøvdal, Internalization mechanisms of the epidermal growth factor receptor after activation with different ligands., PLoS One, 2013, 8, e58148.

49 Y. An, M. Chen, Q. Xue and W. Liu, Preparation and self-assembly of carboxylic acid-functionalized silica, J. Colloid Interface Sci., 2007, 311, 507–513.

50 S. Kralj, M. Drofenik and D. Makovec, Controlled surface functionalization of silica-coated magnetic nanoparticles with terminal amino and carboxyl groups, J. Nanoparticle Res., 2011, 13, 2829–2841.

51 I. Khmara, M. Koneracka, M. Kubovcikova, V. Zavisova, I. Antal, K. Csach, P. Kopcansky, I. Vidlickova, L. Csaderova, S. Pastorekova and M. Zatovicova, Preparation of poly-L-lysine functionalized magnetic nanoparticles and their influence on viability of cancer cells, J. Magn. Magn. Mater., 2017, 427, 114–121.

52 E. L. da Rosa, Kinetic effects of TiO2 fine particles and nanoparticles aggregates on the nanomechanical properties of human neutrophils assessed by force spectroscopy, BMC Biophys., 2013, 6, 11.

53 N. S. Kehr, B. Ergün, H. Lülf and L. De Cola, Spatially controlled channel entrances functionalization of zeolites l, Adv. Mater., 2014, 26, 3248–3252.

54 E. Huerta-García, S. G. Márquez-Ramírez, M. del P. Ramos-Godinez, A. López-Saavedra, L. A. Herrera, A. Parra, E. Alfaro-Moreno, E. O. Gómez and R. López-Marure, Internalization of titanium dioxide nanoparticles by glial cells is given at short times and is mainly mediated by actin reorganization-dependent endocytosis, Neurotoxicology, 2015, 51, 27–37.

55 F. Danhier, To exploit the tumor microenvironment: Since the EPR effect fails in the clinic, what is the future of nanomedicine?, J. Control. Release, 2016, 244, 108–121.

56 J. Gautier, E. Allard-Vannier, E. Munnier, M. Soucé and I. Chourpa, Recent advances in theranostic nanocarriers of doxorubicin based on iron oxide and gold nanoparticles, J. Control. Release, 2013, 169, 48–61.

57 A. Schroeder, D. A. Heller, M. M. Winslow, J. E. Dahlman, G. W. Pratt, R. Langer, T. Jacks and D. G. Anderson, Treating metastatic cancer with nanotechnology, Nat. Rev. Cancer, 2011, 12, 39–50.

58 E. Fröhlich, The role of surface charge in cellular uptake and cytotoxicity of medical nanoparticles, Int. J. Nanomedicine, 2012, 7, 5577–5591.

59 B. B. S. Cerqueira, A. Lasham, A. N. Shelling and R. Al-Kassas, Nanoparticle therapeutics: Technologies and methods for overcoming cancer, Eur. J. Pharm. Biopharm., 2015, 97, 140–151.

60 C. Wilhelm, C. Billotey, J. Roger, J. N. Pons, J. C. Bacri and F. Gazeau, Intracellular uptake of anionic superparamagnetic nanoparticles as a function of their surface coating, Biomaterials, 2003, 24, 1001–1011.

61 T. dos Santos, J. Varela, I. Lynch, A. Salvati and K. A. Dawson, Effects of Transport Inhibitors on the Cellular Uptake of Carboxylated Polystyrene Nanoparticles in Different Cell Lines, PLoS One, 2011, 6, e24438.

62 S. Vranic, N. Boggetto, V. Contremoulins, S. Mornet, N. Reinhardt, F. Marano, A. Baeza-Squiban and S. Boland, Deciphering the mechanisms of cellular uptake of engineered nanoparticles by accurate evaluation of internalization using imaging flow cytometry, Part. Fibre Toxicol., 2013, 10, 2–17.

63 P. K. Mattila and P. Lappalainen, Filopodia: molecular architecture and cellular functions, Nat. Rev. Mol. Cell Biol., 2008, 9, 446–454.

64 D. Vignjevic, M. Schoumacher, N. Gavert, K.-P. Janssen, G. Jih, M. Laé, D. Louvard, A. Ben-Ze'ev and S. Robine, Fascin, a novel target of beta-catenin-TCF signaling, is expressed at the invasive front of human colon cancer., Cancer Res., 2007, 67, 6844–6853.

65 A. M. Bannunah, D. Vllasaliu, J. Lord and S. Stolnik, Mechanisms of nanoparticle internalization and transport across an intestinal epithelial cell model: effect of size and surface charge, Mol Pharm, 2014, 11, 4363–4373.

CHAPTER 5

CONCLUSIONS AND FUTURE WORK

In this final chapter, a general overview of the major findings of the work developed under the scope of the thesis is given, highlighting the relationship between the results presented in all chapters and subchapters and the most relevant conclusions. Finally, some ideas for the future work are also proposed.

5.1. GENERAL OVERVIEW AND CONCLUDING REMARKS

5.1.1 GENERAL OVERVIEW

The increasing number of new cases of cancer encourages the search for new methodologies for cancer detection or treatment. Thus, different approaches have been developed to target therapy for specific human sites/tissues. One of them is the use of nanomaterials as carriers for drug delivery systems (DDS). These DDS have expanded rapidly with new advances in biomedical sciences and this is a field of vital importance in medicine and healthcare. An ideal DDS is a system that should prevent premature degradation of the therapeutic agents, improve their bioavailability, enhance the efficacy and increase the tolerability of the drugs. Also, the carrier must maintain drug concentrations within their therapeutic window, by controlling the drug release rates, and reach the specific target(s) – such as tumor cells and tumor tissue - to enhance their accumulation in the target environment and increase their penetration in cells, with low cytotoxicity.

In this context, organic and inorganic nanomaterials, as polymeric nanoparticles, liposomes, dendrimers, magnetic nanoparticles, mesoporous nanoparticles and zeolite structures, have a range of structural and physical properties that are suitable for therapeutic delivery systems. The diverse and highly controlled structural properties of zeolites as nanostructures make them interesting candidates for a variety of medical and healthcare applications, so it is important to understand their effect *in vitro* and *in vivo*. Another important challenge is to understand the mechanisms related to the internalization of these zeolite nanoparticles by cells. During this work, different approaches were explored: i) how small drug molecules interact with zeolites and the interaction with mesoporous silica structures was also compared; ii) how DDS prepared with these porous structures act *in vitro* and *in vivo* iii) how zeolites act as magnetic resonance imaging agents; iv) how zeolite nanoparticles interact with living cells; and v) how the functionalization of zeolite surface could influence the uptake by human cells.

5.1.2. CONCLUDING REMARKS

This work is a continuation of the line of research of our group, from which the potential of DDS based in zeolites for colorectal cancer treatment was already reported. Thus, in this work, in addition of the evaluation of the effect of DDS on colorectal cancer, their potential was also investigated in breast cancer treatment.

In the last years, some literature data has been showing the correlation between the use of anti-inflammatory drugs and reduced incidence of cancer. Thus, this work started by the exploration of the use of salicylic acid (SA) for breast cancer treatment. For this purpose, salicylic acid was loaded into zeolite (NaY) and mesoporous structures (MCM-41 and SBA-

15), resulting in three different DDS, SA@NaY, SA@MCM-41, and SA@SBA-15. It was observed that mesoporous structures loaded more efficiently SA molecule than the zeolite structure. The found differences could be explained by the different pore size of the structures. NaY has smaller pores than mesoporous structures, being expected lower loading capacity. From the drug release studies performed in simulated body fluid at 7.4 and 37 °C, we demonstrated that in the first 15 min, there was an initial burst with around 50% of drug released. The kinetics of these studies demonstrated that the release of SA from NaY fits the Korsmeyer-Peppas model, while Higuchi model fits the release from mesoporous structures. The drug bioactivity studies, carried out in two breast cancer cell lines (Hs 578T and MDA-MB-468), demonstrated that SA@MCM-41 and SA@SBA-15 were able to decrease cell growth of both cell lines, while SA@NaY did not ehibit any effect on cell viability. Mesoporous structures were the most promising among the porous structures tested, when both loading capacity and antitumor activity were considered. However, bearing in mind that the major objective of this work was to explore the potential of zeolites as DDS, NaY was chosen to be explored in further studies in order to select the best DDS, using a classical anticancer drug, 5-fluorouracil (5-FU).

We further explored the use of zeolite NaY as host for DDS preparation with 5-FU for *in vitro* models of colorectal and breast cancer, comparing them with other zeolitic structures (NaA and ZSM5) and one titanosilicate (ETS-10). Compared to NaA and ZSM5, which have small and medium pores respectively, NaY presents large pores. Similarly, in the SA study, it was observed that the pore size has influence in the loading of 5-FU into the hosts. NaY and ETS-10 (large pores) loaded higher amounts of 5-FU than the other zeolitic structures. Drug release studies, conducted at pH 7.4, 5.8 and 2.0 to mimic the pH of blood, intestine, and stomach, also demonstrated the effect of pore size on drug release. It was found that large pore structures have highest release rates due to the higher amount of adsorbed drug. The integrity of the molecular structure of 5-FU was maintained in all tested pH values, and the pH did not affect 5-FU release. These findings, show that silica structures could protect the drug from the body fluids. Parent zeolites are non-toxic for colon cancer and breast cancer cells, since they did not affect cell viability/growth. In the whole, the DDS used have proven to be effective on reduction of cell viability and potentiation of 5-FU.

In the part of the thesis where we explored the use of zeolites as hosts for drug loading, were selected zeolite NaY and a synthetized disc-shaped zeolite L (LTL structure) for further studies. 5-FU was successfully loaded into these zeolites. *In vitro* studies revealed that both parent zeolites are non-toxic for cells, while DDS reduced cell viability of Hs 578T and RKO cells significantly. It is known that smaller particles (< 100 nm) could be used for systemic administration, while larger particles (> 100 nm) will have more potential for topical administration. Also, the colloidal stability is an important factor for intravenous administration.

All zeolite structures used in this work, had particles higher than 100 nm and did not present a good colloidal stability.

In addition to colorectal and breast cancer cells, we investigated the effect of DDS *in vitro* in melanoma cells in order to explore the potential of these materials for topical applications. The obtained results suggest that these materials are promising for topical applications since the DDS reduce cell viability of melanoma cancer cells in a significant way. The *in vivo* viability assays of the DDS was performed using the chick embryo chorioallantoic membrane as model (CAM) for breast and colon cancer cells implantation. Thus, the DDS induced a reduction in tumor perimeter for Hs 578T cells, while no reduction was detected for RKO tumors, under the concentration of DDS used. In addition to the concentration used, penetration of the DDS should also be more difficult in 3D tumor structures, which may explain the lack of effect in RKO tumors.

The results obtained from these studies showed that beyond the type of zeolitic structure selected for DDS preparation, the efficacy of DDS is quite dependent on the cell type and the features of the tumors. Nevertheless, independently of these factors, overall, the results presented in this thesis demonstrated the potential of zeolites for DDS preparation.

Consequently, we went deeper into the use of zeolites for biomedical applications, exploring the potential of these structures as hybrid materials to be used in magnetic resonance imaging (MRI) or hyperthermia treatments. Thus, the reaction between zeolite NaY and the magnetic nanoparticles led to attachment of the magnetic nanoparticles on the zeolite surface (MZNCs), which was confirmed through different characterization techniques. The possibility of zeolite NaY magnetization to be used as MRI contrast agent, was assessed by analyze of T_2-weighted on Hs 578T cells. It was observed that T_2 signal intensity decreases as iron concentration increases, being lower for MZNCs, exhibiting darker MRI images in the condition corresponding to cells incubated with MZNC.

MZNCs have proved to be non-toxic to breast cancer and epithelial mammary cells, showing less cytotoxicity than the parent zeolite. It was also proved by TEM that MZNCs are able to be internalized by cells. These results confirm the potential of zeolite NaY to be used as MRI agent. Combining the potential of zeolites as DDS with the results obtained in this work, and after the optimization of colloidal properties of zeolites, it is expected that zeolites could be used in hyperthermia for cancer therapy enhancing the efficacy of the drugs.

Another main purpose of this work was the assessment of the endocytic pathways involved in the zeolite internalization by cells. It was verified that MZNCs are able to be internalized by cells. So, we also studied how the parent zeolites interact with living cells. Zeolite L used in these studies was successfully synthesized, originating disc-shaped nano particles with 400 nm. Thanks to its features, this zeolite has lower tendency to form aggregates than NaY. It was observed that after 5 min of incubation the cells started already to engulf NaY, while zeolite

L have some nanoparticles already internalized for the same time period. These results demonstrate the importance of the shape of the particles in the internalization process. In addition to zeolite shape, another aspect which influences nanoparticles internalization, is the cell type. Comparing the internalization rate in different cell lines under the same incubation conditions, we observed that cancer cells are faster in zeolite nanoparticle internalization, compared to normal cells. The high internalization rate observed for the cancer cells, must be related not only to their higher permeability, but also to their faster growth and higher metabolic rates than normal cells, whose growth is slower. Six pharmacological inhibitors were used to determine the endocytic pathway involved in the zeolite nanoparticle internalization by the selected cell lines. From all the inhibitors used, only the inhibitors of caveolin-dependent endocytosis and microtubule dependent pathways affected cell internalization, which demonstrates that in the studied cell lines, zeolite nanoparticles are internalized via a caveolin-mediated process and this internalization is also dependent on microtubule polymerization.

The surface chemistry of the zeolites plays also an important role in their uptake by cells. Normally, positive charged materials are more internalized by cells due to the negative charge of the cell membrane. Our findings also support this trend, with positively-charged zeolites being higher internalized than negatively-charged zeolites. It was also found that the internalization is time-dependent with higher quantity of zeolite nanoparticles internalized after 24 h of incubation than at 4 h.

Summarily, the use of zeolite structures as carriers for DDS revealed to be a promising approach, however it is highly influenced by the surface chemistries, forms and sizes of zeolite nanoparticles and cell type. Also, this thesis highlights the importance to better understand the endocytic mechanisms underlying zeolite internalization to design more efficient targeted DDS and enhance the potential of zeolites to be used in different biomedical approaches.

5.2. FUTURE WORK

DDS preparation using zeolite structures as hosts has been denoted as a promising approach and this thesis contributed with important findings to understand how zeolite nanoparticles interacts with living cells. However, their *in vivo* application and toxicity remains challenging and more experimental work should be carried out to provide further insights on the use of these materials in cancer therapy.

In the preliminary studies, it was observed that salicylic acid is suitable to be used in breast cancer treatment when loaded into mesoporous silica. In order to improve the effect of this drug into the zeolite DDS, additional zeolitic structures should be evaluated.

Taking into account the achievements with 5-FU loaded into the zeolite structures and the good results obtained with salicylic acid loaded into mesoporous structures, the combination of the drugs loaded into the zeolite structures should be explored, as a combined therapy. For that purpose and considering the promising results obtained with 5-FU, it should be also combined with other chemotherapeutic drugs, such as paclitaxel or doxorubicin, to take advantage of the synergic effect of both drugs and improve the effect against cancer cells.

In order confirm of the internalization mechanisms, the endocytic pathways should be studied in other cell lines to verify if the same pathways are used by zeolites to enter different cells. Also, the internalization pathways used by other zeolites should be studied, to verify if the internalization pathways are dependent of the zeolite structures. Specific details as to how the endocytic proteins might affect the internalization of zeolite nanoparticles warrant further studies. For this purpose it would also be relevant to confirm the effect of the pharmacological inhibitors through downregulation of specific endocytic proteins involved in zeolite internalization.

Although zeolite functionalization with positive groups enhances its cellular uptake *in vitro*, *in vivo* tumor accumulation should be studied. Furthermore, zeolite surface should be functionalized with other ligands, such as antibodies, in order to target them to specific places.

In vivo studies using the CAM model should be optimized and additional *in vivo* models such as the murine model (mice xenografts) should be used, to study the effect of zeolite and DDS *in vivo*. In these studies, in addition to the effect of the DDS in tumor reduction, cancer cell proliferation, invasion and angiogenesis, should be also evaluated. It would be also important to assess the formation of reactive oxygen species (ROS) to understand if these materials can induce formation of free-radicals and consequently induce oxidative stress.

The possible bioaccumulation of zeolites as hosts is also still a challenge to be tackled to understand if these materials can be eliminated from the body or if they need to be modified to avoid bioaccumulation in the liver.

Taking into account the promising results obtained with melanoma cells, topical applications of DDS based on zeolites should be further explored, since the skin cancer incidence has been increasing over the last years and it is estimated that the frequency of this type of cancer increases as a result of increased exposure to solar UV radiation.